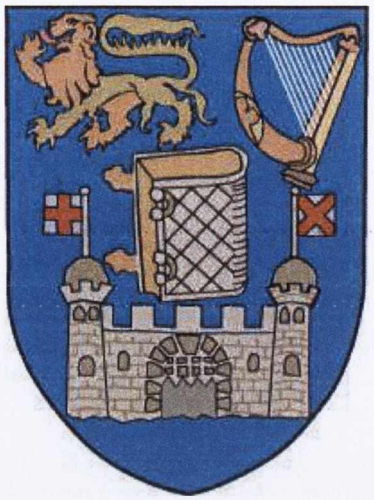

Electron correlation and magnetism in molecules and solids

By

Andrea Droghetti

A thesis submitted for the degree of
Doctor of Philosophy
School of Physics
Trinity College Dublin

October 2011

Declaration

I, Andrea Droghetti, hereby declare that this dissertation has not been submitted as an exercise for a degree at this or any other University.

It comprises work performed entirely by myself during the course of my Ph.D. studies at Trinity College Dublin. I was involved in a number of collaborations, and where it is appropriate my collaborators are acknowledged for their contributions.

A copy of this thesis may be lended or copied by the Trinity College Library upon request by a third party provided it spans single copies made for study purposes only, subject to normal conditions of acknowledgement.

Abstract

In order to understand the magnetic properties of solids and molecules, an accurate description of the underlying microscopic many-electron systems is required. This can be achieved through several theoretical and computational methods, which account for the electron-electron interactions and for quantum effects within different levels of approximation. In this thesis, we apply some of these methods [density functional theory (DFT), Hartree-Fock (HF), random phase approximation (RPA), continuum and lattice quantum Monte Carlo (QMC)] to the study of various problems of current interest within the field of spintronics.

First we investigate the physics of defects in wide-gap oxide and nitride materials in order to understand the puzzling experimental reports of ferromagnetism in undoped thin-films and nanoparticles (often called d^0 magnetism). We show that these cannot be explained by a simple picture in which magnetic interactions between hole centers percolate through the sample.

We then introduce the Anderson-Hubbard model, which describes correlated electrons in narrow impurity bands. The magnetic properties are studied with HF and the RPA. We attempt to relate some of our results to the physics of d^0 magnets and, more generally, of diluted magnetic materials. For such a model, many quantities can be accurately calculated by using the, so called, auxiliary field QMC method. Therefore, this is presented and the details of our own implementation are briefly discussed.

Finally we move our attention from solids to molecules and we analyze the issues related to the correct description of the electronic and magnetic properties of Fe^{2+} molecules. Results of DFT calculations are benchmarked with those of continuum QMC calculations revealing that even advanced developments of DFT systematically fail in describing the electronic structure of these systems. Furthermore we point out how the magnetic ground state depends strongly on the crystalline environment. Ultimately we predict that, for a related class of molecules, called cobalt-dioxolenes, the valence tautomeric interconversion (i.e. the intercorversion between two different

isomers with the Co ion in different oxidation and magnetic states) can be controlled by applying an external electric field.

Acknowledgments

During the course of my postgraduate studies I received help and support from a large number of people, without whom none of this research would have been possible.

First of all, I would like to thank my supervisor Prof. Stefano Sanvito. I have benefited greatly from his advice and teaching during my time in his research group. He has continuously provided new and interesting topics for my research and I have deeply admired his natural ability to look at every problem from a very intuitive and phenomenological point of view. Furthermore he has always shown deep appreciation for my work and he has actively encouraged my rapidly growing interest for many-particle physics and quantum Monte Carlo techniques.

I would like then to thank our external collaborators. Firstly, Prof. Roberta Sessoli and Dr. Giordano Poneti, who have introduced me to the physics and chemistry of cobalt-dioxolone molecules. I am also very grateful for their kind hospitality during my visit in Florence and for the careful reading of one of our manuscripts. Secondly, I would like to thank Prof. Dario Alfè, that I had occasion to visit in University College London. Our on-going work on spin-transition molecules would have not been possible without his valuable help and his technical expertise in continuum quantum Monte Carlo methods. Finally I must mention Dr. Cristian Degli Esposti Boschi, previously in Unversity of Bologna and now in CNR, for useful discussions about strongly correlated electronic systems and for constantly showing interest for my studies here in Dublin.

Stefano's group has grown large and it currently counts several postdocs and postgraduate students. Among them I must mention Dr. Ivan Rungger and Dr. Chaitanya Das Pemmaraju. Through their constant teaching I have learnt how to perform density functional theory calculations and how to relate the results to experiments. Furthermore I am deeply grateful for their patience and kindness while helping me to solve many computational issues and for constantly providing good advice and support to my research.

I must then thank Dr. Thomas Archer (who was our system administrator during my

first year within the group and who still represents the go-to-guy for every computer related problem), Dr. Nadjib Baadji (whose insights into the physics of magnetic molecules have been very useful), Dr. Akinlolu Akande, (with whom I had many interesting discussions about the Hubbard model), and a new student, Awadhesh Narayan (that I helped in the very early stage of his research and whose curiosity has been source of inspiration for many new studies).
Many other postgraduate students within the group have provided useful advice for my research and, moreover, have been good friends through these years. These are Sankar Kusanakurthi (with whom I shared a nice flat for long time and who is now back home trying to become a famous movie director), Mauro "Magneta" Mantega, and Sandip Bhattacharya (who constantly drag me to parties), Aaron Hurley (who introduced me to Irish sports), Nuala Caffrey and her boyfriend Stephen Power (with whom I have shared the hobby of hiking).
Other members of the group include Amaury de Melo Souza, Dr. Igor Popov and all those I have shared the office with during these four years: Anna Pertsova, Kapildeb Dolui, Thomas Cathcart and Dr. Maria Stamenova. Furthermore I must mention the former members of the group: Ruairi Hanafin, Cormac Toher and Alex Rocha.

It would not be possible to undertake research such as this without funding. The Science Foundation of Ireland and the European Union paid my fees and maintenance, and also provided support for attending conferences. The calculations presented in this thesis were performed in the Trinity Centre for High Performance Computing (TCHPC) and the Irish Centre for High End Computing. The staff from TCHPC, particularly Jimmy Tang, who worked as system administrator for a few years, also provided technical assistance both on their cluster s well as on our own internal network.

Finally I deeply thank my lovely parents. Although they regretted that their only son had left for the rainy and cold Ireland, they have always supported my decision and my interested for science.

Contents

Chapter 1

General Introduction

1.1 Electron correlation and magnetism

Quite a large number of problems in condensed matter and molecular physics can be described within a single-particle picture, i.e. by assuming that each electron moves in an effective potential, which is the sum of the potential created by the positive ions and the average potential of all the other electrons (Hartree potential) [1]. In this case, by recalling the interpretation of the wave-function as a probability amplitude, for a two-electron system, for example, the probability of finding the first electron labelled 1 in the postion r_1 and the second electron 2 in the position r_2 is given by $P(r_1, r_2) = P(r_1)P(r_2)$, i.e. by the composed probability of two independent events. Unfortunately the single-particle picture is not able to provide a satisfactory microscopic explanation of most of the magnetic properties of solids and molecules and a description of the electron-electron Coulomb interaction, beyond that provided by the simple Hartree potential, is required [2, 3]. The motions of electrons is then no longer independent as they try to avoid each other. By recalling once again the probabilistic interpretation of quantum mechanics, $P(r_1, r_2)$ is not equal to $P(r_1)P(r_2)$, i.e. events are *correlated*.

The correlation among electrons implies an additional energy lowering in a real quantum mechanical system. The electronic correlation energy is divided in two contributions: 1) the exchange energy (sometimes called Fermi correlation energy), which arises from the requirements of the Pauli principle, and 2) the "proper" correlation energy[1].

Since the very early stages of quantum mechanics, many theoretical and computa-

[1] In the rest of the thesis, when we refer to the correlation energy, we always mean this second contribution. The first is called exchange energy so that confusion will be hopefully avoided.

tional methods, which accounts for the electronic correlation within different levels of approximation and accuracy, have been developed [4, 5]. Their application to the study of atoms, molecules, solids and effective models have led to a deep understanding of the microscopic origin of different magnetic properties and even to the predictions of novel physical effects and materials.
In this thesis, we discuss several of such methods [density functional theory (DFT), Hartree-Fock (HF), random-phase approximation (RPA), lattice and continuum quantum Monte Carlo (QMC)] and we employ them to a few problems of current interest stemmed from the fascinating fields of the *spintronics* and *molecular spintronics*.

1.2 Spintronics

More than 70 years ago, Mott understood for the first time the importance of the spin in order to describe the motion of electrons in a ferromagnetic transition metal [6]. He then proposed that the current was carried by "two-fluids" of electrons with opposite spin and that each fluid experienced a different resistance depending on the magnetization of the metal[2]. After 50 years, this idea led to the discovery of the giant magneto-resistance (GMR) effect [8, 9] and to the birth of the field of spintronics or spin-electronics [10, 11, 12]. Broadly speaking, the term spintronics refers to the study of all spin-related phenomena in materials and, more specifically, to the modelling of spin-polarized electron transport problems. The ultimate goal is that of designing devices, which, by exploiting both the charge and the spin degrees of freedom of the electrons, would implement new functionalities. GMR-based devices form already the functional elements of the read-head of modern hard-disk drives and many new technological breakthroughs lie ahead.
Historically spintronics effects have been studied mainly in metals, but considerable research effort has been recently dedicated to make semiconductor spintronics devices [13, 14]. Indeed these would be easily integrated with the currently existing semiconductor technologies and would combine logic and memory functions. Furthermore, in semiconductors, the spin can be, in principle, manipulated electronically by exploiting the spin-orbit coupling [15, 16], although this task is practically very challenging.

[2]Note that, in condensed matter physics, other models, proposed within different contexts, are referred as "two-fluid model". For example, a two-fluid model was introduced by Tisza and Landau in order to describe the superfluid ^{4}He (see, for example, reference [7]). Furthermore, in Chapter 4, we we will discuss Bhatt's two-fluid model proposed to explain low-temperature transport experiments for doped Si.

1.3 Diluted magnetic semiconductors, diluted magnetic oxides and d^0 magnets

In order to design semiconductor spintronics devices, efficient means to inject strongly spin-polarized currents into semiconductors are needed. Ferromagnetic semiconductors (FS), such as the Eu monochalcogenides (EuO, EuS, EuSe) [17], would be ideal spin injectors because of the very small resistance mistmatch with the normal semiconductors. Unfortunately, however, all known FS have Curie temperatures of only few Kelvins and can not be used for practical device applications (which require Curie temperatures well above room-temperature). Therefore, *diluted magnetic semiconductors* (DMS) [18, 19, 20], which are non-magnetic semiconductors doped with a small percentage of transition metal (TM) atoms, have been widely investigated. The prototype DMS is Mn:GaAs discovered in the late 90s [21, 22]. Here the substitution of some Ga atoms with Mn supplies both localized spins and carries (holes). A particularly strong exchange coupling between these carries and the localized spins is responsible for the ferromagnetism through a mechanism proposed by Zener [23, 24] many decades ago. The critical temperature is determined by the Mn and hole concentration, and the peak value achieved is of almost 200K [25, 26]. On the one hand, this Curie temperature is remarkably high when compared to that of FS. On the other hand, it is still far below room-temperature and it can not be pushed further up by increasing the Mn doping without inducing the presence of precipitates (such as MnAs) and hole-compensating defects (such as Mn interstitials).
Because of this practical limits on the achievable Curie temperature of Mn:GaAs, many physicists and materials scientists, inspired by Dietl's theoretical prediction about room-temperature ferromagnetism for Mn-doped ZnO [24], have moved their attention toward the TM doped oxide semiconductors (ZnO, TiO_2,In_2O_3, SnO_2 etc...). These are often called *diluted magnetic oxides* (DMO). Despite the large amount of experimental and theoretical investigations on these materials, their physics has proven very difficult to understand and their magnetic properties have been very controversial (see, for example, references [27, 30, 28, 29] and references therein). Indeed there have been several experimental reports of ferromagnetism as well as paramagnetism and even spin-glass behavior. The state of art of the research on DMO can be summarized through the two following statements [31, 32, 34, 33]:

1) Well-crystallized single-phase bulk TM-doped oxides and defect-free thin films are paramagnets.

2) Highly defective thin films and nanoparticles of TM doped oxides exhibit unusual magnetic properties, which can not be easily explained.

The research about the magnetic properties of oxide semiconductors has recently led to even more puzzling results. Indeed ferromagnetism has been also claimed for highly defective samples, which were not explicitly doped with TM atoms. After the first surprising report of ferromagnetism in HfO_2 [35], many other studies have been able to show that nanoparticles and defect-rich thin films present an unexpected ferromagnetic-like response to an applied magnetic field (see, for example, references [37, 38, 39, 40, 41, 42, 43, 44, 45]). Because of the lack of partially filled d shells in these materials, this phenomenon is called d^0 or *phantom* magnetism [36][3]. Although experimental results are sometimes ascribed to systematic errors and negligence in the measurements [46], the rapidly increasing number of available data suggests that these properties are intrinsic to the materials and are most probably related to either point or extended defects. On the one hand, a common empirical recipe to obtain a d^0 magnet consists in growing samples of poor quality and with a very high surface/volume ratio. On the other hand, a clear understanding of the magnetic properties of these materials is an extremely complicated issue. Indeed, not even the exact origin, the magnitude, the concentration and the spatial distribution of the magnetic moments can be easily determined.
The study of d^0 magnetism in oxides represents a specific problem within the more general research line, whose goal consists in finding ferromagnetic materials with partially filled $2p$ orbitals [47, 48, 49]. If these materials were made, they would be very attractive. Firstly, the exchange interaction in the $2p$ shell is calculated to be up to three times larger than that in the $3d$ [50]. This, together with the large spin-waves stiffness theoretically predicted [51], would implay a very high Curie temperature. Secondly, light elements have a small spin-orbit coupling so that these materials would be characterized by a long spin relaxation time and spin coherence length. Unfortunately, the p shells are usually fully filled and their bandwidth is large. Therefore they cannot sustain a magnetic moment and no ferromagnetic p-based material has been realized so far[4]. However, in the recent years, several promising experimental and

[3]Although, in the literature, this phenomenon is often (if not always) called d^0 or *phantom ferro*magnetism, we prefer to talk about *magnetism* as the physics of these materials is controversial and no solid demonstration of ferromagnetic order has ever been provided. In the following chapters, the expression d^0 ferromagnetism will be sometimes used to refer to experimental studies meaning that their authors claim ferromagnetism.

[4]Note that some molecular crystals exhibit magnetic order (although not ferromagnetism). For example solid O orders in a complex antiferromagnetic structure at low temperature [52] and Rb_4O_6

theoretical results have been achieved by studying graphene-related nanostructures [55]. The study of carbon-based magnetism represents now an active and rapidly growing research field [56].

In order to describe and understand the physics of DMS, DMO and d^0 magnets, two complementary theoretical approaches have been followed. On the one hand, effective models have been proposed by assuming that few "ingredients" (such as disorder, screened electron-electron interaction, exchange coupling between carriers and localized magnetic moments, etc.) are important to understand the main phenomenology. Electronic, magnetic and thermodynamic properties can then be calculated and the comparison between theoretical and experimental results indicates whether the model is able to capture the most relevant features of the problem or whether any important degree of freedom is neglected. This approach was very successful in the case of Mn:GaAs, for which the theory built on the Zener model accounts qualitatively, and often even quantitatively, for most of the magnetic, thermodynamic, transport and optical properties (see references [19, 57] and references therein).

On the other hand, *ab-initio* electronic structure calculations, such as DFT [58, 59, 60, 61], have been widely employed. These return a detailed description of the electronic and magnetic properties specific to each material and, in principle, do not require any assumption as they are based on the solution of the many-electron Schrödinger equation. However, this solution practically relies on some approximations (for example, in case of DFT, the so called exchange-correlation part of the energy functional is unknown and needs to be approximated) and these can drastically influence the final results and sometimes even lead to incorrect predictions.

Mn:GaAs was deeply investigated by using "conventional" DFT [62, 63]. The results are consistent with the main features of the theory built on the Zener's model and the mechanism for the ferromagnetism is nowadays relatively well established. In contrast, standard DFT calculations fail to describe the correct physics of magnetic and non-magnetic impurities in wide-gap materials. The study of DMO and d^0 magnets is then more problematic. The main reason of this failure is the presence of the self-interaction error in conventional DFT [64]. This loosely means that an electron feels part of its own electrostatic potential and repels itself. Thus the energy level of localized states, for which the self-interaction error is larger, are returned too high in energy. This generally leads to incorrect descriptions of the electronic structures of most of the oxides, to incorrect predictions for the position of defect states within the band gap and to failures in the description of hole self-trapping processes [65].

was predicted to be an anionogenic half-metal [53], but measured spin-glass [54].

Therefore, sophisticated functionals, which are approximately corrected for the self-interaction error, must be employed in order to describe accurately these materials. The main goal of the first part of this thesis is to investigate the theoretical issues related to the DFT description of d^0 magnets. This work is rooted in the long-standing research activity of the group in the field of DMS and DMO [62, 66, 67, 68, 69, 70, 71, 72, 73, 75, 80, 76, 77, 78, 79, 80, 81, 82, 83, 84] . Furthermore we also propose an effective model, which could describe some of the properties of either d^0 magnets or DMS, and we develop the computational tools required to calculate many quantities of interest. We believe that the use of effective models is a valuable complementary theoretical approach to *ab-initio* electronic structure simulations as it provides qualitative information about thermodynamic properties, causes of electron localization such as disorder, and genuine many-particle effects, not easily addressed by DFT.

1.4 Molecular spintronics and transition metal complexes

In recent times, the fascinating field of molecular electronics [85], which aims at making electronic devices by using organic molecules, has seen a rapid growth of interest. The typical molecular electronics device consists of either a single molecule or an organic monolayers sandwiched between metallic electrodes. This set up was first proposed by Aviran and Ratner [86] and realized much later by Reed and coworkers [87]. Since the first pioneering works, many molecular devices have been realized and they have been shown to exhibit several interesting features in their current-voltage characteristics.

The combination of the basic ideas behind molecular electronics with concepts mutated from spintronics has given birth to the field of molecular spintronics [88, 89, 90, 91]. Here the goal is that of implementing spintronics devices at the molecular level. This can be accomplished either by using organic molecules and magnetic electrodes or molecules possessing an internal spin degree of freedom and non-magnetic electrodes. In this second case, the molecules posses several spin states, which, in principle, can be inferred by an electrical readout. For this idea to work, means to control and manipulate the states of the molecules need to be found. As magnetic fields do not have enough spatial resolution to address selectively single molecules, the best strategy consists in looking for systems, whose spin state can be changed by some external stimuli such as electromagnetic radiation or static electric fields. Typical examples of this kind of systems are spin-crossover transition metal complexes

[92, 93] and some related coordination compounds such metal dioxolenes [94, 95, 96]. In spin crossover molecules a change in the distribution of the electrons in the d orbitals results in a low (LS) to high spin (HS) transition. In contrast, metal dioxolenes have different isomers with electronic structures that differ in charge distribution and spin state.
Recently some transport experiments were performed for transition metal complexes revealing very interesting behaviors and puzzling results [97, 98, 99, 100, 101]. The research on these molecules in the context of spintronics applications is still at the very initial stage and it is expected to grow rapidly in the near future.
In the last part of this thesis we discuss the issues related to the theoretical description of spin-crossover and cobalt-dioxolene molecules. Different *ab-initio* electronic structure techniques will be compared providing not only some new methodological foundations, but also some new insight into the physics and chemistry of these systems.

1.5 Dissertation layout

Two main subjects of research are discussed in this thesis. The main focus of the first part is on the theoretical description of d^0 magnets and, in general, of diluted magnetic materials. Methodological issues, results obtained by DFT calculations and effective models will be carefully discussed. In contrast, the focus of the second part is mainly on spin-crossover and Co-dioxolene molecules.
In Chapter 2, we provide a review of some electronic structure methods used throughout our research. These consist mainly of DFT and continuum quantum Monte Carlo. We explain the main ideas behind these methods and briefly discuss technical aspects, which are useful in order to better understand our results. We finally introduce the Hubbard model, which is discussed in detail in some of the following chapters.
In Chapter 3, we discuss the phenomenon of d^0 magnetism and the methodological issues related to its description by DFT calculations. We then introduce the atomic self-interaction correction (ASIC) to standard DFT and we present the results of some materials simulations.
In Chapter 4, we propose a model to describe diluted magnetic materials and we provide a detailed review of some approximate methods (mean-field and random phase approximations), that we use in order to calculate physical quantities and properties of interest.
In Chapter 5, the auxiliary field quantum Monte Carlo method is explained. This

allows the accurate numerical computation of several quantities for a wide class of models. The implementation of this method in our own code is discussed and some test calculations are presented. Such code will be used in future to study dilute magnetic systems and also to investigate the physics of polymeric chains.
In Chapther 6, we discuss spin-crossover and Co-dioxolene molecules. The first part of the chapter deals mainly with methodological issues. Here, we systematically compare results of DFT and continuum quantum Monte Carlo calculations for different transition metal complexes. This allows us to understand how different approximations affect the predicted magnetic properties for these systems. In the second part we theoretically predict a novel physical effect: the electric-field controlled valence tautomeric interconversion for Co-dioxolene molecules.
Finally, at the end of the dissertation we draw some general conclusions on the work presented.

Chapter 2

Ab-initio electronic structure methods and effective models

2.1 The electronic structure problem

The basic goal of electronic structure calculations is to describe systems of N_e electrons and N_N nuclei [102]. The non-relativistic general Hamiltonian is

$$\hat{H}_{tot} = -\frac{\hbar^2}{2m_e}\sum_{n=1}^{N_e}\nabla^2_{\mathbf{r}_n} - \frac{\hbar^2}{2M_i}\sum_{i=1}^{N_N}\nabla^2_{\mathbf{d}_i} + \\ + \sum_{n<m}^{N_e}\frac{e^2}{|\mathbf{r}_n - \mathbf{r}_m|} + \sum_{i<j}^{N_N}\frac{e^2 Z_i Z_j}{|\mathbf{d}_i - \mathbf{d}_j|} - \sum_{n=1}^{N_e}\sum_{i=1}^{N_N}\frac{e^2 Z_i}{|\mathbf{r}_n - \mathbf{d}_i|}\,. \tag{2.1}$$

The first and the second term are respectively the electronic and nuclear kinetic energy. The third, the forth and the last term are the electron-electron, the nucleus-nucleus and the electron-nucleus Coulomb interaction. $\mathbf{r}_n$ denotes the position of the n-th electron and $\mathbf{d}_i$ that of the i-th nucleus. Since the mass of the electrons m_e is much smaller than those of the nuclei M_i, the electron dynamics happens at a time-scale much faster than that of the nuclei. Therefore the Born-Oppenheimer (BO) approximation [102] is commonly used and the nuclei are assumed to be classical particles generating a static time-independent potential in which the electrons move. The system of electrons can then be described by the electronic time-independent Schrödinger equation

$$\hat{H}\Psi = E\Psi\,. \tag{2.2}$$

By introducing the coordinate $\mathbf{x}_n \equiv (\mathbf{r}_n, \sigma_n)$, which includes both electronic postion and spin, $\Psi \equiv \Psi(\mathbf{x}_1, ..., \mathbf{x}_{N_e})$ denotes the many-electron wave-function, while the

electronic Hamiltonian is

$$\hat{H} = \hat{T} + \hat{V}_{ee} + \hat{V}_{eN} \,, \tag{2.3}$$

where

$$\hat{T} = -\frac{1}{2} \sum_{n=1}^{N_e} \nabla^2_{\mathbf{r}_n} \,, \tag{2.4}$$

$$\hat{V}_{ee} = \sum_{n<m}^{N_e} \frac{1}{|\mathbf{r}_n - \mathbf{r}_m|} \,, \tag{2.5}$$

$$\hat{V}_{eN} = -\sum_{n=1}^{N_e} \sum_{i=1}^{N_N} \frac{Z_i}{|\mathbf{r}_n - \mathbf{d}_i|} \,. \tag{2.6}$$

We note that, in these definitions, we have introduced the atomic units ($\hbar = m_e = e = 1$), which will be used throughtout this work.

2.2 Non-interacting electronic systems

Although the BO approximation simplifies the electronic structure problem, the Schrödinger equation (2.2), is far from being easily solvable. Only if we neglect the electron-electron interaction (2.5), the problem will become trivial. Indeed the Hamiltonian (2.1) will then reduce to the sum of single-particle Hamiltonians, each of them associated to the single-particle Schrödinger equation

$$\left[-\frac{1}{2}\nabla^2_{\mathbf{r}} - \sum_{i=1}^{N_N} \frac{Z_I}{|\mathbf{r} - \mathbf{d}_i|} \right] \psi_\alpha(\mathbf{x}) = e_\alpha \psi_\alpha(\mathbf{x}) \,. \tag{2.7}$$

In order to satisfy the Pauli principle, the non-interacting many-particle wave-function has to be written as an anti-symmetrized product or Slater determinant of the N_e occupied single-particle wave-functions $\{\psi_\alpha\}_{\alpha=1,\ldots,N_e}$

$$D(\mathbf{X}) = \frac{1}{\sqrt{N!}} \begin{vmatrix} \psi_1(\mathbf{x}_1) & \psi_1(\mathbf{x}_2) & \ldots & \psi_1(\mathbf{x}_{N_e}) \\ \psi_2(\mathbf{x}_1) & \psi_2(\mathbf{x}_2) & \ldots & \psi_2(\mathbf{x}_{N_e}) \\ . & . & . & . \\ . & . & . & . \\ . & . & . & . \\ \psi_{N_e}(\mathbf{x}_1) & \psi_{N_e}(\mathbf{x}_2) & \ldots & \psi_{N_e}(\mathbf{x}_{N_e}) \end{vmatrix}$$

where $\mathbf{X} = (\mathbf{x}_1, \mathbf{x}_2, ..., \mathbf{x}_{N_e})$. The ground state energy E_0 is the sum of the eigenvalues e_α of the N_e occupied single-particle eigenstates

$$E_0 = \sum_{\alpha=1}^{N_e} e_\alpha \,. \tag{2.8}$$

The single-particle orbitals are often assumed to be products of spatial and spin factors

$$\psi_\alpha(\mathbf{x}_n) = \psi_\alpha(\mathbf{r}_n)\delta_{\sigma_\alpha,\sigma_n} \,. \tag{2.9}$$

If the determinant contains $N_\uparrow$ orbitals with $\sigma_\alpha = \uparrow$ and $N_\downarrow = N_e - N_\uparrow$ orbitals with $\sigma_\alpha = \downarrow$, it is an eigenstate of $\hat{S}^z$ with eigenvalue $(N_\uparrow - N_\downarrow)/2$.

2.3 The Hartree-Fock method

The electronic structure problem can be conveniently reformulated by using the variational principle. Indeed it can be shown [103] that every eigenstate of the Schrödinger Eq. (2.2) is a stationary point of the functional

$$E[\Psi] = \frac{\langle\Psi|\hat{H}|\Psi\rangle}{\langle\Psi|\Psi\rangle} \tag{2.10}$$

where $\hat{H}$ is the Hamiltonian (2.3),

$$\langle\Psi|\hat{H}|\Psi\rangle = \sum_{\sigma_1,...\sigma_{N_e}} \int d\mathbf{r}_1 ... d\mathbf{r}_{N_e} \Psi^*(\mathbf{x}_1, ..., \mathbf{x}_{N_e}) \hat{H} \Psi(\mathbf{x}_1, ..., \mathbf{x}_{N_e}) \tag{2.11}$$

and

$$\langle\Psi|\Psi\rangle = \sum_{\sigma_1,...\sigma_{N_e}} \int d\mathbf{r}_1 ... d\mathbf{r}_{N_e} |\Psi(\mathbf{x}_1, ..., \mathbf{x}_{N_e})|^2 \,. \tag{2.12}$$

In particular, excited states are saddle-points, while the ground state, Ψ_0, corresponds to the absolute minimum. An immediate consequence is that, for a trial wave function Ψ_T, which belongs to a subspace of the full Hilbert space, the energy $E_V = E[\Psi_T]$ is an upper bound to the exact ground state energy $E[\Psi_0] = E_0$, i.e.

$$E_V \geq E_0 \,, \tag{2.13}$$

with the equality satisfied when $\Psi_T = \Psi_0$.

In the Hartree-Fock method [102, 58], the subspace of the trial wave-functions is

chosen to be that of the single Slater determinants. Then, the optimization of the trial wave-function performed by minimizing the expectation value of $\hat{H}$ with respect to the single-particle orbitals $\psi_\alpha(\mathbf{r})$ leads to the Hartree-Fock equations

$$\epsilon_\alpha \psi_\alpha(\mathbf{r}) = \Big[-\frac{1}{2}\nabla_{\mathbf{r}}^2 + V_{eN}(\mathbf{r}) \Big] \psi_\alpha(\mathbf{r}) + \tag{2.14}$$

$$+ \sum_{\beta=1}^{N_e} \int d\mathbf{r}' \frac{|\psi_\beta(\mathbf{r}')|^2}{|\mathbf{r}-\mathbf{r}'|} \psi_\alpha(\mathbf{r}) - \sum_{\beta=1}^{N_e} \delta_{\sigma_\alpha,\sigma_\beta} \int d\mathbf{r}' \frac{\psi_\beta^*(\mathbf{r}')\psi_\alpha(\mathbf{r}')}{|\mathbf{r}-\mathbf{r}'|} \psi_\beta(\mathbf{r}) \,,$$

where the eigenvalues ϵ_α are Lagrange multipliers which ensure the orthonormality of the single-particle orbitals. These equations need to be solved self-consistently. Because of Koopmans' theorem [104], each of these eigenvalues is identified as the energy required to remove one electron from that particular eigenstate without perturbing the rest of the system. i.e. it corresponds to the vertical ionization energy.
The electron-electron interaction is approximately described by the two terms in the second line of Eq. (2.14). The first is called the electrostatic Hartree term, while the last one is the exchange one. It arises from the antisymmetric nature of the wave-function and keeps two electrons of like-spin apart. The difference between the ground state energy E_0 and the Hartree-Fock energy E_{HF} defines the correlation energy

$$E_C = E_0 - E_{HF} \,. \tag{2.15}$$

It contains the quantum many-particle contribution to the total energy, which is not accounted for by the Pauli principle. The correlation energy is usually distinguished between static and dynamic. The dynamic one is associated to electrons occupying the same orbital and is related to the cusp discontinuity in the many-electrons wave-function for two spatially coincident electrons. The static correlation is associated to electrons in different orbitals close in energy and it is sometimes called "near-degeneracy effect".
By using the Hartree-Fock method, we can retrieve about 98% of the total energy. However, the correlation energy, which is the remaining 2%, is very important for chemistry. For example, it accounts for about 50% of the binding energy of the nitrogen molecule.

2.4 Wave-function based methods

The correlation energy can be calculated by using multi-determinant wave-functions. This is the strategy followed by the configuration interaction (CI) method [104, 105],

in which the wave-function is written as a linear combination of Slater determinants, whose orbitals are taken from HF and held fixed. The coefficients of such a linear combination are then calculated by requiring that the total energy should be a minimum. The full correlation energy is then recovered if a full CI calculation is carried out, i.e. if all the possible determinants are included[1]. However the number of Slater determinants increases factorially with the number of electrons. This imposes a practical limit to the size of the systems that can be considered and full CI can be used only to study very small molecules (already H_2O is a challenging task). The computational cost can be then reduced by including only some determinants. This is done by considering low-energy excitations from a reference determinant (usually the HF ground state) as in truncated CI. For example if only double excited states are included we have "CI with Doubles", whose computational cost is N_e^6.

The Multi-Configuration Self-Consistent Field (MCSCF) method [105] is basically a CI scheme in which not only the coefficients in front of the determinants are optimized by the variational principle, but even the orbitals used to construct the determinants are. This method usually accounts for all the static correlation, but not for the dynamic one. In the Complete Active Space Self-Consistent Field (CASSCF) method, the orbitals are divided in active and inactive spaces. The orbitals in the inactive space are always either empty or doubly occupied. Within the active space a full MCSCF is performed. The common notation CASSCF(n, m) indicates that n electrons are distributed in all possible ways in m orbitals. The active space is usually limited to 10-12 electrons/orbitals.

Other widely-employed quantum chemistry post-HF methods are the second and forth order Moller-Plesset perturbation theory (MP) [105], which scale as N_e^5 (second order MP) and N_e^6 (forth order MP) and coupled cluster methods (CCSD) [105, 106], which also scale as N_e^6.

As none of this quantum chemistry methods is able to describe solids and large molecules, a different approach is required. This is density functional theory (DFT) [102, 58, 59, 105].

[1] In reality even a full CI calculation does not recover the full correlation energy as the HF orbitals are expressed using finite basis sets (see below when it is described how orbitals are usually expanded in basis functions in electronic structure calculations).

2.5 Density Functional Theory

DFT provides a way to reformulate the electronic structure problem in terms of the electron density $n(\mathbf{r})$. When the normalization condition $\langle\Psi|\Psi\rangle = 1$ is imposed, this is defined by

$$n(\mathbf{r}) = n^{\uparrow}(\mathbf{r}) + n^{\downarrow}(\mathbf{r}), \tag{2.16}$$

where

$$n^{\sigma}(\mathbf{r}) = N_e \sum_{\sigma_2,...\sigma_{N_e}} \int d\mathbf{r}_2 ... d\mathbf{r}_{N_e} |\Psi(\mathbf{x}_1, \mathbf{x}_2, ..., \mathbf{x}_{N_e})|^2 \tag{2.17}$$

is the spin-polarized electron density, which gives the probability of finding an electron of spin σ at a position $\mathbf{r}$. The electron density is normalized so that

$$N_e = \sum_{\sigma=\uparrow,\downarrow} \int d\mathbf{r}\, n^{\sigma}(\mathbf{r}). \tag{2.18}$$

The practical advantage of DFT is easily understood. Indeed, while the many-particle wave-function $\Psi(\mathbf{x}_1, \mathbf{x}_2, ..., \mathbf{x}_{N_e})$ depends on $2 \times 3N_e$ variables, the electron density is a function only of the 3 spatial coordinates.
Just for clarity, in the following section we will assume that the electrons are spinless particles and the generalization of DFT to spin-carrying particles is briefly described in section 2.5.4.

2.5.1 The Hohenberg-Kohn theorem

The core of DFT is represented by the Hohenberg-Kohn (HK) theorem [60], which can be summarized through the following statements:

- The external potential $V_{ext}(\mathbf{r})$ is determined, within a trivial additive constant, by the ground state density $n(\mathbf{r})$. Since $n(\mathbf{r})$ determines the number of electrons through Eq. (2.18), it also determines the wave function and any other observable of a many-particle system.

- The total energy is a functional of the density

$$E = E[n] = T[n] + V_{ee}[n] + V[n] = F[n] + V[n]. \tag{2.19}$$

$T[n]$ is the functional of the kinetic energy, $V[n]$ is the functional associated to the external potential $V_{ext}(\mathbf{r})$ and $V_{ee}[n]$ is the functional of the electron-electron interaction potential energy. $F[n] = T[n] + V_{ee}[n]$ is a universal functional as it is independent on the external potential defining a particular system.

- For a trial density $n_T(\mathbf{r})$, we have

$$E_0 \leq E[n_T]\,, \tag{2.20}$$

where E_0 is the ground state energy. The equality holds if $n_T(\mathbf{r})$ coincides with the ground state electron density. In other words, the energy is variational with respect to the density as well as to the wave-function [see Eq. (2.13)].

2.5.2 The Kohn-Sham scheme

Although the HK theorem establishes that the ground state density can be obtained by minimizing the functional (2.19), this turns out to be a very complicated problem in practice. Indeed the functional $F[n]$ is not known and the trial density has to fulfill many constraints. However, in 1965, Kohn and Sham proposed a clever solution [61]. They suggested to map the many-particle system onto a reference system of non-interacting particles moving under the influence of a fictitious effective potential that produces the same ground state density and total energy as the interacting one. All modern day practical DFT calculations are based on the Kohn-Sham (KS) scheme. First the energy functional is rewritten in the equivalent form

$$E[n] = T_s[n] + V[n] + J[n] + E_{xc}[n]\,, \tag{2.21}$$

where

$$E_{xc}[n] = T[n] - T_s[n] + V_{ee}[n] - J[n] \tag{2.22}$$

is the exchange-correlation energy,

$$J[n] = \frac{1}{2}\int \frac{n(\mathbf{r})n(\mathbf{r}')}{|\mathbf{r}-\mathbf{r}'|} d\mathbf{r}d\mathbf{r}' \tag{2.23}$$

is the classical Coulomb repulsion energy for a charge density $n(\mathbf{r})$,

$$V[n] = \int d\mathbf{r}\, n(\mathbf{r}) V_{ext}(\mathbf{r}) \tag{2.24}$$

and $T_s[n]$ is the kinetic energy of the reference system of non-interacting particles. $E_{xc}[n]$ contains all the information about the many-particles and the non-classical contributions to the total energy (exchange and correlation energy). Unfortunately we do not know an exact expression for this term, which needs to be approximated (see discussion below).

Finally, the reference system is described by the single-particle Schrödinger-like equations

$$\left[\frac{1}{2}\nabla_{\mathbf{r}}^2 + V_{KS}(\mathbf{r})\right]\psi_\alpha^{KS}(\mathbf{r}) = \epsilon_\alpha \psi_\alpha^{KS}(\mathbf{r}) \tag{2.25}$$

with $\langle \psi_\alpha^{KS} | \psi_\beta^{KS} \rangle = \delta_{\alpha\beta}$. The Kohn-Sham effective potential is defined as

$$V_{KS}(\mathbf{r}) = V_{ext}(\mathbf{r}) + V_H(\mathbf{r}) + V_{xc}(\mathbf{r}) \tag{2.26}$$

where

$$V_{ext}(\mathbf{r}) = \frac{\delta V[n]}{\delta n(\mathbf{r})} \tag{2.27}$$

is the external potential, which includes the electron-nucleus interaction,

$$V_H(\mathbf{r}) = \frac{\delta J[n]}{\delta n(\mathbf{r})} = \int d\mathbf{r}' \, \frac{n(\mathbf{r}')}{|\mathbf{r} - \mathbf{r}'|} \tag{2.28}$$

is the electrostatic Hartree potential [see first term in the second row of Eq. (2.14)] and

$$V_{xc}(\mathbf{r}) = \frac{\delta E_{xc}[n]}{\delta n(\mathbf{r})} \tag{2.29}$$

is the exchange-correlation potential.
The fermionic non-interacting ground state wave function for this reference system can then be written as a Slater determinant containing the N_e lowest energy KS orbitals ψ^{KS}. The electron density is

$$n(\mathbf{r}) = \sum_{\alpha=1}^{N_e} |\psi_\alpha^{KS}(\mathbf{r})|^2 \, . \tag{2.30}$$

It is possible to generalize this to non-integer occupations, so that the density becomes

$$n(\mathbf{r}) = \sum_\alpha f_\alpha |\psi_\alpha^{KS}(\mathbf{r})|^2 \, , \tag{2.31}$$

with the sum extendend over all the KS wave-functions. The coefficients $f_\alpha \in [0, 1]$ are the occupation number of the eigenstates with energy ϵ_α. The correct set of $\{f_\alpha\}$ is the one that minimizes the energy functional with the constraint $N_e = \sum_\alpha f_\alpha$.
We can notice that, within the KS scheme, the non-interacting kinetic energy $T_s[n]$ can by calculated exactly by using the KS wave-functions

$$T_s = \sum_\alpha f_\alpha \int d\mathbf{r} \, \psi_\alpha^{KS}(\mathbf{r}) \Big(-\frac{1}{2}\nabla_{\mathbf{r}}^2 \Big) \psi_\alpha^{KS}(\mathbf{r}) \, . \tag{2.32}$$

This is in contrast to the so-called "first generation" of density functional calculations, such as the Thomas-Fermi theory [58], where $T_s[n]$ as well as $E_{xc}[n]$ required an approximation.

The KS equations must be solved self-consistently like the HF equations. However, the KS effective potentital is a local operator so that DFT is computationally much less expensive than HF. Furthermore, in many cases, DFT has been found to perform better than HF. Indeed, although DFT describes exchange-related effects only in an approximate way, it recovers part of the electronic correlation energy, which is completely neglected in the HF method.

The total electronic energy is not just the sum of the single-particle eigenvalues, but it has to include the, so called, double-counting corrections. It then reads

$$E = \sum_{\alpha=1}^{N_e} \epsilon_\alpha + E_{xc}[n] - \int d\mathbf{r} V_{xc}(\mathbf{r}) n(\mathbf{r}) - \frac{1}{2} \int d\mathbf{r} d\mathbf{r}' \frac{n(\mathbf{r}) n(\mathbf{r}')}{|\mathbf{r} - \mathbf{r}'|} . \tag{2.33}$$

As mentioned earlier, within the BO approximation, the positions of the atomic nuclei enters only as parameters into the electronic Hamiltonian. Once the KS equations have been solved for a given arrangement of the atomic nuclei, we can also extract the forces acting on the static nuclei in their current configuration by using the Hellman-Feynman theorem [102]. The force on a nucleus I is then given by

$$\mathbf{F}_i = -\frac{\partial W}{\partial \mathbf{d}_i} , \tag{2.34}$$

where

$$W = E + V_{NN} \tag{2.35}$$

and

$$V_{NN} = \sum_{i<j}^{N_N} \frac{Z_i Z_j}{|\mathbf{d}_i - \mathbf{d}_j|} \tag{2.36}$$

is the classic nucleus-nucleus interaction energy. Equation (2.34) can be used to calculate the equilibrium geometries of molecules and solids, within the BO approximation, by varying all the $\mathbf{d}_i$ until the energy W is a minimum or, equivalently, $\mathbf{F}_i = 0$.

2.5.3 Interpretation of the Kohn-Sham eigenvalues

As we have explained, the Kohn-Sham scheme provides a mapping between the real many-particle problem and a fictitious system of non-interacting particles. KS eigenstates are, strictly speaking, just "mathematical devices", which allow for the calculation of the electron density, but which do not represent the molecular orbitals of

the many-electron system. The eigenvalues ϵ_α are merely Lagrange multipliers which enforce the orthonormality of the KS eigenstates. Unfortunately, Koopmans' theorem is not valid within DFT. This is instead replaced by Janak's theorem [107], which states that a KS eigenvalue ϵ_α is equal to the derivative of the total energy functional with respect to the occupation f_α of the eigenstate ψ_α^{KS}, i.e.

$$\epsilon_\alpha = \frac{\partial E}{\partial f_\alpha} . \tag{2.37}$$

The KS eigenvalues do not represent then the true excitation energies of a system. However, there is one exception: the highest occupied KS eigenvalue, ϵ_{N_e} [108]. This is equal to the negative of the ionization energy I, i.e. $\epsilon_{N_e} = -I$. This relation is only valid for the exact exchange correlation potential though, and in many cases the ionization potential is better calculated as a total energy difference

$$I = E(N_e - 1) - E(N_e) , \tag{2.38}$$

where $E(N_e)$ is the ground state energy of a system of N_e electrons. In the same way the electron affinity, A, can be calculated as

$$A = E(N_e) - E(N_e + 1) . \tag{2.39}$$

This shows that the electron affinity of a system of N_e electrons is just the ionization potential of a system of $N_e + 1$ electrons or, by using the Janak theorem, $-A = \epsilon_{N_e+1}(N_e + 1)$ (from now on, the notation $\epsilon_\alpha(N)$ indicates the α-th KS eigenvalue for a system of N electrons).

Despite the auxiliary nature of the KS eigenvalues, it is empirically found that, in many situations, they provide a reasonable first approximation to the actual energy levels of extended systems. Therefore, many band-structure calculations of solids are usually calculations of the KS eigenvalues and, although this simplification has proven successful for many systems, we must be aware of its lack of a solid theoretical foundation.

The band-gap of either a molecule or a semiconductor comprising N_e electrons is defined as [58, 109]

$$\Delta = -A + I = E(N_e + 1) - E(N_e) - [E(N_e) - E(N_e - 1)] \tag{2.40}$$

and, for the exact exchange-correlation, we have

$$\begin{aligned} \Delta &= \epsilon_{N_e+1}(N_e + 1) - \epsilon_{N_e}(N_e) = \\ &= \Big(\epsilon_{N_e+1}(N_e) - \epsilon_{N_e}(N_e)\Big) + \Big(\epsilon_{N_e+1}(N_e + 1) - \epsilon_{N_e+1}(N_e)\Big) . \end{aligned} \tag{2.41}$$

This is not equal to the KS band-gap Δ_{KS}, which represents the difference between the energies of the highest occupied and lowest unoccupied KS eigenstate, i.e. $\Delta_{KS} = \epsilon_{N_e+1}(N_e) - \epsilon_{N_e}(N_e)$. That is because the exact exchange-correlation energy functional is characterized by the derivative discontinuity [109]

$$\left.\frac{\delta E_{xc}[n]}{\delta n(\mathbf{r})}\right|_{N_e+\delta} - \left.\frac{\delta E_{xc}[n]}{\delta n(\mathbf{r})}\right|_{N_e-\delta} = \Delta_{xc} \tag{2.42}$$

where δ is an infinitesimal shift of the electron number N_e. Δ_{xc} is system-dependent, but position-independent. This derivative discontinuity insures that molecules dissociate with integer particle number at a large separation. We then have

$$\Delta = \Delta_{KS} + \Delta_{xc} \tag{2.43}$$

and, since $\Delta_{xc} > 0$, the KS band gap is usually smaller than the real one. Notably, the size of the derivative discontinuity is unknown and we must be careful in DFT calculations while extracting information that depends on the size of the band-gap or on the position of the un-occupied KS eigenstates.

2.5.4 Spin-polarized DFT

The generalization of DFT to collinear spin-polarized systems [58, 110] is achieved by introducing the magnetization

$$m(\mathbf{r}) = n^{\uparrow}(\mathbf{r}) - n^{\downarrow}(\mathbf{r}) \tag{2.44}$$

in addiction to the electron density $n(\mathbf{r})$ as fundamental quantity to define the energy functional. Spin-up and spin-down electrons satisfy the two independent KS equations

$$\left[\frac{1}{2}\nabla^2_{\mathbf{r}} + V^{\uparrow}_{KS}(\mathbf{r})\right]\psi^{KS}_{\alpha\uparrow}(\mathbf{r}) = \epsilon_{\alpha\uparrow}\psi^{KS}_{\alpha\uparrow}(\mathbf{r})\,, \tag{2.45}$$

$$\left[\frac{1}{2}\nabla^2_{\mathbf{r}} + V^{\downarrow}_{KS}(\mathbf{r})\right]\psi^{KS}_{\alpha\downarrow}(\mathbf{r}) = \epsilon_{\alpha\downarrow}\psi^{KS}_{\alpha\downarrow}(\mathbf{r})\,, \tag{2.46}$$

where

$$V^{\sigma}_{KS}(\mathbf{r}) = V_{ext}(\mathbf{r}) + V_H(\mathbf{r}) + V^{\sigma}_{xc}(\mathbf{r})\,. \tag{2.47}$$

In non-relativistic calculations and in absence of an external magnetic field, the Hartree potential $V_H(\mathbf{r})$ and the external potential $V_{ext}(\mathbf{r})$ do not depend on the spin, but

$$V^{\sigma}_{xc}(\mathbf{r}) = \frac{\delta E_{xc}[n^{\uparrow}, n^{\downarrow}]}{\delta n^{\sigma}(\mathbf{r})}\,. \tag{2.48}$$

In some systems, we have $V_{xc}^{\uparrow} - V_{xc}^{\downarrow} = B_{xc}/2 \neq 0$ so that the presence of the internal magnetic field B_{xc} accounts for a spontaneous magnetization.
The general procedure for a non-collinear spin calculation is similar [102, 111]. However, in that case, four electron densities are needed and the KS equations becomes matrix vector equations.

2.5.5 Exchange-correlation functionals

In principle the KS formalism is exact. However the exchange-correlation energy functional is unknown and it has to be approximated.
The most simple approximation, already suggested by Hohenberg and Kohn [60], is the local density approximation (LDA) (or its spin-polarized generalization called the local spin density approximation, LSDA). Here, we assume that, at each point in space, the exchange-correlation energy per particle is given by the value for the homogeneous electron gas $e_{xc}(n^{\uparrow}(\mathbf{r}), n^{\downarrow}(\mathbf{r}))$, so that

$$E_{xc}^{\mathrm{LSDA}}[n^{\uparrow}, n^{\downarrow}] = \int d\mathbf{r}\, n(\mathbf{r}) e_{xc}(n^{\uparrow}(\mathbf{r}), n^{\downarrow}(\mathbf{r}))\,. \tag{2.49}$$

The functional $e_{xc}(n^{\uparrow}(\mathbf{r}), n^{\downarrow}(\mathbf{r}))$ has been computed accurately by using Quantum Monte Carlo [112] and various analytic parametrizations exist [113, 114]. LDA has been applied successfully in solid state physics to study many metallic as well as semiconducting materials and it usually reproduces bulk properties (lattice constants, bulk moduli, etc.) within few percent of the experiments. The success of LDA for systems, which are quite different from the electron gas, is notable. This can be partially explained by a systematic partial error cancellation: typically LDA underestimates the exchange energy, but it overestimates the correlation one. The result is an unexpected good value for E_{xc}.
In contrast, for quantum chemistry type of calculations, LDA is usually not accurate enough to permit a quantitative description of the chemical bonds in molecules (the so-called "chemical accuracy"requires calculations with an error less than 1 kcal/mol= 0.04336 eV/electron). In order to improve upon LDA, various flavors of the generalized gradient approximation (GGA) were introduced [115, 118, 116, 119] and they have become very popular in quantum chemistry. Here, the idea is to include information about the inhomogeneity of the charge density by including the gradient of the spin-polarized electron density in the definition of the energy density

$$E_{xc}^{\mathrm{GGA}}[n^{\uparrow}, n^{\downarrow}] = \int d\mathbf{r} f(n^{\uparrow}(\mathbf{r}), n^{\downarrow}(\mathbf{r}), \nabla n^{\uparrow}(\mathbf{r}), \nabla n^{\downarrow}(\mathbf{r}))\,. \tag{2.50}$$

The most popular GGA functional is perhaps the one due to Perdew, Burke and Ernzerhof (PBE) [115]. Another example of GGA functional is the BP86, which combines the Becke88 exchange functional [116] with the Perdew86 correlation functional [117]. In solid-state physics, the improvements of GGA over LDA are not substantial. Furthermore, despite many successes, both fail drastically for materials with localized electrons, occupying atomic d and f shells (these materials are usually referred as "strongly correlated"). In contrast, GGA performs better than LDA in describing chemical bonds by correcting for the tendency of LDA to overbind molecules. However, the chemical accuracy has not been reached yet by GGA either and neither LDA nor GGA describe Van der Waals forces as their exchange-correlation potential decay exponentially instead of as $-1/r$.

A new generation of functionals is represented by the so-called orbital-functionals [120]. Among these we must cite the meta-GGAs [59]. These are functionals which depend, in addition to the density and its gradient, on the KS kinetic energy density

$$\tau^{\sigma}(\mathbf{r}) = -\frac{1}{2}\sum_{\alpha} f_{\alpha} |\nabla_{\mathbf{r}} \psi^{KS}_{\alpha\sigma}(\mathbf{r})|^2 \,. \tag{2.51}$$

This additional degree of freedom is used to satisfy additional constraints on E_{xc}. Meta-GGAs are a new class of functional and their potential and their failures have not been fully examined yet.

The so called hybrid functionals have become very popular among chemists, first, and then among condensed matter physicists as well. They were initially proposed, for example by Becke [126], within the framework of the adiabatic connection theorem [121, 122, 123, 124, 125]. These mix a fraction of exact HF exchange to the LDA(GGA) exchange according to the general formula

$$E_{xc}^{\text{hybrid}} = aE_{x}^{\text{exact}} + (1-a)E_{x}^{\text{LDA(GGA)}} + E_{c}^{\text{LDA(GGA)}} \,. \tag{2.52}$$

where the constant a is either estimated theoretically or fitted experimentally. Hybrid functionals are known to improve the description of the thermochemistry of molecular systems. Furthermore, despite the computational effort required to compute the HF exchange with periodic boundary conditions, they have been recently applied to solids as well. The most popular hybrid functional is perhaps B3LYP [127]. It is defined as

$$E_{xc} = 0.8E_{x}^{\text{LDA}} + 0.2E_{x}^{\text{HF}} + 0.72\Delta E_{x}^{\text{B88}} + 0.19E_{c}^{\text{VWN3}} + 0.81E_{c}^{\text{LYP}} \tag{2.53}$$

where E_{x}^{LDA} is the LDA exchange, while $\Delta E_{x}^{\text{B88}}$ is the gradient corrections to the Becke88 exchange [116]. E_{c}^{VWN3} and E_{c}^{LYP} indicate respectively the Vosko-Wilk-Nusair III [113] and the Lee-Yang-Parr correlation functional [119]. The coefficients

in Eq. (2.53) are determined by fitting atomization energies, electron and proton affinities and ionization potentials of atoms and molecules belonging to a specific set (the Pople's G2 [128]).
Another popular hybrid functional is PBE0 [129, 130] defined as

$$E_{xc}^{\mathrm{PBE0}} = \frac{1}{4}E_x^{\mathrm{HF}} + \frac{3}{4}E_x^{\mathrm{PBE}} + E_c^{\mathrm{PBE}}, \tag{2.54}$$

where E_x^{PBE} and E_c^{PBE} denote respectively the PBE exchange and correlation energies [115]. This functional is "parameter-free" in the sense that the amount of Hartree-Fock exchange included is not determined by fitting experimental data, but is based on the theoretical arguments of Ernzerhof et al. [131, 132, 133].
A very popular hybrid functional among condensed matter physicists is the HSE03 [134]. Here, in order to increase the computational efficiency and to simulate the effect of the electronic screening in solids, the long-range part of the HF exchange in the PBE0 functional has been cut and substituted by the corresponding density functional part. The exchange-correlation functional then reads

$$E_{xc}^{\mathrm{HSE}} = \frac{1}{4}E_x^{\mathrm{HF,sr},\mu} + \frac{3}{4}E_x^{\mathrm{PBE,sr},\mu} + E_x^{\mathrm{PBE,lr},\mu} + E_c^{\mathrm{PBE}}, \tag{2.55}$$

where (sr) and (lr) denote the short- and long-range parts of the respective exchange interactions (either HF or PBE exchange). The separation of the HF and PBE exchange interactions into a short- and a long-range part is accomplished through a decomposition of the Coulomb kernel

$$\frac{1}{r} = S_\mu(r) + L_\mu(r) = \frac{\mathrm{erfc}(\mu r)}{r} + \frac{\mathrm{erf}(\mu r)}{r}, \tag{2.56}$$

where $r = |\mathbf{r} - \mathbf{r}'|$ and μ is the parameter that defines the range separation. Here μ is related to a characteristic distance, $2/\mu$, at which the short-range interactions become negligible. Empirically it was found that the optimal range-separation parameter μ is between 0.2 and 0.3 Å^{-1}.
Strictly speaking, the way hybrid functionals are practically implemented do not fully fit in the DFT framework. Indeed, the exchange potential is derived by taking the functional derivative with respect to the single-particle orbitals (and not the density) and the resulting single-particle Schrödinger equations have the form of the Hertree-Fock equations with a non-local potential and with a weight factor in front of the Fock term.
In contrast for an orbital-dependent E_{xc}, we can obtain a local potential $V_{xc}^{\sigma}(\mathbf{r})$, in the

spirit of the KS scheme, by using the so-called optimized effective potential (OEP) method or simply the optimized potential method (OPM) [135, 136, 59, 120]. However, the solution of the OEP integral equation is quite complicated to be practical and useful approximations to the OEP need to be considered. One of such approximations is, for example, due to Krieger, Li and Iafrate (KLI) [137].

An alternative approach to improve upon LDA and GGA is to incorporate certain corrections into functionals tailored to rectify a subset of problems. For example, for the class of materials, that we have mentioned previously and that have localized electrons in d or f shells, the LSDA+U method, introduced by Anisimov [138], is usually employed. Here the LSDA exchange and correlation functional is replaced by a orbital dependent energy, which shifts occupied d (f) orbitals to lower energies whereas unoccupied ones are shifted to higher energies. Although this method provides a good qualitative description of transition metal and rare-earth oxides, it is not fully *ab initio* as it relies on two parameters, usually indicated with U and J[2].

Finally the so-called self-interaction (SI) error intrinsic to LDA and GGA [64, 141] deserves a more detailed description. This originates from the non-zero value of the Hartree energy for a system composed of just one electron. In HF, the SI in the Hartree energy is exactly cancelled by a corresponding contribution in the exchange energy . However, when we consider approximate forms for the exchange, the self-interaction is only partially cancelled and the rigorous KS-DFT condition

$$J[n_\alpha^\sigma] + E_{xc}[n_\alpha^\sigma, 0] = 0\,, \tag{2.57}$$

for the orbital density $n_\alpha^\sigma = |\psi_{\alpha\sigma}^{KS}|^2$ of the fully occupied KS orbital $\psi_{\alpha\sigma}^{KS}$, is not satisfied. A direct consequence of the SI in LDA/GGA is that the KS potential becomes too repulsive and exhibits an incorrect asymptotic behavior [64].

The self-interacting nature of semi-local KS potentials generates several failures in describing elementary properties of atoms, molecules and solids. For example, negatively charged ions (H^-, O^-, F^-) and molecules are predicted to be unstable by LDA [142]. Furthermore the KS HOMO is usually nowhere near the actual ionization potential [64]. Transition metal oxides are described as small-gap Mott antiferromagnets (MnO, NiO) or even as ferromagnetic metals (FeO, CoO) instead of charge transfer insulators [143].

Finally exchange-correlation functionals affected by the SI do not present the derivative discontinuity as a function of the occupation [107]. Semi-local funcionals in fact

[2] A particularly simple and transparent form of the LSDA+U functional, which is also rotationally invariant, redefines the U parameter as an effective parameter $U_{\text{eff}} = U - J$ [139]. The calculation of U_{eff} has been discussed by Cococcioni et al. [140] within a linear response approach.

continuously connect the orbital levels of systems of different integer occupation. This means that, when adding an extra electron to an open shell system, the KS potential does not jump discontinuously by $I - A$. This drawback is responsible for the incorrect dissociation of heteronuclear molecules into charged ions.

2.5.6 Computational methods

In modern codes which implement the KS-DFT scheme, there are two main features, which mostly affect the efficiency and the accuracy: 1), the basis set over which the KS eigenvectors are expanded and, 2), the way, in which the core electrons, which reside in atomic shells close to the nuclei, are treated.

Basis set

For solids, by taking advantage of the periodicity and of the Bloch's theorem, KS orbitals can be expanded in plane-waves [102]

$$\psi_{\alpha}^{KS}(\mathbf{r}) = \sum_{\mathbf{k}} C_{\alpha,\mathbf{k}} e^{i\mathbf{kr}}\,, \tag{2.58}$$

where $\mathbf{k}$ is the wave-vector. In order to calculate many properties such as the number of electrons in a band, the total energy etc., it is essential to integrate over $\mathbf{k}$ throughout the Brillouin zone. There are then two convergence parameters that need to be fine-tuned for every calculation: the Brillouin zone sampling and a cutoff radius in the reciprocal space to truncate the sums over wave-vectors. This is equivalent to a cutoff of the highest electronic kinetic energy. For localized states with large kinetic energies, a sufficiently large cutoff value is required so that the computational cost increases. Plane-wave codes are becoming very popular among condensed matter physicists because they are relatively easy to implement and very efficient Fast Fourier transform techniques are available.
In contrast, in quantum chemistry, eigenstates are usually expanded over a finite number, N_{basis}, of atom-centered basis functions

$$\psi_{\alpha}^{KS}(\mathbf{r}) = \sum_{n=1}^{N_{basis}} C_{\alpha n}\phi_n(\mathbf{r} - \mathbf{d}_i)\,, \tag{2.59}$$

where the orbital $\phi_n(\mathbf{r} - \mathbf{d}_i)$ is any numerical function that decays radially outwards from a nucleus located at $\mathbf{d}_i$. It could be, for example, a Slater-type orbital (STO) [104, 105] or a numerical orbital. Gaussian functions (GTOs) [104, 105] have been

very popular among chemists mainly because they can be factorized and multi-center integrals are easy to evaluate. In contrast, STOs and numerical orbitals describe atomic wave-functions better than GTOs and a smaller N_{basis} is then required. Furthermore STOs reproduce better the "tail" of the wave-functions and satisfy the Kato cusp condition [152] at the nuclei, while GTOs (and any linear combination of them) do not.

Localized basis sets are usually preferred to plane-waves to study finite systems such as molecules and clusters. Indeed, in this case, although plane-wave codes can be used in a supercell approach, a large number of plane-waves is needed as the electronic density is concentrated on a small fraction of the total volume of the supercell. Finally, recent times have seen the increased use of direct space methods where the KS equations are solved directly in real space by expanding the orbitals over a fine numerical grid.

Pseudopotentials

Electrons in molecules and solids can be divided in two groups: valence electrons and core electrons ("core-valence partition"). The core electrons are usually part of closed shells and they are strongly bounded to atoms. Therefore they do not play any significant role in the chemical bonding and the individual nuclear and core electron potential can be replaced by a single effective potential ("pseudopotential" or "effective core potential"), which describes their net effect on the valence electrons. The pseudopotential offers the massive advantage of drastically reducing the number of electronic states in the calculation. Both empirical and *ab-initio* pseudopotentials are commonly employed. The latter are derived by inverting the free atom Schrödinger equation for a given reference electronic configuration and forcing the pseudo wave-function to coincide with the true valence wave function beyond a certain distance, the cut-off radius [102]. The pseudo wave-function is also required to have the same norm as the true valence wave-function and not to have any node. Finally the pseudo-energy eigenvalues should match the true valence eigenvalues. The requirement of "norm-conservation" is the key step in making transferable pseudopotentials [144]. This means that a pseudopotential constructed for an atom can faithfully describe the valence properties of molecules and solids. In order to satisfy the above constraints, a pseudopotential has to be "semilocal", acting differently upon different angular momenta l. These semilocal potentials can be rewritten in a form that separates long and short range components. The long range component is local and corresponds to the Coulomb tail. Kleinman and Bylander [145] suggested that the non-local part

can be written as a separable potential transforming the semi-local potential into a truly non-local pseudopotential.
In some plane-wave codes, the so-called ultrasoft pseudopotentials are used [149]. These attain much smoother (soft) wave-functions (so considerably fewer plane-waves are need to represent the charge density), but still reproduce accurate results. This is achieved by relaxing the norm-conservation constraint.
The drawback of using pseudopotentials is that all the information on the wave-functions close to the nuclei are lost. A different approach is the augmented-plane-wave (APW) method [146], in which the space is divided into atom-centered augmentation spheres, where the wave-functions are expanded over atomic-like partial waves, and a bonding region outside the spheres, where some envelope functions are defined. The partial waves and the envelope functions are then matched at the boundaries of the spheres.
A more general approach is the projector augmented wave (PAW) method [147, 148]. This is based on the introduction of "auxiliary" smooth wave-functions connected to the all-electron wave-functions by a linear transformation, which is assumed to be unity except within spheres centered on the nuclei. It is then possible to write every quantity, that depends on the "real" wave-functions in terms of the auxiliary wave-functions. The PAW method has the big advantage that all-electron calculations are performed at the computational cost of pseudopotentials calculations.

2.5.7 DFT codes

For the results presented in this thesis, we have employed several DFT codes. First, many calculations were carried out by using a development version of the SIESTA code [150]. SIESTA belongs to the class of (norm-conserving) pseudopotential-localized basis set codes. The basis set consists of numerical orbitals, which are the product of a numerical radial function and a real spherical harmonic. Within our group, many useful features have been added. Among them we must mention the functional LSDA+U, the atomic self-interaction correction (ASIC) [151] (described in depth in chapter 3, the exact exchange and the self-interaction corrected LSDA/GGA within the KLI approximation.
Secondly, to study molecules, we have used intensively the quantum chemistry codes NWCHEM [153] and GAMESS [154]. These utilizes GTOs and perform either all-electron or effective core approximated calculations. Finally the plane-wave codes VASP [156] and QUANTUM ESPRESSO [155] have been also widely considered. VASP uses the PAW method or ultra-soft pseudopotentials. QUANTUM ESPRESSO

uses either pseudopotentials (both norm-conserving and ultrasoft) or PAW.

2.6 Continuum Quantum Monte Carlo

Although many successes in materials modelling can be ascribed to DFT, DFT may be quite inaccurate for some very interesting problems. On the one hand, existing DFT methods fail in describing strongly correlated systems or van der Waals dispersion interactions [59], although much progress has been done in developing functionals to tackle those two specific problems (for example, we have already mentioned the LSDA+U functional, which provides a good description of the charge-transfer insulators). On the other hand, DFT is somehow unable to give predictions of useful accuracy for the adsorption energy of molecules on surfaces. Even more drastically, in some cases, results depend strongly on E_{xc} and there is no way of knowing in advance which functional to trust. For example, this is the case for the surface formation energies and of the "spin-gap" of transition metal complexes (see chapter 6). For many of these problems, quantum Monte Carlo (QMC) techniques [158, 159, 160] are considerably more accurate than DFT so that their use is very appealing. Furthermore, as they rely on extensive statistical samplings, they are naturally well suited to large parallel machines and will play a fundamental role in computational material science in the future years [157].
We will present below a short review of the two QMC techniques, variational and diffusion Monte Carlo, which have been extensively employed in electronic structure calculations.

2.6.1 Variational Monte Carlo

Variational Monte Carlo (VMC) is based on a combination of the variational principle, Eq. (2.13), and the Monte Carlo method to evaluate integrals [161].
The functional $E[\Psi]$, defined in Eq. (2.10), can be evaluated for a trial wave-function Ψ_T and reads

$$E_0 \leq E_V = E[\Psi_T] = \frac{\int \Psi_T^*(\mathbf{R})\hat{H}\Psi_T(\mathbf{R})d\mathbf{R}}{\int \Psi_T^*(\mathbf{R})\Psi_T(\mathbf{R})d\mathbf{R}} \tag{2.60}$$

where $\mathbf{R} = (\mathbf{r}_1, ..., \mathbf{r}_{N_e})$ [Note that the spin variables in Eq. (2.60) are implicitly summed over (see reference [158] for details)]. We can then write

$$E_V = \int p(\mathbf{R})E_L(\mathbf{R})d\mathbf{R}\,, \tag{2.61}$$

where

$$p(\mathbf{R}) = \frac{|\Psi_T(\mathbf{R})|^2}{\int |\Psi_T(\mathbf{R}')|^2 d\mathbf{R}'} \tag{2.62}$$

is a probability distribution and the function

$$E_L(\mathbf{R}) = \Psi_T^{-1}(\mathbf{R}) \hat{H} \Psi_T(\mathbf{R}) \tag{2.63}$$

is called "local energy".
In VMC, the Metropolis algorithm [161] is used to sample a set of points $\{\mathbf{R}_m, m = 1, ..M\}$ from the probability distribution $p(\mathbf{R})$. At each of these points the local energy is evaluated and the variational energy can be estimated as

$$E_V \approx \frac{1}{M} \sum_{m=1}^{M} E_L(\mathbf{R}_m) \,. \tag{2.64}$$

Analogously, other expectation values of operators can be calculated by VMC.
The main issue in VMC consists in finding an appropriate trial wave-function. This will be discussed very briefly in the following paragraph. However, we can already notice that when Ψ_T is a single Slater determinant, VMC reduces to the HF method. In contrast, if we could chose Ψ_T to be the exact ground state wave-function, the local energy would have the costant value E_0 over the entire configuration space (zero-variance principle).

2.6.2 Trial wave-functions

As we have just seen, the accuracy of a VMC calculation depends strongly on the trial wave-function. Furthermore the repeated evaluation of the trial wave-function, its gradient and its laplacian, is the most computational demanding part of a VMC calculation. Therefore the trial wave-function has to be written in a compact form which allows a rapid evaluation. VMC simulations normally use a trial wave-function of the Slater-Jastrow form

$$\Psi_{SJ} = e^{J(\mathbf{R})} D^{\uparrow}(\mathbf{r}_1, ..., \mathbf{r}_{N_\uparrow}) D^{\downarrow}(\mathbf{r}_{N_\uparrow+1}, ..., \mathbf{r}_{N_e}) \,. \tag{2.65}$$

In this expression the Slater determinant (2.2) is replaced by the product of determinants of spin-up and spin-down orbitals and Ψ_{SJ} is not antisymmetric on exchange of electrons with opposite spins. However, this has no effects on the expectation values of spin-independent operators [158]. The orbitals in the Slater determinants are

usually obtained by an HF or DFT (LDA) calculation. The Jastrow factor $e^{J(\mathbf{R})}$ is a positive and totally symmetric function, which includes correlation effects by making the wave-function explicitly dependent on the separation between particles (see section 2.6.5 for some details). The wave-function (2.65) has to satisfy the electron-electron and the electron-nucleus Kato-cusp condition [152], which leads to a smooth behavior of the local energy [158].

The physics described by the Slater-Jastrow wave-function is rather transparent. On the one hand, as described in the HF method, the antisymmetry of the wave-function creates the "exchange-hole" which keeps electrons of like-spin apart. On the other hand, the effect of the Jastrow factor is that of reducing the amplitude of the wave-function whenever two electrons (both of parallel and antiparallel spin) get close, thus creating the "correlation-hole".

The Jastrow factor usually depends on a set of parameters $\{\alpha\}$, i.e $J = J(\mathbf{R}, \{\alpha\})$. The trial wave-function can then be further improved by optimizing these parameters[3]. In order to do so, we need a cost-function, which is a function to be minimized. The most natural choice is the energy. Indeed the variational principle insures that by improving the wave-function, the energy will tend to the ground state energy from above. However, we can also chose the variance of the energy. In this case the zero-variance principle tells us that as Ψ_T approaches the true ground state wave-function, the statistical fluctuations will become smaller and the local energy will tend to a constant, E_0. Since optimizing the wave function is a technically complex problem involving the development of numerical stable minimization algorithms, we will not discuss the details and we prefer to refer to the specialized literature (see, for example [158, 160], and references therein).

2.6.3 Diffusion Monte Carlo

Unfortunately, an expression for the VMC wave-function like that in Eq. (2.65) does not have enough variational freedom to represent the true wave-function. VMC is then able to capture between 60% and 80% of the correlation energy and it might not be accurate enough for some problems. Diffusion Monte Carlo (DMC) must then be used.

DMC is a stochastic method, which projects out the ground state from an initial state.

[3]There is, of course, no absolute restriction on optimizing the the Slater part as well. A higher order technique, which allows to recover a bigger fraction of the correlation energy, also involves functions with optimizable parameters. However optimization of both the Jastrow factor and these other functions, can not be done for polyatomic systems because of the high computational cost.

To understand the general idea, we can consider the time-dependent Schrödinger equation for an Hamiltonian $\hat{H} = -\frac{1}{2}\nabla^2_{\mathbf{R}} + V(\mathbf{R})$

$$i\frac{\partial}{\partial t}\Phi(\mathbf{R},t) = -\frac{1}{2}\nabla^2_{\mathbf{R}}\Phi(\mathbf{R},t) + \Big[V(\mathbf{R}) - E_T\Big]\Phi(\mathbf{R},t) \tag{2.66}$$

and re-write it in imaginary time, $\tau = it$, as

$$-\frac{\partial}{\partial \tau}\Phi(\mathbf{R},\tau) = -\frac{1}{2}\nabla^2_{\mathbf{R}}\Phi(\mathbf{R},\tau) + \Big[V(\mathbf{R}) - E_T\Big]\Phi(\mathbf{R},\tau)\,. \tag{2.67}$$

The off-set energy E_T, whose purpose will be clear later, is called "reference energy" and it only affects the wave-function normalization. The formal solution of Eq. (2.67) is obtained by expanding $\Phi(\mathbf{R},\tau)$ in the eigenstates of the Hamiltonian $\{\phi_i\}$ and reads

$$\Phi(\mathbf{R},\tau) = \sum_i e^{-\tau(E_i - E_T)} c_i \phi_i(\mathbf{R})\,, \tag{2.68}$$

with $c_i = \langle \phi_i | \Phi \rangle$.
In the limit of long times, for $c_0 \neq 0$ and by adjusting E_T to be equal E_0, we find

$$\Phi(\mathbf{R}, \tau \to \infty) = c_0 \phi_0\,, \tag{2.69}$$

since excited states decay in imaginary time away exponentially. In other words, for a wave-function $\Phi(\mathbf{R})$, whose overlap with the ground state is non-zero, the operator $e^{-\tau(\hat{H}-E_T)}$ acts a projector to the ground state itself as $\tau \to \infty$.
By looking carefully at Eq. (2.67) and by assuming that $\Phi(\mathbf{R},\tau)$ is a probability distribution, we note that:

- By ignoring the second term on the right-hand side, the imaginary-time Schrödinger equation is isomorphic to a diffusion equation, which can be simulated by random walks where random walkers diffuse in a $3N_e$-dimensional space.

- By ignoring the first term on right-hand side, the imaginary-time Schrödinger equation is isomorphic to a rate equation with a position-dependent rate constant.

Therefore, in principle, a numerical simulation, in which random walkers diffuse through a $3N_e$-dimensional space, reproduce in regions of low potential and die in regions of high potential ("branching" process) would lead to a stationary distribution proportional to $\Phi(\mathbf{R})$, from which the expectation values would be obtained.
However, this simple scheme for the DMC algorithm presents two main issues. The

first issue is of numerical character and it is related to the presence of the potential in the rate costant of the branching process. Because of the divergence of the potential when two particles are coincident, the walkers rate of "births" and "deaths" diverges. This leads to numerical stability problems.
The second issue is of fundamental character. It is related to the assumption that $\Phi(\mathbf{R})$ is a probability distribution. Indeed, this assumption is clearly in contrast with the anti-symmetric nature of the electronic wave-function. $\Phi(\mathbf{R})$ must have both positive and negative regions separated by a nodal surface, i.e. the $(3N_e - 1)$ dimensional hypersurface for which a wave-function is zero and across which it changes sign. This issue is the so-called "fermion sign problem", which is dealt by the "fixed node approximation" (FNA) [164, 165]. This consists in introducing an approximate nodal surface, which is usually obtained from a trial wave-function $\Psi_T(\mathbf{R})$ and which the walkers are not allowed to cross. The FNA then divides the configuration space into regions called "nodal pockets". Finally, the Tilling theorem [166], which states that all nodal pockets are equivalent and related by permutation symmetry, insures us that we need to sample only one of these. This theorem is also connected to the variational principle for the DMC ground state energy. The following properties can then be proved [158]:

a) the fixed-node energy is an upper bound to the exact ground state energy,

b) the fixed-node error decreases quadratically in the error of the nodal surface of $\Psi_T(\mathbf{R})$.

These, of course, imply that, if $\Psi_T(\mathbf{R})$ has the exact nodal surface of the ground state wave-function, the fixed-node energy will coincide with the ground state one.
Practically, the FNA is introduced through the definition of the "importance-sampled wave distribution" $f(\mathbf{R}, \tau)$ [162, 163]. This is obtained by multiplying $\Phi(\mathbf{R}, \tau)$ by the trial wave-function $\Psi_T(\mathbf{R})$, i.e.

$$f(\mathbf{R}, \tau) = \Psi_T(\mathbf{R})\Phi(\mathbf{R}, \tau)\,. \tag{2.70}$$

By requiring that the nodal surface of $\Phi(\mathbf{R}, \tau)$ coincides with that of $\Psi_T(\mathbf{R})$, we can then force $f(\mathbf{R}, \tau)$ to be positive and this effectively becomes a probability distribution.
Substituting $f(\mathbf{R}, \tau)$ in Eq. (2.67) for $\Phi(\mathbf{R}, \tau)$, we obtain the "importance-sampled imaginary-time Schrödinger equation" (ISITSE)

$$\frac{\partial f}{\partial \tau} = -\frac{1}{2}\nabla^2_{\mathbf{R}} f + \nabla_{\mathbf{R}}[\mathbf{v}f] + [E_L - E_T]f \tag{2.71}$$

where E_L is the local energy, Eq. (2.63), and

$$\mathbf{v}(\mathbf{R}) = \Psi_T^{-1}(\mathbf{R})\nabla_{\mathbf{R}}\Psi_T(\mathbf{R}) \tag{2.72}$$

has the form of a drift velocity. We note that the three terms on the right-hand side of the ISITSE, Eq. (2.71), can be associated to a diffusion, a drift and a branching process, respectively.

Interestingly, the drift term in Eq. (2.71) acts as a "quantum force", which carries walkers along the direction of increasing $|\Psi_T|$ so that the most important parts of the wave-function are sampled more often. In the same way, the drift velocity carries away the walkers from the nodal surface of Ψ_T as required by the FNA.

We also note that, in the ISITSE (2.71), the rate constant depends on the local energy, which is a relatively uniform quantity particularly when Ψ_T satisfied the Kato cusp condition. The numerical issue outlined above is then circumvented and the DMC algorithm becomes stable.

The ISITSE can be rewritten in the integral form

$$f(\mathbf{R},\tau) = \int G(\mathbf{R} \leftarrow \mathbf{R}', \tau - \tau') f(\mathbf{R}', \tau') d\mathbf{R}' \tag{2.73}$$

where the Green function

$$G(\mathbf{R} \leftarrow \mathbf{R}', \tau - \tau') = \langle \mathbf{R} | e^{-\tau(\hat{T}' + \hat{E}_L - E_T)} | \mathbf{R}' \rangle \tag{2.74}$$

is solution of the ISITSE provided the initial condition $G(\mathbf{R} \leftarrow \mathbf{R}', 0) = \delta(\mathbf{R} - \mathbf{R}')$. In the equation above we have defined

$$\hat{T}' = -\frac{1}{2}\nabla_{\mathbf{R}} + (\nabla_{\mathbf{R}} \cdot \mathbf{v}) + \mathbf{v} \cdot \nabla_{\mathbf{R}} \tag{2.75}$$

and $\hat{E}_L$ is the local energy operator defined by the equation $\hat{E}_L|\mathbf{R}\rangle = E_L(\mathbf{R})|\mathbf{R}\rangle$.

For very small time steps ("short -time approximation"), we can use the Trotter-Suzuki formula for the exponential of a sum of operators

$$e^{-\tau(\hat{T}' + \hat{E}_L - E_T)} = e^{-\tau(\hat{E}_L - E_T)/2} e^{-\tau \hat{T}'} e^{-\tau(\hat{E}_L - E_T)/2} + O(\tau^3) \tag{2.76}$$

to rewrite the Green function as

$$G(\mathbf{R} \leftarrow \mathbf{R}', \tau) \approx G_D(\mathbf{R} \leftarrow \mathbf{R}', \tau) G_B(\mathbf{R} \leftarrow \mathbf{R}', \tau) \,. \tag{2.77}$$

Here, $G_D(\mathbf{R} \leftarrow \mathbf{R}', \tau)$ is the Green function for a drift-diffusion process, which, assuming costant drift velocity $\mathbf{v}$ between $\mathbf{R}$ and $\mathbf{R}'$, is

$$G_D(\mathbf{R} \leftarrow \mathbf{R}', \tau) \equiv \langle \mathbf{R} | e^{-\tau \hat{T}'} | \mathbf{R}' \rangle \approx \frac{1}{(2\pi\tau)^{3N/2}} \exp\left(- \frac{[\mathbf{R} - \mathbf{R}' - \tau \mathbf{v}(\mathbf{R})]^2}{2\tau} \right), \tag{2.78}$$

while

$$G_B(\mathbf{R} \leftarrow \mathbf{R}', \tau) = \exp\left(-\frac{\tau}{2}\left[E_L(\mathbf{R}) + E_L(\mathbf{R}') - 2E_T\right]\right) \tag{2.79}$$

is called branching factor. Therefore, the process described by $G_D(\mathbf{R} \leftarrow \mathbf{R}', \tau)$ is simulated by making each walker, associated to a configuration $\mathbf{R}'$, drift through a distance $\mathbf{v}(\mathbf{R}')\tau$ and then diffuse by a random distance drawn by a Gaussian distribution of variance τ. Finally, each walker either "reproduces" or "dies" so that on average $G_B(\mathbf{R} \leftarrow \mathbf{R}', \tau)$ walkers continue from the new position $\mathbf{R}$. A DMC simulation consists then in repeating these steps many times, and after an equilibration time, the configurations will be distributed according to $f = \Psi_T \Phi$.

As we have seen in the discussion above, the FNA is the only fundamental approximation in DMC. All the others are "technical" approximations and can be accounted for by improving the numerical algorithms or by double-checking the results. Firstly, the short-time approximation leads to a dependence of the DMC results on the time steps and the results must be extrapolated to $\tau \to 0$. Secondly, the assumption of constant drift velocity between $\mathbf{R}'$ and $\mathbf{R}$, violates the detailed balance-condition for DMC [158]

$$G(\mathbf{R} \leftarrow \mathbf{R}', \tau)\Psi_T(\mathbf{R}')^2 = G(\mathbf{R}' \leftarrow \mathbf{R}, \tau)\Psi_T(\mathbf{R})^2\,, \tag{2.80}$$

but this can be re-imposed by introducing a reject/accept step [158]. Thirdly, by controlling the reference energy, which appears in the branching factor, we can keep the population of walkers almost constant thus preventing it from either increasing exponentially or dying out. However, changing the value of E_T during a simulation introduces a positive bias in the DMC total energy, which, can usually be easily estimated by performing different calculations for different average populations.

The expectation value of the energy is commonly computed in DMC by using the so called mixed estimator:

$$\begin{aligned} E_{DMC} &= \lim_{\tau\to\infty} \frac{\langle e^{-\tau\hat{H}/2}\Psi_T|\hat{H}|e^{-\tau\hat{H}/2}\Psi_T\rangle}{\langle e^{-\tau\hat{H}/2}\Psi_T|e^{-\tau\hat{H}/2}\Psi_T\rangle} = \lim_{\tau\to\infty} \frac{\langle e^{-\tau\hat{H}}\Psi_T|\hat{H}|\Psi_T\rangle}{\langle e^{-\tau H}\Psi_T|\Psi_T\rangle} = \\ &= \frac{\langle\Phi|\hat{H}|\Psi_T\rangle}{\langle\Phi|\Psi_T\rangle} = \frac{\int f(\mathbf{R},\tau)E_L(\mathbf{R})d\mathbf{R}}{\int f(\mathbf{R},\tau)d\mathbf{R}} \approx \frac{1}{M}\sum_m E_L(\mathbf{R}_m)\,, \end{aligned} \tag{2.81}$$

where $\mathbf{R}_m$ denotes M samples of $f(\mathbf{R})$ resulting from a DMC run. Furthermore DMC satisfies the zero-variance principle as well as VMC, i.e. the variance of the energy goes to zero as the trial wave-function Ψ_T goes to an exact eigenstate.

Finally we would like to make a further comment about the fixed-node approximation and the trial wave-function Ψ_T. Indeed, although, in principle, Ψ_T should be

optimized within DMC to reproduce the optimal nodal-surface, which minimizes the DMC energy, in practice this turns out to be computationally too expensive and technically tricky. The trial wave-function is then generally optimized by VMC. For a trial wave-function of the Slater-Jastrow form, the nodal surface is imposed by the Slater part as the Jastrow factor is positive. The nodal surface is then basically determined by either DFT or HF and this represents one of the main limitations of the fixed-node DMC[4].

2.6.4 Pseudopotentials

The scaling of QMC with the atomic number Z is approximately $Z^{5.5}$ [167, 168] so that applications to heavy atoms are basically impossible. However, like in DFT, pseudopotentials can be used to reduce the effective value of Z and to improve the scaling to $Z^{3.5}$. As we have previously seen, the distinction between core and valence electrons is exact within DFT and it is achieved by simply designating some orbitals as core orbitals and others as valence orbitals. However, in a many-electron framework, the electrons are identical particles and the core-valence partition is an ill-defined concept. Unfortunately, it is not currently possible to construct pseudopotentials for heavy atoms entirely within QMC and it is best to use pseudopotentials constructed from one-particle theories, either HF or DFT. In particular, HF pseudopotentials seem to give systematically better results in QMC than the DFT ones [169]. This is probably because HF neglects all electronic correlations. The QMC calculation reintroduces the valence-valence correlations but neglects core-core correlations, which anyway have a very small indirect effect on valence electrons, and the core-valence correlations. These can be approximately included by using a core-polarization potential, which represents the polarization of the core due to the instantaneous positions of the surrounding electrons and ions (see reference [158] and references therein).
As we have discussed in the context of DFT, modern pseudopotentials are non-local depending on the angular momentum. While the use of non-local pseudoptentials is straightforward in VMC [170, 171], there is an issue in DMC. The fixed-node condition turns out not to be compatible with the non-locality. We are then forced to introduce the, so-called, "potential localization approximation" (PLA) [172] where the non-local pseudopotential acts on the trial wave-function Ψ_T rather than on the DMC wave function Φ. The error incurred is proportional to the square of the error

[4]The nodal-surface can be optimized by VMC by either using a multideterminat wave function or a backflow wave function (see references in [158, 160]). However, throughout this thesis we have always used just a Jastrow-Slater wave function of the form (2.65).

in trial wave-function [172]. However its sign is arbitrary so that DMC is no longer strictly variational. The recent work by Casula et al. [173, 174] eliminates the need for the PLA and restores the variational property.

2.6.5 The CASINO code

The QMC calculations presented in this thesis were carried out by using the CASINO code [160]. CASINO is able to perform VMC and DMC calculations for finite and periodic real systems as well as model systems. Both all-electron and pseudopotential calculations can be performed. The trial wave-function Ψ_T is of Slater-Jastrow type, Eq. (2.65), with

$$J(\{\mathbf{r}_n\},\{\mathbf{d}_i\}) = \sum_{n>m}^{N_e} u(r_{nm}) + \sum_{i=1}^{N_N}\sum_{n=1}^{N_e} \chi_i(r_{ni}) + \sum_{i=1}^{N_N}\sum_{n>m}^{N_e} f_I(r_{ni}, r_{mi}, r_{nm}) \qquad (2.82)$$

where $r_{nm} = |\mathbf{r}_{nm}| = |\mathbf{r}_n - \mathbf{r}_m|$ and $r_{ni} = |\mathbf{r}_{ni}| = |\mathbf{r}_n - \mathbf{d}_i|$. The functions u, χ and f are represented by power expansions with optimisable coefficients. Different coefficients are used for terms involving different spins. Other terms, not used in this work, can be added when using periodic boundary conditions [160]. The orbitals $\psi_n(\mathbf{r})$, which enter in the Slater determinants $D^\uparrow$ and $D^\downarrow$ are passed to CASINO by interfaces with DFT codes (GAUSSIAN, GAMESS, etc.) and can be expressed using GTOs, STOs, plane-waves etc. We have chosen to represent $\psi_\alpha(\mathbf{r})$ through B-splines basis (blip functions) [175]:

$$\psi_\alpha(\mathbf{r}) = \sum_n a_{\alpha n}\Theta_n(\mathbf{r})\,. \qquad (2.83)$$

The functions $\Theta_n(\mathbf{r})$ consist of localized cubic splines centered on the points $\mathbf{R}_n = (X_n, Y_n, Z_n)$ of a regular cubic grid of spacing a

$$\Theta_n(\mathbf{r}) = \varphi((x - X_n)/a)\varphi((y - Y_n)/a)\varphi((z - Z_n)/a) \qquad (2.84)$$

where

$$\varphi(\xi) = \begin{cases} 1 - \frac{3}{2}\xi^2 + \frac{3}{4}|\xi|^3 & 0 \le |\xi| \le 1 \\ \frac{1}{4}(2 - |\xi|)^3 & 1 \le |\xi| \le 2 \\ 0 & |\xi| \ge 2 \end{cases} .$$

The coefficient $a_{\alpha n}$ are extracted from the plane-waves coefficients $C_{\alpha\mathbf{k}}$ of Kohn-Sahm orbitals obtained from a DFT calculation performed using QUANTUM ESPRESSO. Blip functions are much more suitable for QMC calculations than plane-waves. Indeed for any position r there are only 64 non-zero blip functions whatever the nature and

the size of the system is, so that the number of operations to compute $\psi_\alpha(\mathbf{r})$ is the same for every material. In contrast, by using plane-waves, the cost to evaluate many-body wave-functions involves $O(N_e^3)$ operations with a large prefactor depending on the plane-waves cutoff. Furthermore, with respect to other localized basis set (such as GTOs), blip functions are systematically improvable and unbiased as well as plane-waves.
Smooth non-divergent HF pseudopotential (with relativistic corrections), which are suitable for QMC calculations, were developed by Trail and Needs [176, 177].
The performances of CASINO have been tested on thousands of cores and it has been recently improved to run with almost perfect parallel efficiency on 100000 cores [157].

2.7 The Hubbard model

So far, we have mainly focused our attention on theoretical and computational methods, which allow us to solve the electronic structure problem within various approximations and different levels of accuracy. In many cases, however, theorists can resort to simplified models which can provide a qualitative understanding of either a physical effect or a broad class of materials. Such effective models can, in principle, be derived from the electronic structure Hamiltonian (2.3) by renormalization group transformations. These lead to the suppression of the high-energy states and to an effective Hamiltonian which contains only the most relevant interactions (see the discussion about this topic in reference [178]). However, more often, models are proposed based on the theorists' intuition, on phenomenological arguments and on the assumption that only a restricted subset of features (for example a reduced set of the interaction matrix elements) are essential to describe the problem of interest. These models always contain parameters, which are determined by fitting either experiments or results of *ab-initio* calculations. Whenever a model is not able to describe the most important aspects of the system under study, this is because it probably neglects some essential degrees of freedom.
As a first step towards the introduction of one of such effective models, we re-write the electronic structure Hamiltonian (2.3) in the second quantization formalism. This then reads

$$\hat{H} = \sum_{\alpha,\sigma_\alpha,\beta,\sigma_\beta} h_{\alpha\sigma_\alpha,\beta\sigma_\beta}(\hat{c}^\dagger_{\alpha\sigma_\alpha}\hat{c}_{\beta\sigma_\beta} + h.c.) + \frac{1}{2}\sum_{\sigma_\alpha\sigma_\beta\sigma_\gamma\sigma_\delta}\sum_{\alpha\beta\gamma\delta} V_{\alpha\sigma_\alpha,\beta\sigma_\beta,\gamma\sigma_\gamma,\delta\sigma_\delta}\hat{c}^\dagger_{\alpha\sigma_\alpha}\hat{c}^\dagger_{\beta\sigma_\beta}\hat{c}_{\gamma\sigma_\gamma}\hat{c}_{\delta\sigma_\delta}\,, \tag{2.85}$$

where

$$h_{\alpha\sigma_\alpha,\beta\sigma_\beta} = \delta_{\sigma_\alpha,\sigma_\beta} \int d\mathbf{r}\, \psi^*_\alpha(\mathbf{r}) \left[-\frac{1}{2}\nabla^2_{\mathbf{r}} - \sum_{i=1}^{N_N} \frac{Z_i}{|\mathbf{r}-\mathbf{d}_i|} \right] \psi_\beta(\mathbf{r}) \tag{2.86}$$

and

$$V_{\alpha\sigma_\alpha,\beta\sigma_\beta,\gamma\sigma_\gamma,\delta\sigma_\delta} = \delta_{\sigma_\alpha\sigma_\delta}\delta_{\sigma_\beta\sigma_\gamma} \int d\mathbf{r}\, d\mathbf{r}'\, \psi^*_\alpha(\mathbf{r}')\psi^*_\beta(\mathbf{r}) \frac{1}{|\mathbf{r}-\mathbf{r}'|} \psi_\gamma(\mathbf{r})\psi^*_\delta(\mathbf{r}') \,. \tag{2.87}$$

Here $\psi_\alpha(\mathbf{r})$ is the non-interacting wave-function in Eq. (2.7) and $\hat{c}^\dagger_{\alpha\sigma}$ and $\hat{c}_{\alpha\sigma}$ are the usual creation and annihilation operators for an electron of spin σ in the single-particle state ψ_α.

We now introduce the unitary transformations

$$\hat{c}^\dagger_{\alpha\sigma} = \sum_{\mathbf{i}} u_{\alpha\mathbf{i}\sigma} \hat{c}^\dagger_{\mathbf{i}\sigma} \,, \tag{2.88}$$

$$\hat{c}_{\alpha\sigma} = \sum_{\mathbf{i}} u^*_{\alpha\mathbf{i}\sigma} \hat{c}_{\mathbf{i}\sigma} \,, \tag{2.89}$$

where the position $\mathbf{d}_i$ of the i-th ion (called "lattice site") has been re-labelled through the index $\mathbf{i}$ (i.e. $\mathbf{i} \equiv \mathbf{d}_i$). By using these transformations, the Hamiltonian (2.85) becomes

$$\hat{H} = -\sum_{\mathbf{ij}\sigma} t_{\mathbf{ij}} (\hat{c}^\dagger_{\mathbf{i}\sigma} c_{\mathbf{j}\sigma} + h.c.) + \frac{1}{2} \sum_{\sigma,\sigma'} \sum_{\mathbf{ijkl}} \tilde{V}_{\mathbf{i}\sigma,\mathbf{j}\sigma',\mathbf{k}\sigma',\mathbf{l}\sigma} \hat{c}^\dagger_{\mathbf{i}\sigma} \hat{c}^\dagger_{\mathbf{j}\sigma'} \hat{c}_{\mathbf{k}\sigma'} \hat{c}_{\mathbf{l}\sigma} \,, \tag{2.90}$$

where we have defined the hopping amplitude from the site $\mathbf{i}$ to the site $\mathbf{j}$

$$t_{\mathbf{ij}} = -\sum_{\alpha\beta} u^*_{\beta\mathbf{j}\sigma} h_{\alpha\sigma,\beta\sigma} u_{\alpha\mathbf{i}\sigma} \tag{2.91}$$

and the interaction matrix elements

$$\tilde{V}_{\mathbf{i}\sigma,\mathbf{j}\sigma',\mathbf{k}\sigma',\mathbf{l}\sigma} = \sum_{\alpha,\beta,\gamma,\delta} u^*_{\gamma\mathbf{k}\sigma'} u^*_{\delta\mathbf{l}\sigma} V_{\alpha\sigma,\beta\sigma',\gamma\sigma',\delta\sigma} u_{\alpha\mathbf{i}\sigma} u_{\beta\mathbf{j}\sigma'} \,. \tag{2.92}$$

We remark now that, when the wave-functions $\{\psi_\alpha(\mathbf{r})\}$ are Bloch states, the unitary transformations in Eqs. (2.88) and (2.89) represent the mapping to Wannier functions centered on lattice site $\mathbf{i}$ [102].

Interestingly, each of the various matrix elements $\tilde{V}_{\mathbf{i}\sigma,\mathbf{j}\sigma',\mathbf{k}\sigma',\mathbf{l}\sigma}$ provides a different relative contribution to the total electron-electron interaction and, most importantly, some of them can be directly related to a specific physical process (see, for example,

references [3, 178] for a quite detailed discussion). By considering only the so-called on-sites Coulomb terms $\tilde{V}_{\mathbf{i}\uparrow,\mathbf{i}\downarrow,\mathbf{i}\downarrow,\mathbf{i}\uparrow}$ and $\tilde{V}_{\mathbf{i}\downarrow,\mathbf{i}\uparrow,\mathbf{i}\uparrow,\mathbf{i}\downarrow}$ (with $\tilde{V}_{\mathbf{i}\uparrow,\mathbf{i}\downarrow,\mathbf{i}\downarrow,\mathbf{i}\uparrow} = \tilde{V}_{\mathbf{i}\downarrow,\mathbf{i}\uparrow,\mathbf{i}\uparrow,\mathbf{i}\downarrow}$) and neglecting all the others, we obtain the Hamiltonian for the *repulsive* Hubbard model [179]

$$\hat{H} = \sum_{\mathbf{i}\sigma} \epsilon_{\mathbf{i}} \hat{n}_{\mathbf{i}\sigma} - \sum_{\mathbf{i},\mathbf{j}(\mathbf{i}\neq\mathbf{j})} \sum_{\sigma} t_{\mathbf{i},\mathbf{j}} (\hat{c}^{\dagger}_{\mathbf{i}\sigma} \hat{c}_{\mathbf{j}\sigma} + h.c.) + U \sum_{\mathbf{i}} \hat{n}_{\mathbf{i}\uparrow} \hat{n}_{\mathbf{i}\downarrow} \,, \tag{2.93}$$

where $U = 2\tilde{V}_{\mathbf{i}\uparrow,\mathbf{i}\downarrow,\mathbf{i}\downarrow,\mathbf{i}\uparrow}$ is called Coulomb interaction strength (note that the factor 2 comes from the sum over the spins). In the Hubbard Hamiltonian (2.93) we have explicitly indicated the on-site energies $\epsilon_{\mathbf{i}} = -2t_{\mathbf{ii}}$ and the hopping amplitude is often assumed to be non-zero only for nearest neighbor sites.

In spite of its formal simplicity, the model is far from being trivial as it describes the competition between electron itinerancy and atomic localization. Indeed, while the kinetic energy term favors the delocalization of the electrons over the entire lattice, the potential energy term keeps electrons apart so that it leads to integer site occupation and therefore localization. These two opposite tendencies can be clearly understood by considering, on the one hand, the band limit (i.e $U = 0$) and, on the other hand, the atomic limit (i.e. $t_{\mathbf{ij}} = 0$ for every couple of site $\mathbf{i}$ and $\mathbf{j}$). In this two extreme cases the model is very easily solvable.

Most of the interest of condensed matter physicists for the Hubbard model stems from the fact that it is believed to account for the main features of electron correlation in narrow energy bands and then to provide a microscopic qualitative explanation of several many-particle phenomena.

The model has been extensively studied for one-dimensional chains and square and cubic lattices (see, for example, the book by Montorsi [180], which contains some of the most relevant original publications about the Hubbard model). Its electronic and magnetic properties are now quite well understood for the half-filled case (i.e. for the number of electrons equal to the number of sites). In this case, for large U the system is a Mott insulator and the Hubbard Hamiltonian maps onto an antiferromagnetic Heisenberg model [178]. In contrast, much less is known about its physics when the lattice is doped away from this specific limit. For example, it has not been fully understood whether or not, for some parameters values, the model is able to describe itinerant ferromagnetism and superconductivity.

Although the Hubbard model was originally proposed to explain the physics of the transition metal oxides (FeO, CoO, etc.) [179, 181, 182], it is nowdays employed to describe a large number of systems. For example, in recent years, due to the constantly increasing interest in graphene and related materials, many studies about the

Hubbard model on the honeycomb lattice have been published [183, 184, 185]. These led to many interesting results and also to the prediction of a novel quantum spin liquid phase [186].
Furthermore, the achievement of cooling and quantum degeneracy in ultracold gases of fermionic atoms [187, 188, 189, 190, 191] allows nowadays a precise quantitative comparison between the experimental and the theoretical phase diagram of the Hubbard model.
Many extensions and modifications to the Hubbard model have been proposed in order to gain insight into the physics of several interesting many-particle systems. For example, by setting U to negative values, we introduce the *attractive* Hubbard model, which has been used to elucidate many properties of both conventional and high-temperature superconductors [192, 193].
By assuming either random on-site energies or random hopping amplitudes, we obtain the Anderson-Hubbard model. This will be introduced in Chapter 4, when we will discuss the interplay between disorder and magnetism in defective metals. In addition, the Anderson-Hubbard model has been widely studied in order to address the issue of a possible interaction-induced metal-insulator transition in two dimensions and to provide an interpretation of the puzzling results of transport experiments in silicon MOSFETs (see, for example, references [194, 195, 196, 197, 198] and references therein).
Finally many one-dimensional Hubbard-like models, which include either the electron-phonon interaction or the coupling between electrons and classic lattice relaxations, have been proposed in order to describe conjugated polymers and charge-transfer salts (see, for example, references [199, 200, 201, 202, 203, 204, 205] and references therein). The main goal here consists in understanding how different interactions compete to stabilize different phases (metallic, Mott insulating, Peierls insulating, etc.). For example, one of such models (often called Peierls-Hubbard), is defined by the one-dimensional Hamiltonian

$$\hat{H} = \sum_{i\sigma} \epsilon_i \hat{n}_{i\sigma} + \sum_{i,\sigma} [t + \alpha(u_i - u_{i+1})](\hat{c}^{\dagger}_{i\sigma}\hat{c}_{i+1\sigma} + h.c.) + \\ + U \sum_i \hat{n}_{i\uparrow}\hat{n}_{i\downarrow} + \frac{k}{2}\sum_i (u_i - u_{i+1})^2 , \tag{2.94}$$

where u_i is the displacement of the i-th ion, α is the coupling constant between the electronic and ionic degrees of freedom and k is the spring constant.
In one dimension, many analytic methods allow in-depth investigations of both ground

state properties and excitations of quantum many-body systems on a lattice [206]. However all of these methods are highly specialized for the "one-dimensional world" and, therefore, in two and three dimensions an extensive use of numerical simulations is unavoidable. In principle, the Hubbard Hamiltonian (2.93) can be diagonalized exactly. However, for a lattice of N sites, the dimension of the Hilbert space is 4^N. Therefore, even though the number of basis states can be reduced by exploiting symmetries, the system size that can be handled is limited to few sites. By using iterative diagonalization procedures, such as the Lanczos method (see, for example, reference [207] and references therein), it is possible to increase by a few more sites the system size treatable. These methods currently allow the calculation of the ground state properties of the Hubbard model for a lattice of about 20 sites. In order to investigate larger systems, in one dimension, the so called Density Matrix Renormalization Group (DMRG) [208, 209] is commonly employed and it provides highly accurate results. However, for even larger systems than those handled by DMRG and for two and three dimensional lattices, one must employ various approximate methods. For example, in chapter 4, we will discuss the mean-field approximation. This consists in looking for the Slater determinant, which minimizes the energy, and it is therefore the lattice-version of the HF method described in section 2.3. Interestingly, the one and two dimensional Hubbard model has been also recently studied through the lattice extension of DFT (see, for example, references [210, 211, 212, 213, 214]). Unfortunately however, it is often hard to establish firmly whether and within which parameter values range the results of the mean-field approximation and, likewise, of many other approximate methods are reliable. In contrast, quantum Monte Carlo methods provide the most accurate numerical approach to compute many quantities of interest for system sizes too large to be reached by exact diagonalization and for arbitrary lattices. Therefore, several algorithms have been developed specifically for the Hubbard model since the '80s. One such method will be discussed in detail in Chapter 5.

Chapter 3

Predicting d^0 magnetism

3.1 Introduction

In the recent years, many reports of d^0 ferromagnetism in wide-gap oxides (ZnO, TiO_2, SnO_2, MgO, etc.) have followed one another (see, for example, references [35, 37, 38, 39, 40, 41, 42, 43, 44, 45]). These usually concern either undoped samples (mainly thin films and nano-particles) or samples intentionally doped with light element atoms such as C and N [216, 217, 215, 218] . In the first case, the magnetic properties are usually ascribed to the presence of vacancies, while, in the second, to the dopant itself. Unfortunately, it is hard to experimentally characterize the concentration and the distribution of these point defects. When the magnetism is observed in N and C doped thin films, the position of the impurities within the crystal (interstitial, substitutional, etc.) is not established with certainty and even the possibility that doping is only indirectly connected to the magnetism (for example by promoting the formation of the actual defects responsible for that) cannot be ruled out. Therefore, in spite of the large research effort, no solid demonstration of the connection between the proposed point defects and the magnetism has been achieved yet.
In this scenario, DFT calculations can be very helpful in order to investigate the physical properties of d^0 magnets. Indeed, in principle, the shallow or deep nature of each defect can be determined and several quantities of interest (such as defect formation energies, magnetic moment magnitudes and exchange coupling constants) can be accurately calculated. One can then provide a list of defects which are likely to be responsible for the magnetism.
Computational studies about d^0 magnets usually attribute the formation of magnetic moments to holes at acceptor sites (see, for example, references [75, 221]). Then the magnetic coupling is justified through the degree of delocalization of the impurity

state [222]. Critically most of the predictions are based on calculations performed with either LSDA or GGA (see, for example, [219, 220, 221]). In the next section we will point out some of the shortcomes of LSDA/GGA, which can lead to incorrect predictions for defect-related magnetism.

In order to partially correct for the LSDA/GGA drawbacks and obtain reliable results, we have employed the atomic self-interaction correction (ASIC) developed within our group and implemented in the SIESTA code by Pemmaraju et al. [151]. ASIC is based on the pseudo-SIC method originally proposed by Filippetti and Spaldin [224] and we give a quick summary of it in section 3.3.

In section 3.4.2, we first present our results for MgO. We start by discussing the physics of B, C and N substituting for O. Although there are no published experimental reports of ferromagnetism for these systems[1], they represent good examples to illustrate the main issues related to the theoretical description of d^0 magnets and to show the subtle interplay, that exists, between covalency, polaronic distortion, charge localization and magnetic coupling. In contrast, several reports of ferromagnetism exist for undoped MgO [45, 225, 226, 227, 228, 229]. Here magnetism is often claimed to be somehow related to cation vacancies. The results of many electron spin resonance (ESR) measurements for the Mg vacancy, V_{Mg}, have been available since the 1970s [250, 251]. The availability of experimental data, establishing the nature of V_{Mg}, sets then a stringent test for DFT predictions obtained with different exchange-correlation functionals. In particular, the results of LSDA/GGA can be compared to beyond-LSDA approaches. For this problem, in addition to ASIC , we have used two other such methods. The first is the HSE hybrid-DFT functional, briefly discussed in section 2.5.5. This represents a promising tool to study many properties of solid state systems, in particular wide-gap materials [230, 231]. For instance, it was recently shown to be able to describe correctly the interplay between electronic properties and lattice distortion in the DMS Mn:GaN [232] and in oxides as complex as $BaBiO_3$ [233]. The second is the LSDA+U method, which was also mentioned in section 2.5.5.

Finally we discuss the ground state electronic and magnetic properties of several acceptor defects in GaN, for which no beyond-LSDA descriptions existed at the time we started our research.

We have decided not to present the results of the calculations, we have performed for ZnO. We have deeply studied the electronic properties of the Zn vacancy and of vari-

[1]Parkin and coworkers have claimed ferromagnetism for N-doped MgO [218], but their results have not been published so far.

ous substitutional defects, such as C and N substitutional for O and Li substitutional for Zn. However, most of the results, portray, in case of ZnO, a phenomenology very similar to that of MgO. Thus they do not add any new fundamental understanding to the physics of defects in oxides. Furthermore some studies, employing beyond-LSDA techniques have been recently published [235, 234, 236, 237] and their results agree qualitatively, and often even quantitatively, with ours.

3.2 Pitfalls of LSDA and GGA

3.2.1 Band gap problem

The first shortcome of LSDA (and GGA) is the underestimation of the band-gap. This is often manifested either by a conduction band minimum (CBM) which is too low or a valence band maximum (VBM), which is too high. For example, the gap of ZnO is 3.45 eV, while the LSDA Kohn-Sham band-gap Δ_{KS} is 0.80 eV as the VBM is too high in energy [238]. As explained in section 2.5.3, the KS band-gap is not supposed to coincide with the "real" band-gap, which is calculated as $\Delta = -A + I$. Therefore one could consider the band-gap problem as a "false" problem deriving from the misinterpretation of the non-physical KS eigenvalues. However, as discussed in detail by Lany and Zunger [239], for LSDA and GGA, this is an actual problem since $\Delta = -A + I$ converges to Δ_{KS} for large extended systems. In other words, for semiconductors, Δ_{KS} provides an estimate of the actual LSDA band-gap Δ.
For what concerns impurity- and defect-related magnetism, the underestimation of the band gap has important consequences. If the band gap is too small, the impurity band will be resonating either in the conduction or in the valence band of the host semiconductor and, if it is partially-occupied, it will spin-split the bottom of the conduction (top of the valence) band promoting long-range magnetic coupling between the point defects. A method, which allows a self-consistent correction of the band edges of the host semiconductor, while returning the correct hybridization with the impurity band, is then required.

3.2.2 Incorrect description of hole self-trapping

It is well established experimentally that holes bound to acceptor defects in wide-gap semiconductors and oxide insulators are often localized ("self-trapped") by the symmetry breaking of defect orbitals and lattice distortions forming small bound polarons [240, 241]. A standard example of a system which has a self-trapped hole

is Al-doped α-quartz SiO_2 [242]. Here, when an Al atom substitutes a Si atom, one among the four Al-O bonds gets considerably longer than the others. Such a distortion is associated with the localization of the Al-induced hole. However LSDA and GGA fail in describing the correct physics with this failure being caused by the residual self-interaction. The self-interaction energy is higher for localized states than for highly delocalized ones. Therefore LSDA and GGA always return delocalized hole states lower in energy than the self-trapped ones. This concept is also clearly discussed by Chan, Lany and Zunger [236, 234] through an analysis of the energy as a function of the continuous (fractional) electron number, $E(N)$. These authors remark that the failure of LSDA to localize stems fundamentally from the convex rather than linear shape of $E(N)$ between integer occupations. This is a clear manifestation of the self-interaction error.
As LSDA fails to localize impurity states and to describe the local crystal symmetry breaking around acceptor defects, most of the calculations carried out return metallic (often half-metallic) ground states and large magnetic interactions (see, for example, [219]).

3.3 ASIC

The modern theory of self-interaction correction (SIC) in DFT is due to the work of Perdew and Zunger [64]. Their method consists in removing the self-Hartree and self-exchange correlation energy of all the occupied KS orbitals from the LDA exchange functional. Thus the SIC functional is

$$E_{xc}^{SIC}[n^{\uparrow}, n^{\downarrow}] = E_{xc}^{LDA}[n^{\uparrow}, n^{\downarrow}] - \sum_{\alpha\sigma}^{\text{occupied}} (J[n_{\alpha}^{\sigma}] + E_{xc}^{LDA}[n_{\alpha}^{\sigma}, 0]), \tag{3.1}$$

where J is the Hartree energy (2.23) functional and $n_{\alpha}^{\sigma} = |\psi_{\alpha\sigma}^{KS}|^2$.
The SIC functional belongs to the class of orbital-dependent functionals and the search for its energy minimum is non-trivial. Indeed, E_{xc}^{SIC} is not invariant under unitary transformations of the occupied KS orbitals and then the KS method becomes either nonorthogonal or size-inconsistent. However these problems can be avoided [243, 244, 245] by introducing a second set of orbitals $\phi_{\alpha\sigma}$, which are related to the canonical KS orbitals by a unitary transformation M

$$\psi_{\alpha\sigma}^{KS} = \sum_{\beta} \mathrm{M}_{\alpha\sigma}^{\beta} \phi_{\beta\sigma}. \tag{3.2}$$

The functional can then be minimized by varying both the orbitals $\psi^{KS}_{\alpha\sigma}$ and the unitary transformation M, leading to the system of equations

$$\hat{H}_{\alpha\sigma}\psi^{KS}_{\alpha\sigma} = (\hat{H}_{0\sigma} + \Delta\hat{V}^{SIC}_{\alpha})\psi^{KS}_{\alpha\sigma} = \epsilon^{SIC}_{\alpha\sigma}\psi^{KS}_{\alpha\sigma} \tag{3.3}$$

$$\psi^{KS}_{\alpha\sigma} = \sum_{\beta} \mathrm{M}^{\beta}_{\alpha\sigma}\phi_{\beta\sigma} \tag{3.4}$$

$$\Delta\hat{V}^{SIC}_{\alpha} = \sum_{\beta} \mathrm{M}^{\beta}_{\alpha\sigma} V^{SIC}_{\beta} \frac{\phi_{\beta\sigma}}{\psi^{KS}_{\alpha\sigma}} = \sum_{\beta} V^{SIC}_{\beta}\hat{P}^{\phi}_{\beta} \tag{3.5}$$

where $\hat{H}_{0\sigma}$ is the LDA Hamiltonian, $\hat{P}^{\phi}_{\beta}\psi^{KS}_{\alpha\sigma}(\mathbf{r}) = \phi_{\beta\sigma}(\mathbf{r})\langle\phi_{\beta\sigma}|\psi^{KS}_{\alpha\sigma}\rangle$ and $V^{SIC}_{\alpha} = V_H([n_\alpha],\mathbf{r}) + V^{\sigma,LDA}_{xc}([n^{\uparrow}_{\alpha},0],\mathbf{r})$ with V_H and V_{xc} the Hartree and the LDA-xc potential respectively. In Eq. (3.3), we have used the fact that, at the energy minimum, the matrix of the SIC KS-eigenvalues is diagonalized by the KS orbitals ψ^{KS}_{α}. Notably, such a minimization scheme can be readily applied to extended systems without loosing the Bloch representation of the KS orbitals.

Finally the ASIC method consists in taking two drastic approximations in Eq. (3.3). Firstly, assume that the orbitals $\phi_{\beta\sigma}$ are atomic-like orbitals $\Phi_{\beta\sigma}$ thus that

$$\sum_{\beta} V^{SIC}_{\beta}(\mathbf{r})\hat{P}^{\phi}_{\beta} \rightarrow \alpha \sum_{\beta} \tilde{V}^{SIC}_{\beta}(\mathbf{r})\hat{P}^{\Phi}_{\beta}, \tag{3.6}$$

where $\tilde{V}^{SIC}_{\beta}(\mathbf{r})$ and $\hat{P}^{\Phi}_{\beta}$ are the SIC potential and projector associated with the atomic orbital $\Phi_{\beta\sigma}$. Secondly, replace the non-local projector with its expectation value $p_{\beta\sigma} = \sum_{\alpha} f_{\alpha\sigma}\langle\psi^{KS}_{\alpha\sigma}|\hat{P}^{\Phi}_{\beta}|\psi^{KS}_{\alpha\sigma}\rangle$. Finally the ASIC potential reads

$$V^{ASIC}_{\sigma}(\mathbf{r}) = \alpha \sum_{\beta} \tilde{V}^{SIC}_{\beta}(\mathbf{r})p_{\beta\sigma}. \tag{3.7}$$

Note that in this expression a factor α appears. This is an empirical scaling term that accounts for the fact that the ASIC orbitals Φ do not coincide with those that minimize the SIC functional of Eq. (3.1). By construction $\alpha = 1$ in the atomic limit while it vanishes for the homogeneous electron gas. Intermediate values are expected for situations different from these two extremes and, an extensive test [151] shows that a value of $\alpha = 1/2$ describes well a vast class of mid- to wide-gap semiconductors.

Finally a comment about the total energy is needed. The present theory is not variational since the KS potential in ASIC cannot be related to a functional by a variational principle. We then use the expression of Eq. (3.1) for the energy, in which the orbital

densities are those calculated by ASIC. Filippetti et al. [246] have recently developed a variational version of the ASIC, but we did not use it in this work.
Despite its simplicity, ASIC gives important improvements over LSDA/GGA in describing wide-gap semiconductors[2] and it is able to partially fix some of the above mentioned pitfalls. First, as discussed in detail by Pemmaraju et al. [151], ASIC is able to increase the band-gap of oxides and nitrides obtaining a remarkable agreement between the KS band-gap and the experimental one (for $\alpha \approx 1/2$). Furthermore the ASIC band structures usually compare very well with those extracted from photoemession measurements. ASIC, represents then a "poor man's" method to calculate quasiparticles energies for medium- and wide-gap insulators. Pemmaraju et al. [80] have applied ASIC to study magnetism in Co:ZnO. Their results indicate that, not only the band structure of the ZnO is described quite accurately, but also that the Co e_g states are returned deep inside the gap consistently with the experimental reports. The incorrect hybridization between these states and the bottom of the conduction band, returned by LSDA, is then drastically reduced by ASIC and no long-range magnetic coupling between Co atoms is found.
Furthermore, as the failure of LSDA in describing self-trapped holes originates from the self-interaction error, we expect ASIC to be able to predict the formation of small polarons. In order to verify this we have carried out several test calculations for the prototypical case of the Al substituting Si in SiO_2, Al_{Si}. We have considered a 36 atom supercell and the atomic coordinates are optimized with standard conjugate gradient until the forces are smaller than 0.04 eV/Å. The LSDA local geometry of Al_{Si} has four Al-O bonds of equal lengths, 1.73 Å, and the hole spreads uniformly over the four O atoms. In contrast, relaxation with ASIC produces a distortion: three of the Al-O bonds relax to 1.67 Å, while the forth gets considerably longer, 1.94 Å. Such a distortion is associated with the localization of the Al-induced hole, which occupies the orbital along the elongated bond. This picture is qualitatively consistent with the experimental one mentioned above and the results already obtained by Avezac et al. [242].

[2]Unfortunatelly ASIC becomes ineffective for materials with homonuclear bonds, such as Si and Ge, in which valence and conduction bands have the same atomic orbital character. In this situation, the ASIC potential shifts the bands in an almost identical way, without producing any quantitative change to the band-gap.

3.4 Materials simulations

3.4.1 Computational details

As we have already mentioned, our calculations are performed by using the standard DFT code SIESTA with the LSDA functional and a development version implementing the ASIC and the LSDA+U functional. We treat core electrons with norm-conserving Troullier-Martin pseudopotentials, while the valence charge density and all the operators are expanded over a numerical orbital basis set, including multiple-ζ and polarized functions. The real space grid has an equivalent cutoff larger than 500 Ry. Calculations are performed with supercells of various sizes including k-point sampling over at least 10 points in the supercell Brillouin zone. Relaxations are performed with standard conjugate gradients until the forces are smaller then 0.04 eV/Å. For the case of the V_{Mg} in MgO, we also perform additional GGA and HSE calculations using the VASP package. A planewave energy cutoff of 520 eV and a $3 \times 3 \times 3$ Γ-centered k-point mesh are employed. For the HSE functional, the default values of 0.25 and 0.2 are used respectively for the fraction of the short-range part of the Hartree-Fock exchange, which is mixed with the PBE one, and for the screening parameter μ (see section 2.4.5). Geometry optimization is carried out by using conjugate gradients.

System	d_{LSDA}	μ_{LSDA}	d_{ASIC}	μ_{ASIC}
MgO: $\mathrm{B_O}$	2.19 (6)	3	2.20 (6)	3
MgO: $\mathrm{C_O}$	2.18 (2), 2.15 (4)	2	2.18 (4), 2.15 (2)	2
MgO: $\mathrm{N_O}$	2.10 (6)	1	2.15 (4), 2.10 (2)	1

Table 3.1: Summary table of the LSDA and ASIC calculated bond lengths, d (in Å), and magnetic moments, μ (in μ_{B}), for the various MgO defects investigated. In bracket the number of bonds of a given length.

3.4.2 MgO

B, C and N doped MgO

In this first section we consider the full trend of light dopants B, C and N in MgO. O substitutional defects $\mathrm{A_O}$ (A = B, C, N) in MgO introduce respectively 3, 2 and 1 hole, so that the filling of the $\mathrm{A_O}$ $2p$ shell is respectively 1/2, 2/3 and 5/6. In Fig. 3.1 we report the density of states for a 96 atom supercell doped with a single $\mathrm{A_O}$ and

projected over the A_O $2p$ orbitals. For all the impurities both the LSDA and ASIC return a spin-polarized ground-state with a magnetic moment as large as the number of holes. The details of the charge distribution around A_O are however profoundly different in LSDA and ASIC.

Let us look at the single acceptor N_O first. A magnetic ground state means that the hole is fully spin-polarized. The problem is then that of distributing a single hole among the three $2p$-orbitals forming the chemical bonds with the Mg cations. LSDA predicts a spin-polarized ground state with the Fermi level cutting across a 2/3 filled minority N-$2p$ impurity band. LSDA atomic relaxation is isotropic with a N-Mg bond-length slightly larger (2.10Å) than that between O and Mg, 2.08Å. This half-metallic ground state, together with the considerable energy overlap between the O $2p$ and N $2p$ orbitals (see Fig. 3.1), is suggestive of a N ferromagnetic order. In fact, the calculated ΔE for a 96 atom cell and dopants placed at second nearest neighbors is 120 meV and ferromagnetic. Note however, that we can realistically think that this partially filled degenerate p configuration is sensitive to Jahn-Teller distortion. This can not be captured by LSDA, due to the erroneous over-delocalization of the hole, but it is described by an ASIC calculation. ASIC in fact leads to the expansion of two of six N-Mg bonds (2.15 Å) with the consequent N-$2p$ levels splitting into a doubly degenerate occupied level just above the MgO valence band and an empty singlet. These are separated by an energy gap of approximately 3 eV. In this distorted configuration the magnetic moment is entirely localized over the longer of the p bonds as it can be clearly seen from Fig. 3.2, where we present the ASIC magnetization isosurface. As it is, MgO:N is an insulator and the only mechanism left for magnetic coupling between N_O is superexchange. This is expected to be extremely weak, since the first available Mg filled shells to mediate the virtual transition necessary for superexchange are the $2p$, which are extremely deep, leading practically to no coupling. In fact the calculated coupling at second nearest neighbor is only 1 meV.

It is interesting that the physics of N-doped MgO reminds that of the manganites with p orbitals involved in orbital ordering instead of d orbitals. Moreover the p-type distortion investigated here is frustrated, as each of the three degenerate $2p$ orbitals can transform into the singlet. Finally we note that results consistent with ours were obtained by Pardo and Pickett [247] by using LSDA+U and that a similar Jahn-Teller distortion was predicted by Elfimov et al. [248] for N-doped SrO.

Let us now move to C:MgO. This time the minority C-$2p$ shell is singly occupied, leading to a magnetic moment of 2 μ_B for both LSDA and ASIC. For C_O also LSDA predicts Jahn-Teller distortion with four 2.15 Å and two 2.18 Å long Mg-C bonds.

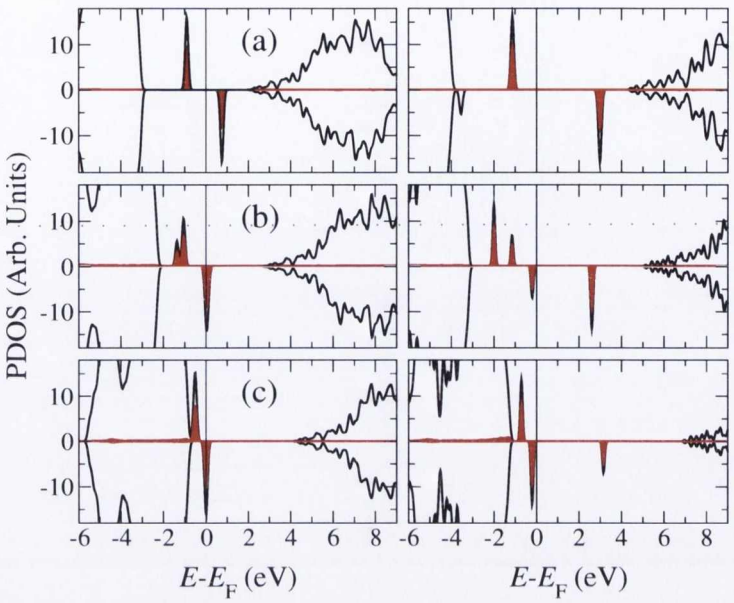

Figure 3.1: Total density of states (black line) and density of states projected over the $2p$ shells of the anion acceptor (red line) for MgO doped respectively with B (a), C (b) and N (c). The left-hand (right-hand) side plots correspond to LSDA (ASIC). The majority (minority) DOS is plotted in the upper (lower) half of each panel.

The LSDA distributes one hole entirely over the $2p$ orbital associated to the long bond but the second spreads evenly over the remaining orbitals again giving a half-metallic ground state (Fig. 3.1b). ASIC modifies the Jahn-Teller distortion into two short (2.15 Å) and four long (2.18 Å) bonds, basically reversing the LSDA geometry. In addition ASIC correctly describes the level occupation giving a filled singlet (shorter bond) separated by about 2.5 eV from an empty doublet. The triple acceptor B_O presents a somewhat less critical situation. Now the B $2p$ impurity band is half-filled and positioned completely within the MgO band-gap. The strong Hund's interaction produces a magnetic ground state with a magnetic moment of 3 μ_B/B for both LSDA and ASIC. For such an occupation the Jahn-Teller mechanism does not operate and the LSDA and ASIC bandstructures are qualitatively similar.

When we look at the magnetic coupling we find, for both N and C, a large magnetic coupling in LSDA, as already said, but practically no coupling in ASIC. The situation is rather different for B where even LSDA does not predict magnetic coupling. Does this mean that ferromagnetism cannot exist in these compounds? The answer to this

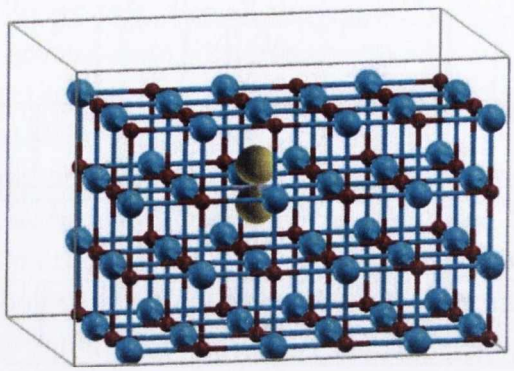

Figure 3.2: Magnetization isosurfaces calculated with ASIC for N_O in MgO. Note that the S=1/2 hole is completely localized along the p_y orbital and it is not evenly distributed along all the bonds. Color code: blue=Mg, red=O, N is not displayed for clarity.

question is not simple and essentially relates to the behavior of the impurities with additional doping. For instance by adding a fractional electronic charge to C_O one should find a situation intermediate between that of C_O and N_O. Such a charge however feels a weaker nuclear potential and certainly localizes less. Although it might occupy one of the empty C_O p orbitals, leading once again to a half-metallic bandstructure, the details of its exact localization are not easy to predict. With this in mind we have performed additional simulations in order to get at least a qualitative understanding of the interplay between extra doping and localization. In doing this one has to consider that we are moving to the border of what DFT can do at the moment. Thus, we now consider C_O and add a fraction of electronic charge Δn to the supercell. This is done by introducing also a positive background uniformly spread over the supercell in order to maintain charge neutrality. One then expects that the electronic structure and the relaxation becomes progressively similar to that of N_O. Our results are presented in Tab. 3.2, where we list the Mg-C bond lengths, d_{Mg-C}, and the cell magnetic moment, μ, as a function of Δn. Importantly all the structural calculations turned out to be sensibly dependent on the initial conditions for the relaxation. In particular we find that all the relaxations initialized at the Δn=0 C_O configuration converged to a local geometry presenting 4 long bonds and 2 short ones, i.e. still presenting the symmetry of C_O. In contrast those initialized at the Δn=0 N_O configuration converged to a local geometry with two long, two short and two intermediate bonds. The changes in the electronic structure as a function of electron doping are illustrated in the cartoon of Fig. 3.3 for the two obtained geometries. In

Δn $(-e)$	$d_{\mathrm{Mg-C}}$ (Å) [C_O-Rel]	$d_{\mathrm{Mg-C}}$ (Å) [N_O-Rel]	μ (μ_B)
0.0	2.176 (4), 2.152 (2)	2.176 (4), 2.152 (2)	2.0
0.2	2.163 (4), 2.146 (2)	2.170 (2), 2.161 (2), 2.143 (2)	1.8
0.4	2.149 (4), 2.136 (2)	2.157 (2), 2.143 (2), 2.131 (2)	1.6
0.6	2.135 (4), 2.120 (2)	2.141 (2), 2.126 (2), 2.120 (2)	1.4
0.8	2.120 (4), 2.110 (2)	2.122 (2), 2.116 (2), 2.112 (2)	1.2
1.0	2.105 (4), 2.099 (2)	2.105 (2), 2.099 (4)	1.0

Table 3.2: Mg-C bond length, $d_{\mathrm{Mg-C}}$, and supercell magnetic moment μ, of C_O as a function of the electron doping Δn. We indicate as [C_O-Rel] the relaxed structure obtained from an atomic relaxation initiated at the Δn=0 C_O geometry, and as [N_O-Rel] that initiated at the Δn=0 N_O geometry. In the bracket beside the bond length we indicate the degeneracy of the particular bond.

both cases the additional charge remains localized at the dopant site and the magnetic moment varies as $\mu = (2 - \Delta n)\mu_B$. The main difference between the electronic structures of the two geometries originates from their different orbital occupation. For the C_O-relaxed structure the fractional charge progressively occupies the minority empty doublet associated to the four long bonds, spreading evenly among them [see Fig. 3.3(a)]. In contrast the p-orbitals of the N_O-relaxed structure form a set of closely spaced singlets. Hence the additional fractional charge occupies the first of the available empty singlets and localized further along the direction of the bond of intermediate length [see Fig. 3.3(b)]. These differences persist up to Δn=1 where the C_O-relaxed structure is metallic, while the N_O-relaxed is insulating.

Unfortunately, as we said above, the ASIC functional, although constructs a valuable potential so that atomic relaxation can be carried out, does not provide accurate total energies. Therefore we cannot distinguish energetically between the two geometries found. We have performed additional ASIC total energy calculations at the un-relaxed C_O and N_O geometries, which seems to suggest a crossover between the two at a doping of Δn=0.5, however also these calculations are affected by an intrinsic lack of accuracy and therefore the result must be taken with caution.

Given this uncertainty we have decided to take a look at the theory for the local vibronic coupling. For manganites the Jahn-Teller distortion is driven by the coupling of doubly degenerate d-shell e_g states to the only two normal modes having the same symmetry. In contrast the $2p$ levels of the N in MgO form a set of degenerate t_{1u} levels, which are coupled with normal modes of symmetry e_g and t_{2g}. Importantly, in this case the e_g modes tend to stabilize a tetragonal distortion, while the t_{2g} a

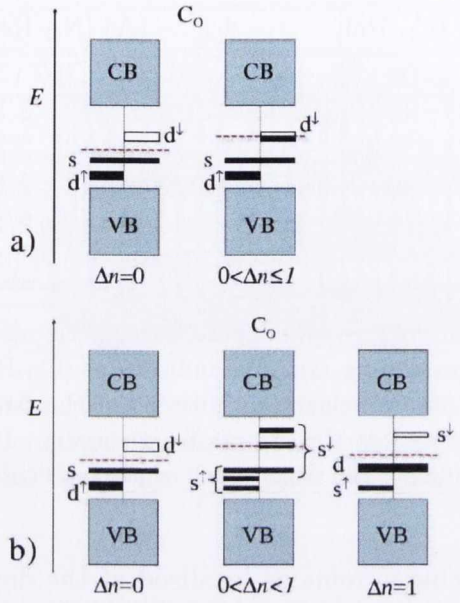

Figure 3.3: (Color on line) Cartoon representing the level occupation of C_O upon electron doping. In panel (a) the energy levels are those of the local geometry obtained from a relaxation initiated at the C_O configuration, while in (b) those obtained from a relaxation initiated at the N_O configuration. For Δn=0, in both cases a doubly occupied spin-polarized doublet ($d^{\uparrow}$) is followed by a doubly occupied unpolarized singlet (s) and separated by the Fermi level (red dashed line) from its minority spin component ($d^{\downarrow}$). Upon doping ($\Delta n > 0$), in (a) the minority doublet gets progressively filled, while in (b) the doublet further splits into two singlets and the additional fractional charge distributes over the lower of the empty minority singlets. In both cases the magnetic moment goes as $\mu = (2 - \Delta n)\mu_B$.

trigonal one resulting in a competition between the two [249]. Furthermore, when anaharmonic corrections are considered, a structure of C_2 symmetry minimizes the energy. It is notable that the highest occupied level for one hole over the impurity in this geometry is $1/\sqrt{2}(p_x \pm p_y)$ and could account for the orbital occupation found for the C_O-relaxed structure at Δn=1. Unfortunately, our relaxations always ends up with a tetragonal distortion and the symmetry around the impurity is never of C_2-type. The vibronic theory then predicts that the ground state is the one with the hole localized on just one of the three p orbitals. Thus we conclude that simple symmetry arguments seem to support the relaxation initiated by the N_O atomic coordinates, i.e. the one converging to a local geometry having two long, two short and two inter-

mediate bonds. After having studied C_O, we briefly take a look at N_O under doping. This time we find that the unpaired singlet gradually fills upon electron doping, thus that the distortion gradually reduces to a perfectly cubic symmetry and the moment follows $\mu = (1 - \Delta n)\mu_B$. Interestingly we find that the residual hole always localizes over the longest of the Mg-N bonds and that no magnetic coupling is found for every Δn, despite the material remains metallic.

Although our calculations, as expected, show difficulties in describing with quantitative accuracy the evolution of the crystalline distortion around the impurity with the extra charge, an important lesson can be learned: for impurity levels deep in the gap, the magnetic moment is stable against charge fluctuations. However, although the distortion can change continuously as a function of the doping, it never disappears completely and the magnetic moment is not able to delocalize out from the impurity site so that ferromagnetism can not be achieved.

Mg vacancy in MgO

ESR experiments dating back to the 1970s have clearly established the localized polaronic nature of V_{Mg} in MgO [250, 251] (although these results seems to have been somehow forgotten). As pointed out by Stoneham *et al.* [241], the cation vacancy can be experimentally found in two charging states: neutral, $V^0{}_{Mg}$, and singly charged, V^-_{Mg}. ESR establishes that the V_{Mg}s, in both the charging states, are deep traps exhibiting states in the gap as opposed to shallow levels at the top of the valence band. In the case of V^0_{Mg}, two holes localize completely on two adjacent oxygen sites. In contrast, for V^-_{Mg}, the only hole is completely localized on one single oxygen anion with an accompanying bond distortion.

We start our theoretical analysis by presenting the LSDA/GGA results. V_{Mg} in MgO

	$V^0{}_{Mg}$	V^-_{Mg}
LSDA	2.19 (6)	2.21 (6)
GGA	2.23 (6)	2.24 (6)
ASIC	2.11 (2), 2.22 (4)	2.13 (1), 2.24 (1), 2.25 (4)
HSE	2.111 (2), 2.253(4)	2.106 (1), 2.225 (1), 2.253 (4)

Table 3.3: Bond lengths (in Å), for V^0_{Mg} and V^-_{Mg} as calculated by different DFT functionals. Bond lengths correspond to the distance from the center of the Mg vacancy site to the O ions in the co-ordination octahedron. In brackets we report the number of bonds of a given length.

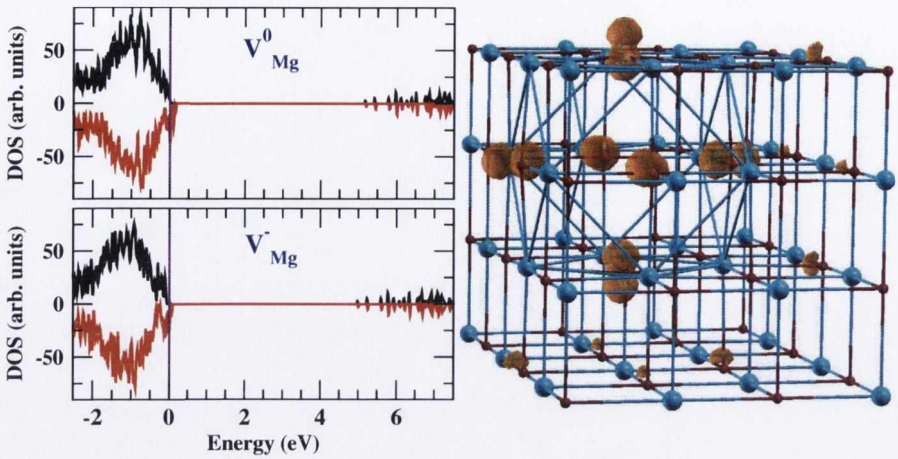

Figure 3.4: LSDA electronic structure of V_{MgO}. (Left) DOS of a MgO supercell containing either $V^0{}_{Mg}$ or V^-_{Mg}. (Right) Charge density corresponding to the minority spin holes at the top of the valence band for $V^0{}_{Mg}$. Note that the hole density is spread uniformly over the O octahedron.

presents a perfect octahedral symmetry which is preserved in LSDA and GGA, even upon lattice relaxation. This is the case for both $V^0{}_{Mg}$ and V^-_{Mg}. The bond lengths resulting from this isotropic relaxation are presented in table 3.3. The associated hole density always spreads uniformly over all the six coordinating O anions with p-orbital lobes pointing towards the center of the vacancy (see Fig. 3.4). For $V^0{}_{Mg}$ a spin triplet, $S = 1$, is obtained, while the spin singlet $S = 0$ cannot be stabilized. In contrast V^-_{Mg} presents a $S = 1/2$ ground state. For both the charging configurations the density of states (DOS) is half metallic as shown in Fig. 3.4 and corresponds to that of a shallow acceptor impurity with hole states situated at the top of the valence band. This picture however does not conform with ESR data.

In contrast, a qualitatively different picture emerges from HSE and ASIC, with the two methods being consistent with each other. Firstly, the lattice relaxation around the vacancy site breaks the octahedral symmetry. For $V^0{}_{Mg}$, two virtual bonds from the center of the vacancy to two opposing O anions are found to shorten with respect to four other bonds lying in the perpendicular plane. In the case of V^-_{Mg}, one of the two previously shorter bonds elongates while the four fold symmetry of the bonds in the perpendicular plane is retained (see Tab. 3.3). The symmetry breaking around the vacany site is also accompanied by a strong localization of the hole density on the O ions nearest to the vacancy forming small polarons (see Fig. 3.5). It should be noted that the octahedrally symmetric solution is a local minimum and in order to

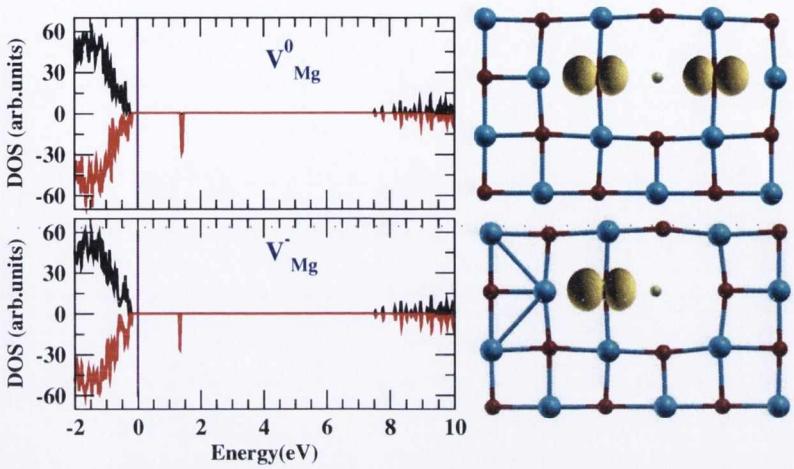

Figure 3.5: ASIC electronic structure of V_{MgO}. (Left) DOS of a MgO supercell containing either $V^0{}_{Mg}$ or V^-_{Mg}. (Top right) Charge density corresponding to the holes of $V^0{}_{Mg}$. Note that the two holes are completely localized on two opposing O ions. (Bottom right) Charge density corresponding to the single hole of $V^0{}_{Mg}$. The hole density is localized on one O ion.

access the lower symmetry ground state it might be necessary to initialize the geometry optimization in a slightly symmetry distorted ionic configuration around the site. HSE returns an energy gain due to the polaronic distortion of 360 meV for $V^0{}_{Mg}$ and 225 meV for V^-_{Mg}, and therefore it establishes that the distorted geometry is considerably more stable than the octahedrally symmetric one regardless of the charging state.

The ground state DOS obtained within ASIC and HSE is shown in Figs. 3.5 and 3.6. In contrast to the shallow acceptor states observed in LSDA/GGA, both $V^0{}_{Mg}$ and V^-_{Mg} exhibit a deep acceptor level in the gap. This is located at $\sim$1 eV ($\sim$1.25 eV) above the valence band maximum (VBM) for HSE (ASIC). It is interesting to note that for the symmetrically relaxed HSE local minimum solution (see lower panels of Fig. 3.6), a shallow acceptor DOS similar that calculated by LSDA is obtained. Thus the deep acceptor ground state is intimately associated to the polaronic bond distortion around the vacancy.

In order to further substantiate the HSE/ASIC results we have carried out additional calculations within LSDA+U mainly looking at the evolution of the ground state as a function of the U parameter (here U is applied to the O-p orbitals). For a given value of U, the total LSDA+U energies obtained at the LSDA and ASIC geometries are compared in Tab. 3.3. The energy difference $\Delta E = E(G_{LSDA}) - E(G_{ASIC})$,

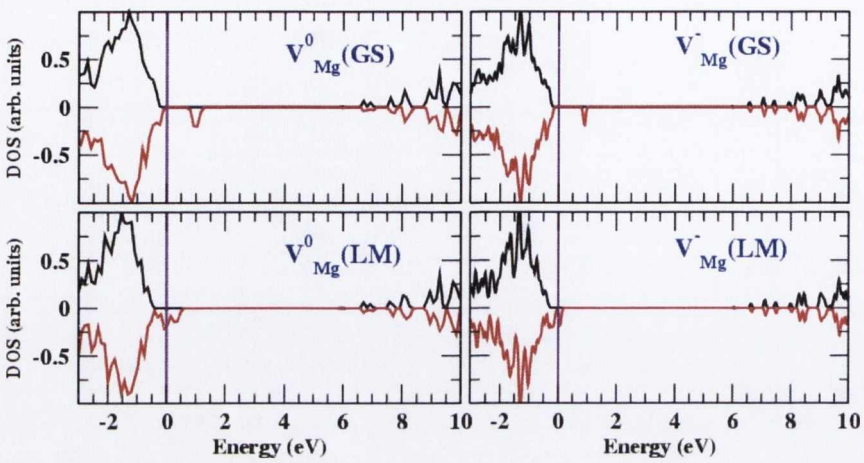

Figure 3.6: DOS calculated with HSE for a MgO supercell containing either $V^0{}_{Mg}$ or V^-_{Mg}. The top two panels show the DOS for the polaronic ground state geometry (labelled GS) of the defects. The bottom two panels show the DOS corresponding to local minima solutions (labelled LM) which preserve the octahedral symmetry around the vacancy sites.

where G_{LSDA} (G_{ASIC}) denotes the LSDA (ASIC) geometry, is shown in Fig. 3.7 as a function of U. As U is increased the bond distorted ASIC geometry is seen to stabilize with respect to the symmetric LSDA geometry and the crossover is found at around $U = 4$ eV for both $V^0{}_{Mg}$ and V^-_{Mg}. Also the nature of the defect ground state changes from shallow to deep acceptor at the crossover point. In wide-gap oxides, the value of U for the O-2p orbitals is estimated to be in the range of 5-7 eV [247]. At U=5 eV, for $V^0{}_{Mg}$ (V^-_{Mg}) the polaronic G_{ASIC} geometry is lower in energy by a robust ~390 meV (160 meV) with respect to the G_{LSDA} geometry. Furthermore the DOS for $V^0{}_{Mg}$ (Fig. 3.7) exhibits a deep acceptor state located at roughly 1.3 eV above the VBM which agrees well with the HSE results.

We now look at the magnetic properties associated to V_{Mg}. For $V^0{}_{Mg}$, the spins of the two holes may be aligned parallel or anti-parallel to each other leading either to a $S = 1$ triplet or a $S = 0$ singlet. LSDA/GGA predict a stable $S = 1$ configuration. However, within HSE/ASIC, the energies of the $S = 1$ and the $S = 0$ solutions are found to be very similar, separated only by 0.75 meV (2 meV) in HSE (ASIC). We have also calculated the inter-defect magnetic coupling interaction between two ($S = 1$) $V^0{}_{Mg}$ centers in a 192 atom supercell. For LSDA two sites separated by 8.34 Å are ferromagnetically coupled with a spin-flip energy of 33 meV (the energy required to reverse the spin of one of the two vacancies). This suggests the stabiliza-

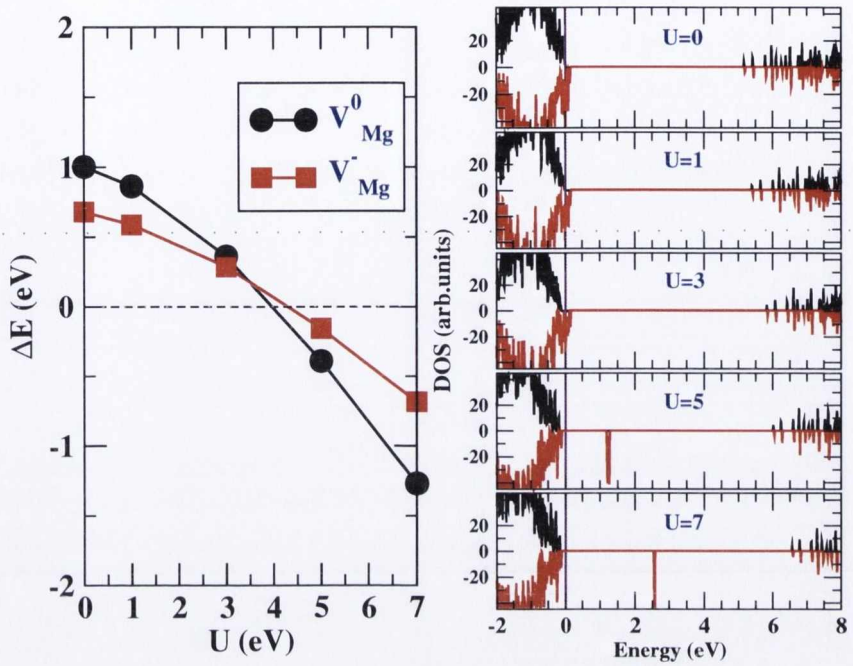

Figure 3.7: (Left) LSDA+U energy difference between the LSDA and ASIC geometries for $V^0{}_{Mg}$ and V^-_{Mg} as a function of U. Note the crossover between the two geometries at $U \sim 4$ eV, when the polaronic ASIC geometry becomes the most stable. (Right) Ground state DOS calculated with LSDA+U as a function of U.

tion of ferromagnetism via magnetic percolation between the holes, provided they are formed at a sufficiently high concentration. In contrast ASIC predicts for the same supercell configuration, a tiny interaction energy of 1 meV. Thus, we find that as soon as the correct polaronic ground state is achieved for the holes, their magnetic interaction virtually disappears.

Before concluding, we add an additional remark on the similarity between $V^-{}_{Mg}$ and the Li impurity substituting Mg (Li_{Mg}). Both are single acceptors located at the cation sublattice. For Li_{Mg} as well, LSDA returns a half-metallic ground state, with the hole completely delocalized on the O ions coordinating the impurity. ASIC instead localizes the hole on one O ion in a distorted polaronic geometry (the Li-O bond lengths are: 2.31 Å(1), 1.93 Å(1), 2.15 Å(4)). This is qualitatively identical to what is found for $V^-{}_{Mg}$. Although we did not find experiments to confirm the ground state of Li_{Mg} in bulk MgO, its nature as a small bound polaron is well established in the case of surfaces and beyond-LSDA electronic structure methods have previously

been used to study this defect in the context of catalysis [252].
In conclusion, we have shown that semilocal LSDA/GGA can lead to qualitative failures in their description of hole centers in MgO. Beyond-LDA approaches that are either self-interaction free or effectively correct for it, are able to reproduce the experimentally observed polaronic ground state. Significantly, the large inter-site ferromagnetic interaction predicted by LSDA is also shown to be an artifact. Thus, the reported high temperature ferromagnetism in MgO cannot be explained by a simple model where magnetic interactions between hole centers percolate through the sample.

3.4.3 GaN

In this paragraph, we summarize some of our LSDA and ASIC results for several acceptor defects in GaN. Although these calculations have been carried out in the context of d^0 magnetism, the characterization of the nature of defects in GaN is overall a very important issue in order to understand its electronic and optical properties. This is because of its technological relevance in the fabrication of green, blue and ultraviolets LEDs and blue lasers. Some of our results have been recently confirmed by more in depth studies [253, 254]

Gallium vacancy

The Ga vacancy, V_{Ga}, is a triple acceptor and it was recently proposed as possible source of d^0 ferromagnetism [220]. Our results, obtained with a 64 atom supercell, indicate that LSDA and ASIC agree on the magnetic ground state of V_{Ga}. However, like for the defects in MgO, the spatial distribution of the moment changes radically depending upon the functional being considered. In fact, in LSDA, the four N surrounding the vacancy move outwards so that the distance from the vacant site is 2.1 Å, about 8% longer than that between Ga and N. Such a displacement is isotropic and the three holes spread uniformly over the four available bond directions of the wurtzite lattice. Thus the material turns out to be half metallic. The magnetic coupling (for two V_{Ga} placed at 6.3 Å from each other) is antiferromagnetic and equal to 145 meV, but the doping of one extra electron per supercell promotes ferromagnetism through a long range double-exchange mechanism. However, the ASIC picture is rather different. Also in this case ASIC allows the hole to localize. The relaxation leads to two bonds 2.14 Å in length and two longer bonds of slightly different lengths (2.28 and 2.31 Å). The longest of the four is fully filled and the three holes localize

on the remaining three. Also for V_{Ga}:GaN self-trapping massively suppresses the magnetic coupling energy which reduces to just 1 meV.

C, Mg and Zn doped GaN

The N substitutional defect, C_N, and the Ga substitutional defects Mg_{Ga} and Zn_{Ga} are all acceptors, which introduce a single hole. Their phenomenology is very similar. LSDA gives a non-magnetic ground state with a very shallow impurity band and the hole evenly distributed over the four almost tetrahedrally coordinated bonds. These are just slightly elongated and their values can be found in Tab. 3.4. The non-magnetic state in LSDA is resistant to supercell size and persists to cells as large as 256 atoms. In contrast, ASIC again captures the Jahn-Teller distortion, with one of the C-Ga and Mg(Zn)-N bonds elongated (these results can also be found in Tab. 3.4). The hole then completely localizes over the longest bond (see Fig. 3.8), and, due to the enhanced degree of localization, the Hund's coupling promotes a spin 1/2 ground state. The ASIC electronic structure then is that of C_N, Mg_{Ga} and Zn_{Ga} being paramagnetic deep traps instead of shallow non-magnetic acceptors.

Interestingly, experiments seems to support our results for Zn_{Ga}. Indeed, in Zn

System	d_{LSDA}	d_{ASIC}
C:GaN	1.96 (4)	1.98 (3), 2.14 (1)
Mg:GaN	2.02 (4)	1.99 (3), 2.26 (1)
Zn:GaN	2.0 (4)	1.96 (3), 2.4 (1)

Table 3.4: Summary table of the LSDA and ASIC calculated bond lengths, d (in Å) for C_N, Mg_{Ga} and Zn_{Ga}. In bracket the number of bonds of a given length.

doped GaN, a blue luminescence band at about 2.9 eV is often observed and it is almost certainly attributed to an optical transition from the conduction band to the Zn_{Ga} level, which should be deep inside the band-gap (see reference [255] and references therein). Furthermore optically detected magnetic resonance (ODMR) studies find a signal which has been attributed to the Zn acceptor [255], whose ground state must be then a triplet.

For the case of Mg_{Ga}, on the one hand, our results seem in stark contrast with the common belief that Mg_{Ga} impurities are shallow acceptors and provide the carriers for p-type conductivity in Mg:GaN. On the other hand, they agree with the results of ODMR measurement, which indicates that the hole is located in an atomic orbital of p-character on a N atom close to the impurity [256, 257]. Lany and Zunger [254] have

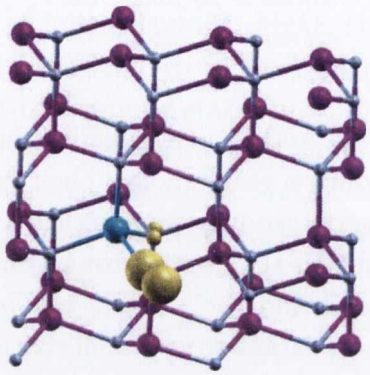

Figure 3.8: Magnetization isosurfaces calculated with ASIC for Mg_{Ga} in GaN. The hole is localized on one of the p_x orbital of the N close to the impurity. Color code: violet=Ga, grey=N, blue=Mg.

recently proposed a solution to this apparent paradox. They have investigated Mg_{Ga} by applying the hole-state potential operator [236] to the N-2p orbitals. Consistentely with our results, they have shown that Mg_{Ga} creates a defect state inside the band gap. This state is mostly localized on one of the p-orbitals of the N atom, that has the longest bond (2.23Å) to the Mg_{Ga}. These authors have pointed out the exceptional character of this defect: although it supports a self-trapped hole state, it has an ionization energy small enough to allow for a sufficient thermal activation of the hole into the valence band. Therefore Mg:GaN is an efficient p-type semiconductor.
Finally, Lyons et al. [253] recently published a study about C_N in GaN. They performed calculations by using the HSE hybrid functional and their results qualitatively agree with ours. Indeed the authors conclude that C_N is a very deep acceptor with a ionization energy of 0.90 eV. Furthermore they argued that C_N could be at the origin of the widely observed yellow luminescence of GaN [255].
In conclusion, from a theoretical and methodological point of view, these acceptor defects are very interesting. Indeed LSDA does not fail just in describing the degree of localization of the hole bounded to the impurity, but it is even not able to correctly predict the formation of the magnetic moment.

3.5 Prospectives for d^0 magnetism

So far, the theoretical research on d^0 magnetism has been mainly focused on describing randomly distributed defects in otherwise perfect crystals. Our results, in parallel with those by Lany and Zunger [234, 236], clearly show how acceptor defects are often well localized and the possibility of magnetic interaction among them has to be ruled out. In contrast, the role of extended defects has not been investigated very extensively.

By reviewing a large number of experimental works for ZnO and by performing new measurements, Straumal et al. [258] have clearly pointed out the correlation that exists between the presence of grain-boundaries in the samples and the reported ferromagnetism.

Maoz et al. [45] prepared MgO nanosheets presenting a very high density of extended defects (about 10^{13} cm^{-2}). Ferromagnetism was reported for temperatures below 50K and it was related to either the grain-boundaries themselves or to vacancies, which tend to segregate there. In this framework, some computational studies by McKenna et al. (see reference [259] and references therein) indicate that, in MgO, electrons can be trapped inside grain-boundaries. Stemming from this interesting result, one can speculate that trapped electrons will be strongly correlated resulting in a magnetic ordered ground state.

Körner et al. [260] have investigated the electronic structure of various grain-boundaries for doped and undoped ZnO. Two are the main conclusions: firstly, impurities tend to segregate around extended defects and, secondly, impurity states, which are deep when the associated defects are inside the bulk material, can become shallow for the defects close to a grain-boundary. This is, for example, what happens for the O substitutional defect N_O. Unfortunately these interesting studies do not discuss any issue related to the magnetism. However one can reasonably expect that, on the one hand, the low-coordinated nature of impurities at extended defects promotes the formation of magnetic moments. On the other hand, for shallow and delocalized defect states, these magnetic moments should be quite strongly coupled. If these suppositions were verified, a major step forward in the understanding of d^0 magnetism would be achieved. Therefore, a theoretical study of the magnetic properties of grain-boundaries in ZnO is currently under way within our group.

Chapter 4

Impurity band magnetism in oxides

At the end of the previous chapter, we discussed some recent experiments, which suggest that ferromagnetism in oxides might be due to charges and impurities segregated at extended defects (interfaces, dislocations and grain boundaries). The ferromagnetism has been then modelled by assuming that electrons partially fill an impurity band, which spin-splits as a consequence of a Stoner-like mechanism [261, 51]. Edwards and Katsnelson [51] have theoretically demonstrated that the spin-wave stiffness D for an half-metallic impurity band is independent on the ground state magnetization. They have also provided an analytic expression for the upper bound on D. Coey et al. [261] have then used this result to explain the unexpected high Curie temperature of many d^0 ferromagnets and the almost temperature-independent value of the saturated magnetization. According to these authors' estimates, spin-wave excitations are largely suppressed in defective magnetic oxides leaving only the high-energy Stoner excitations as main source of demagnetization. The Curie temperature would then be of the order of the band splitting, which can be thousands of Kelvins. Unfortunately Edwards and Katnelson's analytic calculations are performed by employing the coherent phase approximation (CPA) [262]. This is based on the assumption that the real system can be replaced by an ordered effective medium, neglecting then the exact treatment of disorder. Many issues concerning the interplay of electron-electron interaction and disorder in impurity bands are still open and this complex physics has not been fully understood yet. At the same time, the effect of disorder on collective magnetic excitations is much less investigated and therefore even less clear.

Interestingly, in the past, several theoretical studies attempted a description of impurity bands in semiconductors in order to explain some thermodynamics anomalies reported in low-temperatures experiments for P- and B-doped Si [263, 264, 265].

These led to the Bhatt-Lee model of a disordered quantum antiferromagnet, which is able to describe the physics of insulating samples. The "two-fluid" model was later introduced in order to describe "metallic" Si [267]. Here itinerant electrons coexist with localized moments, which arise by the interplay of interaction and disorder [268]. However the two-fluid model does not provide a satisfactory description of the experimental results therefore it probably neglects some important degrees of freedom.
In this chapter we model impurity bands in oxides by a variant of the Hubbard model, in which disorder is included by allowing the on-site energies to assume random values. This is often called Anderson-Hubbard model [269]. We firstly describe in detail the electronic and magnetic properties by using the mean-field approximation (MFA). We then study how the system behaves when an external magnetic field is applied and, finally, we calculate the collective magnetic excitations with the random phase approximation (RPA). This describes the renormalization of the electron-hole Coulomb interaction due to correlation effects [270]. Our work extends the theoretical investigation on the Hubbard-Anderson model by Tusch et al. [269, 271] to cases beyond half-filling and discusses some theoretical results within the context of d^0 magnetism. Although the use of the MFA is not fully justified, we think that it is appropriate for this specific problem. Firstly, the physics of magnetic metals is usually understood by combining the MFA and the RPA for the Hubbard model [272]. Secondly, some of the most interesting results obtained are for weak coupling where the MFA might describe the correct physics of the model. Furthermore, in the future, the same problem can be addressed by using Quantum Monte Carlo techniques (see Chapter 5).

4.1 Anderson-Hubbard model

In order to describe a system of interacting electrons in an impurity band we use an extension of the Hubbard model, often called Anderson-Hubbard model (AHM). This is defined by the Hamiltonian[1]

$$\hat{H} = \sum_{\mathbf{i},\sigma=\uparrow,\downarrow} \epsilon_{\mathbf{i}} \hat{n}_{\mathbf{i}\sigma} + \sum_{<\mathbf{i},\mathbf{j}>,\sigma=\uparrow,\downarrow} t_{\mathbf{ij}} \left(\hat{c}^{\dagger}_{\mathbf{i}\sigma} \hat{c}_{\mathbf{j}\sigma} + h.c. \right) + U \sum_{\mathbf{i}} \hat{n}_{\mathbf{i}\uparrow} \hat{n}_{\mathbf{i}\downarrow} \,, \tag{4.1}$$

where the on-site energies $\epsilon_{\mathbf{i}}$ are assumed to be random variables drawn from a Gaussian distribution with variance Δ^2. By setting $U = 0$ and $t_{\mathbf{ij}} = |t| < 0$ (for every

[1]We remind the notation introduced in section 2.7 according to which $\hat{n}_{\mathbf{i}\sigma} = \hat{c}^{\dagger}_{\mathbf{i}\sigma} \hat{c}_{\mathbf{i}\sigma}$, $\epsilon_{\mathbf{i}}$ represents the on-site energy for the site $\mathbf{i}$, $t_{\mathbf{ij}}$ the hopping probability amplitude between the site $\mathbf{i}$ and the site $\mathbf{j}$ and $U \geq 0$ is the Coulomb interaction strength. The symbol $< \mathbf{i}, \mathbf{j} >$ indicates that the sum extends just to nearest neighbors (NN) sites.

couple of NN sites **i** and **j**), we recover the standard Anderson model, which describes some transport properties of electrons in impurity bands and accounts for disorder-induced localization processes. Indeed in a cubic lattice, for $\Delta/12|t| > 1/2$, all of the states are localized and, at zero-temperature, the system is an Anderson (gapless) insulator. For $\Delta/12|t| = 1/2$ the state of energy equal to zero becomes delocalized and finally, for $\Delta/12|t| < 1/2$, we have both extended and localized states separated by a mobility edge. Then, depending on the position of the Fermi level, the system can be either an Anderson insulator or a metal.

4.2 Mean-field approximation

In this section and in the following one, we will describe the MFA and the RPA for the AHM. Although both techniques are quite standard, we believe that a brief review is nevertheless very useful. We will mainly focus on the equation-of-motion approach. This is very transparent from a physical point of view and allows us to better understand the role of electron correlation in modifying single-particle properties. Although the equation-of-motion approach is routinely employed in nuclear physics [275, 276], it is usually not so familiar to condensed matter physicists, who often prefer the formalism of the many-body perturbation theory [270] (note, however, that the equation-of-motion approach was recently discussed by Berciu et al. for the *sd* model in the context of Mn:GaAs [277]). These two different approaches can be easily related (see section 4.3.4).

4.2.1 Ising-like mean-field approximation

The MFA [7] consists in searching for the state $|0_{MF}\rangle$ composed of N single particle spin orbitals $|\alpha_1\sigma_1\rangle$,$|\alpha_2\sigma_2\rangle$...$|\alpha_N\sigma_N\rangle$:

$$|0_{MF}\rangle = \hat{c}^{\dagger}_{\alpha_1\sigma_1}\hat{c}^{\dagger}_{\alpha_2\sigma_2}...\hat{c}^{\dagger}_{\alpha_N\sigma_N}|-\rangle \tag{4.2}$$

(i.e. $|0_{MF}\rangle$ is assumed to be a Slater determinant), which minimizes the expectation value of the Hamiltonian $\langle 0_{MF}|\hat{H}|0_{MF}\rangle$ (α_i labels the i-th single-particle state of spin σ_i, which enters in the trial Slater determinant, and the state $|-\rangle$ is the vacuum).

The operators $\hat{c}_{\mathrm{i}\sigma}$, $\hat{c}^{\dagger}_{\mathrm{i}\sigma}$ and $\hat{c}_{\alpha\sigma}$, $\hat{c}^{\dagger}_{\alpha\sigma}$ are connected by the unitary transformation:

$$\hat{c}^{\dagger}_{\alpha\sigma} = \sum_{\mathrm{i}} u_{\alpha\mathrm{i}\sigma}\hat{c}^{\dagger}_{\mathrm{i}\sigma}\,, \tag{4.3}$$

$$\hat{c}_{\alpha\sigma} = \sum_{\mathrm{i}} u^{*}_{\alpha\mathrm{i}\sigma}\hat{c}_{\mathrm{i}\sigma}\,. \tag{4.4}$$

We can also introduce the single-particle (zero-temperature) density matrix

$$\rho_{\mathrm{i}\sigma,\mathrm{j}\sigma'} \equiv \langle 0_{MF}|\hat{c}^{\dagger}_{\mathrm{i}\sigma}\hat{c}_{\mathrm{j}\sigma'}|0_{MF}\rangle\,, \tag{4.5}$$

which, by using the transformation (4.3) and (4.4), is equal to

$$\rho_{\mathrm{i}\sigma,\mathrm{j}\sigma'} = \sum_{\alpha\beta} u^{*}_{\alpha\mathrm{i}\sigma}u_{\alpha\mathrm{j}\sigma'}\langle 0_{MF}|\hat{c}^{\dagger}_{\alpha\sigma}\hat{c}_{\beta\sigma'}|0_{MF}\rangle = \delta_{\sigma\sigma'}\sum_{\alpha\leq F} u^{*}_{\alpha\mathrm{i}\sigma}u_{\alpha\mathrm{j}\sigma'}, \tag{4.6}$$

where F indicates the Fermi level. The fact that $\rho_{\mathrm{i}\sigma,\mathrm{j}\sigma'} = 0$, for $\sigma \neq \sigma'$, comes from our choice of $\{|\alpha\sigma\rangle\}$ being spin-orbitals.
Eq. (4.6) tells us that the operator $\hat{\rho}$ associated to the density matrix is a projector onto the space spanned by the occupied orbitals. Then $\hat{\rho}$ alone characterizes a Slater determinant up to a phase. Because of this one-to-one correspondence between a Slater determinant and a single-particle density matrix (modulo a phase), the expectation value $\langle 0_{MF}|\hat{H}|0_{MF}\rangle$ can be written as a functional $E[\rho]$

$$\begin{aligned} E[\rho] &\equiv \langle 0_{MF}|\hat{H}|0_{MF}\rangle = \\ &= \sum_{\mathrm{i},\sigma}\epsilon_{\mathrm{i}}\rho_{\mathrm{i}\sigma,\mathrm{i}\sigma} + \sum_{<\mathrm{i},\mathrm{j}>,\sigma} t_{\mathrm{ij}}\rho_{\mathrm{i}\sigma,\mathrm{j}\sigma} + \\ &+ U\sum_{\mathrm{i}}\rho_{\mathrm{i}\uparrow,\mathrm{i}\uparrow}\rho_{\mathrm{i}\downarrow,\mathrm{i}\downarrow}\,, \end{aligned} \tag{4.7}$$

where the third term is obtained by using Wick's theorem.
The energy minimization then proceeds by imposing that

$$\delta\Big\{E[\rho] - \sum_{\mathrm{i},\mathrm{j},\sigma}\lambda_{\mathrm{i}\sigma,\mathrm{j}\sigma}\rho_{\mathrm{i}\sigma,\mathrm{j}\sigma}\Big\} = 0 \tag{4.8}$$

where the numbers $\lambda_{\mathrm{i}\sigma,\mathrm{j}\sigma}$ are the Lagrange multipliers associated to the constraint of $\rho_{\mathrm{i}\sigma\mathrm{j}\sigma}$ being a density matrix. This constraint can also be written as

$$\begin{aligned} &\textstyle\sum_{\mathrm{i},\mathrm{j},\sigma}\lambda_{\mathrm{i}\sigma,\mathrm{j}\sigma}\rho_{\mathrm{i}\sigma,\mathrm{j}\sigma} = \\ &= \textstyle\sum_{\mathrm{i},\mathrm{j},\sigma}\lambda_{\mathrm{i}\sigma,\mathrm{j}\sigma}\sum_{\alpha\beta}u^{*}_{\alpha\mathrm{i}\sigma}u_{\alpha\mathrm{j}\sigma'}n_{\alpha\sigma}\delta_{\alpha\beta} = \\ &= \textstyle\sum_{\alpha\sigma}E_{\alpha\sigma}n_{\alpha\sigma}\,, \end{aligned} \tag{4.9}$$

where we have defined $E_{\alpha\sigma} = \sum_{\mathrm{i,j}} u^*_{\alpha\mathrm{i}\sigma} \lambda_{\mathrm{i}\sigma,\mathrm{j}\sigma} u_{\alpha\mathrm{j}\sigma}$. We then find that

$$\lambda_{\mathrm{i}\sigma\mathrm{j}\sigma} = \epsilon_{\mathrm{i}} \delta_{\mathrm{ij}} + t_{\mathrm{ij}} \delta_{\mathrm{j}=\mathrm{i}\pm 1} + U \rho_{\mathrm{i}-\sigma,\mathrm{i}-\sigma} \delta_{\mathrm{ij}} \tag{4.10}$$

(with $-\sigma = \downarrow$ if $\sigma = \uparrow$ and vice versa) and the mean-field Hamiltonian reads

$$\hat{H}_{HF} = \sum_{\mathrm{i}\sigma} \left(\epsilon_{\mathrm{i}} + U \langle \hat{n}_{\mathrm{i}-\sigma} \rangle \right) \hat{c}^{\dagger}_{\mathrm{i}\sigma} \hat{c}_{\mathrm{i}\sigma} + \sum_{<\mathrm{i,j}>,\sigma} t_{\mathrm{ij}} \hat{c}^{\dagger}_{\mathrm{i}\sigma} \hat{c}_{\mathrm{j}\sigma} \, , \tag{4.11}$$

where we use the short notation $\langle \hat{n}_{\mathrm{i}-\sigma} \rangle \equiv \langle 0_{MF} | \hat{n}_{\mathrm{i}-\sigma} | 0_{MF} \rangle = \rho_{\mathrm{i}-\sigma,\mathrm{i}-\sigma}$. This is the usual collinear or Ising-like mean-field Hamiltonian for the Hubbard model. Since $\hat{H}_{MF} = \hat{H}_{MF}(\langle \hat{n}_{\mathrm{i}} \rangle)$, the mean-field ground state has to be calculated self-consistently. The eigenvalue that corresponds to and eigenstate $|\alpha\sigma\rangle$ is easily found from Eqs. (4.9) and (4.10) and it is

$$\begin{aligned} E_{\alpha\sigma} = & \sum_{\mathrm{i}} u^*_{\alpha\mathrm{i}\sigma} \epsilon_{\mathrm{i}} u_{\alpha\mathrm{i}\sigma} + \sum_{<\mathrm{i,j}>} u^*_{\alpha\mathrm{i}\sigma} t_{\mathrm{ij}} u_{\alpha\mathrm{j}\sigma} + \\ & + U \sum_{\mathrm{i}} u^*_{\alpha\mathrm{i}\sigma} u_{\alpha\mathrm{i}\sigma} \sum_{\beta} u^*_{\beta\mathrm{i}\downarrow} u_{\beta\mathrm{i}\downarrow} \langle \hat{n}_{\beta\downarrow} \rangle \delta_{\sigma\uparrow} + \\ & + U \sum_{\mathrm{i}} u^*_{\alpha\mathrm{i}\sigma} u_{\alpha\mathrm{i}\sigma} \sum_{\beta} u^*_{\beta\mathrm{i}\uparrow} u_{\beta\mathrm{i}\uparrow} \langle \hat{n}_{\beta\uparrow} \rangle \delta_{\sigma\downarrow} \, . \end{aligned} \tag{4.12}$$

The total energy is then given by

$$E_{TOT} = \sum_{\alpha\sigma} E_{\alpha\sigma} - U \sum_{\alpha,\beta \leq F} \sum_{\mathrm{i}} u^*_{\alpha\mathrm{i}\uparrow} u_{\alpha\mathrm{i}\uparrow} u^*_{\beta\mathrm{i}\downarrow} u_{\beta\mathrm{i}\downarrow} \, . \tag{4.13}$$

We must notice that the total energy is not just the sum of the eigenvalues $E_{\alpha\sigma}$. The origin of the second term on the right-hand side can be easily understood by comparing Eq. (4.7) and the expression for the eigenvalues, Eq. (4.12).

We must then add a comment. In general, the assumption that the states $\{|\alpha\sigma\rangle\}$ are spin-orbitals is very restrictive and, in many cases, the true mean-field ground state can be non-collinear. We have therefore implemented also the non-collinear form of the MFA. However, for the particular kind of disorder (chemical disorder), we have chosen, the mean-field ground-state is always found to be Ising-like. When we consider a lattice with topological disorder (i.e. we assume that each site is connected to a different number of nearest neighbors) or we include off-diagonal disorder (i.e. random hopping amplitude), we find that the non-colliner solution is lower in energy than the Ising-like one. However, for these cases, calculations could hardly be converged and therefore we could not perform systematic studies.

4.2.2 Equation-of-motion approach

In order to illustrate the equation-of-motion approach and how the mean-field approximation can be imposed, let us start by considering the commutator between the AHM Hamiltonian (4.1) and a generic operator $\hat{c}^{\dagger}_{\alpha\sigma}$:

$$\begin{aligned}
[\hat{H}, \hat{c}^{\dagger}_{\alpha\sigma}] = \\
&= \sum_{\beta} \sum_{\mathbf{i}} u^{*}_{\beta \mathbf{i}\sigma} \epsilon_{\mathbf{i}} u_{\alpha \mathbf{i}\sigma} \hat{c}^{\dagger}_{\beta\sigma} + \sum_{\beta} \sum_{<\mathbf{i},\mathbf{j}>} u^{*}_{\beta \mathbf{i}\sigma} t_{\mathbf{ij}} u_{\alpha \mathbf{j}\sigma} \hat{c}^{\dagger}_{\beta\sigma} + \\
&+ U \sum_{\beta,\eta,\gamma} \sum_{\mathbf{i}} u^{*}_{\eta \mathbf{i}\uparrow} u_{\alpha \mathbf{i}\uparrow} u^{*}_{\gamma \mathbf{i}\downarrow} u_{\beta \mathbf{i}\downarrow} \delta_{\sigma\uparrow} \hat{c}^{\dagger}_{\gamma\downarrow} \hat{c}_{\beta\downarrow} \hat{c}^{\dagger}_{\eta\uparrow} + \\
&+ U \sum_{\beta,\eta,\gamma} \sum_{\mathbf{i}} u^{*}_{\eta \mathbf{i}\uparrow} u_{\beta \mathbf{i}\uparrow} u^{*}_{\gamma \mathbf{i}\downarrow} u_{\alpha \mathbf{i}\downarrow} \delta_{\sigma\downarrow} \hat{c}^{\dagger}_{\eta\uparrow} \hat{c}_{\beta\uparrow} \hat{c}^{\dagger}_{\gamma\downarrow} \, .
\end{aligned} \tag{4.14}$$

As we can see, the right-hand side of this equation contains terms involving three creation and annihilation operators. We can now replace each operator of the form $\hat{c}^{\dagger}_{\alpha\sigma} \hat{c}_{\beta\sigma'}$ with its expectation value with respect to the state $|0_{MF}\rangle$ (this is indicated $\langle c^{\dagger}_{\alpha\sigma} c_{\beta\sigma'} \rangle$, consistently with the notation of the the previous section) and write

$$\hat{c}^{\dagger}_{\alpha\sigma} c_{\beta\sigma'} \approx \langle c^{\dagger}_{\alpha\sigma} c_{\beta\sigma'} \rangle \delta_{\alpha\beta} \delta_{\sigma\sigma'} \, . \tag{4.15}$$

This replacement amounts to neglect quantum fluctuations about the expectation value. We then have

$$\hat{c}^{\dagger}_{\gamma\downarrow} \hat{c}_{\beta\downarrow} \hat{c}^{\dagger}_{\eta\uparrow} \approx \langle c^{\dagger}_{\gamma\downarrow} \hat{c}_{\beta\downarrow} \rangle \delta_{\gamma\beta} c^{\dagger}_{\eta\uparrow} \tag{4.16}$$

$$\hat{c}^{\dagger}_{\eta\uparrow} \hat{c}_{\beta\uparrow} \hat{c}^{\dagger}_{\gamma\downarrow} \approx \langle \hat{c}^{\dagger}_{\eta\uparrow} \hat{c}_{\beta\uparrow} \rangle \delta_{\eta\beta} \hat{c}^{\dagger}_{\gamma\downarrow} \tag{4.17}$$

and Eq. (4.14) can be re-written in the "linearized" form:

$$\begin{aligned}
[\hat{H}, \hat{c}^{\dagger}_{\alpha\sigma}] \approx \\
&\approx \sum_{\beta} \sum_{\mathbf{i}} u^{*}_{\beta \mathbf{i}\sigma} \epsilon_{\mathbf{i}} u_{\alpha \mathbf{i}\sigma} \hat{c}^{\dagger}_{\beta\sigma} + \sum_{\beta} \sum_{<\mathbf{i},\mathbf{j}>} u^{*}_{\beta \mathbf{i}\sigma} t_{\mathbf{ij}} u_{\alpha \mathbf{j}\sigma} \hat{c}^{\dagger}_{\beta\sigma} + \\
&+ U \sum_{\beta,\eta} \sum_{\mathbf{i}} u^{*}_{\eta \mathbf{i}\uparrow} u_{\alpha \mathbf{i}\uparrow} u^{*}_{\beta \mathbf{i}\downarrow} u_{\beta \mathbf{i}\downarrow} \langle \hat{n}_{\beta\downarrow} \rangle \delta_{\sigma\uparrow} \hat{c}^{\dagger}_{\eta\uparrow} + \\
&+ U \sum_{\beta,\eta} \sum_{\mathbf{i}} u^{*}_{\eta \mathbf{i}\uparrow} u_{\eta \mathbf{i}\uparrow} u^{*}_{\beta \mathbf{i}\downarrow} u_{\alpha \mathbf{i}\downarrow} \langle \hat{n}_{\eta\uparrow} \rangle \delta_{\sigma\downarrow} \hat{c}^{\dagger}_{\beta\downarrow} \, .
\end{aligned} \tag{4.18}$$

Then, by using the unitary transformations Eqs. (4.3) and (4.4), this becomes

$$\begin{aligned}[\hat{H}, \hat{c}^{\dagger}_{\alpha\sigma}] \approx \\ \approx \sum_{\mathbf{i}} \epsilon_{\mathbf{i}} u_{\alpha \mathbf{i}\sigma} \hat{c}^{\dagger}_{\mathbf{i}\sigma} + \sum_{<\mathbf{i},\mathbf{j}>} t_{\mathbf{ij}} u_{\alpha \mathbf{j}\sigma} \hat{c}^{\dagger}_{\mathbf{i}\sigma} + \\ + U \sum_{\mathbf{i}} u_{\alpha \mathbf{i}\uparrow} \langle \hat{n}_{\mathbf{i}\downarrow} \rangle \delta_{\sigma\uparrow} \hat{c}^{\dagger}_{\mathbf{i}\downarrow} + U \sum_{\mathbf{i}} u_{\alpha \mathbf{i}\downarrow} \langle \hat{n}_{\mathbf{i}\uparrow} \rangle \delta_{\sigma\downarrow} \hat{c}^{\dagger}_{\mathbf{i}\uparrow} \,. \end{aligned} \tag{4.19}$$

Finally, after defining

$$\begin{aligned} E_{\alpha\sigma} u_{\alpha \mathbf{i}\sigma} = \epsilon_{\mathbf{i}} u_{\alpha \mathbf{i}\sigma} + \sum_{\mathbf{j}} t_{\mathbf{ij}} u_{\alpha \mathbf{j}\sigma} + \\ + U u_{\alpha \mathbf{i}\uparrow} \langle \hat{n}_{\mathbf{i}\downarrow} \rangle \delta_{\sigma\uparrow} + U u_{\alpha \mathbf{i}\downarrow} \langle \hat{n}_{\mathbf{i}\uparrow} \rangle \delta_{\sigma\downarrow} \,, \end{aligned} \tag{4.20}$$

we are able to write the equation of motion:

$$[\hat{H}, \hat{c}^{\dagger}_{\alpha\sigma}] \approx E_{\alpha\sigma} \hat{c}^{\dagger}_{\alpha\sigma} \,. \tag{4.21}$$

This equation becomes exact if we substitute $\hat{H}$ with $\hat{H}_{MF}$, as defined by Eq. (4.11), and sets in the MFA within the equation-of-motion approach.

4.3 Random Phase Approximation

4.3.1 Equation-of-motion approach

An excited state $|n\rangle$ for the true ground state of a many-particle system $|0\rangle$ is described by an operator $\hat{Q}^{\dagger}_{n}$

$$|n\rangle = \hat{Q}^{\dagger}_{n} |0\rangle \,, \tag{4.22}$$

which has usually bosonic nature and satisfies the equation of motion

$$[\hat{H}, \hat{Q}^{\dagger}_{n}] = \omega_n \hat{Q}^{\dagger}_{n} \,, \tag{4.23}$$

where ω_n is the energy of the excitation referred to the ground state and, in our specific case, $\hat{H}$ is the Hamiltonian for the AHM. Unfortunately the operator $\hat{Q}^{\dagger}_{n}$ is not known. However, since we are interested in collective magnetic excitations, we can guess that $\hat{Q}^{\dagger}_{n}$ should be related to spin-flip processes. We can then define the spin-flip operators:

$$\hat{b}^{\dagger}_{p\uparrow h\downarrow} = \hat{c}^{\dagger}_{p\uparrow} \hat{c}_{h\downarrow} \,, \tag{4.24}$$

$$\hat{b}_{p\uparrow h\downarrow} = \hat{c}^{\dagger}_{h\downarrow} \hat{c}_{p\uparrow} \,, \tag{4.25}$$

$$\hat{B}^{\dagger}_{p\downarrow h\uparrow} = \hat{c}^{\dagger}_{p\downarrow} \hat{c}_{h\uparrow} \tag{4.26}$$

$$\hat{B}_{p\downarrow h\uparrow} = \hat{c}^{\dagger}_{h\uparrow} \hat{c}_{p\downarrow} \,, \tag{4.27}$$

where we have indicated with the index $p\sigma$ a generic unoccupied mean-field state and with the index $h\sigma$ a generic occupied mean-field state ($\sigma = \uparrow, \downarrow$). Therefore the operators $\hat{b}^{\dagger}_{p\uparrow h\downarrow}$ and $\hat{B}^{\dagger}_{p\downarrow h\uparrow}$, when applied to $|0_{MF}\rangle$, destroy a particle in one occupied state and create a particle in an unoccupied state of opposite spin. These operators are then associated to Stoner excitations. If we indicate with $N_{e\sigma}$ and $N_{o\sigma}$ respectively the number of empty and occupied mean-field states of spin σ, we will have $N_{o\downarrow} \times N_{e\uparrow}$ operators $\hat{b}^{\dagger}_{p\uparrow h\downarrow}$ and $N_{o\uparrow} \times N_{e\downarrow}$ operators $\hat{B}^{\dagger}_{p\downarrow h\uparrow}$. These new operators are quasi-bosonic creation and annihilation operators. This means that they satisfy bosonic commutation relations in the "weak" sense

$$\langle [\hat{b}_{p\uparrow h\downarrow}, \hat{b}^{\dagger}_{p'\uparrow h'\downarrow}] \rangle = \delta_{hh'}\delta_{pp'} \,, \tag{4.28}$$

$$\langle [\hat{b}_{p\uparrow h\downarrow}, \hat{b}_{p'\uparrow h'\downarrow}] \rangle = 0 \,, \tag{4.29}$$

$$\langle [\hat{B}_{p\downarrow h\uparrow}, \hat{B}^{\dagger}_{p'\downarrow h'\uparrow}] \rangle = \delta_{hh'}\delta_{pp'} \,, \tag{4.30}$$

$$\langle [\hat{B}_{p\downarrow h\uparrow}, \hat{B}_{p'\downarrow h'\uparrow}] \rangle = 0 \,, \tag{4.31}$$

$$\langle [\hat{b}_{p\uparrow h\downarrow}, \hat{B}^{\dagger}_{p'\downarrow h'\uparrow}] \rangle = 0 \,, \tag{4.32}$$

$$\langle [\hat{B}_{p\downarrow h\uparrow}, \hat{b}^{\dagger}_{p'\uparrow h'\downarrow}] \rangle = 0 \,, \tag{4.33}$$

where $\langle ... \rangle$ indicates, as before, the average on the mean-field ground state.
We propose that $\hat{Q}^{\dagger}_{n}$ can be approximately written as a linear combination of the spin-flip operators . Thus we make the ansatz:

$$\hat{Q}^{\dagger}_{n} = \sum_{p,h} X^{n}_{p\uparrow h\downarrow} \hat{b}_{p\uparrow h\downarrow} + \sum_{p,h} Y^{n}_{p\downarrow h\uparrow} \hat{B}^{\dagger}_{p\downarrow h\uparrow} \,, \tag{4.34}$$

where $\{X^{n}_{p\uparrow h\downarrow}\}$ and $\{Y^{n}_{p\downarrow h\uparrow}\}$ are the coefficents of this linear combination.
In order to calculate the commutator in Eq. (4.23) we need then all the commutators between the operators $\hat{b}_{p\uparrow h\downarrow}$ and $\hat{B}^{\dagger}_{p\downarrow h\uparrow}$ and the AHM Hamiltonian. Let us start by computing

$$\begin{aligned}
[\hat{H}, \hat{b}_{p\uparrow h\downarrow}] = & \sum_{\alpha} \sum_{\mathbf{i}} \epsilon_{\mathbf{i}} u^{*}_{\alpha \mathbf{i}\downarrow} u_{h\mathbf{i}\downarrow} \hat{c}^{\dagger}_{\alpha\downarrow} \hat{c}_{p\uparrow} - \sum_{\alpha} \sum_{\mathbf{i}} \epsilon_{\mathbf{i}} u^{*}_{p\mathbf{i}\uparrow} u_{\alpha\mathbf{i}\uparrow} \hat{c}^{\dagger}_{h\downarrow} \hat{c}_{\alpha\uparrow} \\
& + \sum_{\alpha} \sum_{<\mathbf{i},\mathbf{j}>} t_{\mathbf{ij}} u^{*}_{\alpha \mathbf{i}\downarrow} u_{h\mathbf{j}\downarrow} \hat{c}^{\dagger}_{\alpha\downarrow} \hat{c}_{p\uparrow} - \sum_{\alpha} \sum_{<\mathbf{i},\mathbf{j}>} t_{\mathbf{ij}} u^{*}_{p\mathbf{i}\uparrow} u_{\alpha\mathbf{j}\uparrow} \hat{c}^{\dagger}_{h\downarrow} \hat{c}_{\alpha\uparrow} \\
& - U \sum_{\alpha,\beta,\gamma} \sum_{i} u^{*}_{\alpha\mathbf{i}\uparrow} u_{\beta\mathbf{i}\uparrow} u^{*}_{\gamma\mathbf{i}\downarrow} u_{h\mathbf{i}\downarrow} \hat{c}^{\dagger}_{\alpha\uparrow} \hat{c}^{\dagger}_{\gamma\downarrow} \hat{c}_{\beta\uparrow} \hat{c}_{p\uparrow} \\
& + U \sum_{\alpha,\beta,\gamma} \sum_{\mathbf{i}} u^{*}_{p\mathbf{i}\uparrow} u_{\alpha\mathbf{i}\uparrow} u^{*}_{\beta\mathbf{i}\downarrow} u_{\gamma\mathbf{i}\downarrow} \hat{c}^{\dagger}_{h\downarrow} \hat{c}^{\dagger}_{\beta\downarrow} \hat{c}_{\alpha\uparrow} \hat{c}_{\gamma\downarrow} \,.
\end{aligned} \tag{4.35}$$

We note that Eq. (4.23) is never exactly satisfied. This is because of the ansatz, we made, for the definition of the operators $\hat{Q}_n^\dagger$ [see Eq. (4.34)]. In fact, while the right-hand side of Eq. (4.23) is a linear combination of spin-flip operators (i.e. it is quadratic in the fermionic creation and annihilation operators), Eq. (4.35) shows that the calculation of the commutator $[\hat{H}, \hat{b}_{p\uparrow h\downarrow}]$ leads to quartic terms. Nevertheless, by proceeding as we did for the MFA and by replacing the products of two fermionic operators with their expectation values over the mean-field ground state, we can make the linearization:

$$\begin{aligned}
[\hat{H}, \hat{b}_{p\uparrow h\downarrow}] \approx & \sum_{\alpha} \sum_{\mathbf{i}} \epsilon_{\mathbf{i}} u^*_{\alpha \mathbf{i}\downarrow} u_{h\mathbf{i}\downarrow} \hat{c}^\dagger_{\alpha\downarrow} \hat{c}_{p\uparrow} - \sum_{\alpha} \sum_{\mathbf{i}} \epsilon_{\mathbf{i}} u^*_{p\mathbf{i}\uparrow} u_{\alpha\mathbf{i}\uparrow} \hat{c}^\dagger_{h\downarrow} \hat{c}_{\alpha\uparrow} \\
& + \sum_{\alpha} \sum_{<\mathbf{i},\mathbf{j}>} t_{\mathbf{ij}} u^*_{\alpha \mathbf{i}\downarrow} u_{h\mathbf{j}\downarrow} \hat{c}^\dagger_{\alpha\downarrow} \hat{c}_{p\uparrow} - \sum_{\alpha} \sum_{<\mathbf{i},\mathbf{j}>} t_{\mathbf{ij}} u^*_{p\mathbf{i}\uparrow} u_{\alpha\mathbf{j}\uparrow} \hat{c}^\dagger_{h\downarrow} \hat{c}_{\alpha\uparrow} \\
& + U \sum_{\alpha} \sum_{\mathbf{i}} u^*_{\alpha \mathbf{i}\downarrow} u_{h\mathbf{i}\downarrow} \langle \hat{n}_{\mathbf{i}\uparrow} \rangle \hat{c}^\dagger_{\alpha\downarrow} \hat{c}_{p\uparrow} - U \sum_{\alpha} \sum_{\mathbf{i}} u^*_{p\mathbf{i}\uparrow} u_{\alpha\mathbf{i}\uparrow} \langle \hat{n}_{\mathbf{i}\downarrow} \rangle \hat{c}^\dagger_{h\downarrow} \hat{c}_{\alpha\uparrow} \\
& + U \sum_{\alpha\beta} \sum_{\mathbf{i}} u^*_{p\mathbf{i}\uparrow} u_{\alpha\mathbf{i}\uparrow} u^*_{\beta\mathbf{i}\downarrow} u_{h\mathbf{i}\downarrow} \langle \hat{n}_{h\downarrow} \rangle \hat{c}^\dagger_{\beta\downarrow} \hat{c}_{\alpha\uparrow} \, . \qquad (4.36)
\end{aligned}$$

In this equation we also use the fact that $\langle \hat{n}_{p\sigma} \rangle = 0$ as the indexes p label unoccupied mean-field states.
By restricting the indexes α and β in the last term on the right-hand side of Eq. (4.36) to always describe a particle-hole pair of mean-field states, we have

$$\begin{aligned}
[\hat{H}, \hat{b}_{p\uparrow h\downarrow}] \approx & \sum_{\alpha} \sum_{\mathbf{i}} \epsilon_{\mathbf{i}} u^*_{\alpha \mathbf{i}\downarrow} u_{h\mathbf{i}\downarrow} \hat{c}^\dagger_{\alpha\downarrow} \hat{c}_{p\uparrow} - \sum_{\alpha} \sum_{\mathbf{i}} \epsilon_{\mathbf{i}} u^*_{p\mathbf{i}\uparrow} u_{\alpha\mathbf{i}\uparrow} \hat{c}^\dagger_{h\downarrow} \hat{c}_{\alpha\uparrow} \\
& + \sum_{\alpha} \sum_{<\mathbf{i},\mathbf{j}>} t_{\mathbf{ij}} u^*_{\alpha \mathbf{i}\downarrow} u_{h\mathbf{j}\downarrow} \hat{c}^\dagger_{\alpha\downarrow} \hat{c}_{p\uparrow} \sum_{\alpha} \sum_{<\mathbf{i},\mathbf{j}>} t_{\mathbf{ij}} u^*_{p\mathbf{i}\uparrow} u_{\alpha\mathbf{j}\uparrow} \hat{c}^\dagger_{h\downarrow} \hat{c}_{\alpha\uparrow} \\
& + U \sum_{\alpha} \sum_{\mathbf{i}} u^*_{\alpha \mathbf{i}\downarrow} u_{h\mathbf{i}\downarrow} \langle \hat{n}_{\mathbf{i}\uparrow} \rangle \hat{c}^\dagger_{\alpha\downarrow} \hat{c}_{p\uparrow} - U \sum_{\alpha} \sum_{\mathbf{i}} u^*_{p\mathbf{i}\uparrow} u_{\alpha\mathbf{i}\uparrow} \langle \hat{n}_{\mathbf{i}\downarrow} \rangle \hat{c}^\dagger_{h\downarrow} \hat{c}_{\alpha\uparrow} \\
& + U \sum_{p'h'} \sum_{\mathbf{i}} u^*_{p\mathbf{i}\uparrow} u_{p'\mathbf{i}\uparrow} u^*_{h'\mathbf{i}\downarrow} u_{h\mathbf{i}\downarrow} \langle \hat{n}_{h\downarrow} \rangle \hat{c}^\dagger_{h'\downarrow} \hat{c}_{p'\uparrow} \\
& + U \sum_{h'p'} \sum_{\mathbf{i}} u^*_{p\mathbf{i}\uparrow} u_{h'\mathbf{i}\uparrow} u^*_{p'\mathbf{i}\downarrow} u_{h\mathbf{i}\downarrow} \langle \hat{n}_{h\downarrow} \rangle \hat{c}^\dagger_{p'\downarrow} \hat{c}_{h'\uparrow} \, . \qquad (4.37)
\end{aligned}$$

This can be written as

$$
\begin{aligned}
[\hat{H}, \hat{b}_{p\uparrow h\downarrow}] \approx & \left(E_{h\downarrow} - E_{p\uparrow}\right)\hat{b}_{p\uparrow h\downarrow} + \\
& + U \sum_{h',p'} \sum_{i} u^*_{p\mathrm{i}\uparrow} u_{p'\mathrm{i}\uparrow} u^*_{h'\mathrm{i}\downarrow} u_{h\mathrm{i}\downarrow} \hat{b}_{p'\uparrow h'\downarrow} + \\
& + U \sum_{h',p'} \sum_{i} u^*_{p\mathrm{i}\uparrow} u_{h'\mathrm{i}\uparrow} u^*_{p'\mathrm{i}\downarrow} u_{h\mathrm{i}\downarrow} \ \hat{B}^\dagger_{p'\downarrow h'\uparrow} \,.
\end{aligned} \tag{4.38}
$$

By proceeding as above, we also have:

$$
\begin{aligned}
[\hat{H}, \hat{B}^\dagger_{p\downarrow h\uparrow}] \approx & \left(E_{p\downarrow} - E_{h\uparrow}\right)\hat{B}^\dagger_{p\downarrow h\uparrow} + \\
& - U \sum_{h',p'} \sum_{\mathbf{i}} u^*_{h\mathbf{i}\uparrow} u^*_{p'\mathbf{i}\downarrow} u_{h'\mathbf{i}\uparrow} u_{p\mathbf{i}\downarrow} \hat{B}^\dagger_{p'\downarrow h'\uparrow} + \\
& - U \sum_{h',p'} \sum_{i} u^*_{h\mathbf{i}\uparrow} u_{p'\mathbf{i}\uparrow} u^*_{h'\mathbf{i}\downarrow} u_{p\mathbf{i}\downarrow} \hat{b}_{p'\uparrow h'\downarrow} \,.
\end{aligned} \tag{4.39}
$$

Eqs. (4.38) and (4.39) allow us to obtain an approximated form for Eq. (4.23), which will lead us to the RPA equations. However, before proceeding further with their derivation we can look at the form of the Hamiltonian for which Eqs. (4.38) and (4.39) are exact. This can be deduced by calculating also the commutators

$$
\begin{aligned}
[\hat{H}, \hat{b}^\dagger_{p\uparrow h\downarrow}] \approx & \left(E_{p\uparrow} - E_{h\downarrow}\right)\hat{b}^\dagger_{p\uparrow h\downarrow} + \\
& - U \sum_{h',p'} \sum_{\mathbf{i}} u^*_{p'\mathbf{i}\uparrow} u_{p\mathbf{i}\uparrow} u^*_{h\mathbf{i}\downarrow} u_{h'\mathbf{i}\downarrow} \hat{b}^\dagger_{p'\uparrow h'\downarrow} + \\
& - U \sum_{h',p'} \sum_{\mathbf{i}} u^*_{h'\mathbf{i}\uparrow} u_{p\mathbf{i}\uparrow} u^*_{h\mathbf{i}\downarrow} u_{p'\mathbf{i}\downarrow} \hat{B}_{p'\downarrow h'\uparrow} \,,
\end{aligned} \tag{4.40}
$$

$$
\begin{aligned}
[\hat{H}, \hat{B}_{p\downarrow h\uparrow}] \approx & \left(E_{h\uparrow} - E_{p\downarrow}\right)\hat{B}_{p\downarrow h\uparrow} + \\
& + U \sum_{h',p'} \sum_{\mathbf{i}} u_{p'\mathbf{i}\downarrow} u_{h\mathbf{i}\uparrow} u^*_{p\mathbf{i}\downarrow} u^*_{h'\mathbf{i}\uparrow} \hat{B}_{p'\downarrow h'\uparrow} + \\
& - U \sum_{h',p'} \sum_{\mathbf{i}} u^*_{p'\mathbf{i}\uparrow} u_{h\mathbf{i}\uparrow} u^*_{p\mathbf{i}\downarrow} u_{h'\mathbf{i}\downarrow} \hat{b}^\dagger_{p'\uparrow h'\downarrow} \,.
\end{aligned} \tag{4.41}
$$

and reads

$$\begin{aligned}\hat{H}_{RPA} = &\sum_{p,h} \left(E_{p\uparrow} - E_{h\downarrow}\right) \hat{b}^{\dagger}_{p\uparrow h\downarrow} \hat{b}_{p\uparrow h\downarrow} + \\ &+ \sum_{p,h} \left(E_{p\downarrow} - E_{h\uparrow}\right) \hat{B}^{\dagger}_{p\downarrow h\uparrow} \hat{B}_{p\downarrow h\uparrow} + \\ &- U \sum_{h',p',h,p} \sum_{\mathbf{i}} u^{*}_{p'\mathbf{i}\uparrow} u_{p\mathbf{i}\uparrow} u^{*}_{h\mathbf{i}\downarrow} u_{h'\mathbf{i}\downarrow} \hat{b}^{\dagger}_{p'\uparrow h'\downarrow} \hat{b}_{p\uparrow h\downarrow} + \\ &- U \sum_{h',p',h,p} \sum_{\mathbf{i}} u^{*}_{h\mathbf{i}\uparrow} u^{*}_{h'\mathbf{i}\uparrow} u_{p'\mathbf{i}\downarrow} u_{p\mathbf{i}\downarrow} \hat{B}^{\dagger}_{p'\downarrow h'\uparrow} \hat{B}_{p\downarrow h\uparrow} + \\ &- U \sum_{h',p',h,p} \sum_{\mathbf{i}} \left(u^{*}_{h'\mathbf{i}\uparrow} u_{p\mathbf{i}\uparrow} a^{*}_{h\mathbf{i}\downarrow} u_{p'\mathbf{i}\downarrow} \hat{b}_{p\uparrow h\downarrow} \hat{B}_{p'\downarrow h'\uparrow} - c.c.\right). \end{aligned} \tag{4.42}$$

While this Hamiltonian is quadratic in the spin-flip operators, it is quartic in the fermionic creation and annihilation operators . Therefore $\hat{H}_{RPA}$ is the simplest Hamiltonian which contains, in an approximated way, correlation effects beyond the mean-field level.

We now go back to the derivation of the RPA equations. As we said, we can now write down an approximated expression for Eq. (4.23) by employing Eqs. (4.38) and (4.39). Then by collecting together all the coefficients for $\hat{b}_{p\uparrow h\downarrow}$ and $\hat{B}^{\dagger}_{p\downarrow h\uparrow}$, we obtain the equations

$$\begin{aligned}&- \left(E_{p\uparrow} - E_{h\downarrow}\right) X^{n}_{p\uparrow h\downarrow} + U \sum_{p'\downarrow,h'\uparrow} \sum_{\mathbf{i}} u^{*}_{p'\mathbf{i}\uparrow} u_{p\mathbf{i}\uparrow} u^{*}_{h\mathbf{i}\downarrow} u_{h'\mathbf{i}\downarrow} X^{n}_{p'\uparrow h'\downarrow} + \\ &- U \sum_{p'\downarrow,h'\uparrow} \sum_{\mathbf{i}} u^{*}_{h'\mathbf{i}\uparrow} u_{p\mathbf{i}\uparrow} u^{*}_{h\mathbf{i}\downarrow} u_{p'\mathbf{i}\downarrow} Y^{n}_{p'\downarrow h'\uparrow} = \omega_n X^{n}_{p\uparrow h\downarrow}, \end{aligned} \tag{4.43}$$

$$\begin{aligned}&\left(E_{p\downarrow} - E_{h\uparrow}\right) Y^{n}_{p\downarrow h\uparrow} - U \sum_{p'\downarrow,h'\uparrow} \sum_{\mathbf{i}} u^{*}_{h'\mathbf{i}\uparrow} u^{*}_{p\mathbf{i}\downarrow} u_{h\mathbf{i}\uparrow} u_{p'\mathbf{i}\downarrow} Y^{n}_{p'\downarrow h'\uparrow} + \\ &+ U \sum_{p'\uparrow,h'\downarrow} \sum_{\mathbf{i}} u_{h\mathbf{i}\uparrow} u_{h'\mathbf{i}\downarrow} u^{*}_{p'\mathbf{i}\uparrow} u^{*}_{p\mathbf{i}\downarrow} X^{n}_{p'\uparrow h'\downarrow} = \omega_n Y^{n}_{p\downarrow h\uparrow}. \end{aligned} \tag{4.44}$$

These equations can be rewritten in the more compact way:

$$\begin{aligned}&\sum_{p'\uparrow,h'\downarrow} A_{p\uparrow h\downarrow,p'\uparrow h'\downarrow} X^{n}_{p'\uparrow h'\downarrow} + \sum_{p'\uparrow,h'\downarrow} B_{p\uparrow h\downarrow,p'\downarrow h'\uparrow} Y^{n}_{p'\downarrow h'\uparrow} = \\ &= \sum_{p'\uparrow,h'\downarrow} \omega_n \delta_{p\uparrow h\downarrow,p'\uparrow h'\downarrow} X^{n}_{p'\uparrow h'\downarrow}, \end{aligned} \tag{4.45}$$

$$\sum_{p'\downarrow,h'\uparrow} D_{p\downarrow h\uparrow,p'\uparrow h'\downarrow} X^n_{p'\uparrow h'\downarrow} + \sum_{p'\uparrow,h'\downarrow} C_{p\downarrow h\uparrow,p'\downarrow h'\uparrow} Y^n_{p'\downarrow h'\uparrow} =$$
$$= \sum_{p'\uparrow,h'\downarrow} \omega_n \delta_{p\downarrow h\uparrow,p'\downarrow h'\uparrow} X^n_{p'\downarrow h'\uparrow} \,, \tag{4.46}$$

where we have defined:

$$A_{p\uparrow h\downarrow,p'\uparrow h'\downarrow} = -(E_{p\uparrow} - E_{h\downarrow})\delta_{p\uparrow h\downarrow,p'\uparrow h'\downarrow} + \\ + U \sum_{\mathbf{i}} u_{p\mathbf{i}\uparrow} u^*_{h\mathbf{i}\downarrow} u^*_{p'\mathbf{i}\uparrow} u_{h'\mathbf{i}\downarrow} \tag{4.47}$$

$$B_{p\uparrow h\downarrow,p'\downarrow h'\uparrow} = -U \sum_{\mathbf{i}} u_{p\mathbf{i}\uparrow} u^*_{h\mathbf{i}\downarrow} u_{p'\mathbf{i}\downarrow} u^*_{h'\mathbf{i}\uparrow} \tag{4.48}$$

$$D_{p\downarrow h\uparrow,p'\uparrow h'\downarrow} = -B^*_{p\downarrow h\uparrow,p'\uparrow h'\downarrow} = U \sum_{\mathbf{i}} u_{h\mathbf{i}\uparrow} u^*_{p'\mathbf{i}\uparrow} u^*_{p\mathbf{i}\downarrow} u_{h'\mathbf{i}\downarrow} \tag{4.49}$$

$$C_{p\downarrow h\uparrow,p'\downarrow h'\uparrow} = (E_{p\downarrow} - E_{h\uparrow})\delta_{p\downarrow h\uparrow,p'\downarrow h'\uparrow} + \\ - U \sum_{\mathbf{i}} u^*_{p\mathbf{i}\downarrow} u_{h\mathbf{i}\uparrow} u_{p'\mathbf{i}\downarrow} u^*_{h'\mathbf{i}\uparrow} \,. \tag{4.50}$$

Finally the Eqs. (4.45) and (4.46) can be easily written in matrix form

$$\begin{pmatrix} \mathbf{A} & \mathbf{B} \\ \mathbf{D} & \mathbf{C} \end{pmatrix} \begin{pmatrix} \mathbf{X}^n \\ \mathbf{Y}^n \end{pmatrix} = \omega_n \begin{pmatrix} \mathbf{X}^n \\ \mathbf{Y}^n \end{pmatrix} . \tag{4.51}$$

The matrix on the left-hand side, which has dimension $(N_{o\uparrow} * N_{e\downarrow}) \times (N_{o\downarrow} * N_{e\uparrow})$, is called RPA matrix. We note that the matrices **A** and **C** are hermitian, while **B** and **D** are not, thus the full RPA matrix is not hermitian either.
Although the RPA matrix is not hermitian, it can be shown that the eigenvalues ω_n will be real if the mean-field ground state $|0_{MF}\rangle$ minimizes the expectation value of the Hamiltonian. A complex value for ω_n signals that the mean-field ground state is unstable. By keeping this in mind and assuming that our mean-field ground-state is always a stable one, from now on, we will always consider ω_n as a real quantity.
Furthermore, when we diagonalize the RPA matrix, we find generally both positive and negative eigenvalues. The origin of the negative eigenvalues can be easily understood by considering the adjoint of the operator $\hat{Q}^\dagger_n$

$$\hat{Q}_n = \sum_{h,p} X^{n*}_{p\uparrow h\downarrow} \hat{b}^\dagger_{p\uparrow h\downarrow} + \sum_{hp} Y^{n*}_{p\downarrow h\uparrow} \hat{B}_{p\downarrow h\uparrow} \,. \tag{4.52}$$

Indeed, by calculating the commutator $[\hat{H}, \hat{Q}_n]$ and proceeding as before, we derive

$$\begin{pmatrix} \mathbf{A} & \mathbf{B} \\ \mathbf{D} & -\mathbf{C} \end{pmatrix} \begin{pmatrix} \mathbf{Y}^{n*} \\ \mathbf{X}^{n*} \end{pmatrix} = -\omega_n \begin{pmatrix} \mathbf{Y}^{n*} \\ \mathbf{X}^{n*} \end{pmatrix} . \tag{4.53}$$

This equation shows us that, for every solution of the RPA equation (4.51) with energy ω_n, we also have a solution $\begin{pmatrix} \mathbf{X}^{n*} \\ \mathbf{Y}^{n*} \end{pmatrix}$ of Eq. (4.53) with energy $-\omega_n$. Then, from the definitions of the operators $\hat{Q}_n^\dagger$ and $\hat{Q}_n$ [Eqs. (4.34) and (4.52)], we see that positive ω_n corresponds to excitations which tend to "rotate" the up spins, while negative ω_n corresponds to excitations which tend to "rotate" the down spins. The sign is just a matter of convention, which allows us to separate the two types of excitations. We have then that an excited state $|n_{RPA}\rangle$ is defined as

$$|n_{RPA}\rangle = \hat{Q}_n^\dagger |0_{RPA}\rangle \quad \text{if } \omega_n > 0 \tag{4.54}$$

$$|n_{RPA}\rangle = \hat{Q}_n |0_{RPA}\rangle \quad \text{if } \omega_n < 0 , \tag{4.55}$$

while the RPA ground state, $|0_{RPA}\rangle$, is defined by

$$\hat{Q}_n |0_{RPA}\rangle = 0 \quad \text{if } \omega_n > 0 \tag{4.56}$$

$$\hat{Q}_n^\dagger |0_{RPA}\rangle = 0 \quad \text{if } \omega_n < 0 . \tag{4.57}$$

4.3.2 Properties of the eigenvalues and eigenvectors of the RPA equation

The RPA eigenvectors $\begin{pmatrix} \mathbf{X}^n \\ \mathbf{Y}^n \end{pmatrix}$ have many interesting properties [276]. Here we list the most important ones and those, which will be useful to relate the equation-of-motion approach and the many-body perturbation theory. These are:

- Orthogonality. In order to demonstate this we, firstly, rewrite Eq. (4.51) in the equivalent form:

$$\begin{pmatrix} \mathbf{A} & \mathbf{B} \\ \mathbf{B}^* & -\mathbf{C} \end{pmatrix} \begin{pmatrix} \mathbf{X}^n \\ \mathbf{Y}^n \end{pmatrix} = \omega_n \begin{pmatrix} \mathbf{X}^n \\ -\mathbf{Y}^n \end{pmatrix} . \tag{4.58}$$

  Then by left-multipling this equation by $(\mathbf{X}^{m\dagger}\ \mathbf{Y}^{m\dagger})$, we obtain

$$\begin{aligned} (\mathbf{X}^{m\dagger}\ \mathbf{Y}^{m\dagger}) \begin{pmatrix} \mathbf{A} & \mathbf{B} \\ \mathbf{B}^* & -\mathbf{C} \end{pmatrix} \begin{pmatrix} \mathbf{X}^n \\ \mathbf{Y}^n \end{pmatrix} = \\ = \omega_n (\mathbf{X}^{m\dagger}\ \mathbf{Y}^{m\dagger}) \begin{pmatrix} \mathbf{X}^n \\ -\mathbf{Y}^n \end{pmatrix} . \end{aligned} \tag{4.59}$$

In contrast, by considering the adjont of Eq. (4.58) and right-multiplying it by $\begin{pmatrix} \mathbf{X}^n \\ \mathbf{Y}^n \end{pmatrix}$, we have[2]

$$\begin{aligned} (\mathbf{X}^{m\dagger}\ \mathbf{Y}^{m\dagger}) \begin{pmatrix} \mathbf{A} & \mathbf{B} \\ \mathbf{B}^* & -\mathbf{C} \end{pmatrix} \begin{pmatrix} \mathbf{X}^n \\ \mathbf{Y}^n \end{pmatrix} = \\ = \omega_m \left(\mathbf{X}^{m\dagger}\ -\mathbf{Y}^{m\dagger}\right) \begin{pmatrix} \mathbf{X}^n \\ \mathbf{Y}^n \end{pmatrix}, \end{aligned} \tag{4.61}$$

so that, if $\omega^n \neq \omega^m$, we will have

$$(\mathbf{X}^{m\dagger}\ \mathbf{Y}^{m\dagger}) \begin{pmatrix} \mathbf{X}^n \\ -\mathbf{Y}^n \end{pmatrix} = 0\,. \tag{4.62}$$

Finally the vectors can be normalized by the condition

$$(\mathbf{X}^{n\dagger}\ \mathbf{Y}^{n\dagger}) \begin{pmatrix} \mathbf{X}^n \\ -\mathbf{Y}^n \end{pmatrix} = \mathrm{sgn}(\omega_n) \tag{4.63}$$

so that $\begin{pmatrix} \mathbf{X}^n \\ \mathbf{Y}^n \end{pmatrix}$ and $\begin{pmatrix} \mathbf{X}^{n*} \\ \mathbf{Y}^{n*} \end{pmatrix}$ have the same norm.

- Completeness. The completeness relation is

$$\sum_n \mathrm{sgn}(\omega_n) \begin{pmatrix} \mathbf{X}^n \\ -\mathbf{Y}^n \end{pmatrix} (\mathbf{X}^{n\dagger}\ \mathbf{Y}^{n\dagger}) = 1\,. \tag{4.64}$$

This can be easily demonstrated by writing a generic vectors $\mathbf{V}$ as a linear combination $\mathbf{V} = \sum_n v_n \begin{pmatrix} \mathbf{X}^n \\ -\mathbf{Y}^n \end{pmatrix}$. By using the orthogonalithy property of the RPA eigenvectors, we then have that

$$v_n = \mathrm{sgn}(\omega_n) \left(\mathbf{X}^{n\dagger}\ \mathbf{Y}^{n\dagger}\right) \mathbf{V} \tag{4.65}$$

and then

$$\mathbf{V} = \sum_n \mathrm{sgn}(\omega_n) \begin{pmatrix} \mathbf{X}^n \\ -\mathbf{Y}^n \end{pmatrix} \left(\mathbf{X}^{n\dagger}\ \mathbf{Y}^{n\dagger}\right) \mathbf{V}\,, \tag{4.66}$$

from which the completeness relation follow.

[2]Note that, while the RPA matrix defined through Eq. (4.51) is not hermitian, the matrix

$$\begin{pmatrix} \mathbf{A} & \mathbf{B} \\ \mathbf{B}^* & -\mathbf{C} \end{pmatrix} \tag{4.60}$$

is hermitian.

- Spurious solutions (i.e. Goldstone modes). Since the AHM is invariant for spin-rotations, we have

$$[\hat{H}, \hat{S}_{\mathbf{i}}^{+}] = 0\,, \tag{4.67}$$
$$[\hat{H}, \hat{S}_{\mathbf{i}}^{-}] = 0\,, \tag{4.68}$$
$$[\hat{H}, \hat{S}_{\mathbf{i}}^{z}] = 0\,, \tag{4.69}$$

where $\hat{S}_{\mathbf{i}}^{-} = \hat{c}_{\mathbf{i}\downarrow}^{\dagger}\hat{c}_{\mathbf{i}\uparrow}$, $\hat{S}_{\mathbf{i}}^{+} = \hat{c}_{\mathbf{i}\uparrow}^{\dagger}\hat{c}_{\mathbf{i}\downarrow}$ and $\hat{S}_{\mathbf{i}}^{z} = \hat{c}_{\mathbf{i}\uparrow}^{\dagger}\hat{c}_{\mathbf{i}\uparrow} - \hat{c}_{\mathbf{i}\downarrow}^{\dagger}\hat{c}_{\mathbf{i}\downarrow}$. However, when we have magnetic phases, the mean-field solutions break the spin-rotational symmetry with respect to a plane, that we assume to be the xy one. This has important effects on the solution of the RPA equations. Indeed the Eqs. (4.67) and (4.68) can be seen as equations of motion and can be rewritten in matrix form as

$$\begin{pmatrix} \mathbf{A} & \mathbf{B} \\ \mathbf{B}^{*} & -\mathbf{C} \end{pmatrix} \begin{pmatrix} \mathbf{S}_{\mathbf{X}}^{-} \\ \mathbf{S}_{\mathbf{Y}}^{-} \end{pmatrix} = 0 \tag{4.70}$$

and

$$\begin{pmatrix} \mathbf{A}^{*} & \mathbf{B}^{*} \\ \mathbf{B} & -\mathbf{C}^{*} \end{pmatrix} \begin{pmatrix} \mathbf{S}_{\mathbf{X}}^{+} \\ \mathbf{S}_{\mathbf{Y}}^{+} \end{pmatrix} = 0 \tag{4.71}$$

where

$$\begin{pmatrix} \mathbf{S}_{\mathbf{X}}^{-} \\ \mathbf{S}_{\mathbf{Y}}^{-} \end{pmatrix} = \begin{pmatrix} \langle h\downarrow|\hat{S}_{\mathbf{i}}^{-}|p\uparrow\rangle \\ \cdots \\ \langle p\downarrow|\hat{S}_{\mathbf{i}}^{-}|h\uparrow\rangle \\ \cdots \end{pmatrix} \tag{4.72}$$

and

$$\begin{pmatrix} \mathbf{S}_{\mathbf{X}}^{+} \\ \mathbf{S}_{\mathbf{Y}}^{+} \end{pmatrix} = \begin{pmatrix} \langle p\uparrow|\hat{S}_{\mathbf{i}}^{+}|h\downarrow\rangle \\ \cdots \\ \langle h\uparrow|\hat{S}_{\mathbf{i}}^{+}|p\downarrow\rangle \\ \cdots \end{pmatrix}. \tag{4.73}$$

These are exact, but spurious, solution of the RPA equation. They correspond to zero energy excitation (i.e. the Goldstone modes) and describe global spin rotations of the mean-field spins. Because of these spurious solutions, the eigenvectors of the RPA equation (4.51) are less than complete.

4.3.3 Many-body perturbation theory approach

The collective magnetic excitations are usually obtained by using the perturbation theory. To remind briefly the procedure, we start by introducing the time-displaced

spin-spin correlation function

$$C_{\mathbf{ij}}(t,0) = -i\langle 0|T\{\hat{S}^-_{\mathbf{i}}(t)\hat{S}^+_{\mathbf{j}}(0)\}|0\rangle \tag{4.74}$$

where $\hat{S}^-_{\mathbf{i}}(t)$ $[\hat{S}^+_{\mathbf{i}}(0)]$ denotes the operator $\hat{S}^-_{\mathbf{i}} = \hat{c}^\dagger_{\mathbf{i}\downarrow}\hat{c}_{\mathbf{i}\uparrow}$ $(\hat{S}^+_{\mathbf{i}} = \hat{c}^\dagger_{\mathbf{i}\uparrow}\hat{c}_{\mathbf{i}\downarrow})$ in the Heisenberg picture. The state $|0\rangle$ is, as before, the true many-particle ground state, whose energy is E_0, and $T\{...\}$ denotes the time-ordered product. The time-Fourier transform of $C_{\mathbf{ij}}(t,0)$ defines the dynamic transverse spin susceptibility [2]

$$\chi^{-+}_{\mathbf{ij}}(\omega) = \int_{-\infty}^{\infty} dt\, e^{-i\omega t} C_{\mathbf{ij}}(t,0) \tag{4.75}$$

which can be expressed in the Lehmann representation [279]

$$\chi^{-+}_{\mathbf{ij}}(\omega) = \sum_n \left[\frac{\langle 0|\hat{S}^-_{\mathbf{i}}|n\rangle\langle n|\hat{S}^+_{\mathbf{j}}|0\rangle}{\omega + \omega_n + i\eta} - \frac{\langle 0|S^+_{\mathbf{j}}|n\rangle\langle n|\hat{S}^-_{\mathbf{i}}|0\rangle}{\omega - \omega_n - i\eta} \right], \tag{4.76}$$

where $|n\rangle$ is a n-th many-particle excited state of energy E_n, $\omega_n = E_n - E_0$ and the limit $\eta \to 0^+$ is implied. The Lehmann representation explicitly shows that the poles of $\chi^{-+}_{\mathbf{ij}}(\omega)$ represent the energies of the collective magnetic excitations.
In order to find the dynamic transverse spin susceptibility (4.75) we have to solve the Bethe-Salpeter equation which, in the ladder diagrams approximation, is [270]

$$\chi^{-+}_{\mathbf{ij}}(\omega) = {}^0\chi^{-+}_{\mathbf{ij}}(\omega) + U \sum_{\mathbf{k}} {}^0\chi^{-+}_{\mathbf{ik}}(\omega)\chi^{-+}_{\mathbf{kj}}(\omega)\,, \tag{4.77}$$

where U is the Coulomb interaction strength in the Hamiltonian (4.1) and ${}^0\chi^{-+}_{\mathbf{ij}}(\omega)$ is the transverse spin susceptibility for the mean-field theory. This is defined as

$${}^0\chi^{-+}_{\mathbf{ij}}(\omega) = \int_{-\infty}^{\infty} dt\, e^{-i\omega t} C^{MF}_{\mathbf{ij}}(t,0) \tag{4.78}$$

with $C^{MF}_{\mathbf{ij}}(t,0) = -i\langle 0_{MF}|T\{\hat{S}^-_{\mathbf{i}}(t)\hat{S}^+_{\mathbf{j}}(0)\}|0_{MF}\rangle$ (we remind that $|0_{MF}\rangle$ denotes the mean-field ground state) and its Lehmann representation reads

$${}^0\chi^{-+}_{\mathbf{ij}}(\omega) = \sum_{\alpha>F,\beta\leq F} \left[\frac{u^*_{\alpha\mathbf{i}\uparrow}u_{\beta\mathbf{i}\downarrow}u^*_{\beta\mathbf{j}\downarrow}u_{\alpha\mathbf{j}\uparrow}}{\omega + E_{\alpha\uparrow} - E_{\beta\downarrow} + i\eta} - \frac{u^*_{\beta\mathbf{i}\uparrow}u_{\alpha\mathbf{i}\downarrow}u^*_{\alpha\mathbf{j}\downarrow}u_{\beta\mathbf{j}\uparrow}}{\omega - E_{\alpha\downarrow} + E_{\beta\uparrow} - i\eta} \right], \tag{4.79}$$

where again the limit $\eta \to 0^+$ is implied. As the numbers $E_{\alpha\sigma}$ are the mean-field energy eigenvalues (4.12), the poles of ${}^0\chi^{-+}_{\mathbf{ij}}(\omega)$ are just the Stoner (mean-field) excitations.

As suggested by Szczech et al. [278] the problem can be further simplified. Indeed, when ω does not coincide with the energy of a Stoner excitation, the $L^3 \times L^3$ matrix ${}^0\chi^{-+}(\omega)$, which has elements ${}^0\chi_{\mathbf{ij}}^{-+}(\omega)$, is symmetric and can be diagonalized by an orthogonal matrix $\mathrm{V}(\omega)$ giving the eigenvalues $\{\lambda_\gamma(\omega)\}$. Furthermore, as we can see from Eq. (4.77), $\mathrm{V}(\omega)$ also diagonalizes the matrix $\chi^{-+}(\omega)$ of elements $\chi_{\mathbf{ij}}^{-+}(\omega)$. Indeed we have

$$\sum_{\mathbf{ij}} V_{\gamma \mathbf{i}} \chi_{\mathbf{ij}}^{-+}(\omega) V_{\mathbf{j}\gamma} = \frac{\lambda_\gamma(\omega)}{1 - U\lambda_\gamma(\omega)} \,. \tag{4.80}$$

Since, as we said, the collective magnetic excitations coincide with the poles of $\chi_{\mathbf{ij}}^{-+}(\omega)$, they are given by the relation

$$1 - U\lambda_\gamma(\omega) = 0 \,. \tag{4.81}$$

In other words, the value of ω (not equal to the Stoner excitation energies), for which one of the eigenvalues of ${}^0\chi^{-+}$ satisfies Eq. (4.81), represents the energy of a collective magnetic excitation.

4.3.4 Connection between the two approaches

So far we have shown that the energies of the collective magnetic excitations can be obtained either by diagonalizing the RPA matrix [Eq. (4.51)] or by exploiting the simple Eq. (4.81) derived from the perturbation theory. We will now establish a connection between the equation-of-motion approach and the many-body perturbation theory formalism [280].

In order to do that, we note that Eq. (4.58) can be rewritten as

$$\begin{aligned} &\mathrm{sgn}(\omega_n) \begin{pmatrix} \mathbf{A} - \omega & \mathbf{B} \\ \mathbf{B}^* & -\mathbf{C} - \omega \end{pmatrix} \begin{pmatrix} \mathbf{X}^n \\ \mathbf{Y}^n \end{pmatrix} (\mathbf{X}^{n\dagger}\ \mathbf{Y}^{n\dagger}) = \\ &= -\mathrm{sgn}(\omega_n) \begin{pmatrix} \omega - \omega_n & \mathbf{0} \\ \mathbf{0} & \omega - \omega_n \end{pmatrix} \begin{pmatrix} \mathbf{X}^n \\ -\mathbf{Y}^n \end{pmatrix} (\mathbf{X}^{n\dagger}\ \mathbf{Y}^{n\dagger}) \,. \end{aligned} \tag{4.82}$$

By adding a sum over n and performing some other trivial algebric manipulations, we arrive at

$$\begin{aligned} &\begin{pmatrix} \mathbf{A} - \omega & \mathbf{B} \\ \mathbf{B}^* & -\mathbf{C} - \omega \end{pmatrix} \sum_n \mathrm{sgn}(\omega_n) \frac{\begin{pmatrix} \mathbf{X}^n \\ \mathbf{Y}^n \end{pmatrix} (\mathbf{X}^{n\dagger}\ \mathbf{Y}^{n\dagger})}{\omega - \omega_n} = \\ &= -\sum_n \mathrm{sgn}(\omega_n) \begin{pmatrix} \mathbf{X}^n \\ -\mathbf{Y}^n \end{pmatrix} (\mathbf{X}^{n\dagger}\ \mathbf{Y}^{n\dagger}) \,. \end{aligned} \tag{4.83}$$

Now by using the completeness relation (4.64), we establish that this equation defines the Green function

$$G(\omega) = -\sum_n \mathrm{sgn}\omega_n \frac{\begin{pmatrix} \mathbf{X}^n \\ \mathbf{Y}^n \end{pmatrix} (\mathbf{X}^{n\dagger}\ \mathbf{Y}^{n\dagger})}{\omega - \omega_n - i\mathrm{sgn}\omega_n \eta}\,, \tag{4.84}$$

where we have also performed the analytic continuation $\omega_n \to \omega_n + i\mathrm{sgn}(\omega_n)\eta$ (with $\eta = 0^+$). After separating the sum over positive and negative ω_n, the Green function becomes

$$\begin{aligned} G(\omega) = &- \sum_{n(\omega_n>0)} \frac{\begin{pmatrix} \mathbf{X}^n \\ \mathbf{Y}^n \end{pmatrix} (\mathbf{X}^{n\dagger}\ \mathbf{Y}^{n\dagger})}{\omega - \omega_n - i\eta} + \\ &+ \sum_{n(\omega_n<0)} \frac{\begin{pmatrix} \mathbf{X}^n \\ \mathbf{Y}^n \end{pmatrix} (\mathbf{X}^{n\dagger}\ \mathbf{Y}^{n\dagger})}{\omega - \omega_n + i\eta}\,. \end{aligned} \tag{4.85}$$

Now, by using Eqs. (4.54), (4.55) and the orthogonality property of the RPA eigenvectors, we have that (for $\omega_n > 0$)

$$\langle n_{RPA}|n_{RPA}\rangle = \sum_{ph} X^*_{p\uparrow h\downarrow} X_{p\uparrow h\downarrow} - \sum_{ph} Y^*_{p\downarrow h\uparrow} Y_{p\downarrow h\uparrow} \tag{4.86}$$

and, at the same time

$$\langle n_{RPA}|n_{RPA}\rangle = \langle n_{RPA}|\hat{Q}^\dagger_n|0_{RPA}\rangle = \tag{4.87}$$

$$= \sum_{ph} X_{p\uparrow h\downarrow} \langle n_{RPA}|c^\dagger_{h\downarrow} c_{p\uparrow}|0_{RPA}\rangle + \sum_{ph} Y_{p\downarrow h\uparrow} \langle n_{RPA}|c^\dagger_{p\downarrow} c_{h\uparrow}|0_{RPA}\rangle\,. \tag{4.88}$$

Therfore, we find that

$$X^{n*}_{p\uparrow h\downarrow} = \langle n_{RPA}|c^\dagger_{h\downarrow} c_{p\uparrow}|0_{RPA}\rangle\,, \tag{4.89}$$

$$Y^{n*}_{p\downarrow h\uparrow} = -\langle n_{RPA}|c^\dagger_{p\downarrow} c_{h\uparrow}|0_{RPA}\rangle\,, \tag{4.90}$$

for $\omega_n > 0$. Similarly, one can verify that

$$X^{n*}_{h\uparrow p\downarrow} = -\langle 0_{RPA}|c^\dagger_{h\downarrow} c_{p\uparrow}|n_{RPA}\rangle\,, \tag{4.91}$$

$$Y^{n*}_{h\downarrow p\uparrow} = \langle 0_{RPA}|c^\dagger_{p\downarrow} c_{h\uparrow}|n_{RPA}\rangle\,, \tag{4.92}$$

for $\omega_n < 0$.

Finally, by using the definitions in Eqs. (4.89), (4.90), (4.91) and (4.92) for the vectors $\{\mathbf{X}^n\}$ and $\{\mathbf{Y}^n\}$, we note that Eq. (4.85) is the Lehmann representation for

$$G(\omega) = \int_{\infty}^{\infty} dt e^{-i\omega t} C_{RPA}(t,0) \tag{4.93}$$

where we have introduced the correlation function

$$\begin{aligned} C_{RPA}(t,0) = &- i \sum_{p\uparrow h\downarrow} \langle 0_{RPA}|T\{\hat{b}_{p\uparrow h\downarrow}(t)\hat{b}^{\dagger}_{p\uparrow h\downarrow}(0)\}|0_{RPA}\rangle + \\ &- i \sum_{p\downarrow h\uparrow} \langle 0_{RPA}|\hat{T}\{B^{\dagger}_{p\downarrow h\uparrow}(t)\hat{B}_{p\downarrow h\uparrow}(0)\}|0_{RPA}\rangle \,. \end{aligned} \tag{4.94}$$

with the spin-flip operators $\hat{b}^{\dagger}_{p\uparrow h\downarrow}$, $\hat{b}_{p\uparrow h\downarrow}$, $\hat{B}^{\dagger}_{p\downarrow h\uparrow}$ and $\hat{B}_{p\downarrow h\uparrow}$ defined in Eqs. (4.24), (4.25), (4.26), (4.27).

We note that the $C_{RPA}(t,0)$ is the RPA analogous of the mean-field correlation function $C_{MF}(t,0) = \sum_{p\uparrow h\downarrow} C^{MF}_{p\uparrow h\downarrow p\uparrow h\downarrow}(t,0)$ with

$$C^{MF}_{p\uparrow h\downarrow p\uparrow h\downarrow}(t,0) = -i\langle 0_{MF}|T\{\hat{b}_{p\uparrow h\downarrow}(t)\hat{b}^{\dagger}_{p\uparrow h\downarrow}(0)\}|0_{MF}\rangle \,. \tag{4.95}$$

$C^{MF}_{p\uparrow h\downarrow p\uparrow h\downarrow}(t,0)$ can be obtained from $C^{MF}_{\mathbf{ij}}(t,0)$ by using the unitary transformations (4.3) and (4.4).

Interestingly, while in the MFA we have that

$$\sum_{p\downarrow h\uparrow} \langle 0_{MF}|\hat{T}\{B^{\dagger}_{p\downarrow h\uparrow}(t)\hat{B}_{p\downarrow h\uparrow}(0)\}|0_{MF}\rangle = 0 \tag{4.96}$$

in the RPA

$$\sum_{p\downarrow h\uparrow} \langle 0_{RPA}|\hat{T}\{B^{\dagger}_{p\downarrow h\uparrow}(t)\hat{B}_{p\downarrow h\uparrow}(0)\}|0_{RPA}\rangle \neq 0 \,. \tag{4.97}$$

This is due to the fact that the RPA ground state contains multi particle-hole admixtures.

Finally we can understand how the connection between the many-body perturbation theory formalism and the equation-of-motion approach emerges. In the previous section we have formally introduced the excitation energies as poles of dynamical quantities, which have been derived by analytically continuing time-displaced correlation functions. In this section we have solved the opposite problem. We have used the energies and the eigenvectors of the collective excitations, obtained by diagonalizing the RPA matrix, in order to to derive the dynamic quantity $G(\omega)$, which represents the Fourier transform of the correlation function $C_{RPA}(t,0)$.

4.4 Mean-field results

In the following sections we will present the results obtained for the AHM at quarter-filling for 3-dimensional (3D) cubic lattices of linear dimension L, i.e. the total number of sites is $N = L^3$ and the total number of electrons is equal to $N/2$. In all this study, we impose $t_{\mathbf{ij}} = -t$ for every couple of NN sites $\mathbf{i}$ and $\mathbf{j}$.
Our investigation extends that of Tusch et al. [269], which considers mainly the half-filling case. These authors showed that, while the defect-free system is either a Slater or a Mott insulator with a Neel-type antiferromagnetic order, disorder tends to close the gap between the lower and the upper Hubbard band and a big portion of the phase diagram of the half-filled 3D AHM is then either metallic or Anderson insulating. The magnetic order is still mainly antiferromagnetic, but disorder removes the Fermi surface nesting of the simple cubic lattice in 3D and, in contrast to what happens for the Hubbard model, a paramagnetic phase can appear also for $U > 0$.
We focus mainly on the quarter-filling case. The system described by the Hubbard model is then a metal and, interestingly, for a simple cubic lattice, the MFA returns a first order phase transition from a paramagnetic to a ferromagnetic ground state at $U/t \approx 3.5$ [273]. We then aim at investigating how disorder affects the magnetic properties and, specifically, whether it suppresses the ferromagnetic order.

4.4.1 General Considerations

When mean-field calculations are performed, in general, different starting states give different final self-consistent solutions. Indeed the energy surface has many local minima and, therefore, the quest for the true ground state is very complicated. In order to explore as many states as possible we have chosen several initial conditions corresponding to

1) a ferromagnetic fully spin-polarized state (i.e. $n_{\mathbf{i}\uparrow} = 0.5$ and $n_{\mathbf{i}\downarrow} = 0.0$),

2) a ferromagnetic slightly spin-polarized state (typically $n_{\mathbf{i}\uparrow} = 0.3$ and $n_{\mathbf{i}\downarrow} = 0.2$),

3) a Neel-type antiferromagnetic state,

4) a paramagnetic state,

5) many different magnetically disordered states obtained by randomly selecting the charge and the spin of every site with the constraint that $\sum_{\mathbf{i}}(n_{\mathbf{i}\uparrow} + n_{\mathbf{i}\downarrow}) = N/2$.

Furthermore, we have also performed calculations at finite temperature by gradually approaching the limit of zero temperature. This should help the convergence to the real ground state pushing the system out from metastable minima.
In order to characterize the magnetic configuration of a state we use, as already done by Dasgupta et al. [281] and Tusch et al. [269], the Fourier transform of the z component of the magnetization

$$S_z(\mathbf{k}) = \frac{1}{L^3} \sum_{\mathbf{i}} m_{\mathbf{i}} e^{i\mathbf{k}\mathbf{i}}, \quad m_{\mathbf{i}} = n_{\mathbf{i}\uparrow} - n_{\mathbf{i}\downarrow} . \tag{4.98}$$

Then, $|S_z(\mathbf{k})|$ has a sharp peak at $\mathbf{k}a = (0,0,0)$ for a ferromagnetic state and at $\mathbf{k}a = (\pi,\pi,\pi)$ for an antiferromagnetic one.
Then, in order to understand whether the system is insulating or metallic, we look at the inverse participation ratio (IPR) [282] defined as

$$IPR(E_{\alpha\sigma}) = \frac{\sum_{\mathbf{i}} |u_{\mathbf{i}\alpha\sigma}|^4}{\left(\sum_{\mathbf{i}} |u_{\mathbf{i}\alpha\sigma}|^2\right)^2} . \tag{4.99}$$

The IPR gives us a direct measure of the degree of localization of a state. Indeed, for a state $|\alpha\sigma\rangle$ delocalized over $N_{\alpha\sigma}$ sites, we have

$$IPR(E_{\alpha\sigma}) \approx \frac{1}{N_{\alpha\sigma}} , \tag{4.100}$$

so that, for a completely delocalized state, the IPR is equal to zero in the thermodynamic limit. For a finite system, the localization threshold can be derived by finite-size scaling arguments [283, 269] and it is

$$IPR_c \approx 1.14/(L^3)^{0.48} . \tag{4.101}$$

Then a state for which $IPR > IPR_c$ will be considered localized.

Before going into the details of the results obtained mainly for lattices of linear dimension $L = 8$[3], we point out a few general features:

i) For small value of the interaction strength U/t (typically between about 1.2 and 0.2) and for every considered value of the variance Δ^2 of the Gaussian distribution from which the on-site energies are drawn, a paramagnetic ground state is found, independently on the initial condition.

[3]Unless esplicitly stated, all the results of MFA calculations presented in this and in the next paragraph refer to cubic lattices of linear dimension $L = 8$.

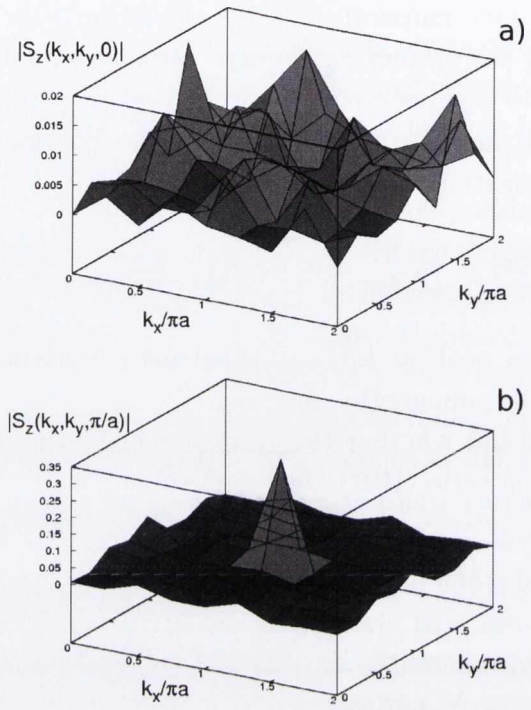

Figure 4.1: Example for a) $S_z(\mathbf{k})$ in the (k_x, k_y) plane at $k_z = 0$ for the disordered magnetic phase and b) $S_z(\mathbf{k})$ in the (k_x, k_y) plane at $k_z = \pi/a$ for the disordered magnetic phase, with a clear highly frustrated Neel-type antiferromagnetic order. These results were obtained for a lattice with $L = 8$.

ii) By increasing the value of U/t (typically above $U/t \approx 1.5$), the calculations, which have initial paramagnetic states, do not converge.

iii) For intermediate values of U/t (typically $1 \lesssim U/t \lesssim 15$ depending on Δ), all the calculations, with a disordered and a ferromagnetic initial state, converge to a disordered final state, which is not usually the same for different initial conditions. In the next section, we will describe better what we mean by disordered state. For the moment it is enough to say that, in that case, although many sites present a quite large magnetic moment, a clear magnetic order can not be recognized. This can be better understood by looking at Fig. 4.1(a), which shows $|S_z(\mathbf{k})|$, in the (k_x, k_y) plane at $k_z = 0$, for a specific realization of

a disordered magnetic state. We then observe many peaks at different values of (k_x, k_y) without distinguishing any dominating one. In contrast, an antiferromagnetic initial condition leads to a solution very similar to the disordered state, but with an enhanced peak at $\mathbf{k} = (\pi/a, \pi/a, \pi/a)$, Fig. 4.1-(b). This seems to indicated that, although the systems is still disordered, the magnetic moments of some sites tend to assume an antiferromagnetic order. An analysis of the total energies shows that solutions, which capture this small feature, have always the lowest energy for $U/t \gtrsim 6$ and $\Delta/t \gtrsim 2$.

iv) As already found by Tusch et al. [269] for the half-filling case, only the magnetic order usually depends on the initial condition, while the total occupation $n_\mathbf{i}$ and the magnitude of the magnetic moments $|m_\mathbf{i}|$ at each site $\mathbf{i}$ do not. Indeed these quantities are determined only by the values of the on-site energies.

4.4.2 Description of the results in details

The electronic properties of the AHM can be analyzed by looking at the IPR for the state at the Fermi level. Indeed if this is smaller than the critical IPR, calculated through Eq. (4.101), the system is metallic otherwise the system is Anderson insulating. Fig. 4.2 shows the IPR for the state at the Fermi level (after performing an average over hundreds of different disorder realizations) as a function of the interaction strength U/t and for various values of Δ/t. We can then observe that, in absence of interaction, the system is metallic for a small amount of disorder and undergoes a metal to insulator transition (MIT) for $\Delta/t \approx 5.2$. Interestingly, for $U/t < 5$, Fig. 4.2 indicates that the interaction promotes an increase in the localization lengths of the state at the Fermi level. For $\Delta/t \approx 6$, the interaction is even able to induce a transition back to the metallic state. This effect, observed also at half-filling, was explained as due to an interaction-induced narrowing of the effective probability distribution for the energy of each site [269].

In order to describe more in detail the results of our calculations we sketch a "magnetic" phase diagram (Fig. 4.3), for a lattice of linear dimension $L = 8$. It shows that, for very small values of U/t, the ground state is always paramagnetic. The charge is not distributed uniformly on each site, but it is divided according to the different on-site energies. However, as soon as U/t slightly increases, magnetic moments form and the disordered phase, mentioned in the previous paragraph, appears. Furthermore by increasing Δ/t, the paramagnetic phase tends to vanish and a few magnetic moments form already for very small values of U/t.

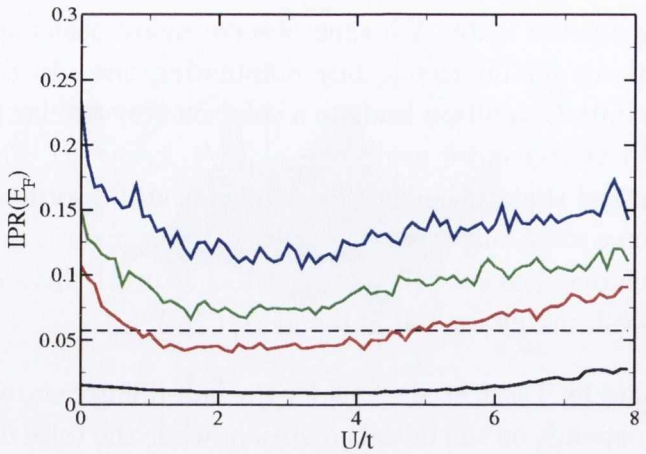

Figure 4.2: IPR for the state at the Fermi energy as a function of U/t for $\Delta/t = 3$ (black line), $\Delta/t = 6$ (red line), $\Delta/t = 7$ (green line) and $\Delta/t = 8$ (blue line). The dashed horizontal line indicates the critical IPR value.

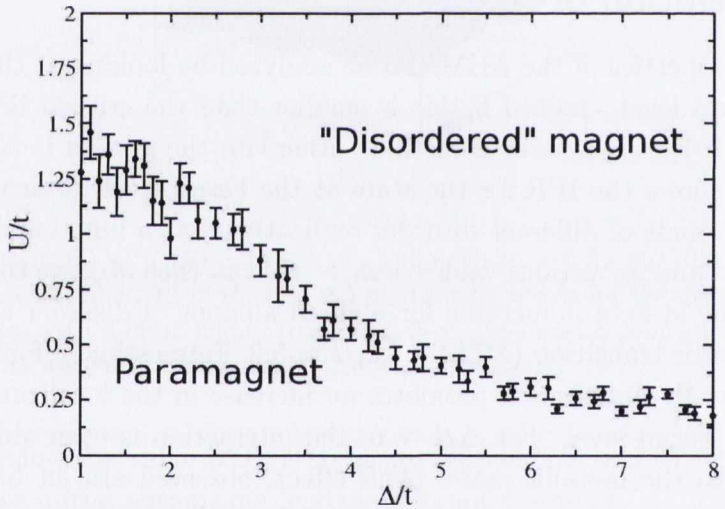

Figure 4.3: Phase diagram which show the border between the paramagnetic and the disordered magnetic phase.

We should remark here that a disordered magnetic phase, intermediate between the paramagnetic and the antiferromagnetic phase, was also found in the half-filling case for lattices with $L = 8$ (and smaller)[269]. However, in that case, the disordered magnetic phase presented very small site magnetic moments $|m_i|$ (typically < 0.05) and disappeared by increasing the lattice size. Therefore, for larger linear dimensions than $L = 8$, a direct transition between the paramagnetic and the antiferromagnetic

phase was observed [271]. In contrast, at quarter filling, $|m_i|$ can reach values of almost one and, performing calculations for lattice sizes up to $L^3 = 14^3$, we did not find any dependence of properties of the disordered magnetic phase on the finite lattice size.

The converged disordered magnetic state of lowest energy (among those that we were able to reach by employing many different initial states) always shows a gradual increase of $|S_z(\mathbf{k})|$ at $\mathbf{k} = (\pi/a, \pi/a, \pi/a)$ for $\Delta/t \gtrsim 2$ and $U/t \gtrsim 7$. This indicates that weak antiferromagentic correlations might start building up among the magnetic moments of some sites.

In order to understand in-depth the origin of the disordered magnetic phase and its

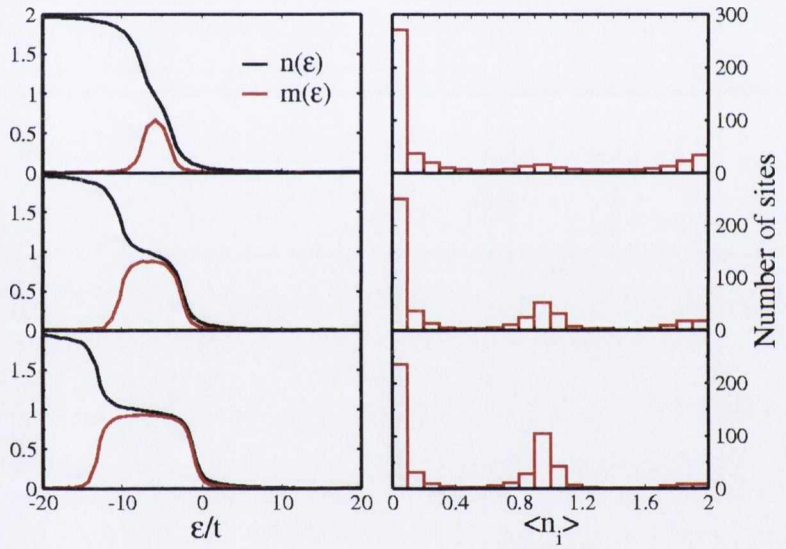

Figure 4.4: $n(\epsilon)$ and $m(\epsilon)$ curves (left-hand side) and histograms of the charge density per site (right-hand side) for $\Delta/t = 8$ and $U/t = 4$ (upper panels), $U/t = 8$ (central panels) and $U/t = 12$ (lower panels).

peculiar dependence on the values of Δ/t and U/t, we have analyzed some quantities directly related to the microscopic properties of the system. More specifically, we have considered the mean charge and the mean magnetic moment for site of on-site energy ϵ

$$n(\epsilon) = \frac{1}{N_\epsilon} \sum_{\epsilon_i = \epsilon} n_i \,, \qquad m(\epsilon) = \frac{1}{N_\epsilon} \sum_{\epsilon_i = \epsilon} m_i \,. \tag{4.102}$$

N_ϵ is there the number of sites with on-site energy equal to ϵ. We have also investigated the following quantity

$$A_F(\epsilon_\mathbf{i}, \sigma) = \frac{1}{N_F} \sum_{\alpha=F} |u_{\alpha\mathbf{i}\sigma}|^2 \tag{4.103}$$

where N_F is the number of eigenstates, whose eigenvalues are equal to the Fermi energy, and the sum over α is restricted to these states. $A_F(\epsilon_\mathbf{i}, \sigma)$, which is clearly zero for a band or a Mott insulator, tells us which sites, in the metallic phase, contribute to the conductivity. The comparison of $m(\epsilon)$ and $A_F(\epsilon_\mathbf{i}, \sigma)$ allows us to understand the interplay between magnetism and metallicity. Further information on the microscopic properties and on the behavior of the system can be obtained also through the histograms of the average charge density for site $\mathbf{i}$, $\langle n_\mathbf{i} \rangle$. These tell us how the charge is distributed among the sites.

We analyze firstly a limiting case of large disorder. Fig. 4.4 shows the curve $n(\epsilon)$ and $m(\epsilon)$ for $\Delta/t = 8$ and $U/t = 4$, $U/t = 8$ and $U/t = 12$, averaged over 40 different disorder realizations. For such an high degree of disorder, the system is an Anderson insulator (see Fig. 4.2). We note that for $U/t = 4$, $n(\epsilon)$ increases monotonically from 0 to 2 while decreasing the on-site energy ϵ. Sites with very high on-site energies are empty, while sites with very low on-site energy are doubly occupied. Intermediate values of ϵ correspond to partially filled sites. In contrast, $m(\epsilon)$ shows a peak when $n(\epsilon) \sim 1$, indicating that half-filled sites are the most spin-polarized and they play a fundamental role in determining the magnetic properties of the model. The histogram for the charge density n (averaged as well over 40 different disorder realizations), shows that half of the sites of the lattice are completely (or almost completely) empty while the others are filled. We expect that for such a large disorder, even for a very small values of U/t, there will be a few sites almost half-filled which then sustain a magnetic moment. This is the origin of the tendency for the paramagnetic ground state to disappear with disorder. The physics becomes much more interesting when we increase the value of U/t. As shown in Fig. 4.4, for $U/t = 8$ and $U/t = 12$, the curve $n(\epsilon)$ is characterized by three plateaus for which we have $n \sim 0$, $n \sim 1$ and $n \sim 2$. At the same time, the histogram, presents three peaks indicating that the majority of the sites are either empty, singly or doubly occupied. This is the result of the Hubbard-like interaction, which tends to favor integer site occupation. Since empty and doubly occupied sites do not carry any magnetic moment, the only sites contributing to the magnetic properties are those half-filled. We might aspect that these sites tend to assume an antiferromagnetic Neel-type order. Indeed $|S_z(\mathbf{k})|$ is characterized by a peak at $\mathbf{k} = (\pi/a, \pi/a, \pi/a)$ [see, for example, Fig 4.1-(b)].

When we decrease Δ/t and the system becomes a metal (see Fig. 4.2), the range of

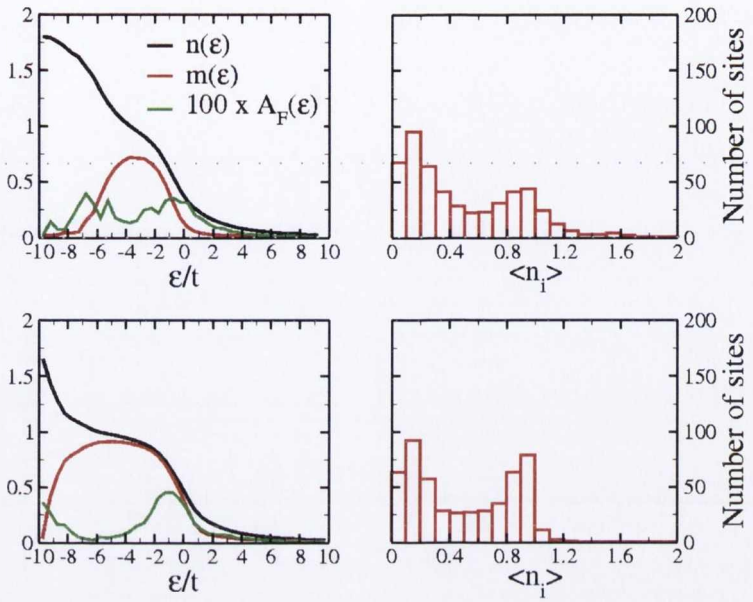

Figure 4.5: Curves $n(\epsilon)$ and $m(\epsilon)$ (left-hand side) and histograms of the charge density for site (right-hand side) for $\Delta/t = 3$ and $U/t = 6$ (upper panels), $U/t = 10$ (lower panels).

values that ϵ can assume decreases. Fig. 4.5 shows $n(\epsilon)$ and $m(\epsilon)$ for $\Delta/t = 3$ and $U/t = 6$, $U/t = 10$. We now note that sites almost never have on-site energies so low or so high to be either doubly occupied or empty. The curve $n(\epsilon)$ becomes also less steep between the plateaus. These changes are also reflected in the histogram for the charge density. Indeed there are no sites with double occupancy and, although we find two peaks in correspondence of $n \sim 0$ and $n \sim 1$, the number of sites almost empty is strongly decreased as compared to the histograms of Fig. 4.4. Furthermore, we have an increasing number of sites with occupancy between 0.3 and 0.6. Fig. 4.5 shows also $A_F(\epsilon)$ (multiplied by 100 for better display). This presents local maxima in regions where $n(\epsilon)$ is rapidly varying and a minimum in correspondence of the plateau for $n \sim 1$. This behavior is very interesting because it indicates that singly occupied sites, which carry large magnetic moments, do not contribute strongly to the state at the Fermi level and then to the conductivity of the system. This is mainly to be ascribed to sites with mean charge density $n \sim 0.2 - 0.6$. In other words the system has two components: one almost insulating but nearly completely spin-polarized, and one metallic. This feature, present also at half-filling [269], is clearly reminiscent of the

two-fluids model proposed by Bhatt et al. [267]. Again the presence of a large number of singly occupied sites induces an enhanced peak of $|S_z(\mathbf{k})|$ at $\mathbf{k} = (\pi/a, \pi/a, \pi/a)$. This comes from the development of antiferromagnetic correlations between the sites which belong to the insulating component of the two-fluids. For large disorder, the metallic component is strongly suppressed since very few sites have an intermediate charge density n between 0.2 and 0.6, Fig. 4.4, and the physics is completely dominated by the insulating component of the two-fluids.

Finally, Fig. 4.6 shows that, for $\Delta/t = 1$ and for $U/t = 6$, $n(\epsilon)$ changes mono-

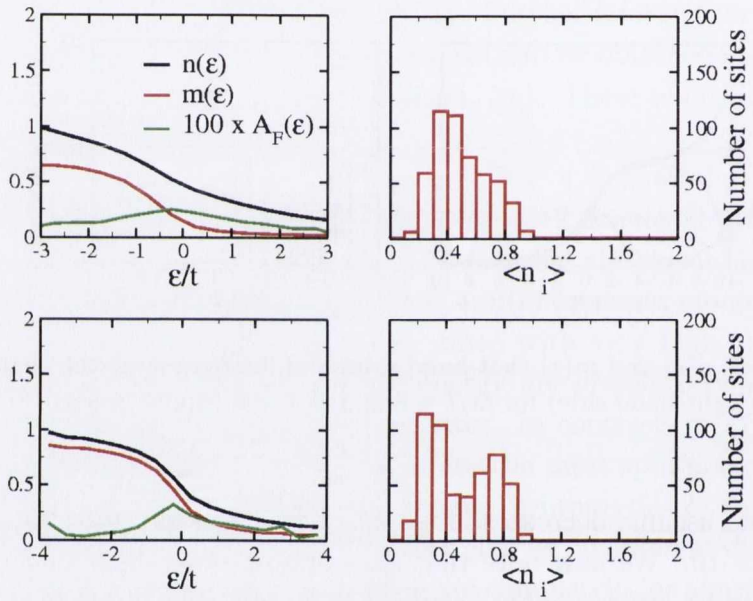

Figure 4.6: Curves $n(\epsilon)$ and $m(\epsilon)$ (left-hand side) and histograms of the charge density for site (right-hand side) for $\Delta/t = 1$ and $U/t = 6$ (upper panels), $U/t = 10$ (lower panels).

tonically and smoothly between $n \sim 0.2$ and $n \sim 0.8$. As shown by the histogram, we have that most of the sites have an occupation equal to about 0.4. Furthermore the function $A_F(\epsilon)$, plotted in Fig. 4.6, is a slowly varying function. This indicates that all sites have non-zero weight for the state at the Fermi level and the metallic component of the two-fluids dominates the physics. Indeed no enhanced peak for $|S_z(\mathbf{k})|$ at $\mathbf{k} = (\pi/a, \pi/a, \pi/a)$ can be found. A sign of the tendency of the system to the formation of the two-fluids can be seen only by increasing the interaction up to $U/t = 10$ (Fig. 4.6). On the one hand, the histogram of the charge density per site indicates that the system starts to decompose into two subsystems with different

site occupancy ($n \sim 0.2$ and $n \sim 0.7$). On the other hand, $A_F(\epsilon)$ shows an increasing weight coming from sites with $n \sim 0.5$.
Finally we must mention that, in a few cases, we have managed to stabilize ground states with ferromagnetic order. These, however, are found only for huge values of U/t (for example, for $\Delta/t = 2$, $U/t > 26$), when practically disorder becomes a small perturbation compared to the electron-electron interaction and we recover the usual Stoner ferromagnetism. However we have not carried out a systematic study of this case as such values of U/t are unrealistically large (and the MFA surely does not provides reliable results).

4.4.3 Effect of a magnetic field

We now investigate the effect of an external Zeeman magnetic field [applied along the z-direction $\mathbf{H} = (0, 0, H)$] on the properties of the AHM at quarter filling. First, it is useful to consider what happens when U is set to zero (i.e. Anderson model). In this case, in the absence of a magnetic field, most of the sites are partially filled (and not spin-polarized), while a few scattered sites have on-site energies either too large to be filled or small enough to result in a double occupancy. By apply a magnetic field, the partially-filled sites become spin-polarized and the M-H curve ($M = \sum_i m_i$) is a straight line typical of a Pauli paramagnet (Fig. 4.7), as expected. However, by increasing further the magnetic field, fully-filled sites develop a magnetic moment by transferring one of the electrons to the almost empty sites characterized by higher on-site energies. This happens when, for a fully-filled site of on-site energy ϵ and an almost empty site of on-site energy $\tilde{\epsilon}$ (with $\epsilon < \tilde{\epsilon}$), the condition $\epsilon + H > \tilde{\epsilon} - H$ is fullfilled. The rearrangement of the charge density within the lattice accounts for the non-linearity of the curve $M(H)$ observed at high magnetic fields.
If we now switch on the interaction U, the physics becomes more complex. As shown in Fig. 4.7, for $U/t = 4$, when there are no weak antiferromagnetic correlations, the magnetization curve shows a clear non-linear response and a saturation for a field H_s whose value depends on Δ/t. This behavior can be explained as follow: first, the field orders the large magnetic moments carried by singly occupied sites so that the magnetic response is Curie-like and, finally, allows for the (almost) double-occupied sites to transfer their minority electron to the (almost) empty sites. If we now assume $t \approx 0.01\,\mathrm{eV} = 116\mathrm{K}$, which is a typical value for an impurity band, we obtain $H_s \approx 2t = 232\mathrm{K}$ (for $\Delta/t = 3$). When this estimate is compared to values of mag-

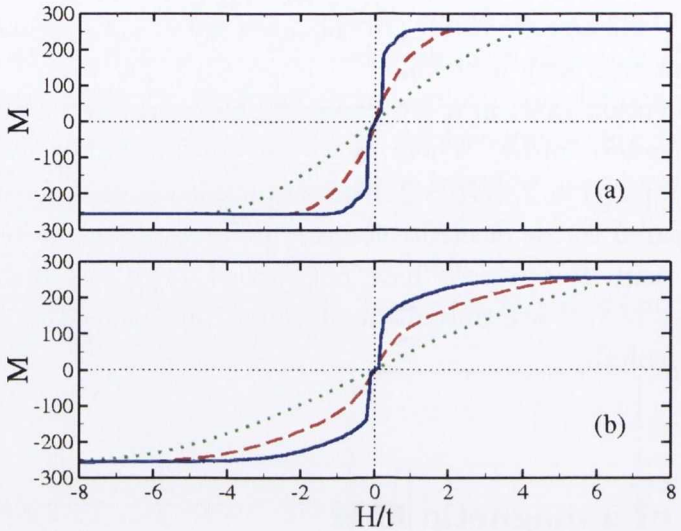

Figure 4.7: Magnetization, M, against the applied magnetic field, H for $\Delta/t = 3$ (a) and $\Delta/t = 6$ (b) with $U/t = 0$ (green dotted line), $U/t = 4$ (red dashed line) and $U/t = 8$ (blue line).

netic fields practically achievable in experiments (a field as large as 1 Tesla on 1 μ_B is equal to 0.671K), we understand that, according to the model, no saturation can be observed for realistic parameters. Hence, the model accounts only for a Curie-like magnetic response due to the re-orientation of the largest magnetic moments.
For $U/t = 8$, the magnetization curve shows a very peculiar shape. This comes from the fact that many sites are half-filled, almost completely spin-polarized and weakly antiferromagnetically coupled. For these sites we can then observe an abrupt transition to the ferromagnetic order similar to what is usually reported in metamagnetic transitions [284].

4.5 Magnetic excitations

In this section we investigate both collective and Stoner magnetic excitations. Many interesting questions can be addressed. Indeed, we can ask ourself, firstly, whether a low-energy spin-wave-like band exists, secondly, how disorder affects the energy spectrum of the excitations and, finally, whether and on what extent they are localized.
As already mentioned in section 4.3, the energy of a Stoner excitation is given by the difference between the energy of an unoccupied mean-field state and the energy of an occupied mean-field state of opposite spin (i.e. $\omega_n^{MF} = E_{p\sigma} - E_{h-\sigma}$).

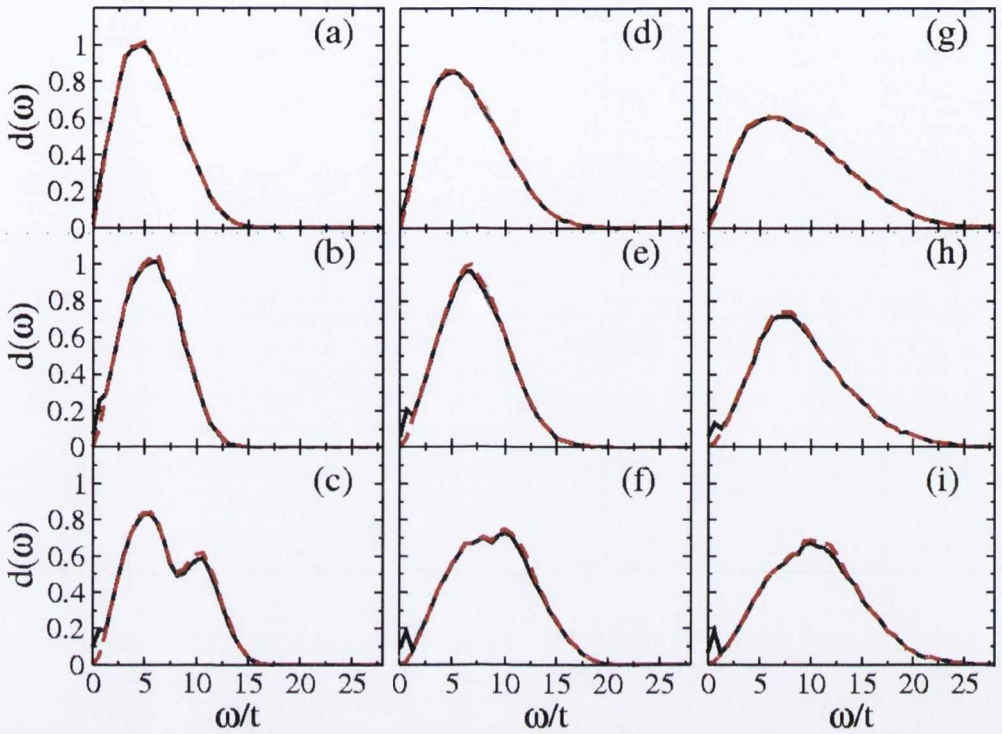

Figure 4.8: DOS of the RPA excitation (black line) and for the mean-field excitations (red dashed line) for $\Delta/t = 2$, $U/t = 4$ (a), $\Delta/t = 2$, $U/t = 8$ (b), $\Delta/t = 2$, $U/t = 12$ (c), $\Delta/t = 4$, $U/t = 4$ (d), $\Delta/t = 4$, $U/t = 8$ (e), $\Delta/t = 4$, $U/t = 12$ (f), $\Delta/t = 6$, $U/t = 4$ (g), $\Delta/t = 6$, $U/t = 8$ (h), $\Delta/t = 6$, $U/t = 12$ (i).

Collective magnetic excitations are calculated within the RPA. We have employed both methods described in section 4.3 and we have considered lattices of linear dimension $L = 4$ and $L = 6$. The diagonalization of the RPA matrix (introduced in section 4.3.1) is an $O(N^3)$ operation and allows the calculations of the excitation energies very quickly for $L = 4$. However, this is unfeasible for larger L because of the high requirements in terms of computer memory. In the latter case, we will present results obtained by applying the method described in section 4.3.3, which unfortunately scales as $O(N^4)$. Therefore calculations can not be extended to larger lattices. As first step, we always check that all the eigenvalues of the RPA matrix are real. As we have already mentioned, this implies that the mean-field ground state is stable and ensures us about the correctness of the results discussed previously.
Because of disorder and the lack of translational symmetry, no band-structure can be

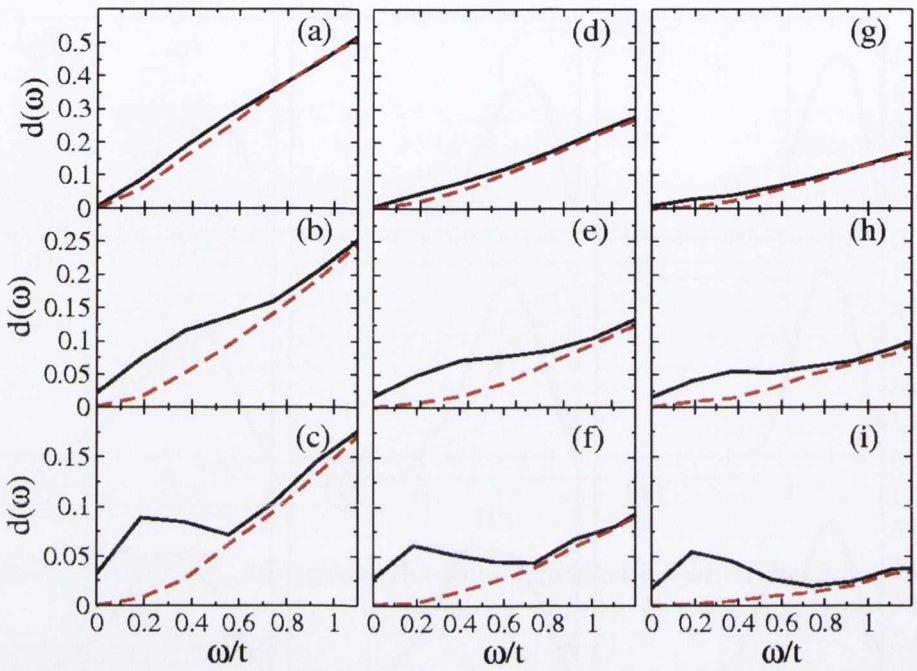

Figure 4.9: DOS of the RPA excitation (black line) and for the mean-field excitations (red dashed line) for lattices with $L = 6$ and $\Delta/t = 2$, $U/t = 4$ (a), $\Delta/t = 2$, $U/t = 8$ (b), $\Delta/t = 2$, $U/t = 12$ (c), $\Delta/t = 4$, $U/t = 4$ (d), $\Delta/t = 4$, $U/t = 8$ (e), $\Delta/t = 4$, $U/t = 12$ (f), $\Delta/t = 6$, $U/t = 4$ (g), $\Delta/t = 6$, $U/t = 8$ (h), $\Delta/t = 6$, $U/t = 12$ (i).

drawn. We then calculate the density of state (DOS) defined as

$$d(\omega) = \frac{1}{L^3} \sum_{\omega_n} \delta(\omega - \omega_n) \,, \tag{4.104}$$

with ω_n the energy of either a Stoner excitation (i.e. $\omega_n = \omega_n^{MF}$) or of a collective magnetic excitation. The DOSs for both types of excitations are shown in Fig. 4.8 for various values of U/t and Δ/t and after performing the average over 40 disorder realizations[4]. As expected, because of the presence of the Goldstone modes, the spectrum of the collective excitations (black continuous line in Fig. 4.8) extends down to zero energy. We note however, that, as a consequence of the metallic or Anderson (gapless) insulating nature of the mean-field ground state, the spectrum of the Stoner excitations (red dashed line in Fig. 4.8) also extends down to zero energy. Interest-

[4]We present only the DOS for positive energies. That is because, for the mean-field states considered, the average DOS for positive and negative energies are essentially identical.

ingly, for $U/t = 4$ [(Fig. 4.8 (a), (d), (g))], the DOS of the excitations, calculated with the MFA and the RPA, are almost indistinguishable. Therefore magnetic excitations are essentially of Stoner type. This can be further demonstrated by looking at Fig. 4.9, where just the low energy part of the DOS, calculated for $L = 6$, is displayed. In contrast, by increasing U/t, the RPA spectrum shows, for $0 \lesssim \omega \lesssim 1$, a clear feature, which is absent in the mean-field one. This indicates that spin-waves dominate the low energy RPA spectrum before being absorbed into the Stoner excitations band. Beside the study of the DOS, a careful examination of the componets of the eigenvectors of the RPA matrix $\{X^n_{p\uparrow h\downarrow}, Y^n_{p\downarrow h\uparrow}\}$ can also be used to determine whether the RPA excitations differ drastically from the mean-field ones. Eqs. (4.89) and (4.90) show that, if a mode of energy ω_n is a pure Stoner excitation, only one of the components $|X^n_{p\uparrow h\downarrow}|$ ($|Y^n_{p\downarrow h\uparrow}|$) will be equal to 1 and all the others will be zero. In contrast, for a spin-wave, we expect many componets different from zero and generally with an amplitude much smaller than one. In Fig. 4.10 we then plot

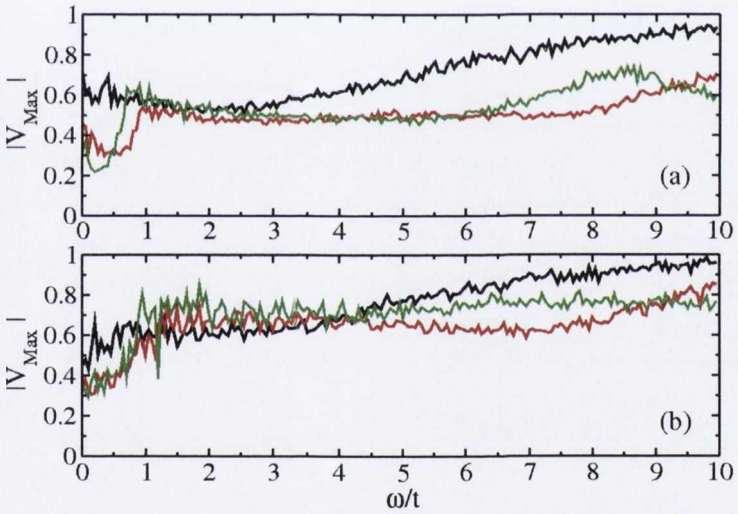

Figure 4.10: $|V_{MAX}(\omega_n)|$ for $\Delta/t = 2$ (a) and $\Delta/t = 6$ (b). The black line corresponds to $U/t = 4$, the red one to $U/t = 8$ and the green one to $U/t = 12$.

the absolute value of the largest component of each eigenvector of the RPA matrix, $|V_{MAX}(\omega_n)| = \max\{|X^n_{p\uparrow h\downarrow}|, |Y^n_{p\downarrow h\uparrow}|\}$, as a function of the energy ω/t (the average is performed again over 40 disorder realizations). Fig. 4.10(a), which refers to $\Delta/t = 2$ and $U/t = 4, 8, 12$, shows very clearly the difference between the excitations for small and large interaction strengths. Indeed, on the one hand, for $U/t = 4$, $|V_{MAX}(\omega)|$ is a smooth function and has an almost constant value of about 0.6. On the other

hand, for $U/t = 8, 12$, we can clearly see that it jumps from about 0.2 to about 0.6 at $\omega \sim 1$. This indicates a change in the character of the spin excitations and reflects the low-energy feature observed in the RPA spectrum and absent in the mean-field one (see Figs. 4.8 and 4.9). The same holds true also for $\Delta/t = 6$ [(Fig. 4.10(b))], in spite of the slight decrease of $|V_{MAX}(\omega)|$ for $U/t = 4$, at low ω, and the less steep profile for $U/t = 8, 6$.

Further insight into the nature of the RPA spin excitations can be obtained by looking at their spatial distribution. By using the unitary transformations (4.3) and (4.4), we can re-write the operators $\hat{Q}_n^\dagger$, defined in Eq. (4.34), as

$$\hat{Q}_n^\dagger = \sum_{\mathbf{ij}} U_{\mathbf{ij}}^n \hat{c}_{\mathbf{i}\downarrow}^\dagger \hat{c}_{\mathbf{j}\uparrow} , \tag{4.105}$$

where the coefficients

$$U_{\mathbf{ij}}^n = \sum_{ph} X_{p\uparrow h\downarrow}^n u_{pj\uparrow}^* u_{hi\downarrow} + \sum_{ph} Y_{p\downarrow h\uparrow}^n u_{hj\downarrow}^* u_{pi\uparrow} \tag{4.106}$$

are normalized so that $\sum_{\mathbf{ij}} |U_{\mathbf{ij}}^n|^2 = 1$. As $U_{\mathbf{ij}}^{n*} = \langle n_{RPA}|\hat{c}_{\mathbf{i}\downarrow}^\dagger \hat{c}_{\mathbf{j}\uparrow}|0_{RPA}\rangle$ (for $\omega_n > 0$), we distinguish two "kinds" of collective excitations: 1) the pure spin-wave excitations, whose spatial probability amplitude is given by $U_{\mathbf{ii}}^{n*} = \langle n_{RPA}|\hat{S}_{\mathbf{i}}^-|0_{RPA}\rangle$ and $U_{\mathbf{ij}}^{n*} \approx 0$ for $\mathbf{i} \neq \mathbf{j}$, and, 2) the spin excitations which present some degrees of charge transfer and whose spatial probability amplitude is given by $U_{\mathbf{ij}}^{n*} \neq 0$ with $\mathbf{i} \neq \mathbf{j}$. Therefore, to probe the nature of the excitations, we have calculated $S_n = \sum_{\mathbf{i}} |U_{\mathbf{ii}}^n|^2$. When $S_n << 1$, the n-th excitation involves charge-transfer, while, when $S_n \approx 1$, the n-th excitation is a pure spin-wave. The mean value of S_n for excitations of energies $0 < \omega_n < 1$ (averaged also over many disorder realizations) is reported in Tab. 4.1 for some representative points in the $(\Delta/t, U/t)$ phase diagram. For comparison we have also calculated the weights of the Stoner excitations in the on-site spin-flip subspace. For an excitation of energy $\omega_n^{MF} = E_{p\downarrow} - E_{h\uparrow}$, this is given by

$$S_n^{MF} = \sum_{\mathbf{i}} |\langle n_{MF}|\hat{c}_{\mathbf{i}\downarrow}^\dagger \hat{c}_{\mathbf{i}\uparrow}|0_{MF}\rangle|^2 = \sum_{\mathbf{i}} |u_{hi\uparrow}|^2 |u_{pi\downarrow}|^2 . \tag{4.107}$$

The mean value for the same energy-range, that we have considered for the RPA excitations, is listed in Tab. 4.2.

We can observe that, for $U/t = 4 = \Delta/t = 4$, the mean S_n is of the same order of magnitude of the mean S_n^{MF}. This indicates that, for these parameters, spin excitations are not just characterized by a large off-site contribution, but are mainly of

	$U/t = 4$	$U/t = 8$	$U/t = 12$
$\Delta/t = 2$	0.05	0.32	0.3
$\Delta/t = 4$	0.1	0.43	0.67
$\Delta/t = 6$	0.21	0.48	0.69

Table 4.1: Mean S_n of RPA excitations of energies $0 < \omega_n < 1$ for selected points in the $(\Delta/t, U/t)$ phase diagram.

	$U/t = 4$	$U/t = 8$	$U/t = 12$
$\Delta/t = 2$	0.02	0.01	0.01
$\Delta/t = 4$	0.02	0.008	0.005
$\Delta/t = 6$	0.02	0.009	0.004

Table 4.2: Mean S_n^{MF} of Stoner excitations of energies $0 < \omega_n^{MF} < 1$ for selected points in the $(\Delta/t, U/t)$ phase diagram.

Stoner type. In contrast, by increasing either Δ or U, S_n increases and becomes at least one order of magnitude larger than S_n^{MF}. Low energy excitations then tend to become true spin-wave excitations. On the one side, the decrease of the charge-transfer character of the excitations for large disorder reflects the increase of the localization of the mean-field states. On the other side, for large U, excitations involving charge-transfer are projected out of the spectrum. This analysis is consistent with that done while inspecting the DOS and provides a more quantitative and microscopic view of the system.

4.6 Discussion and conclusions

The results presented so far on the electronic and magnetic properties of the quarter-filled Anderson-Hubbard model suggest two different behaviors depending on the interaction strength:

1) For small values of the interaction strength (i.e. $U/t \lesssim 4$), all sites share electrons and present very small magnetic moments, which are very weakly coupled. The magnetic excitations are found to have mainly single-particle character. This indicates that the ground state might be weakly correlated and furthermore, the MFA could accurately describe the electronic and magnetic properties of the system [however a solid demonstration of this statement requires the comparison of quantities such as the correlation functions and the

total energy calculated with the MFA and by using either exact diagonalization or Quantum Monte Carlo techniques (see Chapter 5)]. A magnetic transition is found at a non-zero value of U, which depends on the degree of disorder. This transition is not an artifact of the small size of the lattices considered ($L = 8$), but is robust against finite-size scaling and seems to survive in the thermodynamic limit. The real nature of this transition must be further investigated in the future and, although the Fourier transform of the magnetization was used to characterize the magnetic state, the appropriate order parameter should be identified.

2) For large values of the interaction strength (i.e. $U/t > 4$), about half of the sites of the entire lattice develop large magnetic moments and a clear spin-wave feature appears in the low-energy region of the spectrum of the magnetic excitations. This suggests that strong antiferromagnetic correlations develop between a few sites, but these do not percolate through the entire lattice. In other words, the lattice results decomposed into small clusters of sites, which are almost half-filled and carry large magnetic moments, separated by regions where a small fraction of the total electronic charge is found. On the one hand, within each cluster, the magnetic moments are anti-ferromagnetically coupled. On the other hand, only the sites with small occupancy and magnetic moments contribute to the states around the Fermi level and therefore affect the conduction properties of the system. These features are closely related to the two-fluid model. However, we believe that a deep understanding of the physics of this system requires treatments beyond the MFA. Therefore, new studies employing Quantum Monte Carlo techniques (see Chapter 5) will be performed in the future.

As we mentioned in the introduction, our work can be related to previous studies, which model many-electron systems in order to understand d^0 magnetism. In those studies the effect of disorder was either not considered at all [261] or described within drastic approximations [51]. Therefore the mean-field description of the problem led, for some parameters values, to a Stoner ferromagnetic phase, already widely studied in the case of the three dimensional Hubbard model [272, 273]. In contrast, our results demonstrate that no ferromagnetic order is possible, not even at the MFA level, when disorder is exactly accounted for.
However, interestingly, in the case of weakly coupled systems (i.e. $U/t \lesssim 4$), we find that a careful analysis of Fig. 4.8, shows how, by increasing the disorder, the

spectrum of the magnetic excitations becomes broader and the DOS at low-energies decreases. This indicates that magnetic moments are stabilized by disorder and, even more interestingly, that the critical temperature for the magnetic transition should increase by increasing the disorder (this trend is confirmed by some preliminary finite-temperature calculations, which are not included in this thesis). Therefore, our model accounts for the surprisingly high temperature at which the d^0 magnetism is observed. In contrast, unfortunately, we are not able to describe the ferromagnetic-like magnetization curve of d^0 magnets. In fact, for realistic parameters, the model describes a Curie-like magnetic-response, due to the re-orientation of the magnetic moments, and no saturation.

Chapter 5

Quantum Monte Carlo simulations for the Hubbard model

5.1 Introduction

In the previous chapter, we have employed different levels of approximation to account for the electronic correlation in the Anderson-Hubbard model. Unfortunately it is hard to address the accuracy of the mean-field approximation and, even more, of the RPA. In fact this is based on the perturbation theory and, therefore, on the implicit assumption that the system is in a weak coupling regime. However such a regime cannot be easily related to some specific parameter values based solely on either phenomenological or mathematical arguments. In contrast, lattice QMC techniques are the most accurate numerical methods which allow the study of large systems (often even comprising hundreds of sites) on an arbitrary lattice and for arbitrary parameters (although, as we will discuss below, the, so called, minus-sign problem practically forbids the application of these methods to some specific filling factors).
In this chapter we present the auxiliary-field quantum Monte Carlo (AFQMC) method [274, 285, 286] (often also called determinantal quantum Monte Carlo) and we discuss our implementation. The method treats the Hubbard model at finite-temperature within the grand-canonical ensemble and it is based on converting a system of interacting electrons into one of free electrons interacting with (imaginary) time-dependent Ising fields. Furthermore we have also implemented the zero-temperature extension of the method [287, 285], from which we can extract the ground state properties of an electronic system with an a-priori fixed number of particles. Through these methods, we can compute accurately many static quantities (such as the charge density for lattice site, the spin and charge correlation functions, the pairing correlation func-

tion, etc.) and even the (imaginary) time-displaced many-body Green function. This can be used to calculate charge and spin gaps, spin and charge susceptibilities, current density correlation functions, etc. Furthermore, by using the maximum entropy method [288, 289], the time-displaced many-body Green function can be analytically continued to obtain dynamical quantities such as the spectral function and the optical conductivity. These quantities can be directly compared to experimental results such as those obtained with scanning tunneling microscope (STM) and photoemission.
Although our code has been currently employed to tackle different problems of interest for our group, such as the study of disordered interacting systems within the context of DMS and d^0 magnets, and of edge- and defect-related magnetism in graphene, we have decided not to include the results of these on-going investigations in this thesis. We present, however, a quite accurate description of the two-dimensional Hubbard model. This study shows the capabilities of our codes and serves as an extensive test on the reliability of the results that it can provide.
Finally, we have also implemented the Hirsch-Fye algorithm [290] to solve the Anderson impurity model [291]. However, we have decided not to include a discussion of this method in this thesis as the algorithm is well explained in the original literature and it does not require any important numerical improvement. This method will be used to in order understand the physics of magnetic impurities on surfaces and to provide an interpretation to the results of STM measurements. This represents a subject of large interest within our group [292, 293].

5.2 Auxiliary-Field Quantum Monte Carlo

5.2.1 Finite-Temperature algorithm

The grand-partition function is defined by

$$\mathcal{Z} = \mathrm{Tr} e^{-\beta(\hat{H}-\mu\hat{\mathcal{N}})}, \tag{5.1}$$

where

$$\hat{H} = -t \sum_{\mathbf{i},\mathbf{j}(\mathbf{i}\neq\mathbf{j})} \sum_{\sigma} (\hat{c}^{\dagger}_{\mathbf{i}\sigma}\hat{c}_{\mathbf{j}\sigma} + h.c.) + U \sum_{\mathbf{i}} \hat{n}_{\mathbf{i}\uparrow}\hat{n}_{\mathbf{i}\downarrow} \tag{5.2}$$

is the repulsive Hubbard Hamiltonian[1] for a lattice of N sites. μ is the chemical potential, $\beta = T^{-1}$ and $\hat{\mathcal{N}} = \sum_{\mathbf{i}\sigma} \hat{n}_{\mathbf{i}\sigma}$. Unfortunately, $\mathcal{Z}$ can not be easily calculated.

[1]Note that the on-site energies are set equal to zero and $t_{\mathbf{ij}} = t > 0$ for every nearest neighbor sites $\mathbf{i}$ and $\mathbf{j}$.

In fact, as we have already briefly discussed in Chapter 2, because of the interaction term, which is quartic in the operators $\hat{c}_{\mathbf{i}\sigma}$ ($\hat{c}^{\dagger}_{\mathbf{i}\sigma}$), the Hubbard Hamiltonian can not be trivially diagonalized. One way to solve this problem consists then in mapping the Hubbard model onto a related model that describes non-interacting particles.
We start by writing the grand-partition function as

$$\mathcal{Z} = \mathrm{Tr} \prod_{l=1}^{M} e^{\Delta\tau(\hat{H}-\mu\hat{N})}, \tag{5.3}$$

where $\Delta\tau = \beta/M$. This procedure is a discretization of the imaginary time interval $(0, \beta)$ into M time-slices, labelled by an index l. Then, by using the Suzuki-Trotter formula, that we introduced while discussing the DMC method in section 2.6.3, we have

$$\mathcal{Z} \approx \mathrm{Tr} \prod_{l=1}^{M} e^{-\Delta\tau\hat{K}} \exp\Big[-\Delta\tau\Big(U \textstyle\sum_{\mathbf{i}} \hat{n}_{\mathbf{i}\uparrow}\hat{n}_{\mathbf{i}\downarrow} - \mu \sum_{\mathbf{i}}(\hat{n}_{\mathbf{i}\uparrow} + \hat{n}_{\mathbf{i}\downarrow})\Big)\Big], \tag{5.4}$$

where $\hat{K} = -t \sum_{\mathbf{i},\mathbf{j},\sigma}(\hat{c}^{\dagger}_{\mathbf{i}\sigma}\hat{c}_{\mathbf{j}\sigma} + h.c.)$. The breakup of the exponential in the grand-partition function introduces an error of order $\mathcal{O}(\Delta\tau^2 Ut)$ so that it can be made small by increasing the number M of time-slices. We can now introduce the discrete Hubbard-Stratonovich transformation[2] [294]

$$e^{-\Delta\tau U\hat{n}_{\mathbf{i}\uparrow}\hat{n}_{\mathbf{i}\downarrow}} = \sum_{s_{\mathbf{i}}=\pm 1} \prod_{\sigma} e^{\lambda s_{\mathbf{i}}\sigma\hat{n}_{\mathbf{i}\sigma} + \frac{\Delta\tau U}{2}\hat{n}_{\mathbf{i}\sigma}}, \tag{5.5}$$

where $s_{\mathbf{i}} = \pm 1$ is an Ising field and the parameter λ is defined as

$$\lambda = 2\mathrm{arctan}\sqrt{\tanh\left(\Delta\tau U/4\right)}. \tag{5.6}$$

The Hubbard-Stratonovich transformation then replaces the quartic term, that describes the Hubbard interaction at a site $\mathbf{i}$, with a fluctuating classic Ising field coupled to the magnetization $\hat{m}^z_{\mathbf{i}} = \hat{n}_{\mathbf{i}\uparrow} - \hat{n}_{\mathbf{i}\downarrow}$ of that site. Finally, after using the identity (5.5) for each lattice site $\mathbf{i}$ and each time-slice l of width $\Delta\tau$ (so that we introduce $N \times M$ Ising fields labelled as $s_{\mathbf{i}}(l)$), the Hamiltonian becomes quadratic in fermionic operators. Therefore the trace over electronic degrees of freedom can be performed, yielding[3]

$$\mathcal{Z} = \sum_{\{s_{\mathbf{i}}(l)\}} \det \mathrm{O}_{\uparrow} \det \mathrm{O}_{\downarrow}. \tag{5.7}$$

[2]In this thesis, we discuss only the repulsive Hubbard model. However the AFQMC can be used to study the attractive case as well. This is done by introducing a different Hubbard Stratonovich transformation (see, for example, reference [286]).

[3]We use the notation $\{s_{\mathbf{i}}(l)\} \equiv (s_{\mathbf{1}}(1), ..., s_{\mathbf{N}}(1), ..., s_{\mathbf{1}}(M), ..., s_{\mathbf{N}}(M))$

The $N \times N$ matrices O_σ ($\sigma = \uparrow, \downarrow$) are defined as

$$\mathrm{O}_\sigma = \mathrm{I} + \mathrm{B}_M^\sigma \mathrm{B}_{M-1}^\sigma \ldots \mathrm{B}_1^\sigma \,. \tag{5.8}$$

where

$$\mathrm{B}_l^\sigma = e^{-\Delta\tau \mathrm{K}} e^{\mathrm{V}^\sigma(l)} \,. \tag{5.9}$$

The matrices K and $\mathrm{V}^\sigma(l)$ have elements

$$\mathrm{K}_{\mathbf{ij}} = \begin{cases} -t & \text{for } \mathbf{i}, \mathbf{j} \text{ nearest neighbors} \\ 0 & \text{otherwise} \end{cases} ,$$

$$\mathrm{V}^\sigma(l)_{\mathbf{ij}} = [\lambda\sigma s_{\mathbf{i}}(l) - \Delta\tau(\mu - U/2)]\delta_{\mathbf{ij}} \,. \tag{5.10}$$

The grand-partition function (5.7) is therefore expressed as a sum over Ising fields of products of determinants and can be rewritten as

$$\mathcal{Z} = \sum_{\{s_{\mathbf{i}}(l)\}} \rho(\{s_{\mathbf{i}}(l)\}) \,. \tag{5.11}$$

Here we have defined the "effective density matrix"

$$\rho(\{s_{\mathbf{i}}(l)\}) = \det \mathrm{O}_\uparrow \det \mathrm{O}_\downarrow \,. \tag{5.12}$$

This can be used as Boltzamann weight to perform the sum in Eq. (5.7) by using a Monte Carlo technique. The simulation proceeds by sweeping through the space-time lattice and attempting to flip the Ising field at each point of coordinates $(\mathbf{i}, l)$. Adopting the heat-bath algorithm [161], for a given configuration of fields $\{s_{\mathbf{i}}(l)\}$, a new configuration $\{s_{\mathbf{i}}(l)\}'$ is accepted with probability

$$P = \frac{R_\uparrow R_\downarrow}{1 + R_\uparrow R_\downarrow} \,, \tag{5.13}$$

where

$$R_\sigma = \frac{\det \mathrm{O}^\sigma(\{s_{\mathbf{i}}(l)\}')}{\det \mathrm{O}^\sigma(\{s_{\mathbf{i}}(l)\})} \,. \tag{5.14}$$

For a given Ising fields configuration, $\{s_{\mathbf{i}}(l)\}$, the equal-time Green function can be calculted as

$$\langle \hat{c}_{\mathbf{i}\sigma} \hat{c}_{\mathbf{j}\sigma}^\dagger \rangle_{\{s\}} = \left[\left(\mathrm{I} + \mathrm{B}_M^\sigma \ldots \mathrm{B}_1^\sigma \right)^{-1} \right]_{\mathbf{ij}} \,, \tag{5.15}$$

where we use the standard notation $\langle \ldots \rangle = \mathcal{Z}^{-1} \mathrm{Tr}\left[e^{\beta(\hat{H} - \mu\hat{\mathcal{N}})} \ldots \right]$. The matrix of the Green function at a time slice l reads

$$\mathrm{g}_\sigma(l) = \left[\mathrm{I} + \mathrm{B}_{l-1}^\sigma \ldots \mathrm{B}_1^\sigma \mathrm{B}_M^\sigma \ldots \mathrm{B}_l^\sigma \right]^{-1} \,. \tag{5.16}$$

The Green function plays a central role in the simulation. Indeed all the average quantities of interest can be expressed in terms of the Green function (the expectation values of four fermionic operators can be evaluated by employing Wick's theorem). For example, the average occupation per site $\langle n \rangle$ is simply

$$\langle n \rangle = \frac{1}{N} \sum_{\sigma} \sum_{\mathrm{i}} \langle \hat{c}^{\dagger}_{\mathrm{i}\sigma} \hat{c}_{\mathrm{i}\sigma} \rangle = \frac{1}{N} \sum_{\sigma} \sum_{\mathrm{i}} \sum_{l=1}^{M} \left(1 - g_{\sigma}(l)_{\mathrm{ii}}\right) \tag{5.17}$$

and the double occupancy $\langle n_{\uparrow} n_{\downarrow} \rangle$ is

$$\begin{aligned} \langle n_{\uparrow} n_{\downarrow} \rangle &= \frac{1}{N} \sum_{\mathrm{i}} \langle \hat{c}^{\dagger}_{\mathrm{i}\uparrow} \hat{c}_{\mathrm{i}\uparrow} \hat{c}^{\dagger}_{\mathrm{i}\downarrow} \hat{c}_{\mathrm{i}\downarrow} \rangle = \frac{1}{N} \sum_{\mathrm{i}} \langle \hat{c}^{\dagger}_{\mathrm{i}\uparrow} \hat{c}_{\mathrm{i}\uparrow} \rangle \langle \hat{c}^{\dagger}_{\mathrm{i}\downarrow} \hat{c}_{\mathrm{i}\downarrow} \rangle = \\ &= \frac{1}{N} \sum_{\mathrm{i}} \sum_{l=1}^{M} \left(1 - g_{\uparrow}(l)_{\mathrm{ii}}\right) \left(1 - g_{\downarrow}(l)_{\mathrm{ii}}\right) . \end{aligned} \tag{5.18}$$

Furthermore, provided the Green function, the computation of the ratio R_{σ} becomes easy and does not require the direct evaluation of the determinants [286]. When a new configuration is accepted, the update of the Green function proceeds through the Blankenbecler, Scalapino and Sugar (BSS) scheme [295]. This allows the calculation of the Green function to be performed using only N^2 operations per update as compared to the N^3 operations required to compute the matrix (5.16) from scratch. However, after several updating by the BSS procedure, the Green function degrades due to rounding errors and it has to be recomputed. The number of steps for which the BSS procedure can be safely iterated without generating large numerical errors generally depends on the strength of the interaction U and, moreover, on the temperature. When the temperature is decreased, the recalculation of the Green function from scratch has to be more frequent.

So far, we have implicitly assumed that $\rho(\{s_{\mathrm{i}}(l)\})$ can be interpreted as a Boltzmann weight. This assumption would be correct if $\rho(\{s_{\mathrm{i}}(l)\})$ was positive semi-definite. Unfortunately this is not always the case and $\rho(\{s_{\mathrm{i}}(l)\})$ is found to become negative for certain parameters and Ising fields configurations. We then have to use $\rho'(\{s_{\mathrm{i}}(l)\}) = |\rho(\{s_{\mathrm{i}}(l)\})|$ as Boltzmann weight instead of $\rho(\{s_{\mathrm{i}}(l)\})$. Then the expectation value of an observable $\hat{A}$ is calculated as

$$\langle \hat{A} \rangle_{\rho} = \frac{\langle \hat{A} \operatorname{sgn}(\rho) \rangle_{\rho'}}{\langle \operatorname{sgn}(\rho) \rangle_{\rho'}} . \tag{5.19}$$

Here, the supscripts ρ and ρ' indicate that the averages are taken over the distributions $\rho(\{s_{\mathrm{i}}(l)\})$ and $\rho'(\{s_{\mathrm{i}}(l)\})$ respectively. Clearly, when $\langle \operatorname{sgn}(\rho) \rangle_{\rho'}$ is small, long runs are

necessary to compensate statistical fluctuations. This is the "minus-sign problem" for the AFQMC and it is a serious limitation to the efficient application of the algorithm to some cases. The half-filling case represents a special situation in which the particle-hole symmetry insures that $\rho(\{s_{\mathbf{i}}(l)\})$ is positive so that the sign problem is absent[4]. Although the scheme presented above summarizes the essence of the AFQMC method, some technical issues require several further improvements to the algorithm. Firstly, as at low temperature (usually for $\beta \gtrsim 5$), the matrix $\mathrm{I}+\mathrm{O}^{\sigma}$ becomes ill-conditioned, the Green function can not be calculated by simple matrix inversion and a numerical stabilization procedure is required. Therefore, in our code, the Green function can be calculated by using both the method of White et al. [287] and that of Assaad [285]. Secondly, in order to insure the ergodicity of the Monte Carlo simulation for $U > 8$, global spin-flip moves have been introduced [296].

Finally we remark that the AFQMC method allows the calculation of the (imaginary) time-displaced Green function $G_{\mathbf{ij},\sigma}(\tau,\tau') \equiv \langle T\{\hat{c}_{\mathbf{i}\sigma}(\tau)\hat{c}^{\dagger}_{\mathbf{j}\sigma}(\tau')\}\rangle$ ($T\{...\}$ denotes the time ordered product). As we will see, this can be analytically continued to obtain the spectral function and therefore the density of states. By defining the operator $\hat{c}_{\mathbf{i}\sigma}$ in the Heisenberg picture

$$\hat{c}_{\mathbf{i}\sigma}(\tau_l) = e^{\tau_l \hat{H}} \hat{c}_{\mathbf{i}\sigma} e^{-\tau_l \hat{H}}, \tag{5.20}$$

where $\tau_l = l\Delta\tau$, we have that [285, 286]

$$G_{\mathbf{ij},\sigma}(\tau_l) = G^{>}_{\mathbf{ij},\sigma}(\tau_l, 0) \equiv \langle \hat{c}_{\mathbf{i}\sigma}(\tau_l)\hat{c}^{\dagger}_{\mathbf{j}\sigma}(0)\rangle_{\{s\}} = \left[\mathrm{B}^{\sigma}_{l}\mathrm{B}^{\sigma}_{l-1}...\mathrm{B}^{\sigma}_{1}\mathrm{g}^{\sigma}(1)\right]_{\mathbf{ij}}, \tag{5.21}$$

and either

$$G^{>}_{\mathbf{ij},\sigma}(\tau_{l_1}, \tau_{l_2}) \equiv \langle \hat{c}_{\mathbf{i}\sigma}(\tau_{l_1})\hat{c}^{\dagger}_{\mathbf{j}\sigma}(\tau_{l_2})\rangle_{\{s\}} = \left[\mathrm{B}^{\sigma}_{l_1}\mathrm{B}^{\sigma}_{l_1-1}...\mathrm{B}^{\sigma}_{l_2+1}\mathrm{g}^{\sigma}(l_2+1)\right]_{\mathbf{ij}}, \tag{5.22}$$

for $l_1 > l_2$, or

$$G^{<}_{\mathbf{ji},\sigma}(\tau_{l_2}, \tau_{l_1}) \equiv -\langle \hat{c}^{\dagger}_{\mathbf{j}\sigma}(\tau_{l_2})\hat{c}_{\mathbf{i}\sigma}(\tau_{l_1})\rangle_{\{s\}} = -\left[\left(\mathrm{I}-\mathrm{g}(l_1+1)\right)\left(\mathrm{B}^{\sigma}_{l_2}\mathrm{B}^{\sigma}_{l_2-1}...\mathrm{B}_{l_1+1}\right)^{-1}\right]_{\mathbf{ji}}, \tag{5.23}$$

for $l_2 > l_1$.

5.2.2 Zero-temperature algorithm

The AFQMC algorithm can be extended to calculate directly the zero-temperature properties of a system with a fixed number of electrons [285, 287]. Indeed, exactly like

[4]For the attractive Hubbard model the sign problem is absent no matter what the filling is. This is due to the fact that the Ising fields couple only to the charge $\hat{n}_{\mathbf{i}} = \hat{n}_{\mathbf{i}\uparrow} + \hat{n}_{\mathbf{i}\downarrow}$ and not to the magnetization. We then have $O^{\uparrow}(\{s_{\mathbf{i}}(l)\}) = O^{\downarrow}(\{s_{\mathbf{i}}(l)\})$ (see ref. [286]).

in DMC, the ground-state $|\psi_0\rangle$ is obtained by projecting it out of a trial wave-function $|\psi_T\rangle$, with $\langle\psi_0|\psi_T\rangle \neq 0$

$$\lim_{\theta\to\infty} e^{-\theta\hat{H}}|\psi_T\rangle = \lim_{\theta\to\infty} e^{-\theta E_0}\left[|\psi_0\rangle\langle\psi_0|\psi_T\rangle + \sum_{n\neq 0} e^{-\theta(E_n-E_0)}|\psi_n\rangle\langle\psi_n|\psi_T\rangle\right]. \tag{5.24}$$

Then the ground-state expectation value of an observable, $\hat{O}$, can be written in the form[5]

$$\langle\hat{O}\rangle \equiv \frac{\langle\psi_0|\hat{O}|\psi_0\rangle}{\langle\psi_0|\psi_0\rangle} = \lim_{\theta\to\infty} \frac{\langle\psi_T|e^{-\frac{\theta}{2}\hat{H}}\hat{O}e^{-\frac{\theta}{2}\hat{H}}|\psi_T\rangle}{\langle\psi_T|e^{-\theta\hat{H}}|\psi_T\rangle}. \tag{5.25}$$

The trial wave function, which for spinning fermions reads $|\psi_T\rangle = |\psi_{T\uparrow}\rangle \otimes |\psi_{T\downarrow}\rangle$, is taken as the product of one-particle states

$$|\psi_{T\sigma}\rangle = \prod_{\alpha=1}^{\mathcal{N}_\sigma} \sum_{\mathrm{i}=1}^{N} u_{\alpha\mathrm{i}\sigma}\hat{c}^\dagger_{\mathrm{i}\sigma}|-\rangle, \tag{5.26}$$

where $|-\rangle$ is the vacuum, $\mathcal{N}_\sigma$ is the number of electrons of spin σ, the index α labels the single-particles states and N is the number of lattice sites. The coefficients $u_{\alpha\mathrm{i}\sigma} = \langle\mathrm{i}\sigma|\alpha\sigma\rangle$ are the elements of a $N \times \mathcal{N}_\sigma$ matrix U^σ. The single-particle states can be chosen as either those of the non-interacting system (i.e. for $U = 0$) or those obtained through a mean-field calculation (Hlubina et al. have also proposed to use a trial wave-function of Slater-Jastrow type [297]). The quality of the choice of the trial wave-function can generally improve the convergence to the ground-state.
Like in the finite-temperature algorithm, the interval θ can be subdivided in M imaginary-time slices of size $\Delta\tau$ and, by using the Suzuki-Trotter formula with the Hubbard-Stratonovich transformation, Eq. (5.5), the fermionic degrees of freedom can be integrated out. Finally we can write

$$\langle\psi_T|e^{-\theta\hat{H}}|\psi_T\rangle = \sum_{s_\mathrm{i}(l)} \det\mathrm{A}^\uparrow \det\mathrm{A}^\downarrow, \tag{5.27}$$

where, as before, $\{s_\mathrm{i}(l)\}$ are the Ising fields on the sites of a space-time lattice and

$$\mathrm{A}^\sigma = \mathrm{U}^{\sigma T}\mathrm{B}^\sigma_M \ldots \mathrm{B}^\sigma_1\mathrm{U}^\sigma \tag{5.28}$$

is an $\mathcal{N}_\sigma \times \mathcal{N}_\sigma$ matrix built using the matrices U^σ and B^σ_l, which are defined as in Eq. (5.9). We then introduce the Boltzmann weight $\rho(\{s_\mathrm{i}(l)\}) = \det\mathrm{A}^\uparrow \det\mathrm{A}^\downarrow$ so that

[5] From now on, the notation $\langle\hat{O}\rangle$ will indicate either $\frac{\langle\psi_0|\hat{O}|\psi_0\rangle}{\langle\psi_0|\psi_0\rangle}$ or $\frac{1}{\mathcal{Z}}\mathrm{Tr}\left[e^{-\beta(\hat{H}-\mu\hat{\mathcal{N}})}\hat{O}\right]$ according to whether we refer to the expectation values at zero or finite temperature.

the sum can be performed by a Monte Carlo technique with acceptance probability given by Eq. (5.13) and

$$R_\sigma = \frac{\det \mathrm{A}^\sigma(\{s_{\mathbf{i}}(l)\}')}{\det \mathrm{A}^\sigma(\{s_{\mathbf{i}}(l)\})}\,, \tag{5.29}$$

$\{s_{\mathbf{i}}(l)\}'$ and $\{s_{\mathbf{i}}(l)\}$ being again two different configurations of Ising fields. Like in the finite temperature case, $\rho(\{s_{\mathbf{i}}(l)\})$ can become negative and $|\rho(\{s_{\mathbf{i}}(l)\})|$ must be used as Boltzmann weight. It is usually found that a careful choice of the trial wavefunction can improve the expectation value of the sign [301] so that the fermion sign problem can be made slightly less serious.

As before, R_σ can be evaluated avoiding the calculation of the determinants, if the Green function is provided [285]. This can be explicitly obtained by introducing the generating functional

$$\bar{Z}[J] \equiv \langle \psi_T | e^{-\frac{\theta}{2}\hat{H}} e^{J\hat{c}^\dagger_{\mathbf{j}\sigma}\hat{c}_{\mathbf{i}\sigma}} e^{-\frac{\theta}{2}\hat{H}} | \psi_T \rangle \tag{5.30}$$

so that

$$\langle \hat{c}_{\mathbf{i}\sigma}\hat{c}^\dagger_{\mathbf{j}\sigma}\rangle_{\{s\}} = \delta_{\mathbf{ij}} - \left.\frac{\partial \log \bar{Z}}{\partial J}\right|_{J=0} = \delta_{\mathbf{ij}} - \frac{\langle \psi_T | e^{-\frac{\theta}{2}\hat{H}} \hat{c}^\dagger_{\mathbf{j}\sigma}\hat{c}_{\mathbf{i}\sigma} e^{-\frac{\theta}{2}\hat{H}} | \psi_T \rangle}{\langle \psi_T | e^{-\theta\hat{H}} | \psi_T \rangle}\,. \tag{5.31}$$

The matrix of the Green function at a time-slice l can then be easily calculated. It is given by

$$\mathrm{g}_\sigma(l) = \mathrm{I} - \mathrm{R}^\sigma_l (\mathrm{L}^\sigma_l \mathrm{R}^\sigma_l)^{-1} \mathrm{L}^\sigma_l\,, \tag{5.32}$$

with the matrices L^σ_l and R^σ_l, respectively of dimension $\mathcal{N}_\sigma \times N$ and $N \times \mathcal{N}_\sigma$, defined as

$$\mathrm{L}^\sigma_l = \mathrm{U}^{\sigma T} \mathrm{B}^\sigma_M \ldots \mathrm{B}^\sigma_l \tag{5.33}$$

$$\mathrm{R}^\sigma_l = \mathrm{B}^\sigma_{l-1} \ldots \mathrm{B}^\sigma_1 \mathrm{U}^\sigma\,. \tag{5.34}$$

Once again the calculation of these matrices requires the implementation of a stabilization algorithm [285, 287, 298, 299, 300].

Finally the time-displaced Green functions are defined exactly like in Eqs. (5.21), (5.22) and (5.23) and can be calculated in a stable and efficient way through the method proposed by Feldbacher and Assaad [302].

5.3 The maximum entropy method

QMC simulations do not provide any direct way to calculate the spectral function and the density of states. However, as we have seen in Eq. (5.21), we can easily calculate

the time-displaced Green function. When the time is assumed to be a continuous variable, this reads

$$G_{\mathbf{ij}}(\tau) = \frac{1}{2}\sum_{\sigma}\langle \hat{c}_{\mathbf{i}\sigma}(\tau)\hat{c}^{\dagger}_{\mathbf{j}\sigma}(0)\rangle \tag{5.35}$$

for $\tau > 0$. Its space-Fourier transformed $G(\mathbf{k},\tau)$ is related to the spectral function $A(\mathbf{k},\omega)$ by the fluctuation-dissipation theorem through the equation

$$G(\mathbf{k},\tau) = \int_{-\infty}^{\infty} d\omega K(\tau,\omega)A(\mathbf{k},\omega)\,, \tag{5.36}$$

where the kernel is

$$K(\tau,\omega) = \frac{e^{-\tau\omega}}{1+e^{-\beta\omega}}\,, \tag{5.37}$$

at finite temperatures, and

$$K(\tau,\omega) = e^{-\tau\omega} \tag{5.38}$$

at zero-temperature.

We then must invert numerically the integral equation (5.36) in order to obtain $A(\mathbf{k},\omega)$ from $G(\mathbf{k},\tau)$. This had been a problem for long time, but the maximum entropy method (MEM) provides nowadays a quite reliable way to extract the spectral function given a Monte Carlo set of data for $G(\mathbf{k},\tau)$.

We will just briefly sketch the method without addressing its statistical foundations and the many related issues, for which we refer to the original literature [288, 289].

On the one hand, for each discrete imaginary-time $\tau_l = l\Delta\tau$, a QMC simulation produces N_{data} time-displaced Green functions $\{G^{(n)}(\tau_l)\}_{n=1,N_{data}}$ [6], whose average is

$$\bar{G}(\tau_l) = \frac{\sum_{n=1}^{N_{data}} G^{(n)}(\tau_l)}{N_{data}} \tag{5.39}$$

We introduce also the covariance matrix C, whose elements are

$$C_{ll'} = \frac{1}{N_{data}(N_{data}-1)}\sum_{n=1}^{N_{data}}[\bar{G}(\tau_l) - G^{(n)}(\tau_l)][\bar{G}(\tau_{l'}) - G^{(n)}(\tau_{l'})]\,. \tag{5.40}$$

On the other hand, the Eq. (5.36) can be rewritten in the discrete form

$$G(\tau_l) = \sum_i K_{li}A_i\,, \tag{5.41}$$

[6] Here, we assume that we have only one **k**-point so that we do not indicate the explicit dependence of the time-displaced Green function on **k**.

where $A_i = A(\omega_i)\Delta\omega_i$ and $K_{li} = K(\tau_l, \omega_i)$. Then, for a given spectral density $\{A_i\}$ we can define the functional

$$\chi^2 = \sum_{l,l'} [\bar{G}(\tau_l) - G(\tau_l)][\mathrm{C}^{-1}]_{ll'}[\bar{G}(\tau_{l'}) - G(\tau_{l'})] \tag{5.42}$$

where $\bar{G}(\tau_l)$ is the average defined by Eq. (5.39), while $G(\tau_l)$ is the time-displaced Green function corresponding to $\{A_i\}$ and calculated through the Eq. (5.41). C^{-1} is the inverse of the covariance matrix.

The maximum entropy method consists in finding the spectral density $\{A_i\}$, that maximizes the functional

$$Q = \alpha S - \frac{1}{2}\chi^2 , \tag{5.43}$$

where the term

$$S = \sum_i [A_i - m_i - A_i \log(A_i/m_i)] \tag{5.44}$$

represents an entropy. The function $m_i = m(\omega_i)\Delta\omega_i$ is called the default model. It sets the maximum of the entropy to zero when $\{m_i\} = \{A_i\}$. In agreement with the literature [289], we have found that the spectral function depends only weakly upon the default model. Then, we always assume $m_i = 1/c$, with $c^2 = \sum_i m_i^2$, unless we explicitly provide a different model. The external parameter α has to be fixed based on statistical arguments. We have decided to use the classical maximum entropy method (classic MaxEnt) where the most probable value of α is chosen. We have found almost no difference between the spectral functions calculated by the classic MaxEnt and those calculated using the so-called Bryan's method, in which α is addressed by marginalization [303]. In contrast, the so-called historic MaxEnt, where α is fixed so that $\chi^2 = N_{data}$, produces much smoother spectral functions as it tends to underfit the data.

We have used the Bryan algorithm [303] to locate the maximum of Q for different values of α. This algorithm is believed to be appropriate for the analytic continuation problem [289] . We have also checked that our code returns the global maximum by comparing the results with those obtained with the freely distributed code by Sandvik [304], where Q is maximized by simulated annealing.

Finally we must add a couple of comments. Firstly, for the Hubbard model, the first three moments $\mu_m = \int_{-\infty}^{\infty} d\omega\, \omega^m A(\mathbf{k}, \omega)$ $(m = 1, 2, 3)$ of $A(\mathbf{k}, \omega)$ can be easily calculated (μ_0 being just the normalization condition $\mu_0 = 1$). White [305, 306] then suggested a modified expression for χ^2, which incorporates the correct form of μ_1 and μ_2. In contrast, our code returns the correct values of μ_0 and μ_1 up to

the forth decimal digit and that of μ_2 up to the second decimal digit, although we did not impose any constraint on the maximization of Q. Secondly, we perform the diagonalization of the covariance matrix to deal with correlations in imaginary-time for the Green function at a given τ_l.

5.4 Two-dimensional Hubbard model

In this section, we discuss the Hubbard model on a two-dimensional (2D) square lattice of linear dimension L (with periodic boundary conditions). Because many studies have been previously published for this system (see, for example, references [274, 287, 306, 307, 308, 309]), our results can be compared to a large number of available data. Therefore, here, we aim not at providing new insight into the physics of the Hubbard model, but rather to show that our code returns reliable results[7]. We mainly focus on the case of an half-filled band. However, we will also briefly mention a few results for systems doped away from this specific limit in order to show how the sign problem affects the efficiency of the AFQMC algorithm.

For calculations performed at finite temperatures within the grand-canonical ensemble, the number of electrons is fixed by the value of the chemical potential μ. At half-filling, μ can be obtained by imposing the particle-hole symmetry and we have that $\mu = U/2$ for every temperature and every lattice size.

In all our studies, the hopping amplitude is $t = 1$ for nearest neighbor sites and $t = 0$ otherwise, while the on-site energies are kept equal to zero. For the non-interacting system the single-particle states have then energies $E_{\mathbf{k}} = -2(\cos k_x + \cos k_y)$ ($k_x = 2\pi n_x/L$ and $k_y = 2\pi n_y/L$ with $n_x = n_y = 0, ..., L-1$) and the density of states (in the limit $L^2 \to \infty$) has a Van-Hove simgularity at $E = 0$. Most of the calculations that we discuss here, are performed for $U = 4$, although some results for different values of U are sometimes shown for comparison. For $U = 4$, the 2D half-filled Hubbard model is in the intermediate regime between the weak-coupling limit, in which the ground state is an antiferromagnetic insulator because of the singularity in the density of states of the non-interacting system, and the strong-coupling limit, in which the ground state is a Mott insulator. Numerical simulations are often con-

[7]By using our code, we have been able to perform calculations for 2D lattices of linear size up to $L = 16$. However, we have decided not to use the full computational resources available for demonstrative calculations. We will then limit the discussion to lattices of linear size $L = 4, 6, 8, 10$. Recently it was possible to study the half-filled 2D Hubbard model for lattices of about 500 sites [309]. Unfortunately our code is not able to treat such large systems and improvements to the code are currently on-going by introducing BLAS subroutines to perform the linear algebra operations.

sidered unavoidable to investigate this intermediate regime as most of the analytic approximations break down.

For simulations performed by using the zero-temperature algorithm, $\theta = 30$ is found to be large enough to have the system in the ground state and time-steps of $\Delta\tau = 0.05$ are used. For finite-temperature calculations, the time-steps are set to $\Delta\tau = 0.125$. About 2000 equilibration steps are usually performed before starting the statistical accumulation run. In order to obtain correct estimates of error bars, the data are treated by using the re-blocking method [161]. For each quantity, the value of the Monte Carlo correlation time obtained through this method agrees well with that obtained by its direct calculation. The code can sometimes get stuck with a spin-order in a particular direction. Then many runs with different random number seeds and initial configurations for the Ising fields are performed and the values of each quantity are finally averaged.

We start by discussing the electronic properties of the half-filled Hubbard model

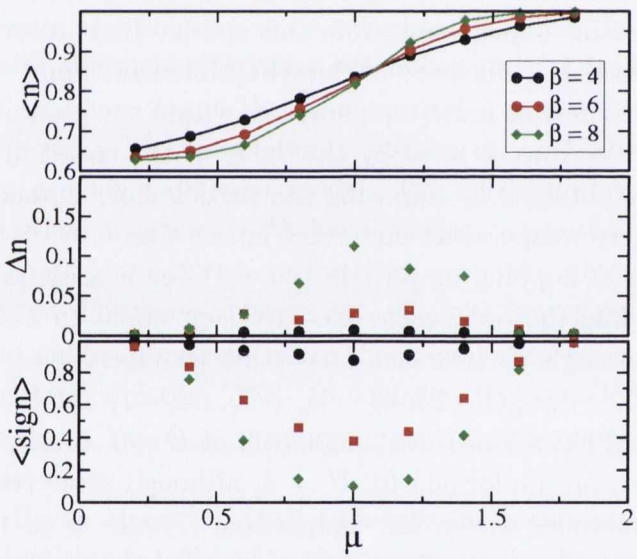

Figure 5.1: Average density $\langle n \rangle$ (top panel), error Δn on the average density (central panel) and average sign as a function of the chemical potential μ (bottom panel) for a 4×4 lattice, for $\beta = 4, 6, 8$ and for $U/t = 4$

and we first work at finite temperature. Within the grand-canonical ensemble, the metallic or insulating character of the system can be understood by calculating the charge-compressibility,

$$\kappa = \frac{\partial \langle n \rangle}{\partial \mu} . \tag{5.45}$$

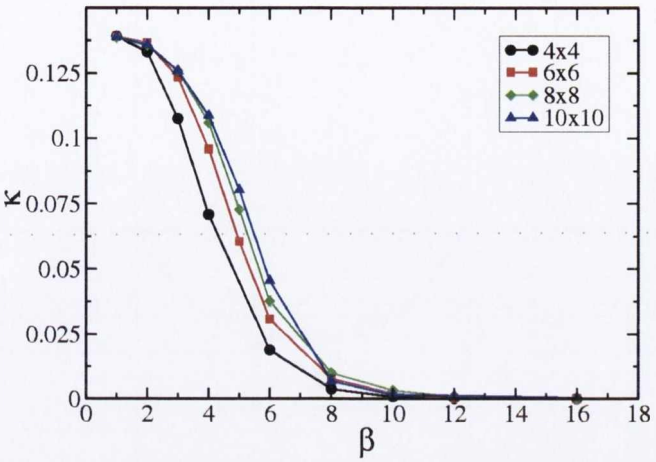

Figure 5.2: Compressibility κ as a function of the inverse temperature β for various sized lattice and for $U = 4$ (error bars are smaller than the size of the symbols).

Here $\langle n \rangle = \sum_{\mathrm{i}} \langle \hat{n}_{\mathrm{i}} \rangle / L^2$ is the average charge-density for lattice site and μ is the chemical potential. When $\langle n \rangle$ does not depend on the chemical potential (i.e. κ vanishes), the system presents a gap so that no particles can be added. For example, Fig. 5.1 (top panel) shows how $\langle n \rangle$ changes as a function of μ for a lattice of linear dimension $L = 4$, for $U = 4$ and for $\beta = 4, 6, 8$[8]. A plateau around $\mu = U/2$, which develops by increasing β (i.e. lowering the temperature), is clearly visible[9]. Although the value of κ can be obtained by fitting the curve $\langle n \rangle$ vs μ, this is more easily calculated through the equation

$$\kappa = \frac{\beta}{L^2} \left(\langle \hat{\mathcal{N}}^2 \rangle - \langle \hat{\mathcal{N}} \rangle^2 \right), \tag{5.46}$$

where $\hat{\mathcal{N}} = \sum_{\mathrm{i}\sigma} \hat{n}_{\mathrm{i}\sigma}$. This equation can be derived from Eq. (5.45) by taking the derivative with respect to μ of $\frac{1}{\mathcal{Z}} \mathrm{Tr} \left[e^{-\beta(\hat{H} - \mu \hat{\mathcal{N}})} \hat{n} \right]$ with $\hat{n} = \hat{\mathcal{N}}/L^2$. κ is plotted in Fig. 5.2, as a function of β, for lattices of various size at half-filling and for $U = 4$. We note that the system becomes insulating for $\beta \gtrsim 8$.

Further insights into the electronic properties are provided by the time-displaced

[8]We do not plot the data for $\mu > U/2$ as these can be inferred from particle-hole symmetry. Indeed $\langle n \rangle(\mu) = 2 - \langle n \rangle(\mu - U/2)$

[9]The apparent plateau at $\langle n \rangle \approx 0.6$ is a finite size effect. Indeed, for a 4×4 lattice and for $U = 0$, a density equal to $10/16 = 0.625$ corresponds to the case when the eigenstates with $\mathbf{k} = (0,0), (\pm\pi/2, 0), (0, \pm\pi/2)$ are fully filled with two electrons. Even after switching on the interaction, the system still does not completely loose memory about the non-interacting spectrum of this particular filling factor.

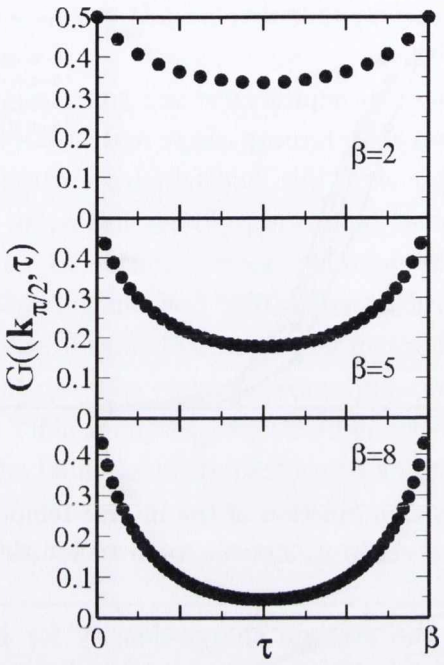

Figure 5.3: Time-displaced Green function $G(\mathbf{k}_{\pi/2}, \tau)$ for $U = 4$, $\beta = 2, 5, 8$ and a lattice with $L = 8$ (error bars are smaller than the size of the symbols).

Green function. Indeed its decay indicates whether the systems develops a gap for charge excitations. In Fig. 5.3 we plot the (space) Fourier transform of the of the finite-temperature time-displaced Green function

$$G(\mathbf{k}, \tau) = \frac{1}{2L^2} \sum_{\sigma} \sum_{\mathbf{ij}} e^{i\mathbf{k}(\mathbf{i}-\mathbf{j})} \langle \hat{c}_{\mathbf{i}\sigma}(\tau) \hat{c}^{\dagger}_{\mathbf{j}\sigma}(0) \rangle \tag{5.47}$$

for a lattice with $L = 8$ and at $\mathbf{k}_{\pi/2} = (\pi/2, \pi/2)$. This momentum lies exactly on the non-interacting half-filled Fermi surface so that, for $U = 0$, $G(\mathbf{k}_{\pi/2}, \tau)$ does not decay in time and is equal to 0.5. In contrast, when the interaction is switched on, $G(\mathbf{k}_{\pi/2}, \tau)$ decays, indicating that the system develops a gap for charge excitations. Furthermore the decay rate becomes faster while decreasing the temperature. Consistentely with the results above, the spectral function $A(\mathbf{k}_{\pi/2}, \omega)$ is found to have a single peak at high temperature, which then splits into two peaks at low temperature. For temperatures in between these two regimes a pseudogap is found [306]. For example, Fig. 5.4 show $A(\mathbf{k}_{\pi/2}, \omega)$, calculated through the MEM, for a lattice of $L = 8$ and for $\beta = 2, 5, 8$ ($U = 4$). The transition from a spectrum with a single peak at $\beta = 2$ to a

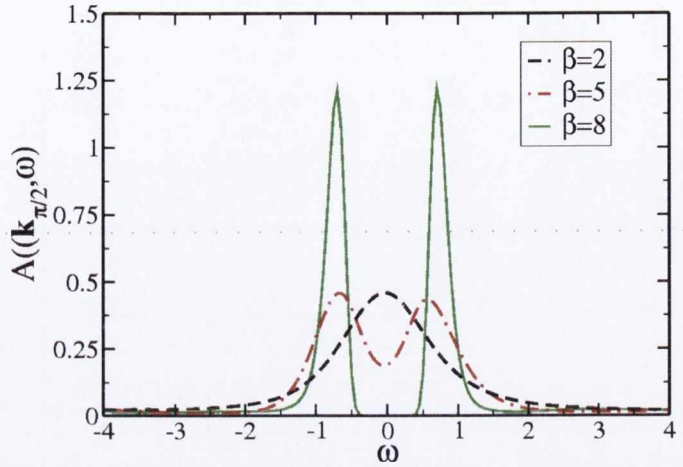

Figure 5.4: Spectral function $A(\mathbf{k}_{\pi/2}, \omega)$ for different inverse temperatures $\beta = 2, 5, 8$, for $U = 4$ and for a lattice with $L = 8$.

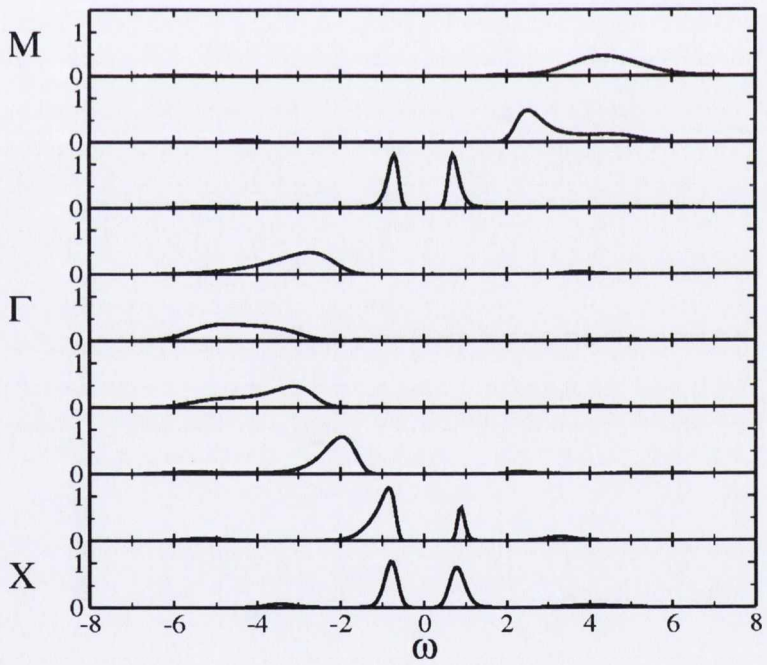

Figure 5.5: Spectral function $A(\mathbf{k}, \omega)$ vs ω for $\mathbf{k}$ along the direction M-Γ-X in the Brillouin zone ($\mathbf{k} = (\pi, \pi)$ at M, $\mathbf{k} = (0, 0)$ at Γ and $\mathbf{k} = (\pi, 0)$ at X). We consider $U = 4$, $\beta = 8$ and a lattice with $L = 8$.

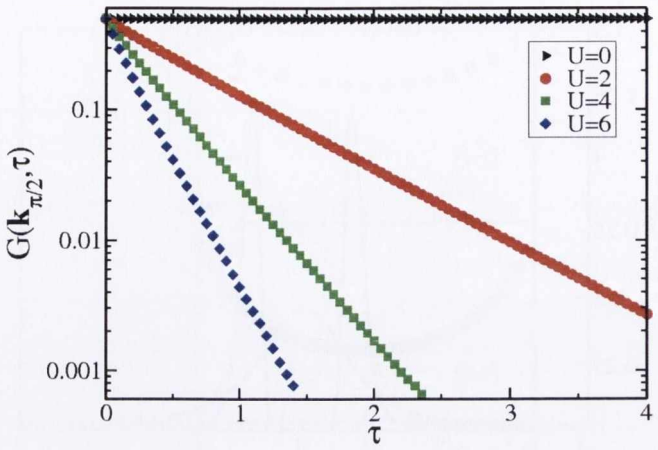

Figure 5.6: Zero-temperature time-displaced Green function $G(\mathbf{k}_{\pi/2}, \tau)$ for $U = 0, 2, 4, 6$ (error bars are smaller than the size of the symbols).

spectrum with two peaks separated by a gap at $\beta = 8$ is clearly visible[10]. In contrast, for $\beta = 5$ the spectrum presents a pseudogap.

In Fig. 5.5 we show the spectral function at various $\mathbf{k}$ vectors in the Brillouin zone for a lattice with linear dimension $L = 8$ and for $\beta = 8$ and $U = 4$. The spectral function has a broad peak at negative (positive) energies for $\mathbf{k}$ inside (outside) the Fermi surface. In contrast, as already shown in Fig. 5.4, for $\mathbf{k}$ on the Fermi surface, the quasi-particle peak splits into two sharp peaks symmetric with respect to $\omega = 0$ and separated by the gap.

The value of the quasi-particle gap at zero-temperature Δ can be extracted from the zero-temperature time-displaced Green function at $\mathbf{k}_{\pi/2} = (\pi/2, \pi/2)$, which is plotted in Fig. 5.6 (note the logarithmic scale). Indeed Δ is calculated from

$$G(\mathbf{k}_{\pi/2}, \tau) \propto e^{-\tau\Delta} . \tag{5.48}$$

For $U = 4$ and a lattice of linear dimension $L = 8$, we then obtain $\Delta = 2.769 \pm 0.001$. For comparison, in Fig. 5.6 we also plot $G(\mathbf{k}_{\pi/2}, \tau)$ for $U = 0$, $U = 2$ and $U = 6$. For $U = 0$, $G(\mathbf{k}_{\pi/2}, \tau)$ does not decay in time and it stays equal to 0.5, while, as expected, $G(\mathbf{k}_{\pi/2}, \tau)$ decays faster for larger values of U reflecting the opening of the quasi-particle gap. We find $\Delta = 1.299 \pm 0.001$ for $U = 2$ and $\Delta = 4.27106 \pm 0.001$

[10]Our spectra often have much sharper peaks that those calculated by White [306]. This might be due to the fact that we did not incorporate information about the moments of the spectral function in the MEM. However, the size of the quasi-particle gap and the value ω, at which the maximum of the peaks is found, are consistently reproduced.

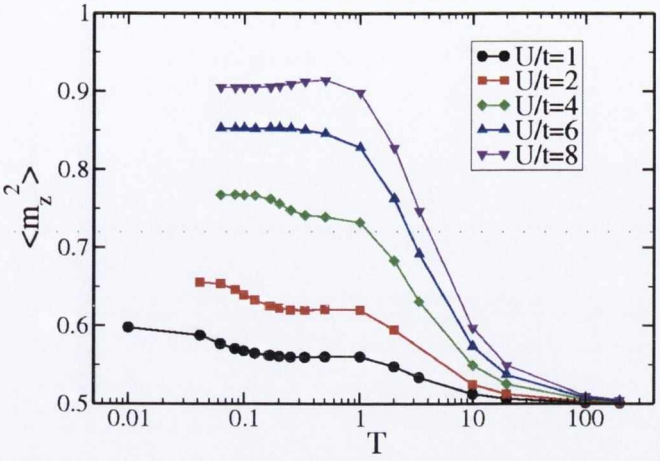

Figure 5.7: Local magnetic moment $\langle \hat{m}_z^2 \rangle$ calculated at different temperatures T and different values of the interaction U for a lattice of linear dimension $L = 6$ (error bars are smaller than the size of the symbols).

for $U = 6$. These values can be compared to mean-field gaps $\Delta_{MF} = 0.86$ ($U = 2$), $\Delta_{MF} = 2.76$ ($U = 4$) and $\Delta_{MF} = 4.96$ ($U = 6$) calculated by solving the equation [3]:

$$1 = \frac{U}{L^2} \sum_{\mathbf{k}} \frac{1}{2\sqrt{E_{\mathbf{k}}^2 + \Delta_{MF}^2/4}}, \tag{5.49}$$

where $E_{\mathbf{k}}$ indicates the energy of a single-particle state for the non-interacting system (see above). The mean-field approximation underestimates the gap for $U = 2$, while this is overestimated for $U = 6$. Interestingly, we find that $\Delta \approx \Delta_{MF}$ for $U = 4$.
Before turning to the investigation of the magnetic properties, we would like to add a comment about the sign problem. The bottom panel of Fig. 5.1 shows the average of the sign $\langle \mathrm{sgn}(\rho) \rangle$ of the Boltzmann weight $\rho = \det \mathrm{O}_\uparrow \det \mathrm{O}_\downarrow$ for various values of the chemical potential. We note that $\langle \mathrm{sgn}(\rho) \rangle$ has a distinct minimum at $\mu = 1$ and becomes almost zero for low temperatures. Since the expectation value of each observable must be calculated as indicated in Eq. (5.19), a small value of the average sign leads to a very large error. For example, the central panel of Fig. 5.1 shows the error Δn on $\langle n \rangle$ as a function of μ and we note that, when the sign problem becomes more pronounced, Δn is large. For bigger lattices, it is practically impossible to compute quantities for temperatures below $T = 1/\beta = 1/6$ and for $\mu \approx 1$. Unfortunately, this value of the chemical potential corresponds to the filling regime, at which the Hubbard model might show superconductivity so that no conclusive results have been achieved so far concerning this interesting problem.

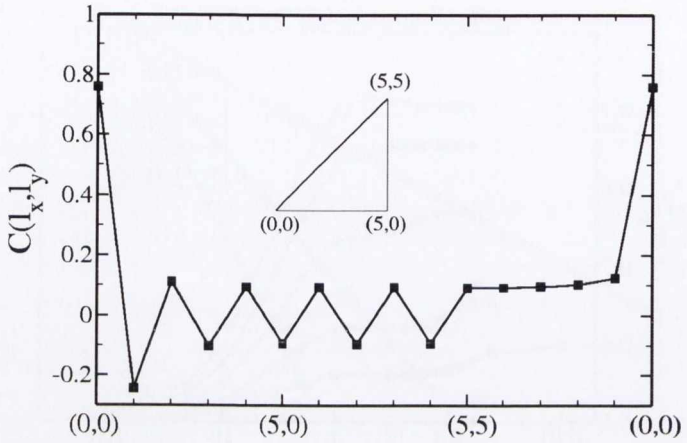

Figure 5.8: Spin-spin correlation function $C(l_x, l_y)$ for $U/t = 4$, $\beta = 16$ and for a lattice of linear dimension $L = 10$ (error bars are smaller than the size of the symbols). The inset shows the direction in real space along which $C(l_x, l_y)$ is calculated (i.e from $(l_x, l_y) = (0, 0)$ to $(5, 0)$ and then from $(5, 0)$ to $(5, 5)$ and finally from $(5, 5)$ back to $(0, 0)$

We finally study the magnetic behavior of the system. This can be understood by calculating the real-space spin-spin correlation function

$$C(\mathbf{l}) = \langle \hat{m}^z_{\mathbf{i}+\mathbf{l}} \hat{m}^z_{\mathbf{i}} \rangle \,, \tag{5.50}$$

where $\hat{m}^z_{\mathbf{i}} = \hat{n}_{\mathbf{i}\uparrow} - \hat{n}_{\mathbf{i}\downarrow}$ [note that an expression for $C(\mathbf{l})$ in terms of the Green function (5.15) can be derived by using Wick's theorem and proceeding like in Eq. (5.18)] Its zero-space separation value defines the local magnetic moment $\langle \hat{m}^2_z \rangle = C(0, 0)$. Fig. 5.7 shows the evolution of $\langle \hat{m}^2_z \rangle$ as function of temperature T for different values of U on a 6×6 lattice. The local moment begins to develop from its uncorrelated value $1/2$ at a temperature set by U, and then saturates at low T. On the one hand, because of quantum fluctuations, the local moment does not reach 1 even at zero-temperature. On the other hand, a large value of the interaction partially suppresses charge fluctuations. The magnetic moment will approach 1 only in the limit of $U/t \to \infty$, but it is already about 0.9 for $U = 8$. Furthermore, we can note that the local moment also makes a further small adjustment at low T. This is due to the onset of magnetic order. While the Mermin-Wagner theorem [178, 310] establishes that long-range magnetic order is forbidden at any finite temperature for an infinite 2D square lattice, we can still speak about an approximate magnetic transition for a finite lattice when correlations extends over the entire lattice [306]. For example, Fig. 5.8 shows $C(\mathbf{l})$ for a lattice of linear dimension $L = 10$, for $\beta = 16$ and for

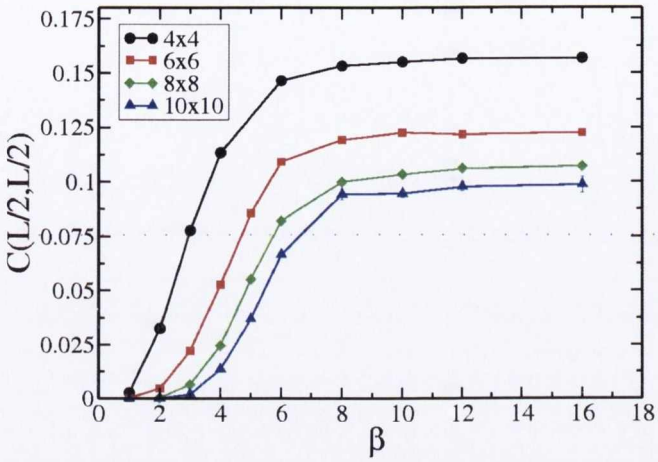

Figure 5.9: Spin-spin correlation function for two point at the maximum separation for various sized lattices as a function of the inverse temperature β and for $U = 4$ (error bars are smaller than the size of the symbols).

$U = 4$. The correlations have a clear antiferromagnetic nature and reach the size of the lattice. This is indicated by the finite value of the correlation function for two points separated by the largest possible distance $C(L/2, L/2)$. Fig. 5.9 shows how $C(L/2, L/2)$ changes as a function of β ($U = 4$). $C(L/2, L/2)$ increases by lowering the temperature until it reaches a saturated value and the correlation length extends over the entire lattice. We note that, for small lattices, $C(L/2, L/2)$ is overestimated and it decreases while increasing the lattice size. It was recently found that this finite size effect becomes small for $L \geq 20$ [309].

The Fourier transform of the real-space spin-spin correlation function defines the magnetic structure factor

$$S(\mathbf{k}) = \frac{1}{L^2} \sum_{\mathbf{l}} e^{i\mathbf{k}\mathbf{l}} C(\mathbf{l}). \tag{5.51}$$

For the half-filling case, because of the antiferromagnetic nature of the correlations, $S(\mathbf{k})$ has a sharp peak at $\mathbf{k} = (\pi, \pi)$. Fig. 5.10 shows $S(\pi, \pi)$ for lattices of various sizes as function of β and for $U = 4$. For comparison, we also plot the zero-temperature values of $S(\pi, \pi)$ (these corresponds to the points at $\beta = 20$). As we can see, for $\beta > 10$, the magnetic structure factor is already converged to its ground-state value for all the cases shown. However, as the size of the system increases, a larger value of β is required to saturate $S(\pi, \pi)$.

Provided the zero-temperature structure factor $S(\pi, \pi)$ for lattices of various size, we

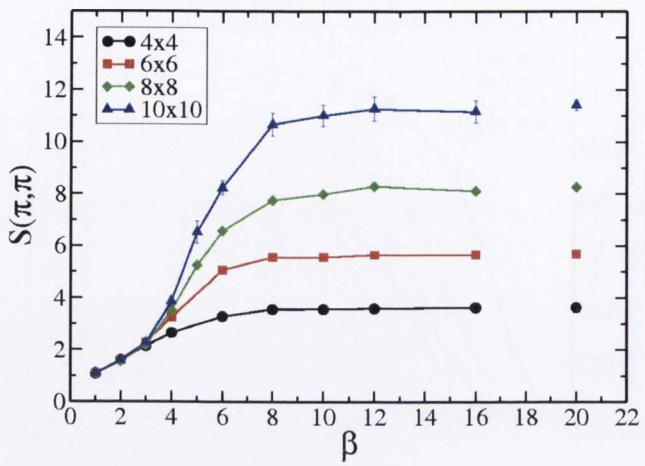

Figure 5.10: Magnetic structure factor $S(\pi, \pi)$ as a function of the inverse temperature β for various sized lattice and for $U = 4$.

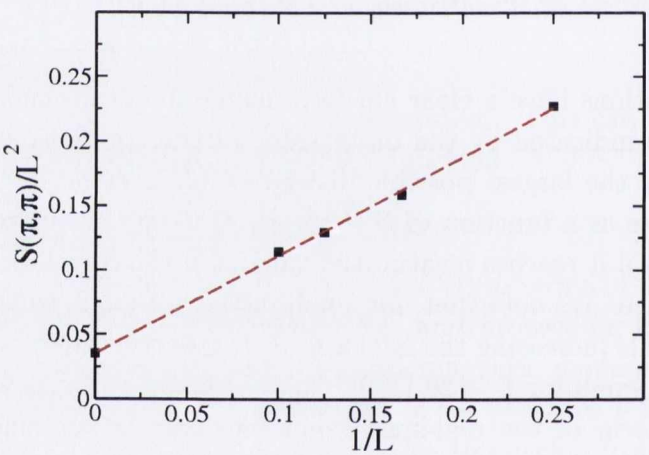

Figure 5.11: Scaling of the zero-temperature structure factor at $\mathbf{k} = (\pi, \pi)$ with the lattice size for $U = 4$. The line is the least-squares fit of the data. The extrapolated value for the infinite lattice (i.e. $1/L = 0$) is non-zero. The error bars are smaller than the size of the symbols.

can finally extrapolate the antiferromagnetic order parameter

$$m_{\mathrm{AF}}^2 = \lim_{L^2 \to \infty} \frac{S(\pi, \pi)}{L^2}, \tag{5.52}$$

which, if non-zero, indicates that the ground state shows long-range antiferromagnetic order. $S(\pi, \pi)/L^2$ is plotted against L in Fig. 5.11 and, by using the scaling relation

[287, 309]

$$\frac{S(\pi,\pi)}{L^2} = \frac{m_{\mathrm{AF}}^2}{3} + \frac{a}{L} \tag{5.53}$$

we obtain $m_{\mathrm{AF}} = 0.325 \pm 0.009$, a value consistent with that reported in other studies [287].

5.5 Summary

In this section we have explained the main ideas beyond the AFQMC method and we have discussed the details of our own implementation. Furthermore we have presented the results of our calculations for the 2D Hubbard model. This study shows the capabilities of our code and serves as an extensive test about the reliability of the results that it can provide.

We believe that the use of the AFQMC method will be necessary to carry on the work presented in the previous chapter and address correlation effects, which might not be accurately described within the mean-field approximation. The interplay between disorder and electron-electron interaction is a very fascinating subject by itself, but, as we have discussed, its study can also provide new insight into the physics of materials such as DMS and d^0 magnets. Furthermore, a topic strictly related to d^0 magnetism is that of defects- and edge-magnetism in graphene. Some studies have already shown that these problems can be accurately dealt through AFQMC simulations [311, 312].

Finally, we are also currently investigating the properties of the Peierls-Hubbard model [defined by the Hamiltonian (2.94)]. This was previously studied by Bhattacharya et al. [313] by combining the mean-field approximation and a (classic) Monte Carlo method to treat respectively the electronic and the ionic degrees of freedom. The Peierls-Hubbard model provides a qualitative description of electron correlation effects in polymeric chains, whose study can be relevant for the rapidly growing research fields of organic electronics and spintronics.

Chapter 6

Switchable transition metal complexes

6.1 Introduction

In nature there is a vast class of molecules whose spin state can be altered by external stimuli (mainly light irradiation and either temperature or pressure variations). Typical examples of such molecules are the spin-crossover transition metal complexes [92, 93]. Here a change in the distribution of the electrons in the d orbitals results in a low (LS) to high spin (HS) transition. Other examples are molecular units based on polycyanometallates, nitroprussides and metal dioxolene systems [94]. Because of electron-charge transfer between either two metal ions or a metal ion and a coordinated ligand, these compounds can adopt different states with electronic structures that differ in charge distribution. As the charge-transfer is often associated with a change in the number of unpaired electrons, a spin transition is also observed.
These systems represent promising candidates for molecular spintronics applications. In fact, devices incorporating spin-crossover molecules are likely to show drastic changes in the current-voltage characteristic curve as consequence of the magnetic transition. However, a real demonstration of the validity of this idea requires a precise control over the state of the molecule and the fundamental question about whether this can be achieved by applying static electric fields has been recently raised [314, 315].
Here we will present some of the results that we have already achieved in order to theoretically address this issue and we will discuss other problems, which will be considered in future studies. The chapter is divided into two main parts. In the first part, we will introduce the spin-crossover molecules and we will mainly discuss

the theoretical issues related to the correct description of their electronic structure. In the second part, we will instead describe the cobalt-dioxolene complexes, which are interesting examples of molecules showing interconversion between redox isomers with different spin states [95, 96]. In this case, our study will focus mainly on phenomenological rather than methodological problems and we will finally predict that the interconversion between the different isomers can be controlled by applying a static electric field.

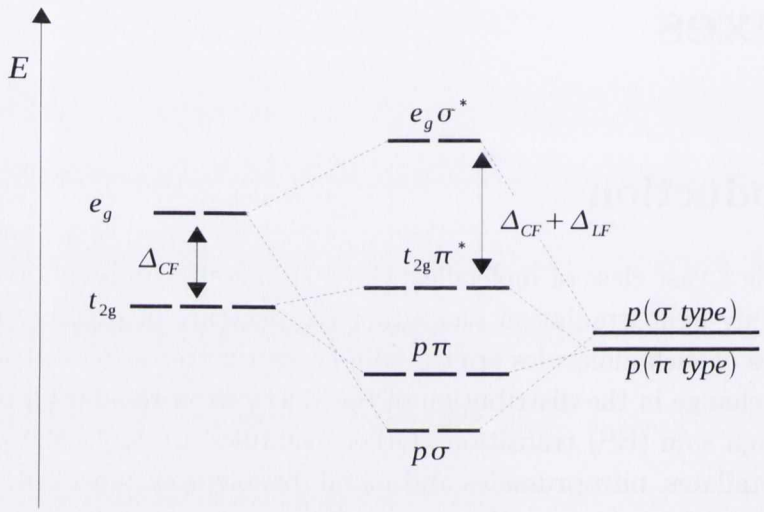

Figure 6.1: Energy level diagram for a transition metal (TM) ion octahedrally coordinated. On the one hand, in crystal field theory, the $3d$ orbitals of the TM ion are splitted by an energy Δ_{CF} because of the electrostatic interaction with the ligands. On the other hand, in ligand field theory, the $3d$ orbitals of the TM ion form covalent bonds with the ligands. In this diagram we assume that each ligand contributes three p-orbitals, one with the positive lobe pointing toward the TM ion (σ type) and two with the lobes perpendicular to this (π-type) (note that the σ and π-type p orbitals are degenerate and they are plotted slightly separated in energy just for better display). The π-type p orbitals couple with the TM t_{2g} orbitals, while the σ-type p orbitals couple with the e_g TM orbitals. Since the π interaction is weaker than the σ one, the antibonding $t_{2g}\pi^*$ orbitals lie lower in energy than the $e_g\sigma^*$ orbitals. The energy splitting between the $t_{2g}\pi^*$ and the $e_g\sigma^*$ orbitals is indicated by $\Delta_{LF}+\Delta_{CF}$.

6.2 Spin crossover molecules

Typical examples of spin-crossover (SC) complexes are molecules presenting a single Fe^{2+} ion (almost) octahedrally coordinated to the ligands, which are usually pyridine or pyrazole rings. In the ground state, because of the large ligand field, the six $3d$ electrons of the Fe occupy the t_{2g}-π^* antibonding orbitals in a spin-zero ($S = 0$) state (see Fig. 6.1 for the notation). However, by increasing the temperature, two electrons are promoted from the t_{2g}-π^* to the e_g-σ^* antibonding orbitals and the high spin $S = 2$ state becomes thermodynamically more stable. This transition is entropy driven and is regulated by the relative Gibbs free energy between the HS and LS states,

$$\Delta G = G_{\mathrm{HS}} - G_{\mathrm{LS}} = \Delta H - T\Delta S\,. \tag{6.1}$$

$\Delta H = H_{\mathrm{HS}} - H_{\mathrm{LS}}$ and $\Delta S = S_{\mathrm{HS}} - S_{\mathrm{LS}}$ indicate respectively the enthalpy and the entropy variation (note that for $\Delta G > 0$ the LS configuration is more thermodynamically stable). Indeed, in SC molecules $\Delta H > 0$, but $S_{\mathrm{HS}} > S_{\mathrm{LS}}$. Therefore for large enough temperatures, the entropic term dominates over the enthalpic one and the molecules transit from the LS to the HS configuration. There are two contributions to the entropy: the first is provided by the spin and the second by the molecule vibrations. Since, according to the ligand field theory, the e_g-σ^* orbitals are more anti-bonding than the t_{2g}-π^*, the transfer of the electrons to the e_g-σ^* orbitals weakens the chemical bond and produces the breathing of the metal ion coordination sphere with consequent softening of the phonon modes and an increase of the vibronic entropy.

The SC transition is usually reported either for molecules in solution or in single crystals and, depending on the strength and on the origin of the inter-molecular interactions, it can have cooperative nature and can be associated to a thermal hysteresis loop.

Interestingly, the transition can be induced also by illumination. This phenomenon is called LIESST effect (Light-Induced-Excited-Spin-State-Trapping) and it is explained through a mechanism involving several excited states [316]. The lifetime of the metastable HS state is usually very long at low temperature as the relaxation to the ground state is due to the weak electronic coupling between these states [317]. The opposite process, in which molecules in the HS metastable state are brought back to their ground state, is also possible and is called reverse LIESST effect.

Some transport experiments for SC Fe^{2+} molecules were recently performed. Takahashi et al. [97] demostrated that the conductivity of the SC-molecular conductor

hybrid $[Fe(qsal)_2][Ni(dmit)_2]\cdot CH_3CH_3CN\cdot H_2O$ has an hysteretic behaviour with temperature. Alam et al. [98] were able to distinguish the spin state of Fe^{2+} complexes, placed on highly oriented pyrolytic graphite surfaces, by STM. Furthermore, Prins. et al. [99] reported a device, made by contacting $[Fe(trz)_3](BF_44)_2$ (trz=triazole)-based nanoparticles between electrods, which shows switching and memory effects. They have observed a sharp increase in the conductance upon heating together with the presence of thermal hysteresis. Finally Meded et al. [100] claimed that an Fe^{2+} molecule undergoes a spin transition induced by electric gating and charging of the ligands in a three-terminal device. A similar scenario was also suggested to explain the results of another transport experiment for a Mn^{2+} molecule [101].

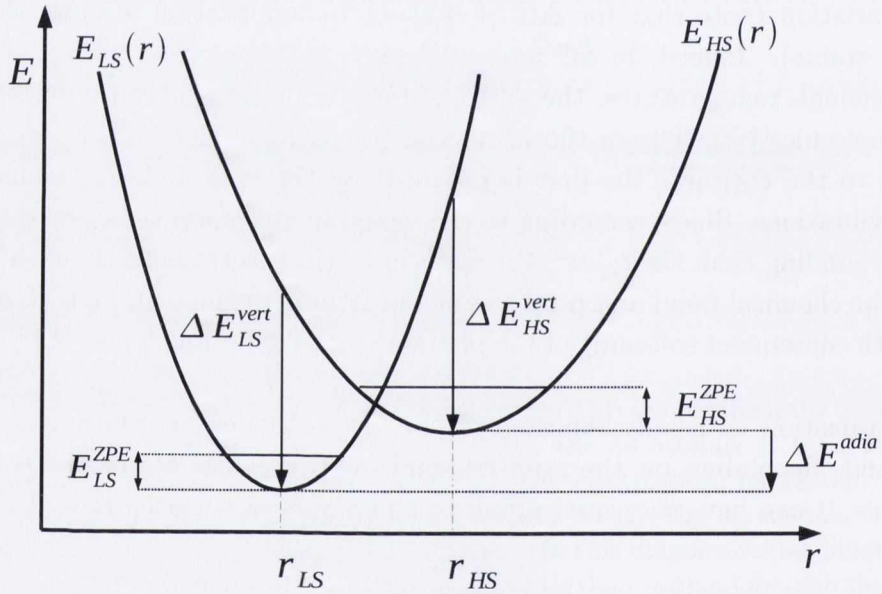

Figure 6.2: Potential energy surface of the HS and LS state of a SC molecule. The coordinate r is a shorthand notation for all of the 3N nuclear coordinates of a molecule. The zero point phononic energies for the HS and LS state, E^{ZPE}_{HS} and E^{ZPE}_{LS}, the adiabatic energy gap, ΔE^{adia}, and the vertical energy gaps, $\Delta E^{\text{vert}}_{LS} = \Delta E^{\text{vert}}(r_{LS})$ and $\Delta E^{\text{vert}}_{HS} = \Delta E^{\text{vert}}(r_{HS})$ are indicated.

6.3 Electronic structure calculations for spin crossover molecules: state of art

When we consider a single molecule in vacuum and at zero temperature, ΔG is nothing but the internal energy difference, which, within the adiabatic approximation, reads

$$\Delta E = \Delta E^{\text{adia}} + \Delta E^{ZPE} . \tag{6.2}$$

Here, $\Delta E^{ZPE} = E^{ZPE}_{HS} - E^{ZPE}_{LS}$ and $E^{ZPE}_{HS(LS)}$ is the zero-point phononic energy of the HS(LS) state.

$$\Delta E^{\text{adia}} = E_{HS}(r_{HS}) - E_{LS}(r_{LS}) \tag{6.3}$$

is the adiabatic energy difference (often called "adiabatic energy gap"). The coordinate r is a shorthand notation for all of the 3N nuclear coordinates of a molecule, while the energies $E_{HS}(r)$ and $E_{LS}(r)$ define the potential energy surfaces (PESs) respectively of the HS and LS state (see Fig. 6.2). In addition to the adiabatic energy gap, we can define also the vertical energy difference ("vertical energy gap")[1]

$$\Delta E^{\text{vert}}(r) = E_{HS}(r) - E_{LS}(r) \tag{6.4}$$

and the difference of vertical energy gaps (DOG)

$$\text{DOG}(r_2, r_1) = \Delta E^{\text{vert}}(r_2) - \Delta E^{\text{vert}}(r_1) . \tag{6.5}$$

Furthermore, a second type of DOG is sometimes considered in the literature [318]. This is defined as

$$\text{DOG}_2(L_2, L_1, r_{L_2}, r_{L_1}) = \Delta E^{\text{vert}}(r_{L_2}) - \Delta E^{\text{vert}}(r_{L_1}) \tag{6.6}$$

where L_1 and L_2 refer to two molecules with the same Fe^{2+} ion, but different ligands. All of these quantities can be computed by using *ab initio* electronic structure methods. In practice, DFT is always the preferred method as SC molecules are composed of at least fifty atoms and a good balance between expected accuracy and computational cost is required. However, there are many issues connected to the theoretical description of SC molecules, which either have not been properly addressed or have not found satisfactory solutions yet. We then list some of them, which have been leading to our research.

[1] We use here the standard terminology employed in the literature about SC molecules. In this chapter, by gap we will always mean either the adiabatic energy difference, Eq. (6.3), or the vertical energy difference, Eq. (6.4). These must not be confused with the actual electronic gap of a molecule defined as the difference between the ionization potential and the electron affinity (see section 2.5.3).

- **Choice of the functional**. Many works by different authors have shown that different functionals can return very different values of the energy gaps for a given compound (see, for example, [319, 318]). The expected order of the various spin states is sometimes not even correctly reproduced. Furthermore, while a functional can be found to predict reasonable values for the gaps of some Fe^{2+} compounds, it can clearly fail to describe correctly others, even at a qualitative level. Despite the lack of common conclusions about the ability of each functional to describe SC molecules, some general trends, that are common to functionals belonging to the same "class", can be recognized. First, *LSDA functionals tend to stabilize the LS state.* This is due to the underestimation of the exchange energy. Second, *hybrid functionals tend to favor HS respect to LS states.* Reiher pointed out that the amount of HF exchange in many hybrid functionals is too large to predict correct energy gaps [321, 320]. He then proposed, for example, a re-parametrization of the B3LYP functional, called B3LYP*, which includes only 15% of the HF exchange (in contrast, the standard version of the B3LYP functional, mentioned in chapter 2, includes 20% of HF exchange). Although B3LYP* is believed to give satisfactory results for some transition metal compounds and has been widely used, it fails in describing the correct spin state of others. It was then suggested that a further reduction of HF exchange could be needed [320, 322]. In contrast, the amount of HF exchange in B3LYP was judged insufficent for the small ions $[Fe(H_2O)_6]^{2+}$ and $[Fe(NH_3)_6]^{2+}$. For these systems it has been argued that PBE0, which includes up to 25% of HF exchange, gives more satisfactory results [328, 329]. In practice, for each compound, the amount of exact exchange can be varied to fit the desired value for the gaps, but no "universally good choice" has been identified so far. Furthermore, it is important to remark that, even when an hybrid functional is found to return values for the energy gaps, that are considered satisfactory, it might not be the optimal functional to describe other molecular properties. Finally GGA and meta-GGA functionals "stay in the middle" and results depend both on the compounds and on the conditions that each functional satisfies by construction. Among them, we must mention the OLYP GGA functional, which was claimed to perform quite well [322, 328, 329].

- **Basis set**. DFT calculations for SC molecules are usually performed using Quantum Chemistry codes, where the wave-functions are expanded either in Gaussian or in Slater-type orbitals. In many cases, the values of the energy gaps depend substantially on the choice of the basis sets and on how extended

they are [324]. Although this is a second order problem compared to the correct choice of the functional, it has to be kept in consideration. In principle, the use of plane-wave codes could solve this problem, but, in practice, plane-wave calculations which use periodic boundary conditions, are computationally very expensive. Indeed a large number of plane-waves is needed as the electronic density is concentrated in a small fraction of the total volume of the supercell. Furthermore very large supercells are usually required. This is due to the fact that SC complexes are often double-positive ions. Therefore a negatively charged background must be introduced in order to preserve the neutrality of the supercell and avoid that the energy diverges. The energy calculated in this way approaches then the one for an isolated system only in the limit of large supercell and, unfortunately, this convergence is slow. Although corrections to the expression of the computed energy have been proposed [325], this effect can be properly accounted for only by considering large supercells and by performing various calculations for supercells of different sizes.

- **Geometry optimization in vacuum and temperature**. While DFT calculations and geometry optimizations are usually carried out for molecules in the "gas phase" at zero temperature, the results are compared with X-ray data for single crystals at a finite temperature. The lack of experimental results for the "gas phase"[2] does not allow then a clear assessment of the quality of the DFT relaxation. Furthermore, each class of functionals returns different metal-ligands bond-lengths. Usually, LSDA functionals give shorter bonds than hybrid functionals, while the GGAs values are in between these two extremes. Although these differences are usually quite small, less then 0.1 Å (to be compared to an average bond-length of about 2 Å and 2.2 Å respectively for LS and HS state), they might strongly affect the electronic properties. Indeed a very delicate balance between crystal field and Hund's coupling establishes the spin state and it can be drastically altered by small errors in the predicted geometry.
  Some authors [322] have carried out DFT studies, which try to include the effect of temperature. The results could then be compared directly to experiments. However these simulations are quite involved, requiring the calculation of the Gibbs free energy, and we have doubts about their reliability as many crystal-related effects, explained in the following point, are discarded.

[2]Experimental data for SC molecules in the "gas phase" could be obtained through the matrix isolation technique [330] (i.e. by trapping SC molecules in a frozen noble gas, for example argon, referred to as a "matrix"). However we are not aware of any study regarding this.

- **Role of lattice and solvent**. As already explained, experiments are usually performed for single-crystals. The lattice, not only, imposes a constraint on the geometry of the single molecules, but also provides a complex electrostatic environment, which is usually not taken into account in DFT simulations. Indeed, SC molecules are usually double positive-charged ions, which are surrounded by counterions in liquid solutions and crystals. Neither the crystal-packing-related-effects nor the electrostatic perturbations have been extensively considered so far in electronic structure calculations. However, they are likely to play a primary role in determining some of the reported electronic and magnetic properties. Therefore the crystal environment can drastically alter the energy gaps. This effect has been suggested also by some of the very few theoretical works, which try to analyze these issues [326, 327]. Furthermore, the critical temperatures and hysteresis loops are experimentally found to depend largely on the counterions and on the functional groups attached to the molecules.
  Finally, the inter-molecule interactions in crystals have usually dispersive nature. Unfortunately they are either not described or badly-described by most of the popular functionals and DFT studies of molecular crystals are usually not fully reliable.

Although this list of problems reminds us how far theorists are from an accurate description of the electronic structure of SC molecules (and transition metal complexes, in general), some important conclusions can be reached once the correct work-strategy is identified. Furthermore, DFT can already be employed to safely extract qualitative and, may be even quantitative, information about properties of SC molecules, if some caution is used. Let us illustrate this point. Firstly, instead of using atomic positions optimized by DFT, experimental geometries, refined through the relaxation of the hydrogen coordinates, must be used [318], when the quality of the DFT predictions has not been assessed. Secondly, we can chose a functional which predicts the expected lowest energy state of each experimental geometry and reproduces, at least qualitatively, the vertical energy gaps. The simulations perfomed with this functional loose then the status of fully *ab-initio* becoming, in spirit, model calculations. Nevertheless they can still provide some valuable results. Thirdly and most importantly, if we aim at extracting fully *ab-initio* electronic properties, it will be likely to identify a series of quantities, which are almost functional-independent. For example, the DOG, defined in Eq. (6.5), has already been demonstrated to be one of such quantities [318]. Indeed it depends only on the shape of the PESs for the HS and LS state, which is believed to be well reproduced by most of the functionals. The large spread in the values of

the gaps, predicted by different functionals, may be due just to relative rigid shifts of the HS and LS PESs. Interestingly, the DOG_2 [defined in Eq. (6.6)] was also found to depend weakly on the functional. This observation is somehow surprising, but it was suggested to be related to the fact that the main source of error in the evaluation of the gaps might come from the not accurate enough description of electronic correlation effects in the transition metal atom. If this argument is correct, systematic errors in Eq. (6.6) will cancel out when two compounds, which contain both an Fe ion, are considered.

Although, we have pointed out how "state of art" DFT calculations can be performed for SC molecules despite their intrinsic limitations, a massive improvement in the theoretical modelling needs to be reached in order to achieve a full understanding of the interesting physics and chemistry of these systems. The main step in this direction consists evidently in providing a detailed assessment of the performances of the various functionals. As pointed out by Fouqueau et al. [328, 329], because of the lack of experimental data for molecules in the "gas phase", this needs to be done by comparing the DFT results to those of highly accurate *ab-initio* calculations, which are able to return benchmark values for gaps, metal-ligands bond-lengths and PESs.

6.4 Electronic structure calculations for small Fe^{2+} complexes

As we have clearly pointed out above, very accurate *ab-initio* calculations must provide the benchmark data set for testing the performaces of DFT when describing the electronic and magnetic properties of SC molecules and, more in general, transition metal complexes. Therefore, in this section, we compare systematically several results of DMC simulations to those of DFT for a few selected molecules. Unfortunately, such a systematic investigation, requires a large use of computational resources so that it can not be performed for molecules containing tens of atoms. We have then focused on the ions $[Fe(H_2O)_6]^{2+}$, $[Fe(NH_3)_6]^{2+}$ and $[Fe(NCH)_6]^{2+}$, which are shown in Fig. 6.3. These are small enough to allow several DMC calculations to be performed at a reasonable computational cost and, more importantly, the study of their electronic structure presents all the problems mentioned above. Furthermore, according to the spectrochemical series [331], which places ligands in order of increasing ligand field

$$I^- < Br^- < Cl^- < S^{2-} < N_3^- < F^- < OH^- < O^{2-} < H_2O < NH_3 < CN^- < CO\,, \tag{6.7}$$

$[Fe(H_2O)_6]^{2+}$, $[Fe(NH_3)_6]^{2+}$ and $[Fe(NCH)_6]^{2+}$ have a different ligand field splitting with that of $[Fe(H_2O)_6]^{2+}$ being the smallest and that of $[Fe(NCH)_6]^{2+}$ the largest[3]. Their detailed study can then reveal trends and whether DFT calculations are plagued by systematic errors. We are also performing some simulations for the $[Fe(CO)_6]^{2+}$ ion, which is predicted to have a even larger crystal field-splitting than that of $[Fe(NCH)_6]^{2+}$. This is then a stable LS complex. However we have decided not to include a discussion of such an on-going work in this thesis.
The results of our DFT calculations are always compared with some results extracted from the literature in order to verify their correctness and, moreover, to stress how quantitative predictions depends strongly on both functionals and basis sets. We also include some data from the literature obtained through wave-function-based methods (CASSCF etc.). We will comment on these and compare them with our DMC results.

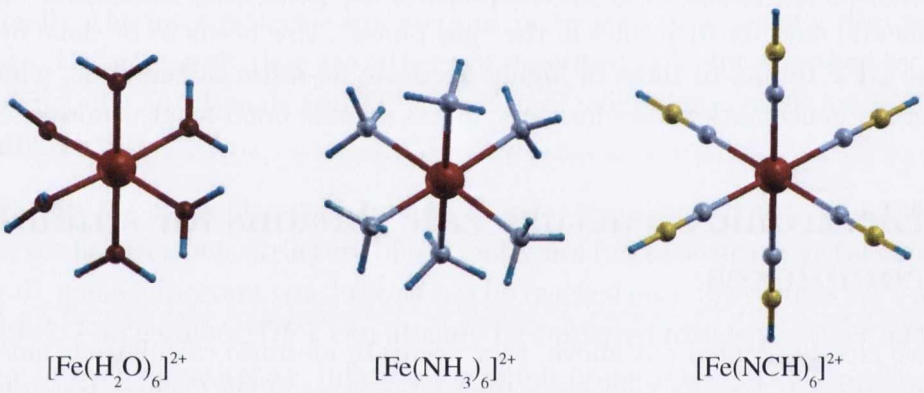

Figure 6.3: The cations $[Fe(H_2O)_6]^{2+}$, $[Fe(NH_3)_6]^{2+}$ and $[Fe(NCH)_6]^{2+}$. Color code: C=yellow, O=red (small sphere), Fe=red (large sphere), N=grey, H=blue.

6.4.1 Computational details

DFT calculations are performed with the NWCHEM code. We use several functionals belonging to different "classes": 1) the default LDA functional, i.e. the Vosko-Wilk-

[3]The ion $[Fe(NCH)_6]^{2+}$ does not exist, but it is often used as a model system in the quantum chemistry literature. It is often predicted to have the adiabatic energy gap of the same order of magnitude of that of SC molecules. In contrast $[Fe(H_2O)_6]^{2+}$ and $[Fe(NH_3)_6]^{2+}$ are known be in a stable HS state.

Nussair parametrization of the Cepereley Alder QMC results for the homogeneous electrons gas, 2) the GGA BP86 functional (mentioned in section 2.5.5) and 3) the two hybrid functionals B3LYP and PBE0 (which were also introduced in section 2.5.5). We have chosen three different basis sets: 1) the 6-31G* basis set (basis set called A), 2) the LANL2DZ basis set and pseudopotential [332] for Fe combined with the basis set 6-31++G** for all other atoms (basis set B) and 3) the triple-zeta polarized basis set of Ahlrichs [333] (basis set C). Geometry optimizations are performed both with and without specifying the molecule point group. The optimizations carried out in these two ways usually return consistent results with bond-lengths differences, which are within ± 0.005Å. We always check that the phonon frequencies are all real so that the final geometries correspond to stable energy minima.

DMC calculations are performed by using the CASINO code. Time-steps of various sizes are used (typically $\Delta\tau = 0.0125, 0.005, 0.001$ a.u.) and energy differences are usually found to be converged with respect to time-step errors already for $\Delta\tau = 0.0125$ a.u. Calculations are performed by using Dirac-Fock pseudopotentials with the PLA (see section 2.6.4). For the ion $[Fe(NCH)_6]^{2+}$, DMC simulations with this approximation are found to be unstable as the number of walkers "explodes". Therefore we used the T-move scheme by Casula, which eliminates the need of the PLA and treats the non-local part of the pseudopotential in a way consistent with the variational principle (see the brief discussion in section 2.6.4). The simulations become then more stable. The single-particle orbitals of the trial wave function are obtained through (LDA) DFT calculations performed with the plane-wave (PW) code QUANTUM ESPRESSO. The same pseudopotentials used for the DMC calculations are employed. The PW cutoff is fixed at 300 Ry and the PW are re-expanded in terms of B-splines (see section 2.6.5). The B-spline grid spacing is $a = \pi/G_{\max}$, where $G_{\max}$ is the length of the largest vector employed in the PW calculations. Periodic boundary conditions are employed for the PW-DFT calculations and supercells as large as 40Å are considered. In contrast, no periodic boundary conditions are imposed for the DMC simulations.

DMC calculations are performed for the molecular geometries previously optimized by DFT. Therefore we can compare the DMC energies of molecular structures obtained by employing different functionals and basis sets. However, for each system, these energy differences are often smaller than the computed error bars. Only LDA returns systematically molecular geometries with much higher DMC energy than those obtained by using either GGA or hybrid functionals.

6.4.2 DFT Results

Functional	Basis set	d_{LS} (Å)	d_{HS} (Å)
LDA	A	1.917	2.052, 2.083, 2.057
BP86	A	1.985	2.152, 2.151, 2.111
BP86	B	2.02	2.174, 2.164, 2.132
BP86	C	2.01	2.161, 2.155, 2.125
B3LYP	A	2.005	2.152, 2.152, 2.111
B3LYP	B	2.003	2.146, 2.157, 2.112
B3LYP	C	2.029	2.172, 2.16, 2.137
PBE0	A	1.99	2.1, 2.145, 2.134
PBE0	B	2.013	2.168, 2.156, 2.129
PBE0	C	2.008	2.152, 2.147, 2.124

Table 6.1: Bond-lengths of $[Fe(H_2O)_6]^{2+}$ in the HS and LS, as calculated with various functionals and basis sets. Note that LDA calculations for the HS state did not coverge in the case of basis set B and C.

$[Fe(H_2O)_6]^{2+}$

The lower energy geometry of $[Fe(H_2O)_6]^{2+}$ is found to have C_i symmetry for both BP86 and hybrid functionals. This is consistent with the results by Pierloot et al. [334]. In contrast, by employing LDA, the geometry optimization hardly converges. We were able to obtain relaxed atomic positions for both the HS and LS states only by using the the basis set A and without specifying the molecule point group.
As expected from the above introductory discussion, the molecule in LS state has shorter metal-ligand bond-lengths than the molecule in HS state (by about 7%). However the details of the geometry depend on both the functional and the basis set. This can be clearly seen by inspecting Tab. 6.1, which reports a full list of the calculated Fe-O bond-lengths for both HS and LS. On the one hand, LDA overbinds as compared to GGA and hybrids. On the other hand, the basis set A tends to shrink the Fe-O bond-lengths when compared to the basis set B and C. Although the choice of the basis set does not affect the bond-lengths as drastically as the functional does, it greatly influences the geometry. The calculations with the basis set A return a quite large inclination (about 5 degrees) of the O-Fe-O axis with respect to the 90 degrees angle it forms with the equatorial plane of the molecule. Furthermore, for basis set A and B, either the axial waters, which form the ligands, move "in" and

Functional	Basis set	ΔE^{adia} (cm^{-1})	ΔE^{adia} (eV)
LDA	A	−3986	−0.494243
BP86	A	−8989	−1.11448
BP86	B	−8381	−1.0391
BP86	C	−8400	−1.0415
B3LYP	A	−11589	−1.43695
B3LYP	B	−11027	−1.36721
B3LYP	C	−11045	−1.36936
PBE0	A	−14670	−1.81894
PBE0	B	−15512	−1.92332
PBE0	C	−14045	−1.74143
LDA [329]		−3316/−3896	−0.411132/−0.483043
LDA [334]		−3365	−0.417207
BP86 [329]		−8985/−8798	−1.114/−1.09081
BP86 [334]		−9934	−1.23166
B3LYP [329]		−11514/−11465	−1.42755/−1.42148
B3LYP [334]		−11590	−1.43698
PBE0 [329]		−14676/−14504	−1.81959/−1.79827
PBE0 [334]		−16076	−1.99317

Table 6.2: Adiabatic energy gap, ΔE^{adia}, for the cation $[Fe(H_2O)_6]^{2+}$. The functional and the basis set used for the each calculation are indicated. We also report several values for ΔE^{adia} extracted from the literature. For these, the notation X/Y indicates that the value X and Y have been obtained by using the same functional, but different basis sets (we remind to the references for details).

the equatorial waters move "out" of their plane or viceversa. These results do not depend qualitatively on the functional. In contrast, all of the O-Fe-O angles are found to be equal to about 90 degrees and the distortion of axial waters disappears when calculations are carried out by using the basis set C.

Tab. 6.2 shows our calculated values for the adiabatic energy gaps (upper part) along with several results from the literature (bottom part)[4][5]. A positive (negative)

[4]Here we report the results from the references only for the functionals that we have considered in our study. However, in the original papers, calculations performed by using many more functionals (and even Hartree-Fock) are carefully described.

[5]Results are reported both in cm^{-1} and eV. This is because, in most of the quantum chemistry literature, energies are expressed in cm^{-1}, while the physics community generally prefers to use the eV.

energy means that the LS state has lower (higher) energy than the HS one. We can clearly see that, for a given functional, our results are of the same order of magnitude as those obtained by other authors. Furthermore, by comparing the values of the adiabatic energy gap obtained with different functionals, we can distinguish a clear trend, summarized through the series:

$$-\Delta E^{\text{adia}}(\text{LDA}) < -\Delta E^{\text{adia}}(\text{GGA}) < -\Delta E^{\text{adia}}(\text{B3LYP}) < -\Delta E^{\text{adia}}(\text{PBE0})\,. \quad (6.8)$$

Indeed LDA returns a small negative value of ΔE^{adia} (≈ -0.4 eV), BP86 increases its absolute value so that $\Delta E^{\text{adia}} \approx -1$ eV and, finally, the B3LYP and PBE0 adiabatic gap is found to be almost -2 eV.

Functional	Basis set	d_{LS} (Å)	d_{HS} (Å)
LDA	A	1.942	2.188, 2.162, 2.160
LDA	C	1.995	2.204, 2.201, 2.214
BP86	A	2.026	2.267, 2.254, 2.253
BP86	B	2.078	2.30, 2.295, 2.274
BP86	C	2.085	2.279, 2.302, 2.289
B3LYP	A	2.076	2.281, 2.281, 2.275
B3LYP	B	2.114	2.315, 2.296, 2.294
B3LYP	C	2.122	2.32, 2.308, 2.283
PBE0	A	2.05	2.254, 2.256, 2.256
PBE0	B	2.082	2.292, 2.277, 2.272
PBE0	C	2.093	2.284, 2.294, 2.263

Table 6.3: Bond-lengths of $[Fe(NH_3)_6]^{2+}$ in the HS and LS, as calculated with various functionals and basis sets. Note that the LDA calculations for the HS state did not coverge in the case of basis set B.

$[\mathbf{Fe(NH_3)_6}]^{2+}$

The optimized structure of ion $[Fe(NH_3)_6]^{2+}$, calculated either by BP86 or by hybrid functionals, has D_3 symmetry for the LS state. This is further lowered to C_2 for the HS state. Our results are again consistent with those of Pierloot et al. [334]. As in the case of $[Fe(H_2O)_6]^{2+}$, we were not able to find the relaxed atomic positions with LDA. Even when the geometry optimization procedure converges, like in the case of the basis set A and C, the minimum is found to be unstable. This is indicated by the

Functional	Basis set	ΔE^{adia} (cm^{-1})	ΔE^{adia} (eV)
LDA	A	8937	1.10808
LDA	C	7746	0.960477
BP86	A	195	0.0241676
BP86	B	708	0.087759
BP86	C	672	0.0834338
B3LYP	A	−5312	−0.658642
B3LYP	B	−4007	−0.496883
B3LYP	C	−4738	−0.587441
PBE0	A	−7695	−0.954114
PBE0	B	−7665	−0.950383
PBE0	C	−7117	−0.882454
LDA	[329]	8817/8187	−1.09317/−1.01506
LDA	[334]	7850/7772/7799	0.973276/0.963606/0.966953
BP86	[329]	241/790	0.0298802/0.0979476
BP86	[334]	−1781/−2099/−1920	−0.220816/−0.260243/−0.23805
B3LYP	[329]	−5260/−4978	−0.652157/−0.617194
B3LYP	[334]	−4920/−5706/−5064	−0.610002/−0.707454/−0.627856
PBE0	[329]	−7799/−7195	−0.966953/−0.892067
PBE0	[334]	−8636/−8807/−8793	−1.07073/−1.09193/−1.09019

Table 6.4: Adiabatic energy gap, ΔE^{adia}, for the cation $[Fe(NH_3)_6]^{2+}$. The functional and the basis set used for each calculation are indicated. We also report several values for ΔE^{adia} extracted from the literature. For these, the notation X/Y indicates that the value X and Y were obtained by using the same functional, but different basis sets. The notation $X/Y/Z$ for the results taken from ref. [334] stands for the values corresponding to the energy difference between the same LS state and three different HS states, that the authors were able to stabilize. This HS states are indicated as ${}^5A_1(D_3)$, ${}^5A(C_2)$, ${}^5B(C_2)$ in that work (see the reference [334] for details).

negative eigenvalues of some phonon modes. Nevertheless we report these results for completeness.

The molecule in LS state has shorter average Fe-ligand bond-lengths than the molecules in HS state (see Tab. 6.3). In contrast to the case of $[Fe(H_2O)_6]^{2+}$, the cation $[Fe(NH_3)_6]^{2+}$ does not show any strong deviation of the N-Fe-N axis with respect to the perpendicular to the equatorial plane for any combination of functionals and basis sets.

Tab. 6.4 shows several values for the adiabatic energy gaps either calculated by us or extracted from the literature. Once again these can be ordered according to the series (6.8). Here, the value of the LDA adiabatic energy gap indicates that $[Fe(NH_3)_6]^{2+}$ is LS. This result is even qualitatively incorrect as this cation is known to be stable in the HS state. BP86 also predicts the LS state as the lowest in energy, although the value of ΔE^{adia} is very small and probably very sensible to the exact details of the calculation. Note that, in contrast to our result and those by Fouqueau et al. [329], Pierloot et al. [334] obtained a negative value equal to about -0.2 eV by using BP86. Finally the hybrid functionals predict the ground state to be HS with $\Delta E^{\text{adia}} \approx -1$eV.

Functional	Basis set	d_{LS} (Å)	d_{HS} (Å)
LDA	C	1.854	2.066, 2.067, 2.11
BP86	C	1.917	2.171, 2.171, 2.155
B3LYP	C	1.974	2.206, 2.201, 2.201
PBE0	C	1.950	2.194, 2.181, 2.181

Table 6.5: Bond-lengths of $[Fe(NCH)_6]^{2+}$ in the HS and LS state as calculated with various functionals and for the basis sets C.

Functional	Basis set	ΔE^{adia} (cm^{-1})	ΔE^{adia} (eV)
LDA	C	19126.3	2.37135
BP86	C	8410.89	1.04282
B3LYP	C	−1667.48	−0.206741
PBE0	C	−3544.58	−0.439472

Table 6.6: Adiabatic energy gap, ΔE^{adia}, for the cation $[Fe(NCH)_6]^{2+}$ calculated with various functionals and the basis sets C.

$[Fe(NCH)_6]^{2+}$

The results for the ions $[Fe(H_2O)_6]^{2+}$ and $[Fe(NH_3)_6]^{2+}$ demonstrate that, although a good choice of the basis set might be important to predict accurately molecular structures, the values of the adiabatic energy gaps are mainly determined by the functional. Indeed, for a given functional, two adiabatic gaps, obtained with two different basis sets, differ at most by a few tens of meV. This has to be compared with the differences in the values predicted by different functionals, which can be of

the order of several hundreds meV. For the ion $[Fe(NCH)_6]^{2+}$ we have then decided to compare only calculations performed using the basis set C, which typically gives us lowest energies.

$[Fe(NCH)_6]^{2+}$ has perfect octahedral symmetry in the LS state. In contrast, the structure of the HS state is predicted to have D_{4h} symmetry by hybrid functionals and C_i symmetry by BP86.

As we did not find any reference to systematic DFT calculations for the adiabatic energy gap of this ion[6], we present only the results of our calculations (Tab. 6.6). Once again the data can be ordered according to the series (6.8). Now, the total energy of the LS state is at least 1 eV lower than that of the HS state for both LDA and BP86. In contrast PBE0 and B3LYP return the HS state as the most stable one and the absolute value of ΔE^{adia} is only a few hundreds meV.

System	Functional	ΔE^{ZPE} (eV)	ΔE^{ZPE} (cm^{-1})
$[Fe(H_2O)_6]^{2+}$	BP86	−0.08195	−661.05
$[Fe(H_2O)_6]^{2+}$	B3LYP	−0.09079	−732.234
$[Fe(H_2O)_6]^{2+}$	PBE0	−0.09308	−750.847
$[Fe(NH_3)_6]^{2+}$	BP86	−0.17413	−1404.58
$[Fe(NH_3)_6]^{2+}$	B3LYP	−0.16099	−1298.62
$[Fe(NH_3)_6]^{2+}$	PBE0	−0.17636	−1422.58
$[Fe(NCH)_6]^{2+}$	BP86	−0.16593	−1338.46
$[Fe(NCH)_6]^{2+}$	B3LYP	−0.15367	−1239.56
$[Fe(NCH)_6]^{2+}$	PBE0	−0.13846	−1116.86

Table 6.7: Energy difference between the phononic zero point energy of the HS and LS state calculated with the various functionals employed in this work (only results for the basis set C are shown).

Zero point phononic energies

So far we have focused only on the adiabatic energy gaps. However the expression for the internal energy difference, Eq. (6.2), contains also a contribution coming from the phononic zero point energies. Tab. 6.7 displays ΔE^{ZPE}, calculated by using the various functionals (results are shown only for the basis set C). ΔE^{ZPE} is always negative (i.e. the zero point energy of the HS state is lower than that of the LS state)

[6]Note that, Bolvin [335] obtained $\Delta E^{\text{adia}} = -0.20$ eV by using B3LYP and by imposing the O_h symmetry for both the HS and the LS state. This value is consistent with ours.

reflecting the weaker Fe-ligand bond of the HS state. Corrections to the total energy of the two states then always tend to stablilize the HS.
In contrast to the adiabatic energy gap, ΔE^{ZPE} is found to be almost functional independent. Indeed, for a given system, the difference between two values of ΔE^{ZPE} obtained with two different functionals, are never larger than 15 meV. This demostrates that the curvature of the PESs is usually very well reproduced by every functional. Therefore the spread in the predicted values of ΔE^{adia} should arise from the rigid shifts of the PES of one spin state with respect to that of another. This observation is consistent with the above mentioned results by Zein et al. [318], which indicates that the DOGs, defined by Eq. (6.5), do not depend on the choice of functional.

Method	Reference	ΔE^{adia} (cm^{-1})	ΔE^{adia} (eV)
CASSCF(6,5)	[328]	−23125	−2.86714
CASSCF(12,10)	[328]	−21180	−2.62599
corr-CASSCF(12,10)	[328]	−17892	−2.21833
CASPT2(6,5)	[328]	−21610	−2.6793
CASPT2(12,10)	[328]	−16185	−2.00668
corr-CASPT2(12,10)	[328]	−12347	−1.53083
SORCI	[328]	−13360	−1.65643
CASPT2(10,12)	[334]	−16307	−2.02181

Table 6.8: Value for the adiabatic energy gap for $[Fe(H_2O)_6]^{2+}$ calculated by using various wave-function methods (the references to the paper from which these values are extracted are given in the second column of table). The values indicated as corr-CASSCF and corr-CASPT denote respectively the CASSCF and CASPT values after having applied the empirical correction of the order of 4000cm^{-1} (see main text). Pierloot et al. [334] provides a very long list of results obtained by using different basis, geometries and symmetries. Here we report only the value that these authors indicate as the "best".

6.4.3 Wave-functions-based methods

Tabs. 6.8 and 6.9 summarize the results of calculations performed by wave-functions methods for the cations $[Fe(H_2O)_6]^{2+}$ and $[Fe(NH_3)_6]^{2+}$. Fouqueau et al. [328, 329] used the complete active space self-consistent field (CASSCF) method with second order perturbative correction (CASPT2). As observed by the authors themselves and by Pierloot et al. [334], these calculations used a too small basis for Fe. Indeed the results were plagued by a systematic error, estimated by considering the ^5D-

Method	Reference	ΔE^{adia} (cm^{-1})	ΔE^{adia} (eV)
CASSCF(12,10)	[329]	−20630	−2.55779
corr-CASSCF(12,10)	[329]	−16792	−2.08194
CASPT2(12,10)	[329]	−12963	−1.60721
corr-CASPT2(12,10)	[329]	−9125	−1.13136
SORCI	[329]	−10390/−11250	−1.2882/−1.39482
CASPT2(12,10)	[334]	−7094	−0.879544

Table 6.9: Value for the adiabatic energy gap for $[Fe(NH_3)_6]^{2+}$ calculated by using various wave-function methods (the references to the paper from which these values are extracted are given in the second column of table). The values indicated as corr-CASSCF and corr-CASPT denote respectively the CASSCF and CASPT values after having applied the empirical correction of the order of 4000cm^{-1} (see main text).

Method	Reference	ΔE^{adia} (cm^{-1})	ΔE^{adia} (eV)
CASPT2(10,6)	[335]	−9033.41	−1.12
CASPT2(10,10)	[335]	−7662.26	−0.95

Table 6.10: Value for the adiabatic energy gap for $Fe(NCH)_6$ calculated using CASPT method.

^1I splitting of the free Fe^{2+} ion. An empirical correction of the order of $4000\,\text{cm}^{-1}$ was then introduced. In the same works, results obtained by spectroscopy-oriented configuration-interaction (SORCI), were also reported. These were stated not to require any empirical correction.

We can observe that the "corrected"-CASPT2 adiabatic energy gaps are slightly smaller than those calculated by SORCI. In contrast, Pierloot et al. [334] performed calculations with basis sets of larger size. For $[Fe(NH_3)_6]^{2+}$, their best CASPT2 adiabatic gap agrees fairly well with the corrected-CASPT2 and SORCI results. However for $[Fe(H_2O)_6]^{2+}$, they found a significantly larger (in absolute value) ΔE^{adia}. In any case, although these calculations are an improvement compared to the previous ones, the basis sets are probably still too small. This is clearly demonstrated by the still quite large error (about $500\,\text{cm}^{-1}$) on the atomic ^5D-^1I excitation energy.

Concerning the geometry, we must note that, while Fouqueau et al. [328, 329], obtained larger Fe-ligands bond-lengths with CASSCF than with GGA and hybrid functionals (about 0.05Å for both HS and LS), the CASPT2 results by Pierloot et al. [334] suggest that all flavours of DFT (but LDA) might systematically overestimate them.

Finally Tab. 6.10 displays some CASPT2 results for the $[Fe(NCH)_6]^{2+}$ ion obtained by Bolvin [335]. Here the geometry was forced to have octahedral symmetry for both the HS and LS state. The Fe-ligand bond-length was found to be 1.92 Å and 2.14 Å respectivelly for the LS and the HS state.

Details DFT geom. opt.	$\Delta\tau$ (a.u.)	E_{LS}(eV)	E_{HS}(eV)	ΔE^{adia} (eV)
func. BP86 (Basis C)	0.0125	−6127.211(9)	−6129.720(8)	−2.51(1)
func. BP86 (Basis C)	0.005	−6127.218(9)	−6129.90(2)	−2.65(1)
func. BP86 (Basis C)	0.001	−6127.54(9)	−6130.19(4)	−2.65(9)
func. B3LYP (Basis C)	0.0125	−6127.09(2)	−6129.74(1)	−2.65(2)
func. B3LYP (Basis C)	0.005	−6127.36(1)	−6129.89(2)	−2.54(1)
func. B3LYP (Basis C)	0.002	−6127.44(3)	−6130.01(2)	−2.57(4)
func. B3LYP (Basis C)	0.001	−6127.5(1)	−6130.10(2)	−2.6(1)
func. PBE0 (Basis C)	0.125	−6127.220(9)	−6129.804(8)	2.58(1)
func. PBE0 (Basis C)	0.005	−6127.44(2)	−6129.94(2)	−2.50(3)
func. PBE0 (Basis C)	0.001	−6127.66(6)	−6130.18(4)	−2.52(7)

Table 6.11: DMC total energy for the LS state, DMC total energy for the HS state and adiabatic energy gap of the ion $Fe(H_2O)_6]^{2+}$. The molecular structures were optimized by DFT using the functionals and the basis sets listed in the first column. The time-steps chosen for the DMC simulation are also indicated. Differences in energy are well converged for $\Delta\tau = 0.005$ a.u..

6.4.4 DMC results and discussion

Tabs. 6.11, 6.12 and 6.13 display the DMC total energies[7] of the HS and LS states of the ions $[Fe(H_2O)_6]^{2+}$, $[Fe(NH_3)_6]^{2+}$ and $[Fe(NCH)_6]^{2+}$. The molecular geometries were obtained by optimization with DFT and both, the functional and the basis set used, are indicated in the first column. We can note that, in most cases, the DMC energies have an error bar not small enough to establish firmly which functional returns the lowest energy structure for a given complex and spin state[8]. However, the size of these errors represent an upper bound to the value of the energy differences. We can then argue that, according to DMC, the molecular geometries predicted with

[7]Note that the notation $E = -5957.57(1)$ eV stands for $E = (-5957.57 \pm 0.01)$ eV

[8]Only the molecular structures predicted with LDA have systematically higher energies than those predicted with GGA or hybrid functionals. This is not surprising since the calculation of the phonon modes reveals that these structures are not even associated to a stable minimum of the LDA total energy.

Details DFT geom. opt.	$\Delta\tau$ (a.u.)	E_{LS}(eV)	E_{HS}(eV)	ΔE^{adia} (eV)
func. LDA (Basis C)	0.0125	−5234.92(1)	−5236.93(1)	−2.01(1)
func. LDA (Basis C)	0.005	−5235.33(2)	−5237.17(1)	−1.84(2)
func. LDA (Basis C)	0.001	−5235.69(5)	−5237.36(5)	−1.67(7)
func. BP86 (Basis C)	0.0125	−5235.56(1)	−5237.162(9)	−1.60(1)
func. BP86 (Basis C)	0.005	−5235.78(1)	−5237.37(1)	−1.58(1)
func. BP86 (Basis C)	0.001	−5235.98(3)	−5237.55(5)	−1.57(5)
func. B3LYP (Basis C)	0.0125	−5235.516(9)	−5237.15(1)	−1.63(1)
func. B3LYP (Basis C)	0.005	−5235.77(1)	−5237.36(1)	−1.59(1)
func. B3LYP (Basis C)	0.001	−5236.01(3)	−5237.59(4)	−1.58(5)
func. PBE0 (Basis B)	0.0125	−5235.60(1)	−5237.21(1)	−1.61(1)
func. PBE0 (Basis B)	0.005	−5235.89(2)	−5237.40(2)	−1.51(2)
func. PBE0 (Basis B)	0.001	−5236.14(3)	−5237.67(9)	−1.53(9)
func. PBE0 (Basis C)	0.0125	−5235.57(1)	−5237.133(8)	−1.56(1)
func. PBE0 (Basis C)	0.005	−5235.88(2)	−5237.37(1)	−1.49(1)
func. PBE0 (Basis C)	0.001	−5236.10(3)	−5237.60(2)	−1.50(4)

Table 6.12: DMC total energy for the LS state, DMC total energy for the HS state and adiabatic energy gap of the ion $[Fe(NH_3)_6]^{2+}$. The molecular structures were optimized by DFT using the functionals and the basis sets listed in the first column. The time-steps chosen for the DMC simulation are also indicated. Differences in energy are well converged for $\Delta\tau = 0.005$ a.u..

Details DFT geom. opt.	$\Delta\tau$ (a.u)	E_{LS}(eV)	E_{HS}(eV)	ΔE^{adia} (eV)
func. BP86 (Basis C)	0.0125	−5957.57(1)	−5959.30(1)	−1.73(2)
func. BP86 (Basis C)	0.005	−5957.57(2)	−5959.32(2)	−1.75(3)
func. B3LYP (Basis C)	0.0125	−5957.94(1)	−5959.32(1)	−1.38(2)
func. B3LYP (Basis C)	0.005	−5957.96(2)	−5959.33(2)	−1.37(3)
func. PBE0 (Basis C)	0.0125	−5957.94(1)	−5959.291(9)	−1.35(1)
func. PBE0 (Basis C)	0.005	−5957.95(3)	−5959.30(1)	−1.35(3)

Table 6.13: DMC total energy for the LS state, DMC total energy for the HS state and adiabatic energy gap of the ion $[Fe(NCH)_6]^{2+}$. The molecular structures were optimized by DFT using the functionals and the basis sets listed in the first column. The time-steps chosen for the DMC simulation are also indicated. Differences in energy are well converged for $\Delta\tau = 0.0125$ a.u..

BP86, B3LYP and PBE0 differ, at most, by few tens of meV.
In contrast, adiabatic energy gaps are calculated with great confidence as these are found of the order of the eV for all of the ions (right-most column in Tabs. 6.11, 6.12

and 6.13). DMC values must be then compared to those calculated previously by DFT. On the one hand, LDA and BP86 do not often return even the correct sign of ΔE^{adia} and predict the LS state as the stable one. On the other hand, hybrid functionals return always the HS state lower in energy than the LS one, but the absolute value of ΔE^{adia} is largely underestimated. However, we can observe an interesting fact: in all three cases, the B3LYP adiabatic gap is smaller (in absolute value) than the PBE0 one by about 0.3 eV and this, in turn, is smaller (in absolute value) than the DMC one by a value between 0.6 and 0.9 eV. These regularities in the behavior of the different functionals, suggest a systematic error within DFT. Furthermore, we can argue that this error decreases by increasing the amount of HF exchange in the functional (we remind that B3LYP includes 20% of exact exchange while PBE0 25%). Based on this observation we have performed further DFT calculations by using the Becke "half and half" functional (Becke-HH) [336], in which the amount of HF exchange is increased up to 50%[9] . The calculated adiabatic energy gaps for all

System	ΔE^{adia} (cm^{-1})	ΔE^{adia} (eV)
$[Fe(H_2O)_6]^{2+}$	-18223	-2.25937
$[Fe(NH_3)_6]^{2+}$	-13556	-168077
$[Fe(NCH)_6]^{2+}$	-12029	-1.491484

Table 6.14: Adiabatic energy gap, ΔE^{adia}, for the three cations $Fe(H_2O)_6]^{2+}$, $[Fe(NH_3)_6]^{2+}$ and $[Fe(NCH)_6]^{2+}$ calculated by using the Becke "half and half" functional (only results for the basis set C are shown).

of the three ions are displayed in Tab. 6.14. We note that these values agree fairly well with those calculated with DMC. These results suggest that the failure of DFT in describing transition metal complexes can be related to a drastic underestimation of the exchange energy[10]. However we are aware that our study does not currently allows to draw any firm conclusions as, in order to do that, a systematic comparison with a much larger set of molecules would be required. In particular, so far, we have focused on ions, which are stable HS complexes. In contrast, the agreement between the Becke-HH functional and the DMC might not hold for systems, which either have

[9]Note that, in the NWCHEM code, only an approximate version of this functional is currently implemented (the details can be found in the documentation [337]).

[10]Hartree Fock predicts too large adiabatic energy gaps (about as twice as the size returned by DMC) [334]. This seems to indicate that, while a large fraction of exact exchange must be used, correlation effects must be also described accurately in order to predict correctly the properties of transition metal complexes.

a LS ground state or which undergo a SC transition. This will be the subject of further studies.

Finally, wave-function based methods return adiabatic energy gaps of the same order of magnitude of those predicted by DMC. However a direct comparison of the values turns out to be complicated because the CASSCF and the CAST2 methods depend quantitatively on the basis sets used and on the orbitals, which enter in the active space. The adiabatic energy gaps of the ions $Fe(H_2O)_6]^{2+}$ and $[Fe(NH_3)_6]^{2+}$calculated with CASPT2 by Fouqueau et al. [328, 329] agree fairly well with our DMC ones. The empirical correction discussed above worsens the agreement and the SORCI results do not agree quantitatively with ours either. A deep understanding of these differences is outside our actual capabilities. However we would like to remark once again the common conclusion reached by both wave-functions based methods and DMC: the HS state of these three complexes is always more stable than the LS one by more than 1 eV.

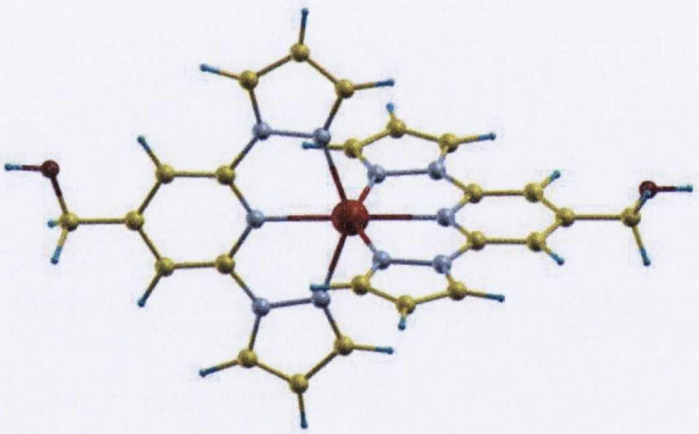

Figure 6.4: The cationic unit $[FeL_2]^{2+}$. Color code: C=yellow, O=red (small sphere), Fe=red (large sphere), N=grey, H=blue.

6.5 *Ab-initio* study of the molecule $[FeL_2](BF_4)_2$

After having investigated a few "model" Fe^{2+}-complexes, we now discuss some results of DFT and DMC calculations for the molecule $[FeL_2](BF_4)_2$ (L=2,6-dypirazol-1-yl-4-hydroxymethylpyridine) [338]. This consists of a cation (shown in Fig. 6.4), which

	d_{LS} (Å)	d_{HS} (Å)
Exp.	1.909, 1.991, 1.912, 1.985, 1.980, 1.992	2.105, 2.163, 2.103, 2.160, 2.170, 2.153
B3LYP	1.933(2), 2.011(4)	2.185(2), 2.218(2), 2.222(2)

Table 6.15: Experimental (first line) and calculated (second line) Fe-N bond-lengths for the cation $[FeL_2]^{2+}$. The geometry optimization (in "vacuum") was performed by using the B3LYP functional and the basis set C. For the data in the second line, we report in bracket the number of bonds of a given length.

Method	$\Delta E^{\text{vert}}(r_{LS})$ (eV)	$\Delta E^{\text{vert}}(r_{HS})$ (eV)	ΔE^{adia} (eV)
LDA	2.650	0.032	2.622
BP86	2.448	0.012	2.11
B3LYP	1.650	−0.620	0.691
PBE0	1.120	−1.119	0.321
Becke-HH	0.511	−1.88	−0.989
DMC ($\Delta\tau = 0.0125$ a.u)	0.65(3)	−1.88(9)	−0.32(4)
DMC ($\Delta\tau = 0.005$ a.u)	0.65(3)	−1.87(7)	−0.36(6)

Table 6.16: Adiabatic and vertical energy gaps for the cation $[FeL_2]^{2+}$ calculated with DFT and DMC. The experimetal molecular structure inferred by x-ray measurements was used.

$\Delta\tau$ (a.u.)	geom.	$E_{LS}(r_{LS})$(eV)	$E_{HS}(r_{LS})$(eV)	$E_{LS}(r_{HS})$(eV)	$E_{HS}(r_{HS})$ (eV)
0.0125	exp.	−10939.91(2)	−10939.26(2)	−10938.34(2)	−10940.27(2)
0.005	exp.	−10940.59(2)	−10939.94(2)	−10939.01(2)	−10940.89(3)
0.0125	B3LYP	−10951.21(2)	−10950.96(3)	−10949.80(4)*	−10952.28(4)*
0.005	B3LYP	−10951.88(3)	−10951.62(4)	−10950.51(3)	−10953.07(3)

Table 6.17: DMC energies of the different spin states of the cation $[FeL_2]^{2+}$ (see Fig.6.2 for the definition of the various quantities). Unfortunately we incurred in numerical stability problems when we calculated $E_{HS}(r_{LS})$ and $E_{HS}(r_{HS})$ for the B3LYP geometries and for time-steps $\Delta\tau = 0.0125$ (numbers marked by a star). For these cases, new calculations are being performed by using improved algorithms.

has the Fe atom almost octahedrally coordinated to six N atoms and two counter ions BF_4, which are weakly bounded through hydrogen bonds. The crystal has a monoclinic unit cell containing four formula units. Experiments, performed on single-crystals, have shown that, by lowering the temperature, this molecule undergoes an abrupt HS to LS transition at 271 K with almost no-hysteresis. The spin transition

Functional	$\Delta E^{\text{vert}}(r_{LS})$ (eV)	$\Delta E^{\text{vert}}(r_{HS})$ (eV)	ΔE^{adia} (eV)
B3LYP	1.538	−1.233	0.012
DMC ($\Delta\tau = 0.0125$ a.u)	0.25(4)	−2.48(6)	−1.07(4)
DMC ($\Delta\tau = 0.005$ a.u)	0.26(5)	−2.57(4)	−1.19(4)

Table 6.18: Adiabatic and vertical energy gaps for the cation $[FeL_2]^{2+}$ calculated with B3LYP and DMC. The molecular structure optimized with B3LYP was used.

is accompanied by a decrease in the metal-ligand bond-lengths of about 0.2 Å (see Tab. 6.15). The metastable HS state can also be reached by exploiting the LIESST effect.

DFT and DMC calculations are performed according to the details given in the previous section. As the choice of the basis set does not influence drastically the DFT results, these will be shown only for the basis set C. Although we focus on the cationic unit in the gas phase, we firstly consider the HS and LS geometries inferred from crystallographic measurements. We will then compare the results for this case to those obtained by optimization with the hybrid functional B3LYP.

Tab. 6.16 reports the vertical and the adiabatic energy gaps calculated with DFT and DMC. We analyze firstly the DFT results and note that the ground state of the molecule is predicted to be LS by every functional (but the Becke-HH functional, whose results will be discussed later). However, the series (6.8) is, once again, respected. Here, LDA and BP86 overestimate the energy of the HS state so much that even $\Delta E^{\text{vert}}(r_{HS})$ is predicted to be positive. This is clearly an unphysical result as it would imply that both the ground state and the metastable state of lowest energy would be LS. In contrast, the hybrid functionals return the correct sign of the vertical gaps.

We now compare the DFT gaps with those calculated with DMC. If we assume that DFT is affected by the same systematic error discussed above, the PBE0 adiabatic energy gap should be corrected by a value between −0.6 and −0.9 eV in order to achieve a fairly good agreement with the results of DMC. This is indeed what happens as $\Delta E^{\text{adia}}(\text{DMC}) \approx \Delta E^{\text{adia}}(\text{PBE0}) - 0.6\,\text{eV}$ [which also implies $\Delta E^{\text{adia}}(\text{DMC}) \approx \Delta E^{\text{adia}}(\text{B3LYP}) - 0.9\,\text{eV}$]. Furthermore we also find that $\Delta E^{\text{vert}}(r_{HS})(\text{DMC}) \approx E^{\text{vert}}(r_{HS})(\text{PBE0}) - 0.6\,\text{eV}$ and $\Delta E^{\text{vert}}(r_{LS})(\text{DMC}) \approx E^{\text{vert}}(r_{LS})(\text{PBE0}) - 0.6\,\text{eV}$. These results strongly suggest that most of the observations discussed above, are valid for "real" Fe^{2+} complexes as well as for "model" Fe^{2+} complexes. However, we note that, in this case, the Becke-HH functional largely over-stabilizes the HS state

as compared the the LS state resulting in an adiabatic energy gap of almost -1 eV. This is in contrast with the results obtained for the three small cations, for which ΔE^{adia} calculated with the Becke-HH functional was found to agree fairly well with that calculated with DMC. Interestingly, however, the values of the vertical energy gaps returned by Becke-HH are remarkably similar to the DMC ones. Unfortunately, so far we have not been able to provide a satisfactory explanation for these results.
After optimizing the HS and LS molecular structures in vacuum with B3LYP, the Fe-N bonds elongate slightly as compared to the experimental values and the molecule becomes more symmetric (see Tab. 6.15). B3LYP returns the HS and LS optimized structure lower in energy than the experimental ones of respectively 12.791 eV and 11.656 eV. DMC calculations also confirm that the B3LYP structures are lower in energy than the experimental one (see Tab. 6.17). As shown by Tab. 6.18, the geometric relaxation strongly affects the value of the adiabatic and vertical energy gaps. On the one hand, ΔE^{adia}(B3LYP) is now equal to only 0.012 eV. On the other hand, ΔE^{adia}(DMC) becomes more negative and the HS state in predicted to be more stable than the LS state by more than 1 eV.
So far, we have mainly presented the data without discussing their physical implications and relevance. However our DMC calculations lead to unexpected results, which provide new insight into the phenomenology of Fe^{2+} complexes: *notably, the ground state of the molecule in the gas phase is predicted to be HS.* Although this result, at first glance, seems to contradict the experimental reports about the spin transition, it does not. Indeed, we believe that the spin crossover is not a single-molecule effect, but it strongly depends on the the crystalline environment the molecule is embedded in. As we have already mentioned, the crystal affects the molecule mainly in two ways. Firstly, it provides an effective constraint to the molecular structure, which then turns out to be different from that of the gas phase. Secondly, it generates a complex electrostatic environment around the molecule. On the one hand, by comparing our results for the molecule with the experimental structure to those for the molecule with the optimized structure, we understand how a small contraction of the Fe-ligand bonds and the reduction of the molecular symmetry drastically decrease the absolute value of the adiabatic energy gap. On the other hand, Kepeneckian et al. [326, 327] have shown how the Madelung fields, which act on a molecule embedded in a crystal, can induce a rather large shift in the relative position of the HS and LS PESs. This can even result in a change of the nature of ground state. These two contributions can then combine to stabilize the LS state of the molecule in the crystal and to tune the value of the adiabatic gap so that it lies within the energy range re-

quired to observe the spin transition. Although a quantitative demonstration of this argument requires further investigations (and computational effort!), we can already provide a very rough quantitative argument in support of it. Indeed by adding the approximate estimate of the adiabatic energy gap for the molecule with experimental structure ($\Delta E^{\text{adia}} \approx -0.3$ eV) to the approximate estimate of the relative energy shift of the HS state with respect to the LS state due to the Madelung fields (about 0.5 eV [327]), we obtain an adiabatic energy gap for the molecule in the crystal of the order of 0.2 eV. This value is positive, meaning a LS ground state, and of the order of magnitude that is expected for typical SC molecules (see reference [322] and references therein).
In conclusion, the two main contributions of our study about SC complexes are, so far, the following:

1) We were able to show that the DFT predictions of the vertical and adiabatic energy gaps of Fe^{2+} complexes are plagued by a systematic error. As this error does not seem to depend strongly on the nature of the ligands, it is likely to originate from an inadeguate description of electronic exchange and correlation effects in the Fe ion. In case of the hybrid functionals we were able to give a rough estimate of this error.
   We remark that these observations have been possible because we have not tried to benchmark DFT data for molecules in the gas phase with experimental results, which refer to molecules in crystals and solutions. Instead we compared the energy gaps predicted by DFT with those calculated with DMC, the most accurate electronic structure method that we had available.
   In future, this investigation will be carried on by systematically enlarging the set of molecules studied so that a much clear assessment of the failures of the various DFT functionals can be performed. We also hope that a better understanding of the problem, will lead to the identification and to the development of a functional suitable for the description of Fe^{2+} complexes.

2) We were able to obtain a few results supporting the hypothesis that the spin-crossover transition is not a property of the single-molecule, but of the molecule embedded in a crystalline environment. We are aware that a much more detailed study is needed in this direction and this will be the subject of further research.

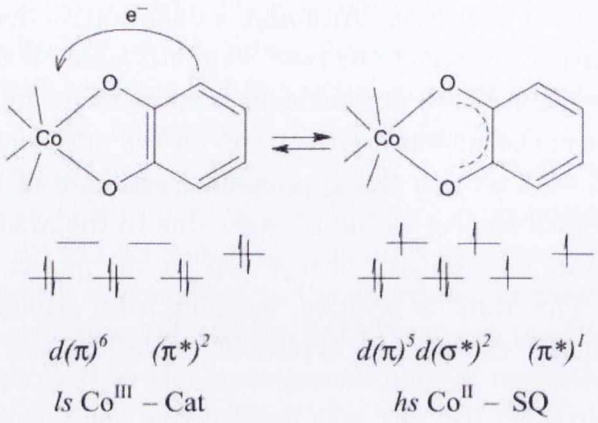

Figure 6.5: Scheme illustrating the basic mechanism for the VTI (figure extracted from reference [96]).

6.6 Co-dioxolene

Co-dioxolene complexes are examples of molecular units, which show an interconversion between redox isomers [95, 96]. There are two key ingredients in such a class of molecules: the transition metal ion and the o-dioxolene group. In general, o-dioxolenes bind to metal atoms in three different oxidation states: di-negative catecholate (Cat), mono-negative semiquinonate (SQ) and neutral quinone (Q). Because of the low covalent character of the bond between o-dioxolene and Co, charge and spin are localized and the molecule maintains well defined oxidation states and magnetic moments. We can then observe the so called valence tautometic interconversion (VTI), which involves an intramolecular electron transfer from a coordinated dioxolene ligand, Cat, to the diamagnetic LS Co^{3+}, yielding a Co^{2+} coordinated to a SQ. The Co^{2+} is then generally reported in HS state with a large unquenced orbital contribution. The VTI process, which is schematically described in Fig. 6.5, is entropy driven similarly to the SC transition. Therefore it can be understood through Eq. (6.1) where the notation LS and HS now indicates the different isomers with LS Co^{3+} and HS Co^{2+}. Furthermore the VTI, in solid state, can also be induced by optical irradiation [339] through an effect essentially analogous to the LIESST. Very recently, it was also reported that this redox isomerism can be promoted by soft X-rays [341].

The strong interplay between charge transfer and spin transition naturally suggests that electric fields might be able to profoundly affect the molecule magnetic proper-

ties making o-dioxolenes particularly interesting systems for spintronics devices.
We will present here our study for the complex Co(Me_2tpa)(DBCat)](PF_6) (Me_2tpa=methil derivatives of tris(2-pyridylmethyl)amine, DBCat = 3, 5-di-*tert*-butylcatecolato)[340, 341], which consists of a cation, shown in Fig. 6.6, and a counter ion PF_6. Our results clearly points out how the VTI, with consequent spin crossover, could, in principle, be induced by a static electric field. Unfortunately, a reliable estimate of the critical field for the VTI is hard to achieve, because of the many issues related to the theoretical description of transition metal complexes. In contrast, we were able to show that quite modest fields (~ 0.05 V/Å) are enough for changing the VTI critical temperature by as much as 100 K. This result is, even quantitatively, more accurate and experimentalists have been trying to verify our predictions [315].

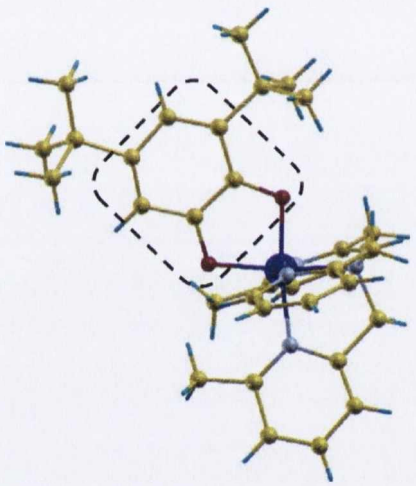

Figure 6.6: The cationic unit of Co-dioxolene complex investigated in this work. The entire cationic unit of the complex Me_2tpa=methil derivatives of tris(2-pyridylmethyl)amine, DBCat = 3, 5-di-*tert*-butylcatecolato is presented and the o-dioxolene is enclosed in the dashed box. Color code: C=yellow, O=red, Co=grey (large sphere), N=grey (small sphere), H=blue.

6.7 Electric field control of VTI in Co-dioxolene molecules

In order to gain phenomenological insights into the physics of the Co-dioxolene molecules by using DFT, we have decided to follow the work strategy discussed in

Isomer	d_{Co-O} (Å)	d_{Co-N} (Å)	E (eV)
LS Co^{3+}-Cat	1.883, 1.898	2.0, 1.947, 2.011, 2.022	0
HS Co^{2+}-SQ	2.004, 2.083	2.169, 2.160, 2.1474, 2.151	2.229
LS Co^{2+}-SQ	1.883, 1.898	2.0, 1.947, 2.011, 2.022	2.789

Table 6.19: Co-O (d_{Co-O}) and Co-N (d_{Co-N}) bond lengths for LS Co^{3+}-Cat and HS Co^{2+}-SQ as determined by X-Ray and used in our calculations. The last column reports the B3LYP total energy of the given configuration, calculated with respect to the total energy of LS Co^{3+}-Cat. LS Co^{2+}-SQ is a fixed spin configuration calculated at the molecular geometry of HS Co^{2+}-SQ.

section 6.3. Therefore we consider experimental molecular geometries determined by standard X-ray data analysis for single crystals (see Tab. 6.19) without further geometrical optimization except for the H atoms. We have then identified some functionals, which return an electronic structure at least qualitatively consistent with the main features observed experimentally. Finally, we try to obtain quantitative predictions by calculating quantities, which depend only on differences of differences of total energies and, as such, should be almost functional independent as systematic errors cancel out.

Achieving a correct description of the Co-dioxolene electronic structure is a difficult task already at a qualitative level. In fact we have to simultaneously assign the oxidation states of both the Co and the dioxolene group, the Co spin state and also, in the case of HS Co^{2+}-SQ, the magnetic exchange coupling between Co and SQ. GGA is inadequate since it largely overestimates the electronic coupling between the Co $3d$ shell and the molecular orbitals of both SQ and Cat. As this shortfall is rooted in the self-interaction error, like the incorrect description of holes self-trapping in oxides, we have decided to employ the ASIC scheme. So far ASIC has been used for molecules mainly in the context of electron transport problems [342] and this represents the first application to magnetic molecules. The ASIC electronic structure will be compared to that obtained with the B3LYP hybrid functional, which will be also used to calculate total energies.

ASIC calculations are performed with the development version of the SIESTA, while, for the B3LYP calculations, we employ the two codes GAMESS and NWCHEM. We use the basis 6-31G* and the triple-zeta polarized basis set of Ahlrichs [333].

Tab. 6.19 displays the energy difference between LS Co^{3+}-Cat, LS Co^{2+}-SQ and the HS Co^{2+}-SQ. These values must be taken with care as they might be plagued by systematic errors similar to those found in the case of the Fe^{2+} complexes. However,

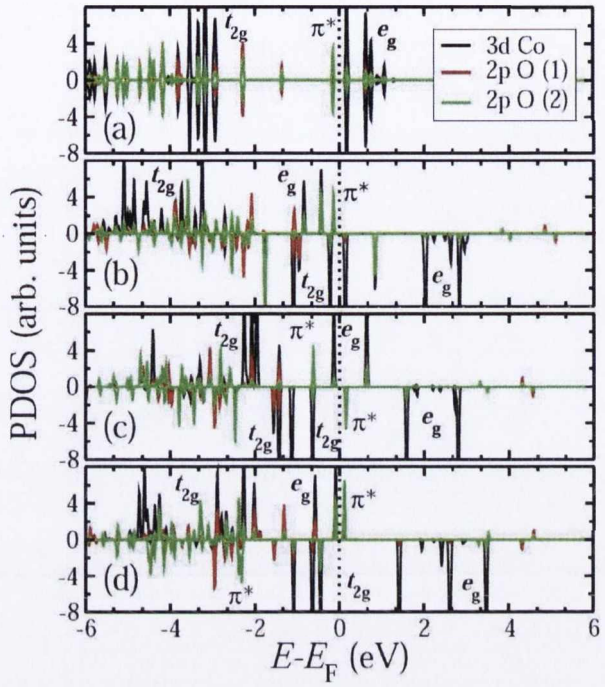

Figure 6.7: Density of states projected over the $3d$ states of the Co and the $2p$ states of the two O atoms, as calculated with ASIC, for a) LS Co^{3+}-Cat b) HS Co^{2+}-SQ c) LS Co^{2+}-SQ and d) HS Co^{2+}-SQ with antiferromagnetic coupling between the magnetic moment of the Co and the one of the SQ.

here, we are basically performing model calculations, and the choice of the functional is practically equivalent to fixing some effective parameters in order to describe qualitatively the experimental starting configuration (i.e. the configuration without applied electric field) for the molecules[11]. B3LYP qualitatively reproduces the relative order of the states and that is what we need. Unfortunately the absolute values of the relative energies appear drastically overestimated with respect to experimentally

[11]This study focuses mainly on a single molecule in vacuum. When starting this work we implicitly assumed that the ground state for this case was the LS Co^{3+}-Cat, like for a molecule in single crystal. However after our systematic investigation of the properties of spin crossover complexes, we have become aware that this might not be true. We think that DMC calculations are needed in order to understand which is the correct ground state of this molecule in the gas phase. However, our prediction holds, at least at a qualitative level, also for the molecule embedded in a crystal. In this case, the enthalpy would not be equal to the total energy (see below), but its calculation would require the inclusion of the pressure term. However, this would not affect the main phenomenological conclusion of the work. Therefore, even if it was not possible to demonstrate the electric field control of the VTI at the single-molecule level, it would be possible to observe it for the molecules in crystals or solutions.

available enthalpies (a few hundred meV) [343, 344], but we were not able to identify a functional which reproduces both the experimental energy gaps and the correct electron and spin localization.

The ASIC calculated density of states (DOS) of the molecule is displayed in Fig.

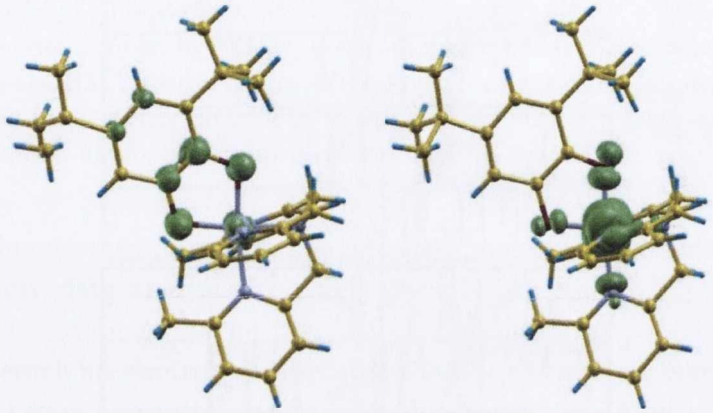

Figure 6.8: Isovalue contour plot for the charge density (local DOS) for the HOMO (left) and LUMO (right) of the LS Co^{3+}-Cat.

6.7. The relative position of the Co-3*d* shell with the molecular orbitals of Cat (SQ) is returned consistently by both ASIC and B3LYP (DOS not shown), although the details of the spectrum might change quantitatively. Since, to our knowledge, there are no spectroscopic data for Co-dioxolene complexes to compare with our calculations and, moreover, we here aim just at modelling the molecule and at capturing the basic qualitative features of its spectrum, Fig. 6.7 should be interpreted as a schematic energy level diagram. We notice that the self-interaction correction returns the expected weak hybridization between the Cat (SQ)-π^* and the Co 3*d* states. The Co 3*d* shell can be clearly recognized in the DOS and it is filled according to the formal oxidation. The symmetry of the highest occupied molecular orbital (HOMO) and the lowest unoccupied molecular orbital (LUMO) can be appreciated by looking at charge density isovalue contour plot (Fig. 6.8). For instance, for LS Co^{3+}-Cat the HOMO is the Cat-π^* state, while the LUMO corresponds to the Co e_g states (see Fig. 6.7). This confirms the ASIC provides a good qualitative description of the molecule electronic structure.

We now proceed to investigate the influence that an electric field, $\mathcal{E}$, has on the VTI. In particular we consider the situation where $\mathcal{E}$ is applied along the direction joining Co with Cat (SQ). In order to reduce the computational overheads we replace the

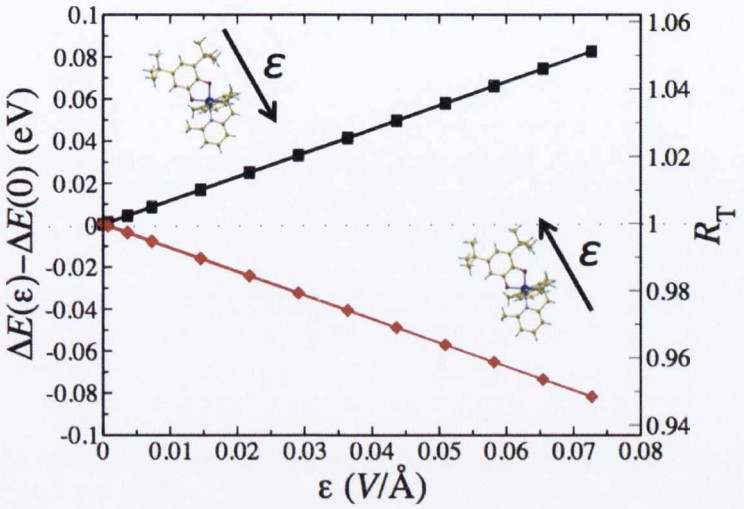

Figure 6.9: Energy difference between HS Co^{2+}-SQ and LS Co^{3+}-Cat, ΔE, as a function of the electric field $\mathcal{E}$ (the energies are calculated with the B3LYP functional). The black line (square symbols) corresponds to electric field pointing toward the quinone, while the red one (diamond symbols) to the electric field pointing toward the Co. The figure also report R_T for the same molecule on right-hand side y-axis.

N ligands with ammonia molecules. This substitution does not bring any relevant modification to the relative position of the Co-3d and the Cat (SQ)-π^* orbitals. It simply effect the total energies, since the energy difference between HS Co^{2+}-SQ and LS Co^{3+}-Cat is found to decrease to 1.591 eV. However this is not an issue as, so far, we have been limiting ourselves to a strictly phenomenological (and not quantitative) description of the problem.

Fig. 6.9 shows the difference, $\Delta E = E_{\mathrm{HSCo^{2+}SQ}} - E_{\mathrm{LSCo^{3+}Cat}}$, between the ground state energies of LS Co^{3+}-Cat and HS Co^{2+}-SQ ($\Delta E > 0$ means $E_{\mathrm{HSCo^{2+}SQ}} > E_{\mathrm{LSCo^{3+}Cat}}$). Such a quantity is plotted as a function of the electric field and with respect to the $\mathcal{E} = 0$ situation. The most important observation is that ΔE depends linearly on $\mathcal{E}$. We recall here that the energy change, ΔE, of a quantum mechanical system under the influence of an external electric field is governed by the Stark effect. This reads

$$\Delta E(\mathcal{E}) \propto \mathbf{p} \cdot \mathcal{E} + \frac{1}{2} \sum_{ij} \mathcal{E}_i \alpha_{ij} \mathcal{E}_j \tag{6.9}$$

where $\mathbf{p}$ is the permanent electrical dipole and α_{ij} the polarizability tensor. Thus the linear dependence found in Fig. 6.9 indicates that the first order Stark effect

dominates the molecule response. Our DFT calculations confirm such an hypothesis and return a finite dipole moment at $\mathcal{E} = 0$ ($|\mathbf{p}|$ is 16.9 Debye for LS Co^{3+}-Cat and 26.3 Debye for HS Co^{2+}-SQ).

An inspection of Fig. 6.9 shows how, interestingly, the energy decreases when the electric field points from the Co to the dioxolene and increases when it is along the opposite direction. This means that ΔE is reduced for the field direction facilitating the VTI electron transfer. We then expect that there is a critical electric field $\mathcal{E}_C$ at which the states LS Co^{3+}-Cat and HS Co^{2+}-SQ become energetically degenerate. When $\mathcal{E}$ exceeds $\mathcal{E}_C$ a VTI occurs leading to the SC and HS Co^{2+}-SQ becomes the new ground state of the molecule. The value of critical field can be extracted by a linear fit. This returns a slope of 1.12 eV/(V/Å) and $\mathcal{E}_C = 1.4$ V/Å. Unfortunately the value for $\mathcal{E}_C$ is not reliable because of the uncertainties on the predicted total energies and, however, it would be too large to observe experimentally an electric field induced VTI. In contrast, since the molecule electrical dipole and polarizability are usually accurately calculated with DFT as long as the charge density distribution is well described, the slope of $\Delta E(\mathcal{E})$ is probably returned even quantitatively correct by our calculations. We can then use this information to obtain more quantitative and well grounded predictions about the electric field modulation of VTI.

In order to do that we start by deriving the expression for the VTI crossover temperature T_C. T_C is defined by the condition $\Delta G = 0$, i.e. it corresponds to the situation where the Gibbs free energies of the two spin configurations become identical. This yields to the equation

$$T_C = \frac{\Delta H}{\Delta S} = \frac{\Delta E}{\Delta S} . \tag{6.10}$$

Here we have set the pressure to zero since we are considering the molecule in vacuum (see footnote 11), and we have approximated the enthalpy at T_C with the zero-temperature total electronic energy. Then, after assuming that the entropy variation, ΔS, does not depend on the electric field, i.e ($\Delta S(\mathcal{E}) \approx \Delta S(0)$), some algebra shows that the ratio between the critical temperature calculated in an electric field, $T_C(\mathcal{E})$, with that in zero field, $T_C(0)$, simply writes

$$R_T = \frac{T_C(\mathcal{E})}{T_C(0)} = \frac{\Delta E(\mathcal{E})}{\Delta E(0)} . \tag{6.11}$$

Importantly R_T is expressed in terms of DFT total energies only. We note that the assumption that entropy variation does not depend on the electric field, required to derive Eq. (6.11), is consistent with our computational strategy of not relaxing the atomic coordinates. However, we have also verified in a few cases that the atomic

relaxation under bias is much smaller than that due to the VTI. Finally, Eq. (6.10) can be rewritten as

$$[T_C(0) - T_C(\mathcal{E})]\,\Delta S(0) = \Delta E(0) - \Delta E(\mathcal{E})\,. \tag{6.12}$$

This equation expresses the difference between the critical temperature for the molecule in an electric field, $T_C(\mathcal{E})$, and that for the molecule in zero field, $T_C(0)$, in terms of the the slope of $\Delta E(\mathcal{E})$. This should be weakly affected by possible systematic errors on the determination of the total energies and should not depend on the functional as long as it returns a good description of the electronic structure of the various states of the molecule. Eq. (6.12) is the core equation of this work and shows that the critical temperature for the VTI in Co-dioxolene complexes can be drastically modified by a static electric field.

By taking the experimental estimate for the entropy variation $\Delta S(0) \approx 0.52$ meV/K [344], we can finally conclude that achievable electric fields can indeed induce large variations in T_C. In fact an electric field of 0.1 V/nm (typical of Stark spectroscopy [345]), pointing from the Co ion to the dioxolene, produces already a change in T_C of about 21 K, and a field of 0.5 V/nm, obtainable in scanning tunnel microscopy experiments can drift T_C by as much as 100 K.

In conclusion, our prediction demonstrates that the application of a static electric field on the molecule represents a physical way to effectively modulate the redox potential of the metal acceptor. This is then an intriguing alternative to the chemical strategy of changing the radical groups of the molecule [344]. Furthermore and most importantly, such an external control of the magnetism of valence tautomeric compounds may open new avenues to the growing field of molecular spintronics.

Chapter 7

Conclusions and future work

In summary, we have discussed several theoretical/computational techniques, which can be employed to study various systems of many interacting electrons. These have then been applied to various problems of current interests, which span from the description of defects in oxide and nitride materials to the prediction of the magnetic properties of transition metal complexes and the solution of effective models.

We began in Chapter 2 by giving a brief overview of various electronic structure methods focusing mainly on DFT and continuum QMC. DFT generally provides accurate quantitative information about the electronic structure of molecules and solids at a relatively low computational cost. Furthermore, many developments, such as hybrid DFT, have been proposed to improve the description of systems, for which LSDA/GGA functional performs poorly. However even the most advanced "beyond-LSDA" methods do not return accurate enough results for a few important problems. In these cases, DMC must be employed (when the computational cost is affordable). Therefore we briefly describe the salient features of the CASINO code, which is an efficient platform to carry out continuum QMC simulations on massively parallel computers.
Toward the end of the chapter, we introduced the Hubbard model and describe its relevance in condensed matter physics.

In the Chapter 3, we presented an overview of the d^0 magnetism and of the issues related to the correct description of the electronic and magnetic properties of point defects in wide-gap materials. We discussed how standard DFT calculations, which employ LSDA/GGA functionals, do not predict the correct degree of localization of impurity states, which are systematically returned too shallow. This is mainly due to

the DFT band-gap problem and to the inability of these functionals to describe hole self-trapping. These failures can be related to the self-interaction error inherent to the LSDA/GGA functionals. We then present the ASIC scheme, which is able to rectify these shortcomings. Finally, some simulations for acceptor defects in MgO and GaN were shown. For the case of the cation vacancy in MgO, a direct comparison between different methods (ASIC, LDA+U, HSE hybrid functional) and experimental results is possible. Our study demonstrates that, *although the states associated with acceptor point defects in wide-gap materials are spin-polarized, they are always very deep and localized by polaronic lattice distortions.* Therefore *no coupling between the magnetic moments is found and the reports of d^0 ferromagnetism can not be explained through a simple picture in which magnetic interactions between hole centers percolate through the sample.*

At the end of the chapter, we review some interesting experimental as well as theoretical results, which suggest that a correlation exists between the presence of extended defects in the samples and the reports of d^0 ferromagnetism. We are currently performing systematic DFT simulations in order to study the electronic and magnetic properties of grain boundaries in oxides, with the hope that they will provide new insights into this puzzling physics.

Finally, we must remark that the accurate *ab-initio* description of defects in oxides and nitrides is an important problem within many research areas such as catalysis, nanoelectronics and photo-voltaic energy devices. Therefore, although our work deals mainly with the controversial topic of d^0 magnetism, our results have a much broader relevance in computational materials science.

In Chapter 4, we introduced the Anderson-Hubbard model, which is believed to account for the main features of electron correlation in narrow impurity bands. We then study its electronic and magnetic properties for the quarter filling case by using the MFA and the RPA. The aim is to understand whether some of the results can be related to the physics of d^0 magnets. This was previously suggested by other authors, who, however, did not consider how disorder affects both single particle states and collective excitations.

The model is found to have two different behaviors depending on the value of the screened Coulomb interaction U.

For large U (i.e. $U/t > 4$) electrons tend to localize over clusters of sites, which carry large magnetic moments. These magnetic moments are antiferromagnetically coupled. In contrast, only sites with low charge occupation and magnetic moments

contribute to the states around the Fermi level and to the conduction properties of the system. This behavior is reminiscent of the two-fluids model originally proposed to describe low-temperatures thermodynamics anomalies in n-doped Si. From a comparison of the MFA and RPA results, we can note that electrons in the insulating component of the two-fluids are strongly correlated. Therefore much more accurate studies, which include many-particle effects beyond the MFA, might be required to describe this system. This can be achieved in the future by using lattice Quantum Monte Carlo techniques (see below).
For small U (i.e $U/t \lesssim 4$) electrons are almost equally spread over the entire lattice and they are likely to be weakly correlated. We observe a transition from a paramagnetic to a magnetic phase at a finite value of U/t, which depends on the degree of disorder. After performing calculations for lattices of various size, we believe that this transition can be correctly described by approaching the thermodynamic limit. Unfortunately, however, we were not able to identify the appropriate order parameter and further studies are required to characterize the nature of the phase transition and provide a solid theoretical foundation to our study.
In contrast to previous works, which neglect the exact treatment of disorder, our results indicates that *no ferromagnetic phase transition occurs* even at the MFA level. Furthermore, for realistic parameters, the magnetic response to an external magnetic field is Curie-like and the magnetization saturates for values of the field much larger than those achievable experimentally. This indicates that the model is not able to predict one of the main feature of d^0 magnetism (i.e. the ferromagnetic-like magnetization curve). Therefore either it misses some important degrees of freedom needed to correctly account for the physics of d^0 magnets or d^0 magnetism can not be related to the behavior of correlated electrons in an impurity band. The solution of this dilemma will be the subject of future investigations.

In Chapter 5 we present the AFQMC method to numerically solve the Hubbard model and we discuss our own implementation. We also provide a brief overview of the MEM, which represents a reliable numerical way to analytically continue the time-displaced Green function into the spectral function. We finally show the result of several simulations for the half-filled Hubbard model on a square lattice. These have mainly a demonstrative value as they can be compared with those extracted from a vast literature. However, many problems of interest, which can be described through Hubbard-like models, will be investigated in the near future. These include the study of magnetic correlations in disordered systems and of the edge- and defect-related

magnetism in graphene. Furthermore one-dimensional Hubbard-like models, which include either the electron-phonon interaction or the coupling between electrons and classic lattice relaxations, have been proposed in order to describe conjugated polymers. Their study might be very relevant for the rapidly growing field of organic spintronics.

In Chapter 6, we moved our attention from solids to molecules. We introduce the spin-crossover transition metal complexes and the Co-dioxolene molecules. These are example of systems, whose magnetic state, can be switched by an external stimuli and, therefore, are good candidates for being incorporated in molecular spintronic devices.
Through a systematic comparison of the results of DFT and DMC calculations for small Fe^{2+} complexes as well as for a large spin crossover molecule, we are able to point out the inaccuracy of the most popular functionals in describing the electronic and magnetic properties of such systems. Our results suggest that *DFT is plagued by a systematic error.* This is likely to originate from an inaccurate description of correlation effects in the Fe ion. On the one hand, we believe that this observation sets a cornerstore for the theoretical research on this class of compounds. On the other hand, our study is just at the very initial stage and, in order to deeply understand the origin of the failures of DFT and better assess the behavior of each functional, we must consider a much larger set of molecule and of computational methods.
Our DMC simulations for Fe^{2+} complexes provide also some important insight into the physics and chemistry of these systems. In fact, our results support the hypothesis that *the spin transition is not a single-molecule property, but it strongly depends on the crystalline environment the molecule is embedded in.* Further studies, which aim at firmly demonstarting this statement, are currently on-going.
In the last part of the chapter, we describe the the Co-dioxolene molecules and we focus mainly on phenomenological rather than methodological issues. We finally predict that *the VTI can be controlled through external static electric fields.* Experimentalist are currently trying to verify this results.
In this work we mainly discuss the behavior of spin-crossover and Co-dioxolene molecules in the gas and crystalline phase. However, in future, we will try to understand how the electronic and magnetic properties change in case of single molecules on surfaces. Although only very few theoretical and experimental results have been achieved so far on this subject, we believe that the research activity will grow rapidly in the next few years. Many interesting questions can then be addressed. These con-

cern, for example, the stability of these compounds on various surfaces, their magnetic ground state and their response to those external stimuli which, for crystals and solutions, are able to induce the spin-crossover transition. Finally a very interesting issue refers to the possibility of inferring, and eventually changing, the spin state through scanning tunnelling microscope manipulations. This will be the ultimate hope for the development of practical device applications.

Bibliography

[1] N.W. Ashcroft, N.D. Mermin, *Solid State Physics* (Saunders College Publishing, Olland, 1986).

[2] R.M. White, *Quantum Theory of Magnetism: Magnetic Properties of Materials*, (Springer-Verlag, Berlin-Heidelberg, 2007).

[3] P. Fazekas, *Lecture Notes on Electron Correlation and Magnetism* (World Scientific, Singapore, 1999).

[4] N.H. March, *Electron Correlation in Molecules and Condensed Phases* (Plenum Press, New York, 1996).

[5] P. Fulde, *Electron Correlations in Molecules and Solids* (Springer-Verlag, Berlin-Heidelberg, 1991).

[6] N.F. Mott, Proc. R. Soc. Lond. A, **153**, 699, 1936.

[7] G. Morandi, E. Ercolessi, F. Napoli, *Statistical Mechanics: An Intermediate Course* (World Scientific, Singapore, 2001).

[8] M.N. Baibich, J.M. Broto,A. Fert, F. Nguyen Van Dau, F. Petroff, P. Etienne, G. Creuzet, A. Friederich, J. Chazelaz, Phys. Rev. Lett., **61**, 2472 (1988).

[9] G. Binash, P. Grünberg, F. Saurenbach, W. Zinn, Phys. Rev. B, **39**, 4828 (1989).

[10] S.A. Wolf, D.D. Awschalom, R.A. Buhrman, J.M. Daughton, S. von Molnár, M.L. Roukes, A.Y. Chtchelkanova, D.M. Treger, Science, **294**, 1488-1495 (2001).

[11] I. Zutic, J. Fabian, S. Das Sarma, Rev. Mod. Phys., **76**, 323 (2004).

[12] M. Ziese, M.J. Thornton (Eds.), *Spin Electronics* (Sringer-Verlag, Berlin-Heidelberg, 2001).

[13] J. Fabian, A. Matos-Abiague, C. Ertler, P. Stano, and I. Zutić, Acta Phys. Slovaca, **57**, 565 (2007), arXiv:0711.1461v1.

[14] D.D. Awschalom, D. Loss, N. Samarth (Eds.) *Semiconductor Spintronics and Quantum Computation* (Springer-Verlag, Berlin-Heidelberg, 2002).

[15] S. Datta, B. Das, Appl. Phys. Lett., **56**, 665 (1990).

[16] Y. Kanai, R. S. Deacon, S. Takahashi, A. Oiwa, K. Yoshida, K. Shibata, K. Hirakawa, Y. Tokura, S. Tarucha, Nature Nanotechnology, **6**, 511 (2011).

[17] F. Holtzberg, *Rare Earth Magnetic Semiconductors*, in: Handbook on Semiconductors (North Holland, Amsterdam, 1980).

[18] T. Jungwirth, J. Sinova, J. Masek, J. Kucera, A.H. MacDonald, Rev. Mod. Phys. **78**, 809 (2006).

[19] A.H. MacDonald, P. Schiffer, N. Samarth, Nature Materials, **4**, 195 (2005).

[20] T. Dietl, Nature Materials, **9**, 965 (2010).

[21] H. Ohno, Science, **281**, 951 (1998).

[22] H. Ohno, J. Magn. Magn. Mater., **200**, 110 (1999).

[23] C. Zener, Phys. Rev., **81**, 440 (1950).

[24] T. Dietl, H. Ohno, F. Matsukura, J. Cibert, D. Ferrand, Science, **287**, 1019 (2000).

[25] T. Jungwirth, K.Y. Wang, J. Masek, K.W. Edmonds, J. König, J. Sinova, M. Polini, N.A. Goncharuk, A.H. MacDonald, M. Sawicki, A.W. Rushforth, R.P. Campion, L.X. Zhao, C.T. Foxon, B.L. Gallagher, Phys. Rev. B, **72**, 165204 (2005).

[26] V. Novák, K. Olejnk, J. Wunderlich, M. Cukr, K. Vỳbornỳ, A.W. Rushforth, K.W. Edmonds, R.P. Campion, B.L. Gallagher, J. Sinova, T. Jungwirth, Phys. Rev. Lett., **101**, 077201 (2008).

[27] R. Janisch, P. Gopal, N.A. Spaldin, J. Phys.: Condens. Matter, **17**, R657 (2005).

[28] W. Prellier, A. Fouchet, B. Mercey, J. Phys.: Condens. Matter, **15**, R1583 (2003).

[29] S.B. Ogale, Adv. Mater., **22**, 3125 (2010).

[30] S.J. Pearton, W.H. Heo, M. Ivill, D.P. Norton, T. Steiner, Semicond. Sci. Technol., **19**, R59 (2004).

[31] J.M.D. Coey, Curr. Opin. Solid State Mater. Sci., **10**, 83 (2007).

[32] J.M.D. Coey, S.A. Chambers, MRS Bulletin, 33, 1053 (2008).

[33] S.A. Chambers, Adv. Mater., **22**, 219 (2010).

[34] J.M.D. Coey, K. Wongsaprom, J. Alaria, M. Venkatesan J. Phys. D, **41**, 134012 (2008).

[35] M. Venkatesan, C.B. Fitzgerald and J.M.D. Coey, Nature, **430**, 630 (2004).

[36] J.M.D. Coey, Solid State Sci., **7**, 660 (2005).

[37] A. Sundaresan, R. Bhargavi, N. Rangarajan, U. Siddesh and C. N. R. Rao, Phys. Rev. B, **74**, 161306(R) (2006).

[38] S. D. Yoon, Y. Chen, A. Yang, T. L. Goodrich, X. Zuo, D. A. Arena, K. Ziemer, C. Vittoria, V. G. Harris, J. Phys.: Condens. Matter, **18**, L355 (2006).

[39] S. D. Yoon, Y. Chen, A. Yang, T. L. Goodrich, X. Zuo, K. Ziemer, C. Vittoria and V. G. Harris, J. Magn. Magn. Mat., **309**, 171 (2007).
S. D. Yoon, Y. Chen, A. Yang, T. L. Goodrich, X. Zuo, K. Ziemer, C. Vittoria and V. G. Harris, J. Magn. Magn. Mat., **320**, 597 (2008).

[40] A.K. Rumaiz, B. Ali, A. Ceylan, M. Boggs. T. Beebe, S. I. Shah, Sol. State Comm., **144**, 334 (2007).

[41] R. P. Panguluri, P. Kharel, C. Sudakar, R. Naik, R. Suryanarayanan, V. M Naik, A. G. Petukhov, B. Nadgorny, G. Lawes, arXiv:0808.1123.

[42] S. Banerjee, M. Mandal, N. Gayathri, and M. Sardar, Appl. Phys. lett., **91**, 182501 (2007).

[43] E. Tirosh, G. Markovich, Adv. Mater., **19**, 2608 (2007).

[44] R. P. Panguluri, P. Kharel, C. Sudakar, R. Naik, R. Suryanarayanan, V. M Naik, A. G. Petukhov, B. Nadgorny and G. Lawes, Phys. Rev. B, **79**, 165208 (2009).

[45] B.M. Maoz, E. Tirosh, M.B. Sadan, G. Markovich, Phys. Rev. B, **83**, 161201(R) (2011).

[46] M.A. Garcia, E. fernandez Pinel, J. de la Venta, A Quesada, V. Bouzas, J.F. Fernàndez, J.J. Romero,M.S. Martìn Gonzàlez, J.L. Costa-Krämer, J.Appl. Phys., **105**, 13925 (2009).

[47] M. Sieberer, J. Redinger, S. Khmelevskyi, P. Mohn, Phys. Rev. B, **73**, 024404 (2006).

[48] G.Y. Gao, K.L. Yao, E. Sasioglu, L.M. Sandratskii, Z.L. Liu, J.L. Jiang, Phys. Rev. B, **75**, 174442 (2007).

[49] A. Droghetti, N. Baadji, S. Sanvito, Phys. Rev. B, **80**, 235310 (2009).

[50] J. F. Janak, Phys. Rev. B, **16**, 255 (1977).

[51] D.M. Edwards and M.I. Katsnelson, J. Phys.: Condens. Matter, **18**, 7209 (2006).

[52] R.J. Meier and R.B. Helmholdt, Phys. Rev. B, **29**, 1387 (1984).

[53] J.J. Attema, G.A. de Wijs, G.R. Blake, R.A. de Groot, J. Am. Chem. Soc., **127**, 16325 (2005).

[54] J. Winterlik, G.H. Fecher, C. Felser, C. Mühle, M. Jansen, J. Am. Chem. Soc., **129**, 6990 (2007).

[55] O.V. Yazyev, Rep. Prog. Phys., **73** 056501 (2010).

[56] T. Makarova, F. Palacio (eds.) *Carbon-Based Magnetism: An Overview of the Magnetism of Metal-Free Carbon-Based Compounds and Materials* (Elsevier, Amsterdam, 2006).

[57] T. Dietl, J. Appl. Phys., **103**, 07D111 (2008).

[58] R.G. Parr, W. Yang, *Density-Functional Theory of Atoms and Molecules*, vol. 16 of The International Series of Monographs on Chemistry (Oxford University Press, Oxford, UK, 1989).

[59] C. Fiolhais, F. Nogueira, M. Marques (eds.), *A Primer In Density Functional Theory* (Springer-Verlag, Berlin-Heidelberg, 2003).

[60] P. Hohenberg, W. Kohn, Phys. Rev., **136** B864 (1964).

[61] W. Kohn, L. Sham, Phys. Rev., 140, A1133 (1965).

[62] S. Sanvito, G.J. Theurich, N.A. Hill, J. of Superconductivity and Novel Magnetism, **15**, 85, (2002).

[63] K. Sato, L. Bergqvist, J. Kudrnovský, P.H. Dederichs, O. Eriksson, I. Turek, B. Sanyal, G. Bouzerar, H. Katayama-Yoshida, V.A. Dinh, T. Fukushima, H. Kizaki, and R. Zeller, Rev. Mod. Phys. **82**, 1633 (2010).

[64] J.P. Perdew, A. Zunger, Phys. Rev. B, **23**, 5048 (1981).

[65] A. Zunger, S. Lany, H. Raebiger, Physics, **3**, 53 (2010).

[66] S. Sanvito, P. Ordejòn, N.A. Hill, Phys. Rev. B, **63**, 165206 (2001).

[67] S. Sanvito, N.A. Hill, Appl. Phys. Lett., **78**, 3493 (2001).

[68] S. Sanvito, N.A. Hill, J. Magn. Magn. Mater., **238**, 252 (2002).

[69] S. Sanvito, N.A. Hill, J. Magn. Magn. Mater., **441**, 242 (2002).

[70] S. Sapra, D. Das Sarma, S. Sanvito, N.A. Hill, Nano Letters, **2**, 605 (2002).

[71] S. Sanvito, Phys. Rev. B, **68**, 054425 (2003).

[72] A. Filippetti, N.A. Spaldin, S. Sanvito, Chem. Phys., **309**, 59 (2004).

[73] M. Wierzbowska, D. Sǹchez-Portal, S. Sanvito, Phys. Rev. B, **70**, 235209 (2004).

[74] A. Filippetti, N.A. Spaldin, S. Sanvito, J. Magn. Magn. Mater., **1391**, 290 (2005).

[75] C.D. Pemmaraju and S. Sanvito, Phys. Rev. Lett., **94**, 217205 (2005).

[76] T. Archer, C. D. Pemmaraju, S. Sanvito, J. Magn. Magn. Mater., **316**, e188 (2007).

[77] R. Hanafin, S. Sanvito, J. Magn. Magn. Mater., **316**, 218 (2007).

[78] C.D. Pemmaraju, T. Archer, R. Hanafin, S. Sanvito, J. Magn. Magn. Mater., **316**, e185 (2007).

[79] T. Archer, R. Hanafin, S. Sanvito, Phys. Rev. B, **78**, 014431 (2008).

[80] C.D. Pemmaraju, R. Hanafin, T. Archer, H.B. Braun, S. Sanvito, Phys. Rev. B, **77**, 054428 (2008).

[81] S. Sanvito, C.D. Pemmaraju, Phys. Rev. Lett., **102**, 159701 (2009).

[82] R. Hanafin, T. Archer, S. Sanvito, Phys. Rev. B **81**, 054441 (2010).

[83] R. Hanafin, S. Sanvito, J. Magn. Magn. Mater., **322**, 1209 (2010).

[84] T. Archer, C.D. Pemmaraju, S. Sanvito, New J. Phys., **12**, 083061 (2010).

[85] F. Chen, J. Hihath, Z. Huang, X. Li and N.J. Tao, Annu. Rev. Phys. Chem. ,**58**, 535 (2007).

[86] A.Aviram, M.A. Ratner, Chem. Phys. Lett., **29**, 277 (1974).

[87] M.A. Reed, C. Zhou, C.J. Muller, T.P. Burgin, J.M. Tour, Science, **278**, 252 (1997).

[88] A.R. Rocha, V.M. Garcia-suarez, S.W Bailey, C.J. Lambert, J. Ferrer, S. Sanvito, Nature Materials **4**, 335 (2005).

[89] L. Bogani, W. Wernsdorfer, nature Materials, **7**,179 (2008).

[90] V.A. Dediu, L.E. Hueso, I. Bergenti and C. Taliani, Nature Materials, **8**, 707 (2009).

[91] S. Sanvito,Chem. Soc. Rev., **40**, 3336 (2011).

[92] O. Kahn, *Molecular magnetism* (VCH, New York, 1993)

[93] P. Gütlich, H.A. Goodwin, in *Spin Crossover in Transition Metal Compounds* (eds. P. Gütlich, H.A. Goodwin) (Springer-Verlag, Berlin-Heidelberg, 2004).

[94] O. Sato, J. Tao, Y.Z. Zhang, Angew. Chem. Int. Ed. **46**, 2152 (2007).

[95] D.N. Hendrickson, C.G. Pierpont, Top. Curr. Chem. **234**, 63 (2004).

[96] A. Beni, C. Carbonera, A. Dei, J.-F. Létard, R. Righini, C. Sangregorio, L. Sorace, J. Braz. Chem. Soc. **17**, 1522 (2006).

[97] K. Takahashi, H.B. Cui, Y. Okano, H. Kobayashi, Y. Einaga, O. Sato, Inorg. Chem., **45**, 5739 (2006).

[98] M.S. Alam, M. Stocker, K. Gieb, P. Müller,M. Haryono, K. Student, A. Grohmann, Angew. Chem. Int. Ed., **49**, 1159 (2010)

[99] F. Prins, M. Monrabal-Capilla, E.A. Osorio, E. Coronado, H.S.J. van der Zant, Adv. Mater. **23**,1545 (2011).

[100] V. Meded, A. Bagrets, K. Fink, R. Chandrasekar, M. Ruben, F. Evers, A. Bernand-Mantel, J.S. Seldenthuis, A. Beukman, H.S.J. van der Zant, Phys. Rev. B, **83**, 245415 (2011)

[101] E.A. Osorio, K. Moth-Poulsen, H.S.J. van der Zant, J. Paaske, P. Hedegard, K. Flensberg, J. Bendixm T. Bjornholm, Nano Lett. **10**(1), 105 (2010).

[102] R. Martin, *Electronic Structure: Basic Theory and Pratical Methods* (Cambridge University Press, Cambridge, 2004).

[103] A. Messiah, *Quantum Mechanics* (Courier Dover Publications, New York, USA, 1999).

[104] A. Szabo and N.S. Ostlund, *Modern Quantum Chemistry* (Dover Publications Inc., New York, USA, 1996).

[105] F. Jensen, *Introduction to Computational Chemistry*, Second edition, (John Wiley Inc., West Sussex, UK, 2007).

[106] R.J. Bartlett, M. Musial, Rev. Mod. Phys., **79**, 291 (2007).

[107] J.F. Janak, Phys. Rev. B, **18**, 7165 (1978).

[108] J.P. Perdew, M. Levy, Phys. Rev. B, **56**, 16021 (1997).

[109] L.J. Sham, M. Schlünter, Phys. Rev. Lett., **51**, 1888 (1983).

[110] U. Von Barth, L.Hedin, J. Phys. C, **5**, 1629 (1972).

[111] J.E. Peralta, G.E. Scuseria, M.J. Frisch, Phys. Rev. B, **75**, 125119 (2007).

[112] D.M Ceperley, B.J. Alder, Phys.Rev.Lett., **45**, 566 (1980).

[113] S.J. Vosko, L. Wilk, M. Nusair, Can.J. Phys., **58**, 1200s (1980).

[114] J.P. Perdew, Y. Wang, Phys. Rev. B, **45**, 13244 (1992).

[115] J.P.Perdew K. Burke, M. Ernzerhof, Phys. Rev. Lett., **77**, 3865 (1996).

[116] A.D.Becke, Phys. Rev. A, **38**, 3098 (1988).

[117] J.P. Perdew, Phys. Rev B, **33**, 8822 (1986).

[118] J.P. Perdew, Y. Wang, Phys. Rev B, **33**, 8800 (1986).

[119] C. Lee, W. Yang, R.G. Parr, Phys Rev. B, **37**, 785 (1988).

[120] S. Kümmel, L. Kronik, Rev. Mod. Phys. **80**, 1 (2008).

[121] J. Harris, R.O. Jones, J. Phys. F: Met. Phys., **4**, 1170 (1974).

[122] O. Gunnarsson, B.I. Lundqvist, Phys. Rev. B, **13**, 4274 (1976), **15**, 6006(E) (1977).

[123] D.C. Langreth, J.P. Perdew, 1977, Phys. Rev. B, **15**, 2884.

[124] M. Levy, in *Density Functional Theory*, edited by J. Keller, and J. L. Gasquez (Springer, New York, 1983).

[125] J. Harris, Phys. Rev. A 29, 1648 (1984).

[126] A.D. Becke, J. Chem. Phys. **96**, 2155 (1992).

[127] P.J. Stephens, F.J. Devlin, C.F. Chabalowski, M.J. Frisch, J. Phys. Chem., **98**, 11623 (1994).

[128] L.A. Curtiss, K. Raghavachari, G.W. Trucks, J.A. Pople, J. Chem. Phys., **94**, 7221 (1991).

[129] M. Ernzerhof, G.E. Scuseria, J. Chem. Phys., **110**, 5029 (1999).

[130] C. Adamo, V. Barone, J. Chem. Phys., **110**, 6158 (1999).

[131] M. Ernzerhof, Chem. Phys. Lett., **263**, 499 (1996).

[132] M. Ernzerhof, J.P. Perdew, K. Burke, Int. J. Quantum Chem., **64**, 285 (1996).

[133] J.P. Perdew,M. Ernzerhof, K. Burke, J. Chem. Phys., **105** 9982 (1996).

[134] J. Heyd, G.E. Scuseria, M. Ernzerhof, J. Chem. Phys., **118**, 8207 (2003), J. Heyd, G.E. Scuseria, M. Ernzerhof, J. Chem. Phys., **124**, 219906 (erratum) (2006).

[135] R.T. Sharp, G.K. Horton, Phys. Rev., **90**, 317 (1953).

[136] J.D. Talman, W.F. Shadwick, Phys. Rev. A, **146**, 256 (1990).

[137] J.B. Krieger, Y. Li, G.J. Iafrate, Phys.Lett. A, **146**, 256 (1990).

[138] V.I. Anisimov, J. Zaanen, O.K. Andersen, Phys. Rev. B, **44**, 943 (1991).

[139] S.L. Dudarev, G.A. Botton, S.Y. Savrasov, C.J. Humphreys, A.P. Sutton, Phys. Rev. B, **57**, 1505 (1998).

[140] M. Cococcioni, S. de Gironcoli, Phys. Rev. B, **71**, 035105 (2005).

[141] A. Filippetti, V. Fiorentini, Eur. Phys. J. B, **71**, 139 (2009).

[142] H.B. Shore, J.H. Rose , E. Zaremba, Phys. Rev. B **15**, 2858 (1977).

[143] K. Terakura, T. Oguchi, A.R. Williams, J. Kübler, Phys. Rev. B, **30**, 4734 (1984).

[144] D.R. Hamann, M.S. Schlüter, C. Chiang, Phys., Rev. Lett. **43**, 1494 (1979).

[145] L. Kleinman, D.M. Bylander, Phys. Rev. Lett., **48**, 1425 (1982).

[146] J.C. Slater, Phys. Rev., **51**, 846 (1937).

[147] P.E.Blöchl, Phys. Rev. B, **50**, 17953 (1994).

[148] G. Kresse, D. Joubert, Phys. Rev. B, **59**, 1758 (1999).

[149] D. Vanderbilt, Phys. Rev. B, **41**, 7892 (1990).

[150] J. M. Soler, E. Artacho, J. D. Gale, A. García, J. Junquera, P. Ordejón and D. Sánchez-Portal, J. Phys.: Condens. Matter, **14**, 2745(2002).

[151] C.D. Pemmaraju, T. Archer, D. Sanchez-Portal and S. Sanvito, Phys. Rev. B, **75**, 045101 (2007).

[152] T. Kato, Comm. Pure Appl. Math., **10**, 151 (1957).

[153] M. Valiev, E.J. Bylaska, N. Govind, K. Kowalski, T.P. Straatsma, H.J.J. van Dam, D. Wang, J. Nieplocha, E. Apra, T.L. Windus, W.A. de Jong, Comput. Phys. Commun., **181**, 1477 (2010).

[154] M.W. Schmidt, K.K. Baldridge, J.A. Boatz, S.T. Elbert, M.S. Gordon, J.H. Jensen, S. Koseki, N. Matsunaga, K.A. Nguyen, S. Su, T.L. Windus, M. Dupuis, J.A. Montgomery, J. Comput. Chem., **14**, 1347 (1993).

[155] P. Giannozzi, S. Baroni, N. Bonini, M. Calandra, R. Car, C. Cavazzoni, D. Ceresoli, G.L. Chiarotti, M. Cococcioni, I. Dabo, A. Dal Corso, S. de Gironcoli, S. Fabris, G. Fratesi, R. Gebauer, U. Gerstmann, C. Gougoussis, A. Kokalj, M. Lazzeri, L. Martin-Samos, N. Marzari, F. Mauri, R. Mazzarello, S. Paolini, A. Pasquarello, L. Paulatto, C. Sbraccia, S. Scandolo, G. Sclauzero, A.P. Seitsonen, A. Smogunov, P. Umari, R.M. Wentzcovitch, J. Phys.: Condens. Matter, **21**, 395502 (2009).

[156] G. Kresse, J. Hafner, Phys. Rev. B **48**, 13115 (1993).

[157] M.J. Gillan, M.D. Towler, D. Alfè, Psi-k Highlight of the Month (February, 2011).

[158] W.M.C. Foulkes, L. Mitas, R.J. Needs, G. Rajagopal, Rev. Mod. Phys. **73**, 33 (2001).

[159] B.L. Hammond, W.A. Lester Jr., P.J. Reyonolds, *Monte Carlo Methods in Ab Initio Quantum Chemistry* (World Scientific, Singapore, 1994).

[160] R.J. Needs, M.D. Towler, N.D. Drummond, P. López Ríos., J. Phys.: Condens. Matter 22, 023201 (2010).

[161] M.E.J. Newman, G.T. Barkema, *Monte Carlo Methods in Statistical Physics* (Clarendon Press, Oxford, 1999).

[162] R.C. Grimm, R.G. Storer, J. Comput. Phys., **7**, 134 (1971).

[163] M.H. Kalos, D. Levesque, L. Verlet, Phys. Rev. A, **9**, 257 (1974).

[164] J.B. Anderson, J.Chem. Phys., **63**, 1499 (1975).

[165] J.B. Anderson, J.Chem. Phys., **65**, 4121 (1976).

[166] D.M. Ceperley, J. Stat. Phys., **63**, 1237 (1991).

[167] D.M. Ceperley, J. Stat. Phys., **43**,815 (1986).

[168] A. Ma, N.D. Drummond, M.D. Towler, R.J. Needs, Phys. Rev. E, **71**, 066704 (2005).

[169] C.W. Greeff, W.A. Lester Jr., J. Chem. Phys., **109**, 1607 (1998).

[170] S. Fahy, X.W. Wang, S.G. Louie, Phys. Rev. B, **42**, 3503 (1990).

[171] S. Fahy, X.W. Wang, S.G. Louie, Phys. Rev. Lett., **61**, 1631 (1998).

[172] L. Mitas, E.L. Shirley, D.M. Ceperley, J. Chem. Phys., **95**, 3467 (1991).

[173] M. Casula, C. Filippi, S. Sorella, Phys. Rev. Lett., **95**, 100201 (2005).

[174] M. Casula, Phys. Rev. B, **74**, 161102 (2006).

[175] D. Alfè, M.J. Gillian, Phys. Rev. B, **70**, 161101(R) (2004).

[176] J.R. Trail, R.J. Needs, J. Chem. Phys., **122**, 174109 (2005).

[177] J.R. Trail, R.J. Needs, J. Chem. Phys., **122**, 014112 (2005).

[178] A. Auerbach, *Interacting Electrons and Quantum Magnetism* (Springer-Verlag, New York, 1994).

[179] J. Hubbard, Proc. R. Soc. A, **276**, 238 (1963).

[180] A. Montorsi, *The Hubbard Model: a Reprint Volume* (World Scientific, Singapore, 1992).

[181] M.C. Gutzwiller, Phys. Rev. Lett., **10**, 159 (1962).

[182] Kanamori, Prog. Theor. Phys., **30**, 275 (1963).

[183] S. Sorella, E. Tosatti, Europhys. Lett., **19**, 699 (1992).

[184] T. Paiva, R.T. Scalettar, W. Zheng, R.R.P. Singh, J. Otima, Phys. Rev. B, **72**, 085123 (2005).

[185] M. Hohenadler, T. Lang, F. Assaad, Phys. Rev Lett., **106**, 10 (2011).

[186] Z.Y. Meng, T.C. Lang, S. Wessel, F.F. Assaad, A. Muramatsu, Nature, **464**, 847 (2010).

[187] B. DeMarco, D.S. Jin, Science **285**, 1703 (1999)

[188] A.G. Truscott, K.E. Strecker, W.I. McAlexander, G.B. Partridge, R.G. Hulet, Science, **291**, 2570 (2001).

[189] K.M. OHara, S.L. Hemmer, M.E. Gehm, S.R. Granade, J.E. Thomas, Science, **298**, 2179 (2002).

[190] M. Köhl, H. Moritz, T. Stöferle, K. Günter, T. Esslinger, Phys. Rev. Lett., **94**, 080403 (2005).

[191] R. Jordens, N. Strohmaier, K. Gunter, H. Moritz, T. Esslinger, Nature, **455**, 204 (2008).

[192] R. Micnas, J. Ranninger, S. Robaszkiewicz, Rev. Mod. Phys., **62**, 113 (1990).

[193] J.A. Wilson, J. Phys.: Condens. Matter, **13**, R945 (2001).

[194] P.J.H. Denteneer, R.T. Scalettar, N. Trivedi, Phys.Rev.Lett., **83**, 4610 (1999).

[195] P.J.H. Denteneer, R.T. Scalettar, N. Trivedi, Phys.Rev.Lett., **87**, 146401 (2001).

[196] P.J.H. Denteneer, R.T. Scalettar, Phys. Rev. Lett. **90**, 246401 (2003).

[197] M.E. Pezzoli, F. Becca, Phys. Rev. B **81**, 075106 (2010).

[198] P.B. Chakraborty, K. Byczuk, D Vollhardt, Phys. Rev. B, **84**, 035121 (2011).

[199] S. Kivelson,D.E. Heim, Phys. Rev. B, **26**, 4278 (1982).

[200] J.E. Hirsch, Phys. Rev. B, **31**, 6022 (1985).

[201] A. Takahashi, Phys. Rev. B, **54**, 79657971 (1996).

[202] E. Jeckelmann, Phys. Rev. B, **57**, 11838 (1998).

[203] H. Fehske, A.P. Kampf, M. Sekania, G. Wellein, Eur. Phys. J B, **31**, 11 (2003).

[204] P. Sengupta, A.W. Sandvik, D.K. Campbell, Phys. Rev. B, **67**, 245103 (2003).

[205] H. Fehske, G.Wellein, G. Hager, A. Weiße, A.R. Bishop, Phys. Rev. B, **69**, 165115 (2004).

[206] T. Giamarchi,*Quantum Physics in One Dimension* (Oxford University Press, Oxford, 2004).

[207] E. Dagotto, Rev. Mod. Phys., **66**, 763 (1994).

[208] S.R. White, Phys. Rev. Lett., **69**, 2863 (1992).

[209] U. Schollwöck, Rev. Mod. Phys., **77**, 259 (2005).

[210] O. Gunnarsson, K. Schonhammer, Phys. Rev. Lett., **56**, 1968 (1986).

[211] K. Schnhammer, O. Gunnarsson, R.M. Noack, Phys. Rev. B, **52**, 2504 (1995).

[212] N.A. Lima, L.N. Oliviera, K. Capelle, Europhys. Lett., **60**, 601 (2002).

[213] N.A. Lima, M.F. Silva, L.N. Oliveira, K. Capelle, Phys. Rev. Lett., **90**, 146402 (2003).

[214] G. Xianlong, M. Polini, M.P. Tosi, V.L. Campo, K. Capelle, M. Rigol, Phys. Rev. B, **73**, 165120 (2006).

[215] C.F. Yu, T.J. Lin, S.J. Sun, H. Chou, J. Phys. D: Appl. Phys., **40**, 6497 (2007).

[216] H. Pan, J.B. Yi, L. Shen, R.Q. Wu, J.H. Yang, J.Y. Lin, Y.P. Feng,J. Ding, L.H. Van and J.H. Yin, Phys. Rev. Lett., **99**, 127201 (2007).

[217] S. Zhou, Q. Xu, K. Potzger, G. Talut, R. Grötzschel, J. Fassbender, M. Vinnichenko, J. Grenzer, M. Helm, H. Hochmuth, M. Lorenz, M. Grundmann and H. Schmidt, Appl. Phys. Lett., **93**, 232507 (2008).

[218] S.S.P. Parkin, unpublish.

[219] H. Peng, H.j. Xiang, S.H.Wei, S.S. Li, J.B. Xia,J. Li, Phys.Rev. Lett., **102**, 017201 (2009).

[220] P. Dev, Y. Xue, P. Zhang, Phys. Rev. Lett., **100**, 117204 (2008).

[221] O. Volnianska, P. Boguslawski, Phys. Rev. B, **83**, 205205 (2011).

[222] G. Bouzerar, T. Ziman, Phys. Rev. Lett., **96**, 207602 (2006).

[223] J. Osorio-Guillén, S. Lany, S.V. Barabash, A. Zunger, Phys. Rev. Lett., **96**, 107203 (2006).

[224] A. Filippetti, N.A. Spaldin, Phys. Rev. B, **67**, 125109 (2003).

[225] J. Hu, Z. Zhang, M. Zhao, H. Qin, and M. Jiang, Appl. Phys. Lett., **93**, 192503 (2008).

[226] N. Kumar, D. Sanyal, A. Sundaresan, Chem. Phys. Lett., **477**, 360 (2009).

[227] J.I. Beltran, C. Monty, L. Balcells, C. Martìnez-Boubeta, Solid State Comm., **149**, 1654 (2009).

[228] C. Martìnez-Boubeta1, J.I. Beltran, Ll. Balcells, Z. Konstantinovič, S. Valencia, D. Schmitz, J. Arbiol, S. Estrade, J. Cornil, B. Martìnez, Phys. Rev. B, **82**, 024405 (2010).

[229] C. Moyses Araujo, M. Kapilashrami, Xu Jun, O.D. Jayakumar, S. Nagar, Y. Wu, C. Århammar, B. Johansson, L. Belova1, R. Ahuja, G.A. Gehring, K.V. Rao, Appl. Phys. Lett., **96**, 232505 (2010).

[230] J. Paier, M. Marsman, K. Hummer, G. Kresse, I.C. Gerber and J.G. Ángyán, J.Chem. Phys. **124**,154709 (2006).

[231] M. Marsman, J. Paier, A. Stroppa and G. Kresse, J. Phys.: Condens. Matter, **20**, 064201 (2008).

[232] A. Stroppa and G. Kresse, Phys. Rev. B, **79**, 201201(R) (2009).

[233] C. Franchini, G. Kresse and R. Podloucky, Phys. Rev. Lett., **102**, 256402 (2009).

[234] J.A. Chan, S. Lany, A. Zunger, Phys. Rev. Lett., **103**, 016404, (2009).

[235] J.L. Lyons, A. Janotti, C.G. Van de Walle, Appl. Phys. Lett., **95**, 252105 (2009).

[236] S. Lany, A. Zunger, Phys. Rev. B, **80**, 085202 (2009).

[237] S. Lany, Phys. Status Solidi B, **248**, 1052 (2011).

[238] J.L.Lyons, A. Janotti, C.G. Van de Walle, Phys. Rev. B, **80**, 205113 (2009).

[239] S. Lany, A. Zunger, Phys. Rev. B, **78**, 235104 (2008).

[240] O.F. Schirmer, J. Phys.: Condens. Matter, **18**, R667 (2006).

[241] A.M. Stoneham, J. Gavartin, A.L. Shluger, A.V. Kimmel, D. Munõz Ramo, H.M. Rønnow, G. Aeppli, C. Renner, J. Phys.: Condens. Matter, **19**, 255208 (2007).

[242] M. Avezac, M. Calandra, F. Mauri, Phys. Rev. B, **71**, 205210 (2005).

[243] J.G. Harrison, R.A. Heaton, C.C. Lin, J. Phys. B, **16**, 2079 (1983).

[244] M.R. Pederson, R.A. Heaton, C.C.Lin, J.Chem Phys., **80**, 1972 (1980).

[245] M.R. Pederson, R.A. Heaton, C.C.Lin, J.Chem Phys., **82**, 2688 (1985).

[246] A. Filippetti, C.D. Pemmaraju, P. Delugas, D. Puggioni, V. Fiorentini, S. Sanvito, arXiv:1106.5993v1.

[247] V. Pardo and W. E. Pickett, Phys. Rev. B, **78**, 134427 (2008).

[248] I.S. Elfimov, A. Rusydi, S.I. Csiszar, Z. Hu,H.J. Lin, C.T. Chen, R. Liang, G.A. Sawatzky, Phys. Rev. Lett., **98**, 137202 (2007).

[249] R. Englman, *The Jahn-Teller Effect In Molecules And Crystals* (John Wiley, London, 1972).

[250] B. H. Rose and L. E. Halliburton, J. Phys. C: Solid State Phys., **7**, 3981 (1974).

[251] L. A. Kappers, F. Dravnieks and J. E. Wertz, J. Phys. C: Solid State Phys., **7**, 1387 (1974).

[252] M. Nolan, G. Watson, Surf. Science, **586**, 25 (2005).

[253] J.L Lyons, A. Janotti, C.G. van de Walle, Appl. Phys. Lett., **97**, 152108 (2010).

[254] S. Lany, A. Zunger, Appl. Phys. Lett., **96**, 142114 (2010).

[255] M.A. Reshchikov, H. Morkoc, J. Appl. Phys., **97**, 061301 (2005).

[256] G.N. Aliev, S. Zeng, J.J. Davies, D. Wolverson, S.J. Bingham, P.J. Parbrook, T. Wang, Phys. Rev. B **71**, 195204 (2005).

[257] G.N. Aliev, S. Zeng, J.J. Davies, D. Wolverson, S.J. Bingham, P.J. Parbrook, T. Wang, Phys. Stat. Sol. (c) **3**, 1892 (2006).

[258] B.B. Straumal, A.A. Mazilkin, S.G. Protasova, A. A. Myatiev, P.B, Straumal, G. Schütz, P.A. van Ajen, E. Goering, B. Baretzky, Phys. Rev B, **79**, 205206 (2009).

[259] K.P. McKenna, A. Shluger, Proc. R. Soc. A, **467**, 2043 (2011).

[260] W. Körner, C. Elsässer, Phys. Rev. B, **81**, 085324 (2010).

[261] J.M.D Coey, K. Wongsaprom, J. Alaria, M. Venkatesan, J. Phys. D: Appl.Phys., **41**, 134012 (2008).

[262] P. Soven, Phys. Rev, **156**, 809 (1967).

[263] M.A. Paalanen, S. Sachev, R.N. Bhatt, A.E. Ruckenstein, Phys. Rev. Lett., **57**, 2061 (1986).

[264] M.J. Hirsh, D.F. Holcomb, R.N. Bhatt, M.A. Paalanen, Phys. Rev. Lett., **68**. 1418 (1988).

[265] M.A. Paalanen, J.E. Graebner, R.N. Bhatt, S. Sachev, Phys. Rev. Lett., **61**, 597 (1998).

[266] R.N. Bhatt, P.A. Lee, Phys. Rev. Lett. **48**, 344 (1982).

[267] M.A. Paalanen, R.N. Bhatt, S. Sachev, Physica B, **169**, 223 (1991).

[268] M. Milovanovíc, S. Sachev, R.N. Bhatt, Phys. Rev. Lett., **63**, 82 (1989).

[269] M .A. Tusch and D.E. Logan, Phys. Rev B **48**, 14843 (1993).

[270] S. Doniach, E.H. Sondheimer, *Green's Functions for Solid State Physicists* (Imperial College Press, London, 1998).

[271] D.G. Rowan, Y.H. Szczech, M.A. Tusch, D.E. Logan, J. Phys.: Condens. Matter **7**, 6853 (1995).

[272] T. Moriya, *Spin Fluctuations in Itinerant Electron Magnetism* (Springer-Verlag, Berlin-Heidelberg, 1985).

[273] D.R. Penn, Phys. Rev., **142**, 350 (1966).

[274] J.E. Hirsch, Phys. Rev. B, **31**, 4403 (1985).

[275] P. Ring, P. Schuck, *The Nuclear Many-Body Problem*,Third Edition (Springer-Verlag, Berlin-Heidelberg, 2004).

[276] J.M. Eisenberg, W. Greiner, *Nuclear Theory Vol.1: Nuclear Models*, Third Edition (North Holland Physics Publ., Elsevier Science Publishers, Amsterdam, 1988).

[277] M. Berciu, R.N. Bhatt, Phys. Rev. B, **66**, 085207 (2002).

[278] Y.H. Szczech, M.A. Tusch, D.E. Logan, J. Phys.: Condens. Matter **9**, 9621 (1997).

[279] A.L. Fetter, J.D. Walecka, *Quantum Theory of Many-Particle Systems* (Dover Publications Inc., New York, 2003).

[280] J.W. Negele, H. Orland, *Quantum Many-Particle System* (Advanced Book Program, Westview Press, US, 1998).

[281] C. Dasgupta, J.W. Halley, Phys. Rev. B **47**, 1126 (1993).

[282] M. Berciu, R.N. Bhatt, Phys. Rev. B, **69**, 045202 (2004).

[283] T.M. Chang, J.D. Bauer, J.L. Skinner, J. Chem. Phys., **93**, 8973 (1990).

[284] J.M.D. Coey, *Magnetism and Magnetic Materials* (Cambridge University Press, Cambridge, 2010).

[285] F.F. Assaad, H.G. Evertz, in *Computational Many-Particle Physics*, edited by H. Fehske, R. Schneider, A. Weiße, Lecture Notes in Physics (Springer-Verlag, Berlin-Heidelberg, 2008).

[286] R.R. dos Santos, Braz.J. Phys. **33**, 36 (2003), cond-mat/0303551.

[287] R.S. White, D.J. Scalapino, R.L. Sugar, E.Y. Loh, J.E. Gubernatis, R.T. Scalettar, Phys. Rev. B, **40**, 506 (1989).

[288] J.E. Gubernatis, M. Jarrel, R.N. Silver, D.S. Sivia, Phys. Rev. B, **44**, 6011 (1991).

[289] M. Jarrell, J.E. Gubernatis, Physics Reports, **269**, 133 (1996).

[290] J.E. Hirsch, R.M. Fye, Phys. Rev. Lett., **56**, 2521 (1986).

[291] A.C. Hewson, *The Kondo Problem to Heavy Fermions*, Cambridge studies in Magnetism (Cambridge University Press, Cambridge, 1997).

[292] A. Hurley, N. Baadji, S. Sanvito, Phys. Rev. B, **84**, 035427 (2011).

[293] A. Hurley, N. Baadji, S. Sanvito, Phys. Rev. B, **84**, 115435 (2011).

[294] J.E. Hirsch, Phys. Rev. B, **28**, 4059 (1983).

[295] R. Blankenbecler, D.J. Scalapino, R.L. Sugar, Phys. Rev. D, **24**, 2278 (1981).

[296] R.T. Scalettar, R.M. Noack, R.R.P. Singh, Phys. Rev. B, **44**, 10502 (1991).

[297] R. Hlubina, S. Sorella, F. Guinea, Phys. Rev. Lett., **78**, 1343 (1997).

[298] G. Sugiyama, S. Koonin, Annals of Physics , **168**, 1 (1986).

[299] S. Sorella, S. Baroni, R. Car, M. Parrinello, Europhys. Lett., **8**, 663 (1989).

[300] S. Sorella, E. Tosatti, S. Baroni,R. Car,M. Parrinello, Int. J. Mod. Phys. B, **1**, 993 (1989).

[301] N. Furukawa, M. Imada, J. Phys. Soc. Jpn., **60**, 3669 (1991).

[302] M. Feldbacher, F.F. Assaad, Phys. Rev. B, **63**, 073105 (2001).

[303] R.K. Bryan, Eur. Biophys. J., **18**, 165 (1990).

[304] http://komet337.physik.uni.mainz.de/Bluemer/Codes/MEM.

[305] S.R. White, Phys. Rev. B, **44**, 4670 (1991).

[306] S.R. White, Phys. Rev. B, **46**, 5678 (1992).

[307] N. Bulut,D.J. Scalapino, S.R. White, Phys. Rev. Lett., **73**, 748 (1994).

[308] A. Moreo, D.J. Scalapino, R.L. Sugar, S.R. White, N.E. Bickers, Phys. Rev. B, **41**, 2313 (1990).

[309] C.N. Varney, C.-R. Lee,Z.J. Bai,S. Chiesa,M. Jarell, R.T. Scalettar, Phys. Rev. B, **80**, 075116 (2009).

[310] M.B. Walker, Th.W. Ruijgrok, Phys. Rev., **171**, 513 (1968).

[311] H. Feldner, Z.Y. Meng, A. Honecker, D. Cabra, S. Wessel, F.F. Assaad, Phys. Rev. B, **81**, 115416 (2010).

[312] H. Feldner, Z.Y. Meng, T.C. Lang, F.F. Assaad, S. Wessel, A. Honecker, Phys. Rev. Lett., **106**, 226401 (2011).

[313] S. Bhattacharya, M.S. Ferreira, S. Sanvito, J. Phys.: Condens. Matter, **23**, 316001 (2011).

[314] M. Ruben, private communication.

[315] G. Poneti, A. Dei, R. Sessoli, private communication.

[316] A. Hauser, J. Chem. Phys.,**94**,2741 (1991).

[317] E. Buhksm G. Navon, M. Bixon, J. Jortner, J. Am. Chem. Soc., **102**, 1918 (1980).

[318] S. Zein, S.A. Borshch, P. Fleurat-Lessard, M.E. Casida, H. Chermette, J. Chem. Phys., **126**, 014105 (2007).

[319] M. Swart, A. Groenhof, A.W. Ehlers, K. Lammertsma, J. Phys. Chem. A, **108**, 5479 (2004).

[320] M. Reiher, Inorg. Chem., **41**, 6928 (2002).

[321] M. Reiher, O. Salomon, B.A. Hess, Theor. Chem. Acc., **107**, 48 (2001).

[322] G. Ganzenmüller, N. Berkaïnem A. Fouqueau, M.E. Casida, M. Reiher, J. Chem. Phys., **122**, 234321 (2005).

[323] L.M.L. Daku, A. Vargas, A. Hauser, A. Fouqueau, M.E. Casida, Chem. Phys. Chem., **6** , 1393 (2005).

[324] M. Güell, J.M. Luis, M.Solá, M. Swart, J. Phys. Chem. A, **112**, 6384 (2008).

[325] G. Makov, M.C. Payne, Phys. Rev. B, **51**, 4014 (1995).

[326] M. Kepenekian, B. Le Guennic, V. Robert, J. Am. Chem. Soc., **131**, 11498 (2009).

[327] M. Kepenekian, B. Le Guennic, V. Robert, Phys. Rev. B, **79**, 094428 (2009).

[328] A. Fouqueau, S. Mer, M. Casida, L.M.L. Daku, A. Hauser, T. Mineva, F. Neese, J. Chem. Phys., **120**, 9473 (2004).

[329] A. Fouqueau, M. Casida, L.M.L. Daku, A. Hauser, F. Neese, J. Chem. Phys., **122**, 044110 (2005).

[330] M.E. Jacox, Chem. Soc. Rev., **31**, 108 (2002).

[331] D. Gatteschi, R. Sessoli, J. Villain, *Molecular Nanomagnets* (Oxford University Press, Oxford, 2006)

[332] P.J. Hay, W.R. Wadt, J. Chem. Phys., **82**, 270 (1985).

[333] A. Schäfer, C. Huber, R. Ahlrichs, J. Chem. Phys., **100**, 5829 (1994).

[334] K. Pierloot, S. Vancoilie, J. Chem. Phys., **125**, 124303 (2006).

[335] H. Bolvin, J. Phys. Chem. A, **102**, 7525 (1998).

[336] A.D. Becke, J. Chem. Phys., **98**, 5648 (1993).

[337] http://www.nwchem-sw.org/index.php.

[338] V.A. Money, J. Elhaïk, M.A. Halcrow, J.A.K. Howard, Dalton Trans., **10**, 1516 (2004).

[339] O. Sato, S. Hayami, Z.-Z. Gu, K. Seki, R. Nakjima, A. Fujishima, Chem. Phys. Lett., **355**, 169 (2002).

[340] P. Dapporto, A. Dei, G. Poneti, L. Sorace, Chem. Eur. J., **14**, 10915 (2008).

[341] G. Poneti et al., Angew. Chem. Int. Ed., **49**, 1954 (2010).

[342] C. Toher, A. Filippetti, S. Sanvito, K. Burke, Phys. Rev. Lett., **95**, 146402 (2005).

[343] A. Bencini et al., J. Mol. Struc., **656**, 141 (2003).

[344] A. Beni, A. Dei, S. Laschi, M. Rizzitano, L. Sorace, Chem. Eur. J., **14**, 1804 (2008).

[345] S.G. Boxer, J. Phys. Chem. B, **113**, 2972 (2009).

Appendix A

Publications stemming from this work

• Predicting d0 magnetism: self-interaction correction scheme, A. Droghetti, C.D. Pemmaraju and S. Sanvito, Phys. Rev. B **78**, 140404(R) (2008).

• Electron doping and magnetic moment formation in N- and C-doped MgO, A. Droghetti and S. Sanvito, Appl. Phys. Lett. **94**, 252505 (2009).

• Polaronic distortion and vacancy-induced magnetism in MgO, A. Droghetti, C.D. Pemmaraju, and S. Sanvito, Phys. Rev. B **81**, 092403 (2010).

• Electric field control of valence tautomeric interconversion in Cobalt Dioxolene, A. Droghetti and S. Sanvito, Phys. Rev. Lett. **107**, 047201 (2011).

• Impurity band magnetism in oxides, A. Droghetti and S .Sanvito, in preparation.

•*Ab-initio* study of small ions $[Fe(H_2O)_6]^{2+}$, $[Fe(NH_3)_6]^{2+}$ and $[Fe(NCH)_6]^{2+}$, A. Droghetti, D. Alfè and S. Sanvito, in preparation.

•*Ab-initio* study of the spin crossover molecule $[FeL_2]^{2+}$ (L=2,6-dypirazol-1-yl-4-hydroxymethylpyridine), A. Droghetti, D. Alfè and S. Sanvito, in preparation.